POLITECNICO DI MILANO

SCUOLA DI INGEGNERIA INDUSTRIALE E DELL'INFORMAZIONE

CORSO DI LAUREA MAGISTRALE IN INGEGNERIA SPAZIALE

Multi-Function Thermal Protection Systems for Aerogravity Assist Missions to the Outer Planets

Lyle Campbell
Numero Matricola: 925564

Relatore:
Prof. Michele Lavagna

Anno accademico 2021/22

Abstract

The gravity assist (GA) is a technique used to increase the orbital energy of interplanetary spacecraft without propellant. A spacecraft can fly close to a celestial body and exchange momentum with the body via gravitational interaction. This momentum exchange slows the massive body imperceptibly, while greatly accelerating the comparatively tiny spacecraft. Several km/s of velocity can easily be gained by the spacecraft 'for free', with more massive planets providing larger velocity changes. The aerogravity assist (AGA) is an extension of the GA technique, whereby the spacecraft enters the atmosphere of the body and flies 'upside down'. The inverted lift force can be thought of as a way to artificially increase the gravity of smaller bodies and increase the benefit of a flyby. Vehicles with high aerodynamic efficiency at hypersonic speeds, and low-drag thermal protection systems capable of handling severe thermal fluxes will be required in order to realise the potential gains of such flybys. This work explores in-depth the previously introduced Thermal AGA (TAGA) concept [1], in which a leading-edge coolant such as water absorbs high aerodynamic heat loads through vaporisation before being expelled for propulsion. Additional endothermic processes and multi-function thermal protection system concepts are explored, resulting in the proposal of an AGA mission with electric propulsion (AGA-EP). The AGA-EP concept is motivated by the incredible heat absorption capabilities of lithium, as well as ongoing research into use of lithium as a propellant for gridded ion thrusters. An interplanetary trajectory to Uranus with an AGA at Mars is defined, a detailed sensitivity analysis of the AGA flyby is conducted, and the preliminary sizing of a thermal protection system for a suitable vehicle geometry is completed. The payload delivery capability of an AGA-EP vehicle to Uranus appears to be competitive with traditional non-atmospheric spacecraft while no longer requiring a Jupiter gravity assist, opening up launch windows every 2-3 years rather than every 12-13 years when Jupiter and Uranus are aligned.

Sinossi

La fionda gravitazionale (Gravity Assist, GA) è una tecnica utilizzata per incrementare l'energia dell'orbita dei veicoli spaziali interplanetari senza l'uso di propellente. Una navicella spaziale, volando nelle vicinanze di un corpo celeste, scambia quantità di moto con il corpo per gravità. Questo scambio di quantità di moto rallenta impercettibilmente il corpo massiccio, mentre accelera notevolmente la navicella spaziale relativamente più piccola. Diversi km/s di velocità possono essere facilmente raggiunti dal veicolo spaziale "gratuitamente", con pianeti più massicci che forniscono cambiamenti di velocità maggiori. L'Aerogravity Assist (AGA) è un'estensione della tecnica GA, in cui però la navicella, entrando nell'atmosfera del corpo, vola "al contrario". La forza di portanza invertita può essere pensata come un modo per aumentare artificialmente la gravità dei corpi più piccoli, traendo maggior profitto da una fionda gravitazionale. Saranno necessari veicoli con elevata efficienza aerodinamica a velocità ipersoniche e sistemi di protezione termica a bassa resistenza in grado di gestire forti flussi termici per poter ottenere i potenziali guadagni di tali passaggi ravvicinati. Questo lavoro esplora in modo approfondito il Thermal AGA (TAGA) precedentemente introdotto [1], in cui un refrigerante all'avanguardia come l'acqua assorbe elevati carichi di calore aerodinamico attraverso la vaporizzazione, prima di essere espulso per la propulsione. Vengono esplorati ulteriori processi endotermici e sistemi di protezione termica multifunzione, con conseguente proposta di una missione AGA dotata di propulsione elettrica (AGA-EP). Il concetto AGA-EP è motivato dalle incredibili capacità di assorbimento del calore del litio, nonché dalla continua ricerca sull'uso di quest'ultimo come propellente per i propulsori ionici a griglia. Viene poi definita una traiettoria interplanetaria verso Urano con un AGA su Marte ed in seguito viene condotta un'analisi di sensibilità dettagliata del flyby AGA. Infine, viene completato il dimensionamento preliminare di un sistema di protezione termica per una geometria adeguata del veicolo. La capacità portante del carico utile di un veicolo AGA-EP su Urano sembra essere competitiva rispetto ai tradizionali veicoli spaziali non atmosferici, pur non richiedendo più l'assistenza gravitazionale di Giove, aprendo finestre di lancio ogni 2-3 anni anziché ogni 12-13 anni quando Giove e Urano sono allineati.

Table of Contents

List of Figures

List of Tables

Nomenclature

Acronyms

AGA	AeroGravity Assist
AGA-EP	AeroGravity Assist with Electric Propulsion
CAD	Computer Aided Design
CEA	Chemical Equilibrium with Applications software
CMC	Ceramic Matrix Composite
DARPA	Defense Advanced Research Projects Agency
EP	Electric Propuslion
GA	Gravity Assist
GNSS	Global Navigation Satellite System
MAGA	Mars AeroGravity Assist
MLI	Multi-Layer Insulation
MMC	Metal Matrix Composite
NASA	National Aeronautics and Space Administration
RCC	Reinforced Carbon-Carbon
RTG	Radioisotope Thermoelectric Generator
TAGA	Thermal AeroGravity Assist
TPS	Thermal Protection System

Symbols, Latin Alphabet

a	Acceleration	m/s^2
A	Flow cross section	m^2
A_t	Nozzle throat cross section area	m^2
AU	Astronomical Unit, 1 AU = 149.6 x 10^6	km
B_v	Blackbody radiative intensity	W/sr
c	Propulsion exhaust velocity	m/s
c*	Combustion chamber characteristic velocity	m/s
$\bar{c}$	Mean atomic/molecular velocity	m/s
C_3	Characteristic energy	km^2/s^2
C_D	Coefficient of drag	
C_f	Friction coefficient	
C_F	Thrust coefficient	
C_H	Stanton number	
C_L	Coefficient of lift	
C_P	Pressure coefficient	
C_w	Chapmin-Rubesin parameter	
d	Diameter	m
D	Drag force	N
Da	Damköhler number	
e	Orbital eccentricity	
E	Energy emission density	W/m^3
E	Elastic modulus	N/m^2
g_0	Gravitational acceleration at Earth's surface	m/s^2
h	Heat transfer coefficient	W/m^2K
h	Specific enthalpy	J/kg
h_{aw}	Adiabatic wall specific enthalpy	J/kg
h_{vap}	Specific enthalpy of vaporisation	J/kg
H	Nozzle-target separation distance	[m]
H_s	Specific stagnation enthalpy	J/kg
I_{SP}	Specific impulse	s
J	Emission coefficient	
k	Thermal conductivity	W/m.K

K_n	Knudsen number	
L	Length of aerodynamic surface	m
L	Thickness of wall for thermal analysis	m
L	Lift force	N
L/D	Lift-to-drag ratio	
L/D_{eff}	Effective lift-to-drag ratio	
M	Mach number	
M	Molecular mass	kg/mol
M_0	Spacecraft mass before propulsive manoeuvre	kg
M_f	Spacecraft mass after propulsive manoeuvre	kg
M_n	Normal component of Mach number	
M	Spacecraft mass	kg
$\dot{m}$	Mass flow rate	kg/s
P	Pressure	Pa
P_0	Total pressure	Pa
Pr	Prandtl number	
q, q_w	Heat flux	W/m^2
r	Radius	m
Re_x	Local Reynolds number	
Re_L	Global Reynolds number	
R_M	Molecular gas constant	m^2/s^2K
r_p	Periapsis radius	km
T	Thrust	N
T	Temperature	K
T_0	Total temperature	K
T/D	Thrust-to-drag ratio	
u	Component of gas flow velocity normal to an oblique shock	m/s
v	Velocity	m/s
v_∞	Hyperbolic escape/excess velocity	km/s
v_p	Periapsis velocity	km/s
w	Component of gas flow velocity parallel to an oblique shock	m/s
x	Linear distance	m

Symbols, Greek Alphabet

α	Angle of attack	radians
α	Flyby departure angle	radians
α	Coefficient of thermal expansion	K^{-1}
β	Oblique shock angle	radians
γ	Ratio of specific heats	
Γ	Radiation loss parameter	
δ	Shock stand-off distance	m
δ	Flyby deflection angle	radians
δ_{atm}	Atmospheric defection angle during an AGA	radians
Δv	'Delta-V', change in spacecraft velocity	km/s
ε	Emissivity	
θ	Deflection angle of supersonic flow	radians
κ	Thermal diffusivity	m^2/s
κ	Planetary atmospheric constant	
κ_v	Absorption coefficient	
Λ	Mean free path length	m
Λ_e	Leading edge sweep angle	
μ	Celestial body gravitational parameter	km^3/s^2
μ	Dynamic viscosity	Pa.s
ρ	Density	kg/m^3

σ	Stefan-Boltzmann constant	
σ	Surface tension	N/m
σ	Axial stress	N/m^2
υ	Poisson's ratio	

Subscripts

∞	Indicates free-stream gas properties
e	Indicates post-shock gas properties
w	Indicates properties of the wall

1 Introduction

1.1 Background

An Aero-Gravity Assist (AGA) is a proposed modification to the well-understood Gravity Assist (GA) manoeuvre which is used to increase the heliocentric orbital energy of spacecraft without propellant usage [2] [3]. Different to a GA, in which the spacecraft remains outside planetary atmospheres, during an AGA manoeuvre the 'aerospacecraft' enters the upper atmosphere of a planet and flies 'upside down', generating a lift vector pointing towards the centre of the planet. This inverted lift force provides the centripetal acceleration required to keep the vehicle on a constant altitude 'orbit' at speeds greater than the planet's escape velocity. A much greater rotation of the incoming velocity vector is then possible, even at the small inner planets [4]. The difference between a regular GA and an AGA is illustrated in Figure 1.

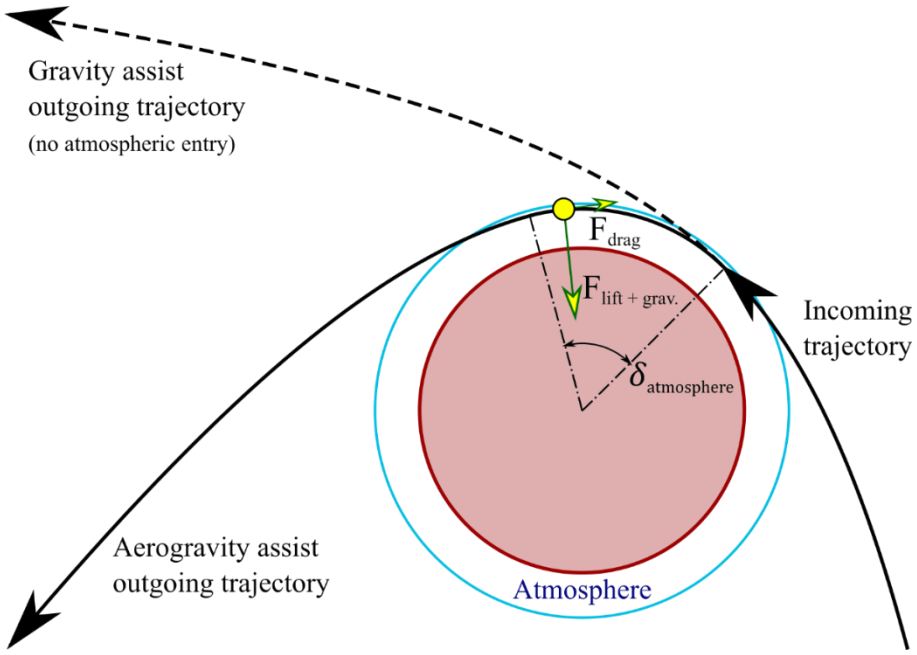

Figure 1 – Typical GA and AGA trajectories in a planetocentric frame.

This increased rotation in the planetocentric frame manifests as a large delta-V in the heliocentric frame. In theory, a delta-V equal to double the flyby hyperbolic escape velocity can be achieved. Thus, AGA can reduce the Earth departure C_3 requirement of interplanetary missions, allowing spacecraft to be more massive for a given launcher. AGA's are particularly well suited to high energy missions, such as those visiting the outer planets or closely approaching the Sun. A key advantage of an AGA is that it can remove the need for GA's at large outer planets like Jupiter, greatly increasing the frequency of launch windows. With AGA manoeuvres, a launch window to the Ice Giants or Pluto occurs approximately every 2 years via a Mars AGA, rather than every 12 years via a Jupiter GA [2] [3].

Figure 1 presents just one realisation of an AGA. AGA's can also be used to implement heliocentric plane changes [5]. Orbital plane changes are propellant-intensive manoeuvres which are necessary for particular missions such as surveying the poles of the Sun or visiting celestial bodies in high-inclination orbits. Additionally, the atmospheric phase of an AGA flyby is not restricted to a fixed altitude, and the flight profile can be varied arbitrarily depending on the mission requirements.

The main disadvantage of an AGA is the increased complexity of the vehicle, as well as several unique technological challenges which must be overcome. The first is the development of a low-drag thermal protection

shaped for hypersonic flight. All of the orbital-class thermal protections systems (TPS) developed to date have been for vehicles with small hypersonic L/D ratios and blunt body shapes. For an efficient AGA, long and slender wedge-shaped vehicles called waveriders will likely be required, as they can achieve greater hypersonic L/D ratios. However, waveriders require sharp leading edges, which will be subject to significantly higher thermal fluxes than any other previous spacecraft. Such a radically different spacecraft shape will also likely create numerous architecture and system configuration problems. Spacecraft have historically been compact designs somewhat resembling cuboids or cylinders, while a waverider will require a much flatter and longer packaging of its systems. Finally, robust guidance and control strategies must be developed.

1.2 Research Objective

The AGA concept and useful trajectories have been preliminarily demonstrated in the literature [2] [3] [4] [6] with the assumption that an aerospacecraft with sufficient aerodynamic performance can be created. Additionally, the aerodynamic shapes required to generate the requisite high lift-to-drag ratios in the hypersonic regime have been developed and proposed, namely waveriders [7] [8] [9] [10]. The results of these previous works appear promising, but they depend strongly on the validity of assumptions regarding practical vehicle shapes, masses, and thermal protection system (TPS) performance.

In order to explore the AGA concept further and progress the state of the art, these assumptions must be tested. This present work focuses in particular on the TPS of an AGA waverider. The sensitivities of aerodynamic performance and overall mission performance to practical geometric, thermal, and mass considerations are probed in order to validate or invalidate some of the assumptions underlying the previous works.

The specific objectives of this work are to:

- Conduct a ‘pre-phase A’ level system analysis on the thermal protection system.
    - Identify an interplanetary trajectory which exploits the benefits of AGAs, as example.
    - Create a steady-state aerothermal model of a representative flat-plate flying a low-energy AGA trajectory.
    - Estimate thermal fluxes on key regions of the vehicle via engineering correlations.
    - Select vehicle dimensions which balance thermal and aerodynamic performance.
- Propose thermal protection system architecture(s).
    - Propose technologies for the nose, leading edge, and acreage regions.
    - Model thermal behaviour using engineering correlations and steady state 1D models.
    - Estimate material thicknesses, fluid flow rates, system pressures etc.
    - Identify opportunities for re-use of the TPS, or integration with other vehicle systems.
- Evaluate important metrics for thermal protection systems architecture(s).
    - Mass
    - Volume
    - Power
    - Influence on other vehicle sub-systems
- Comment on the concept feasibility and propose topics for further investigation.

The feasibility of an AGA mission is evaluated by comparing the payload mass that could be delivered by an AGA vehicle to the payload mass that could be delivered by a more traditional non-atmospheric spacecraft. Comparable mission profiles are assumed for both cases. Several early-stage mission proposals are taken as references. The other advantages of AGA are of questionable value if this fundamental criteria cannot be satisfied.

1.3 Report Overview

Chapter 2 provides a brief review of GAs and then progresses to a more detailed consideration of AGAs. A recent evolution of AGAs, the Thermal Aerogravity Assist (TAGA), is discussed. Finally, an introduction to the Tisserand plane is given, and its uses for planning AGA missions is explored.

Chapter 3 gives a background on hypersonic waveriders and presents selected results from the literature which outline the predicted capabilities of these vehicles. Two real-world hypersonic vehicles are discussed as case studies, with the goal of providing context for later discussions. The unique challenges involved with designing an AGA waverider are explained further.

Chapter 4 is a short overview of the state of the art in aerospace thermal protection systems. The basic physical principles of the most common schemes are introduced, with emphasis being given to the systems typically employed on hypersonic aircraft and orbital re-entry vehicles.

The original work of this report begins in Chapter 5, in which various energy-absorbing processes are analysed and considered for use in a combined thermal protection / propulsion system. Both the energy absorption capabilities and propulsion capabilities are considered for the most promising materials.

Chapter 6 begins by introducing the Uranus reference missions. Representative aerodynamic properties for the waverider vehicle are selected based on trends from the literature, and the Tisserand plane is used to plan AGA missions comparable to the non-atmospheric reference missions.

Chapter 7 details the MATLAB model that was created to analyse the atmospheric flight phase of the AGA. The aerodynamic, gas-dynamic, and thermal sub-routines are explained in detail and validated against comparable studies from the literature. Upper and lower limits of various vehicle geometric parameters are selected and justified, as well as the vehicle mass and maximum thermal loads. A sensitivity analysis is conducted by sweeping through all the vehicle geometry permutations and evaluating the effect on numerous variables such as peak thermal fluxes, total absorbed heat load, and aerodynamic efficiency. One geometry is selected for a more detailed analysis in the following TPS chapter.

Chapter 8 takes requirements from the sensitivity analysis and proposes a TPS architecture which balances peak thermal fluxes, coolant loads, and total TPS mass. A discretised TPS solution is proposed with a combination of passive and active cooling strategies employed in different regions of the vehicle. The AGA TPS and payload masses are estimated and compared to the reference missions.

Chapter 9 summarises the results of this work, discusses the limitations in the analysis, and proposes topics for future work.

2 Review of Planetary Flybys

Travel in space is governed by the gravitational forces of the Sun and celestial bodies. Modifications to orbital characteristics such as eccentricity, semi-major axis, or orbital energy occur by changing the velocity of the spacecraft at given points in space and time.

These velocity changes can be implemented by variety of different mechanisms and over a wide range of time scales. All methods involve expelling mass from the spacecraft or interacting with the space environment. Chemical propulsion systems create hot gases via chemical reactions within the spacecraft before accelerating and expelling the gases via a gas-dynamic nozzle. They operate for seconds to minutes at a time, generating exhaust velocities of about 2-5 km/s and thrust levels ranging from about 0.1N to several MN [11]. Electric propulsion systems typically ionise a gas and then accelerate it to between 10-50 km/s using electric and/or magnetic fields [11]. These high efficiency electrical systems generate thrusts on the order of μN and mN and must operate for months or years at a time. Solar sails are also in development, which function by deflecting incoming photons, changing the momentum of both the photons and the spacecraft. They don't require any propellant, but do require long periods of operation as they can typically only generate vehicle accelerations on the order of $\mu m/s^2$ [12].

While these systems operate on different physical principles and time scales, they all require hardware on the spacecraft, be it propellant tanks and thrusters, or deployable sail structures. Gravity assists from planetary flybys can provide this 'free' velocity change via a gravitational interaction.

2.1 Gravity Assist

Gravity assists have been implemented on virtually all deep-space missions to date as a way to reduce the required Earth escape speed and spacecraft propellant load, thus increasing the scientific payload mass. The spacecraft flies close to a celestial body and exchanges kinetic energy in the heliocentric frame. The topic has been covered in detail in numerous texts [13] [14]. In a standard gravity assist, the vehicle does not enter the atmosphere of the planet, should one exist. Figure 2 illustrates the general concept.

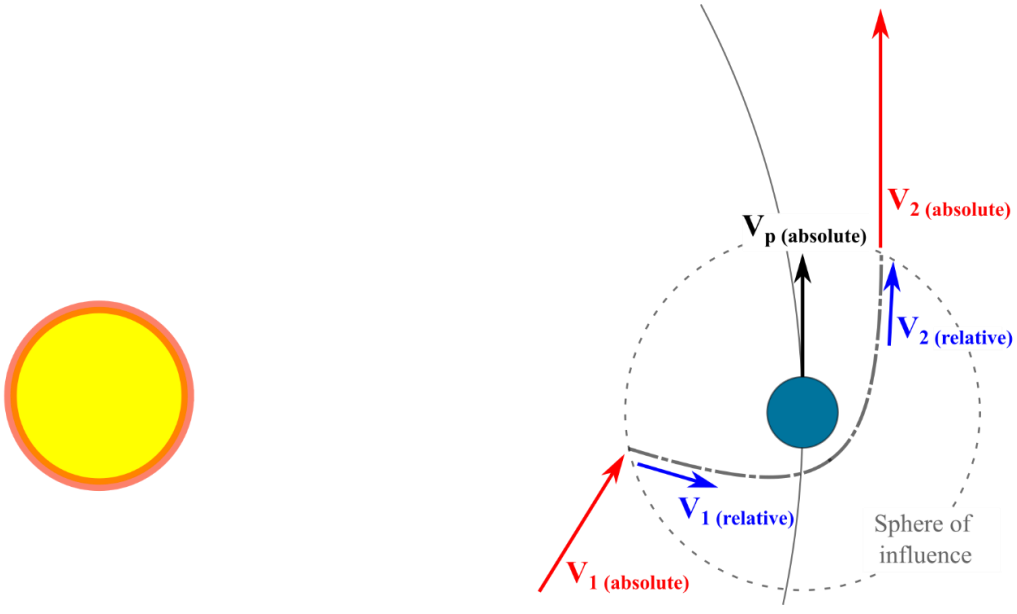

Figure 2 –Planetary flyby gravity assist schematic.

Velocity triangles are typically used to analyse the velocity or energy gains from a GA. Again, this topic is detailed in the aforementioned references. The rotation of a vector can be represented by a 'difference vector' connecting the endpoints before and after the rotation. The magnitude of this vector provides the ΔV. It is clear from Figure 3 that larger hyperbolic velocities and larger flyby deflections result in a large ΔV vector.

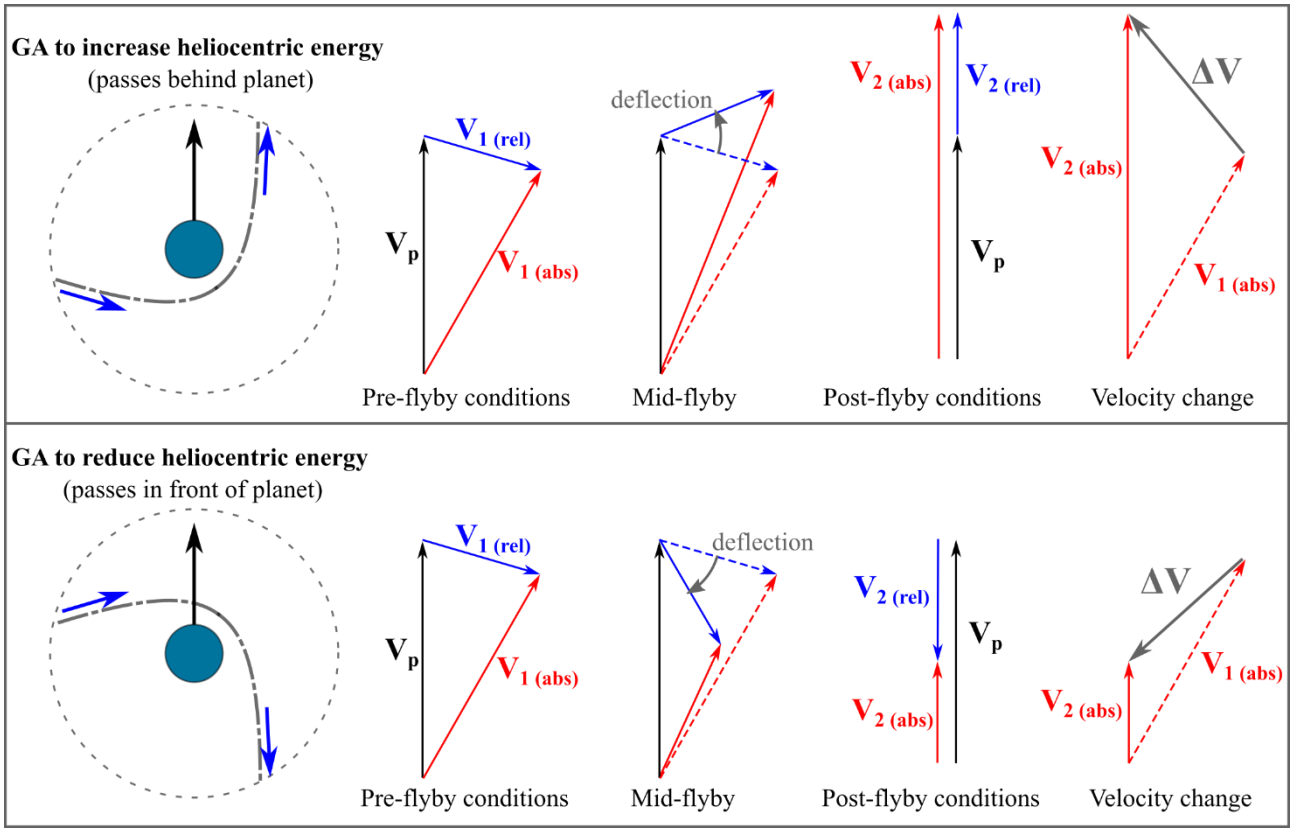

Figure 3 – Velocity triangles for gravity assists. Adapted from [4].

If the goal of a GA is to implement a large heliocentric plane change or change in heliocentric energy, a key performance parameter is the planetocentric deflection angle that can be achieved with a given relative velocity. Higher deflections at higher relative speeds result in 'stronger' gravity assists, which produce larger velocity changes in the heliocentric frame. Equations 1 and 2 characterise gravity assist deflections in the planet frame.

$$e = 1 + \frac{r_p \, v_\infty^2}{\mu} \qquad 1$$

$$\delta = 2 \sin^{-1}\left(\frac{1}{e}\right) \qquad 2$$

From Equation 2 it is clear that a large deflection angle δ requires a small eccentricity e. From Equation 1, it can be seen that in order to achieve a small eccentricity, the flyby periapsis r_p should be small, the hyperbolic escape velocity v_∞ should be small, and/or the planet gravitational parameter μ should be large. The ratio of a planet's surface radius to its gravitational parameter indicates how favourable a planet is for a strong gravity assist, with a small ratio being better. The motivation for a Jupiter flyby can be seen clearly in Table 1.

	Surface radius [km]	μ [km^{3}s^{-2}]	r/μ	δ (v_∞ = 1 km/s)	δ (v_∞ = 10 km/s)
Mars	$4.28 * 10^4$	3390	7.9×10^{-2}	135°	13°
Earth	$3.99 * 10^5$	6371	1.6×10^{-2}	160°	45°
Jupiter	$1.27 * 10^8$	69911	5.5×10^{-4}	176°	143°

Table 1 – Parameters of selected planets and their gravity assist 'efficiency'.

As mentioned above, v_∞ should be small in order to achieve a high deflection angle. However, a large value of v_∞ is necessary to extract a large Δv from the GA. All planets can achieve the maximum flyby deflection of 180° if the escape velocity is zero. This produces a parabolic trajectory, which is not useful from a planetary exploration point of view as the spacecraft would simply enter a heliocentric orbit almost identical to that of the planet it is departing from. For high energy missions a high flyby velocity is needed, but as can also be seen

from Table 1, small planets rapidly lose deflection capability as the escape velocity increases. The aerogravity assist might be a method worth investigating more to overcome this gravitational deflection limit, provided that drag losses can be reduced to a low level.

2.2 Aerogravity Assist

At the periapsis of a non-circular orbital trajectory such as occurs during a GA, the high tangential velocity of the spacecraft demands a centripetal acceleration which is greater than the gravitational acceleration provided by the planet. Therefore, the spacecraft can't remain on a circular trajectory and it 'drifts' to higher altitudes, dumping its excess kinetic energy into gravitational potential energy. The basic concept of an aerogravity assist is to enter the atmosphere of the planet and use aerodynamic lift to bridge the 'acceleration gap', allowing the spacecraft to temporarily remain within the atmosphere and achieve a high flyby deflection angle. Figure 4 illustrates the different phases of an AGA, assuming a circular atmospheric trajectory for simplicity. In actuality, the atmospheric trajectory can be varied in 3D. It is important to note that the incoming and outgoing hyperbolic trajectories cannot be symmetric, as the spacecraft loses some speed and energy to aerodynamic drag. A vehicle with a hypersonic lift-to-drag ratio of at least about 2.33 [15] is necessary for a productive AGA flyby.

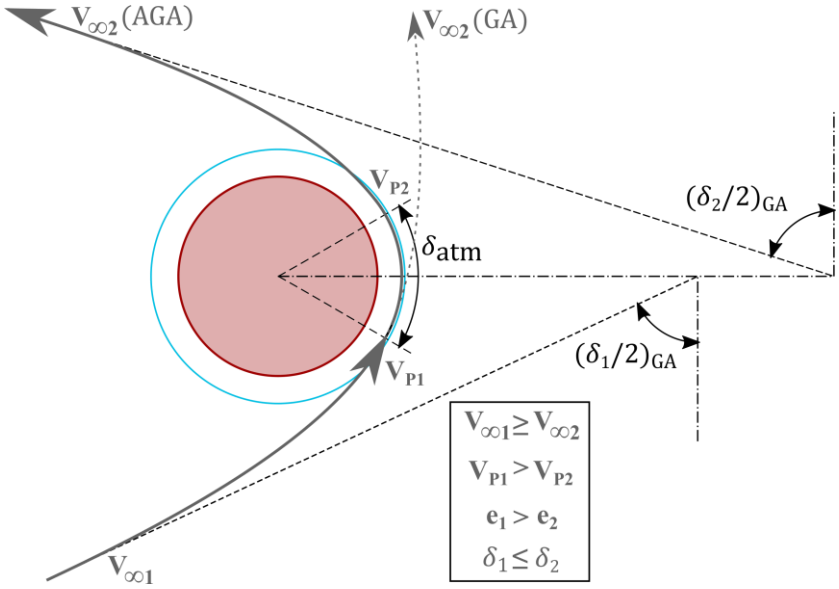

Figure 4 –Phases of an AGA with circular atmospheric trajectory. Adapted from [7].

Equations 3 and 4 [8] provide an analytical method of estimating the periapsis and escape velocity losses respectively. These equations assume a vehicle with constant lift-to-drag (L/D) ratio flying at a constant altitude over a given atmospheric deflection angle. As will be seen later, these assumptions do not degrade the prediction accuracy significantly, and they are suitable for the initial analyses conducted in this work.

$$v_{p2} = \sqrt{v_{p1}^2 * \ exp\left(\frac{-2\delta_{atm}}{L/D}\right) - \frac{\mu}{r_p}\left(exp\left(\frac{-2\delta_{atm}}{L/D}\right) - 1\right)} \quad (3)$$

$$v_{\infty 2} = \sqrt{v_{\infty 1}^2 * \ exp\left(\frac{-2\delta_{atm}}{L/D}\right) + \frac{\mu}{r_p}\left(exp\left(\frac{-2\delta_{atm}}{L/D}\right) - 1\right)} \quad (4)$$

The total deflection from an AGA flyby is the sum of the atmospheric deflection angle, the gravity-only deflection on the incoming half of the hyperbolic trajectory, and the gravity-only deflection on the outgoing half of the hyperbolic trajectory, recalling that the outgoing velocity is reduced due to drag losses. Equations 5 and 6 [7] combined with Figure 4 summarise the deflection calculation.

$$\delta_{TOT} = \delta_{atm} + \frac{\delta_{GA,in}}{2} + \frac{\delta_{GA,out}}{2} \quad (5)$$

$$\delta_{TOT} = \delta_{atm} + \sin^{-1}\left(\frac{1}{e_{in}}\right) + \sin^{-1}\left(\frac{exp\left(\frac{2\delta_{atm}}{L/D}\right)}{e_{out}}\right) \quad (6)$$

δ_{atm} can be selected to control the total deflection of an AGA flyby, depending on the mission requirements. Total deflection values even above 180° could be selected if high energy loss or aerocapture is desired. The vehicle L/D ratio and drag losses apply practical constraints to the maximum atmospheric flight angle for a productive flyby, as will be discussed in section 1.1. Typical interplanetary AGA missions analysed in the literature discuss atmospheric flight speeds of 10-20 km/s with L/D ratios of about 4-10 [6] [7] [8].

2.3 Thermal Aerogravity Assist

Relatively sharp leading edges are required to realise the high aerodynamic performance necessary for an AGA vehicle, and the combination of these small radii and super-orbital flight speeds produce large thermal fluxes. In the literature, leading edge radii in the range of 5–30 cm have been considered for vehicles of length 8-40 m flying at about 8-11 km/s in the Mars atmosphere [1] [15]. Using the engineering correlations of Tauber [16] for convective heating of stagnation points and leading edges during re-entry, the aforementioned works predicted peak thermal fluxes in the range of about 10-80 MW/m^2 for an AGA vehicle. At the trailing edge of these vehicles, the heat fluxes dropped to less than 1 MW/m^2. For context, the Space Shuttle Orbiter thermal tiles could handle heat fluxes of about 0.3 MW/m^2 on re-entry [17], while the actively cooled Space Shuttle Main Engine could handle heat fluxes up to 160 MW/m^2 [18].

Clearly, active cooling of the nose and leading edges will likely be required for an AGA vehicle. Several authors have mentioned in passing that a coolant could be used to absorb this heat via vaporisation and then expelled to produce thrust during the atmospheric flight phase. Murakami [1] was the first to analyse such a solution in detail, naming the developed technique a Thermal AeroGravity Assist (TAGA).

Murakami analysed a Mars TAGA vehicle which used water as the multi-purpose coolant/propellant. He took the Voyager 1 mission as a reference and aimed to find a TAGA mission which could match Voyager 1's post-Saturn flyby heliocentric orbital energy, but with a reduced Earth departure C_3. The proposed solution used a Mars TAGA followed by a Jupiter GA, and improved the allowable spacecraft launch mass on a Titan IIIE from Voyager 1's 930 kg to 3200 kg. Of the 3200 kg, 982 kg would be water, leaving 2124 kg for TPS dry mass and other spacecraft systems. Figure 5 illustrates the architecture of the cooling scheme envisioned by Murakami.

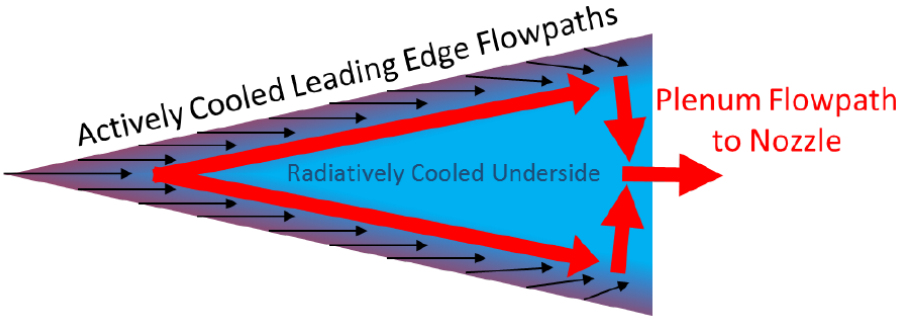

Figure 5 – Schematic of the cooling scheme envisioned by Murakami [1].

When longitudinal thrust is added a portion of the drag is effectively cancelled out. The vehicle longitudinal deceleration is reduced, and the 'natural' L/D ratio is increased to an 'effective' L/D ratio, as detailed in Equation 12.

$$L/D_{eff} = \frac{L}{D - T} \quad (7)$$

If the thrust-to-drag ratio is assumed constant throughout the flight, Equations 3 through 6 can be used with L/D_{eff} substituted for the natural L/D.

2.4 The Tisserand Plane for AGA Mission Planning

Equations 3 through 6 allow simple evaluation of the effect of the selected atmospheric deflection angle and vehicle L/D ratio on the AGA total deflection and drag loss in the planetocentric frame. However, these calculations alone don't indicate if the mission objectives on an AGA are satisfied. Typically, either the change in heliocentric orbital plane or the change in heliocentric orbital energy are the target criteria for an AGA. From the above equations alone it is not clear when the velocity loss associated with an increased atmospheric deflection angle begins to outweigh the potential gains from the increased deflection angle. A heliocentric perspective is required to understand this trade-off.

The gains of an AGA can be measured in several ways, depending on the mission objective. The heliocentric plane change, change in apoapsis, or change in orbital energy are some examples. The Tisserand Plane is a tool commonly used during the initial scoping of interplanetary missions with GAs [19] when the apoapsis or orbital energy are of interest. It can easily be extended to AGA missions and has the benefit of highlighting the optimal flyby deflection for a given heliocentric orbital energy. Important limitations of the Tisserand approach are that all orbits are considered Keplerian and experience no perturbations, the planets are co-planar and on circular orbits, and that it provides no comment on the time-of-flight and orbit phasing. The spacecraft delta-V predicted by the Tisserand approach should thus be treated as a theoretical minimum, and a suitable margin applied.

The Tisserand plane features the periapsis of a given orbit along the x axis, and either apoapsis, orbital period, or orbital energy along the y axis. Apoapsis, orbital period, and orbital energy for a given periapsis are all linked by simple equations, and so these can simply be thought of as different scaling options for the same information. A stable and fixed orbit, such as those of the planets, can be represented as points on this plane. The orbits of Venus, Earth, and Mars are labelled in Figure 6.

Encounters with a given planet can mapped onto the Tisserand plane based on the relative encounter velocity, the flyby periapsis, and the departure angle, which is explained in Figure 7. For each combination of planet, flyby altitude, and escape velocity, there is a family of possible heliocentric orbits which appear as curves on the Tisserand plane. These lines are shown in Figure 6 with their planetocentric escape velocities labelled. The heliocentric apoapsis of the spacecraft's initial orbit cannot be below the circular orbit of the target planet or an encounter would not occur. Likewise, the heliocentric periapsis of the spacecraft's orbit post-flyby cannot be above the planet's circular orbital radius.

During a normal GA, the entry and exit speeds are the same, and so the variation in the spacecraft orbit is confined to a single v_∞ curve. Several such GAs can be chained together sequentially to produce a larger effect, as shown in Figure 8 for the popular Venus-Earth-Earth Gravity Assist (VEEGA) trajectory which significantly reduces the C_3 required to reach Jupiter [20].

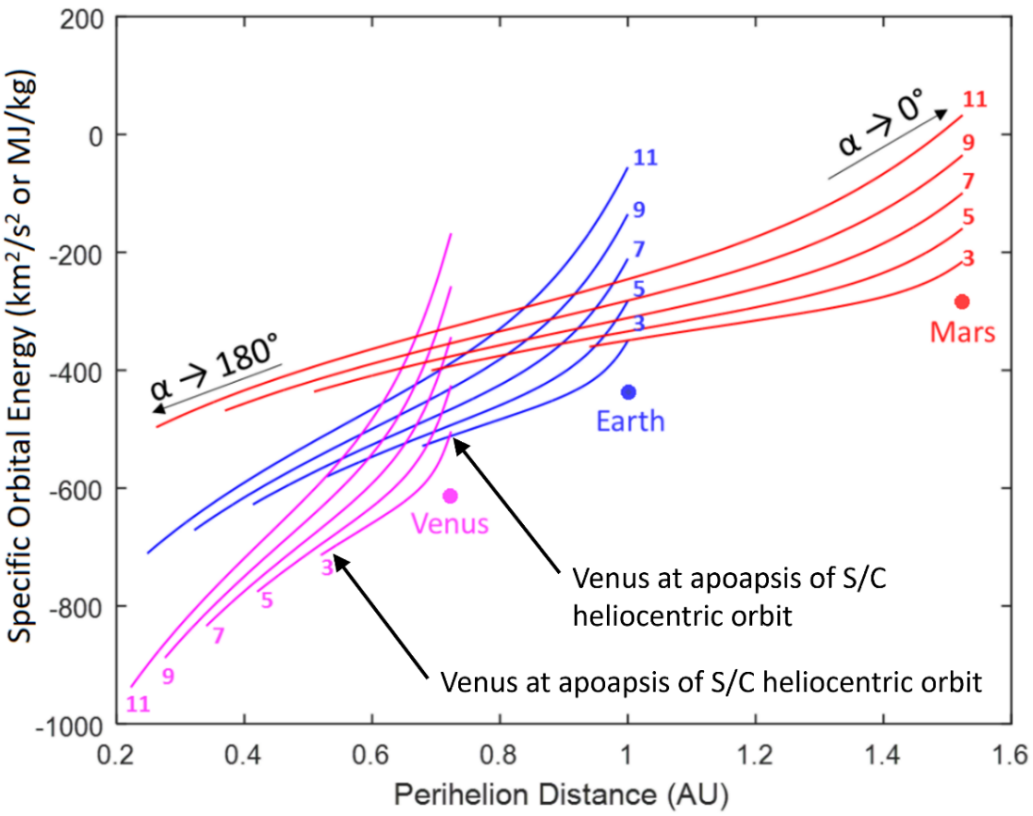

Figure 6 – Energy Tisserand plane for flybys with a periapsis altitude of 100 km. Adapted from [1].

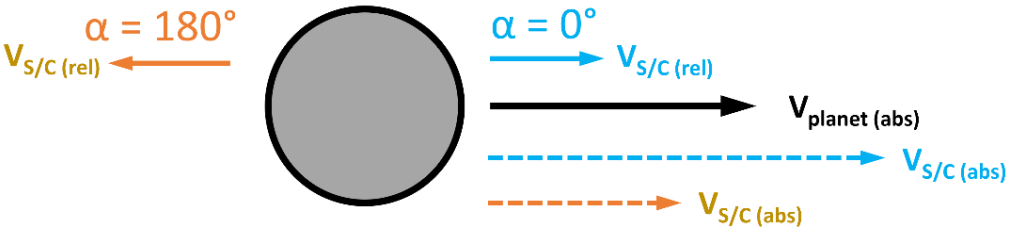

Figure 7 – Departure angle schematic.

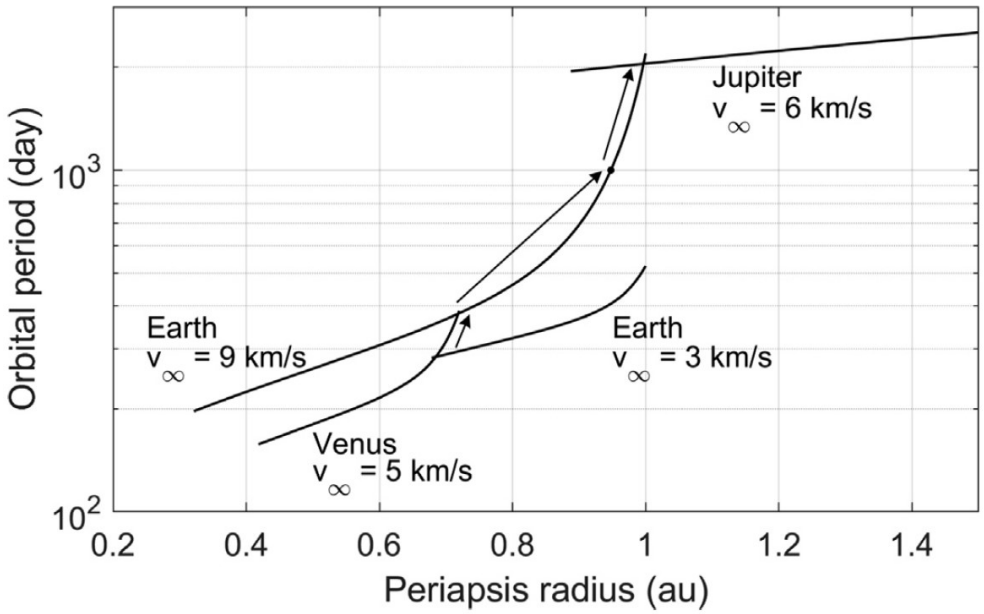

Figure 8 – Orbital period Tisserand plane showing the VEEGA trajectory to Jupiter [20].

The v_∞ curves can be augmented with markers to show the maximum possible traversal along a given line with a single gravity assist. For more massive planets, the maximum deflection at a given velocity will be larger, and the markers will be more widely spaced. This concept is illustrated in Figure 9. Also illustrated in Figure 9 are the heliocentric periapsis-apoapsis curves for AGAs of Mars by both a high performance waverider with an L/D ratio of 7, and a moderate performance waverider with an L/D of 5. The curves are projected from the initial encounter α angle through to 180°. It is immediately clear that an AGA allows deflections much greater than would be possible with a single GA alone, especially at low mass planets like Mars.

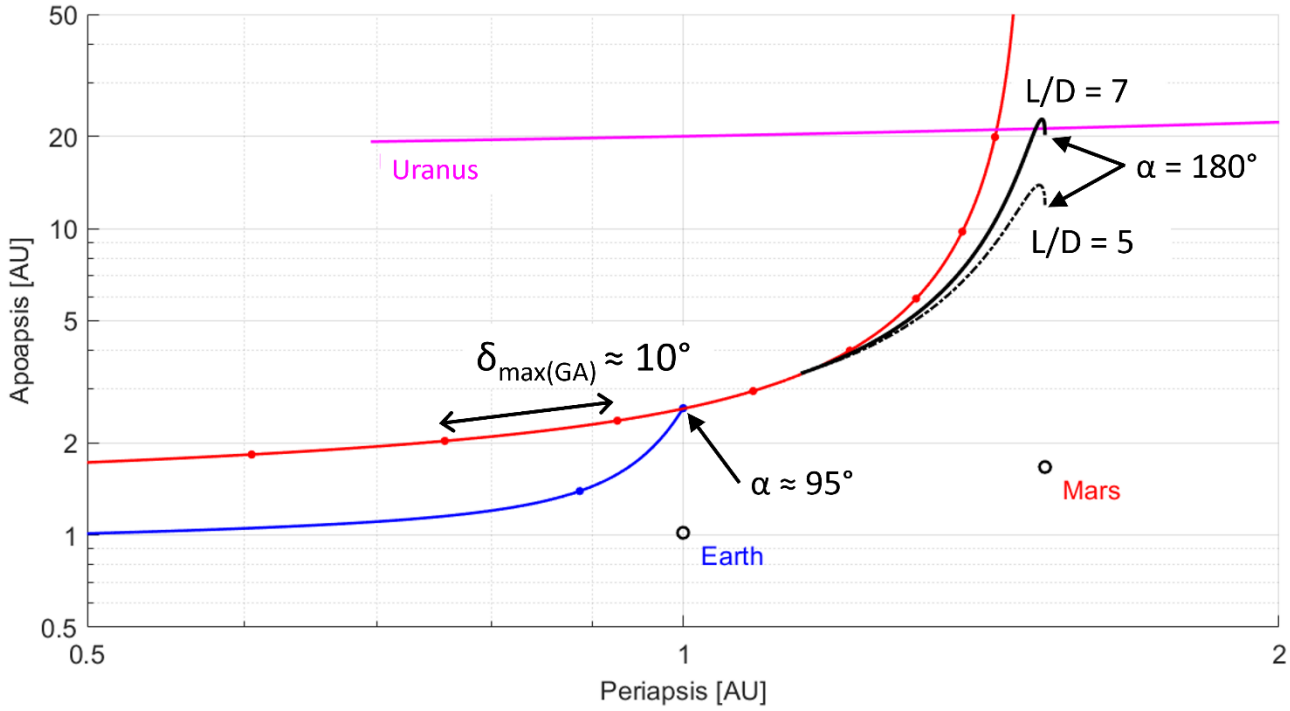

Figure 9 – Apoapsis Tisserand plane of a Mars AGA with varying L/D ratios.

The energy loss due to drag is also clearly visible; as the deflection angle increases, the apoapsis deficit between the ideal GA curve and the drag-affected AGA curves increases. The deficit is more pronounced when the L/D is lower. Eventually a point is reached past which any further increase in the deflection angle reduces the post-flyby heliocentric energy and apoapsis.

The Tisserand plane provides a good first-pass analysis of the 'energy-validity' of a proposed mission for both GA and AGA applications. The level of accuracy provided is sufficient for this present work as the planets considered have relatively low inclinations and eccentricities.

A critical limitation of the Tisserand plane is that it doesn't consider phasing of the orbits. A trajectory which is energetically possible may not be possible in reality if inconvenient orbital resonances exist, or the transfer time between planets may be excessive as multiple orbits are required before the spacecraft and next planet are collocated in space and time.

As the outer planets in the Solar system have orbital periods approximately 2 orders of magnitude greater than the inner planets [21], their velocity can be neglected for initial analyses of direct missions. The synodic period of Earth and the AGA planet then defines the launch window frequency for an AGA mission. In reality, both the Earth-to-AGA planet and AGA planet-to-target alignment will be non-ideal, and so a higher mission delta-V will be required than predicted by the Tisserand plane analysis.

3 Review of Hypersonic Waveriders

Only a brief introduction to waveriders will be given here. The present work needed only a representative estimate of the L/D of an efficient hypersonic vehicle. A detailed investigation of the vehicle geometry was not warranted given the high level of the analysis.

3.1 The Basic Concept

As the freestream Mach number of a supersonic or hypersonic flow around a body increases, the maximum possible L/D ratio rapidly decreases. This is largely due to the rapid increases in wave drag that are brought about by the increasing shock-wave strength as the flight speed increases [10]. As an illustrative example, a Boeing 707 cruising at just below Mach 1 has a maximum L/D of about 20, while an idealised flat plate cruising at Mach 10 has a maximum L/D of about 6.5 [10].

Research into improving hypersonic L/D ratios led to the development of a class of vehicles called waveriders. Waveriders have geometries such that the shock on the lifting side of the vehicle remains attached to the leading edge, and minimal high-pressure gas can leak around to the low-pressure surface on the top [10]. Any high-pressure gas leaking around to the top surface will both reduce the underside average pressure and increase the top side average pressure, thus reducing the pressure differential providing lift.

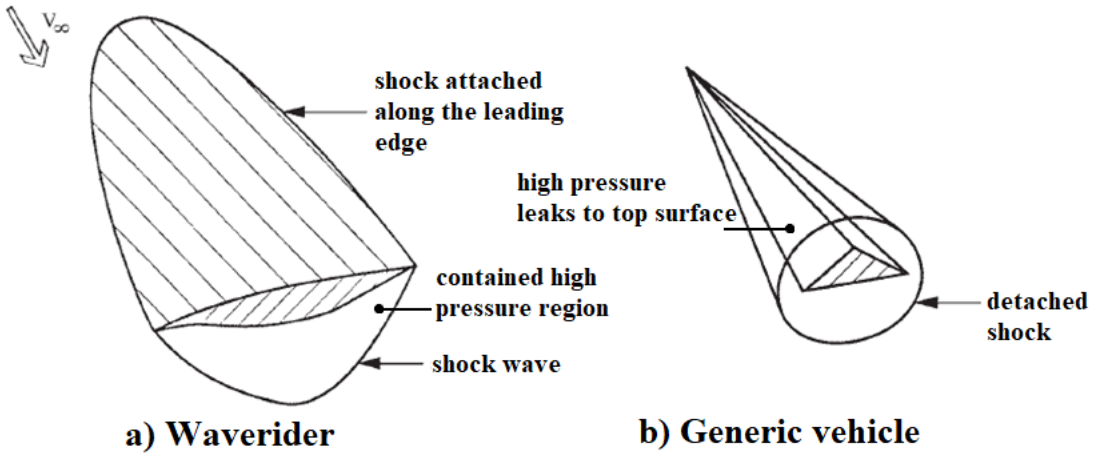

Figure 10 – Illustration of (a) a waverider's attached shock and (b) the pressure leakage of a generic body. Adapted from [10]

The key advantage of this pressure-sealing effect is that it allows waveriders to generate the required lift at a lower angle of attack than generic vehicles [10]. Since the wave drag is directly related to the angle of attack, this implies a lower drag and thus higher L/D at the operating point, as shown in Figure 11.

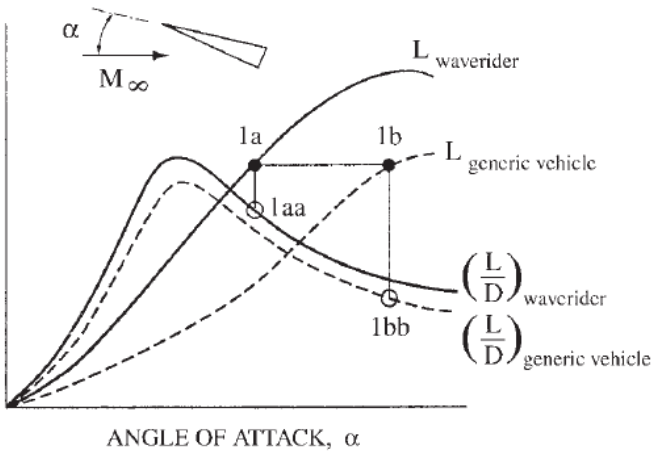

Figure 11 – Operational L/D advantages of waveriders over generic vehicle shapes [10].

In general, waveriders are designed by first choosing a shock flowfield generated by a reference geometry such as a wedge or a cone. The leading edge is then created by drawing 'arbitrary' lines along the generated shock surface from the tip to the base of the vehicle [10]. Figure 12 and Figure 13 illustrate the generation of wedge-defined and cone-defined waveriders respectively. Initial analyses and optimisations of waveriders considered only inviscid drag, leading to poor performance once viscous effects were introduced.

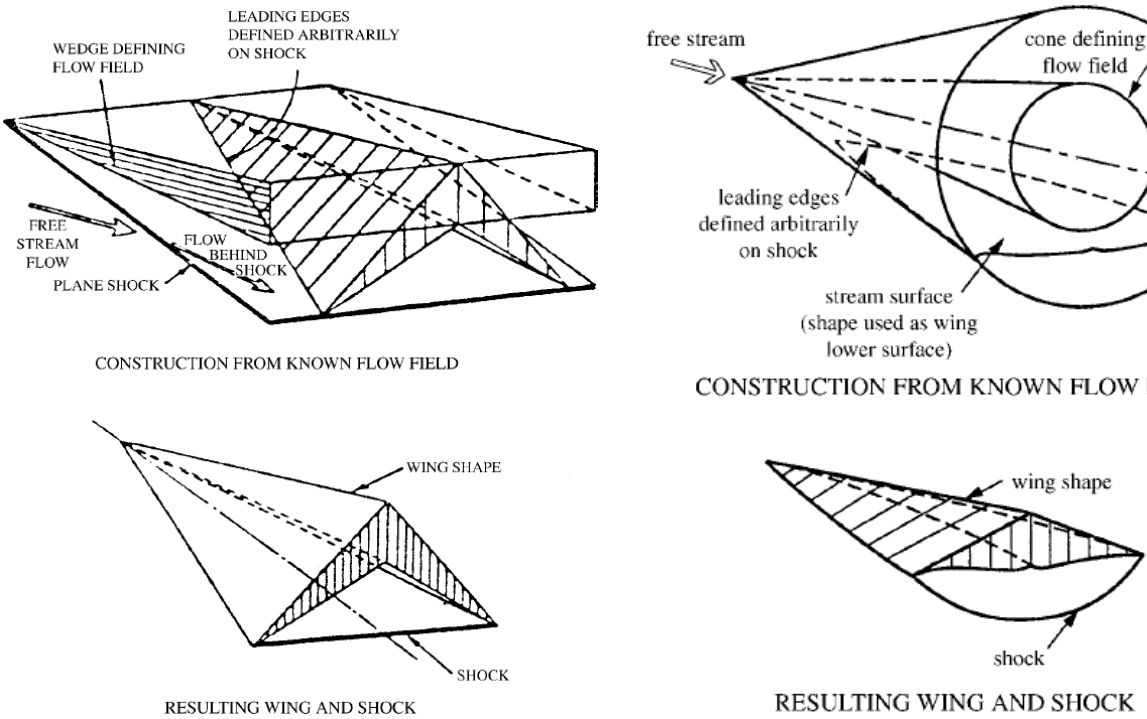

Figure 12 (Left) – Generation of a Caret-wing waverider from a wedge flow field [10].
Figure 13 (Right) – Generation of a waverider from a conical flow field [10].

3.2 Viscous Optimised Waveriders

Anderson et al. at the University of Maryland created numerical routines which considered viscous effects when optimising vehicle geometries. In general, the optimisation procedure attempted to also minimise the wetted area of the vehicle, and thus reduce the skin-friction drag [10]. This class of vehicles are referred to as viscous optimised waveriders. Some examples are shown in Figure 14.

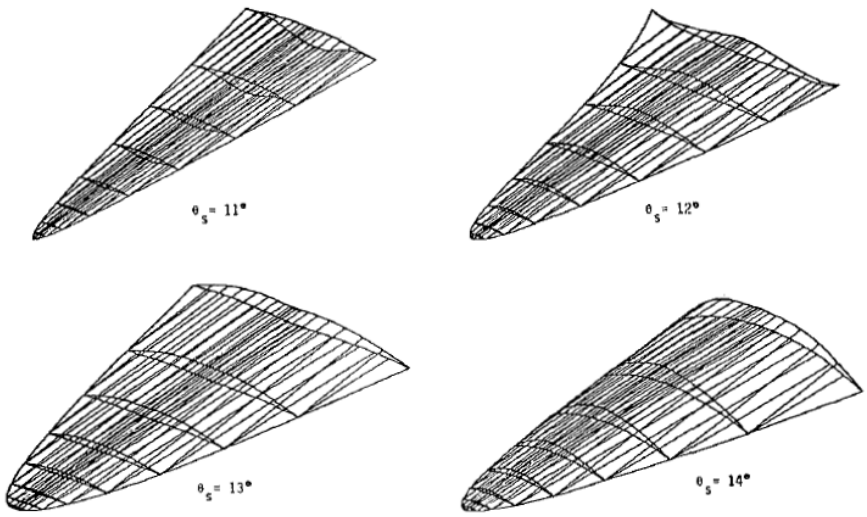

Figure 14 – Several viscous-optimised waverider geometries [9]

3.3 Waverider Performance

Several relations have been proposed in the literature for the upper limits of waverider aerodynamic performance at varying Mach numbers. Kuchemann [22] originally proposed Equation 8, which provides a kind of 'L/D barrier. A revised version of this equation was later proposed based on the improved performance of viscous optimised waveriders [9], reproduced here as Equation 9. Figure 15 overlays the curves formed by these equations onto various numerical and experimental data.

$$\left(\frac{L}{D}\right)_{max} = \frac{4(M+3)}{M} \approx 4 \; as \; M \to \infty \qquad 8$$

$$\left(\frac{L}{D}\right)_{max} = \frac{6(M+2)}{M} \approx 6 \; as \; M \to \infty \qquad 9$$

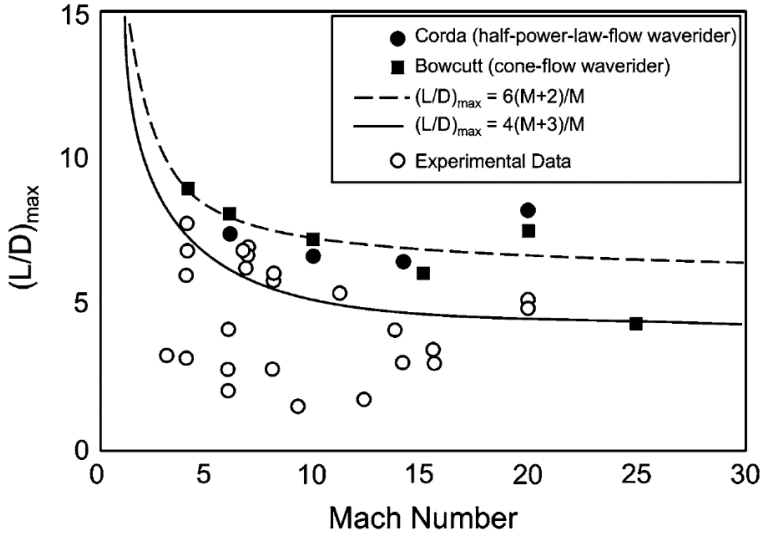

Figure 15 – Comparison of L/D relations with numerical and experimental data [23].

Aerodynamic performance favours long vehicles where large Reynolds numbers reduce the relative effect of viscous drag, as can be seen in Figure 16 and Figure 17. However, the improved aerodynamic performance must be traded with the probable increase in vehicle mass. The practical upper limit to vehicle length is limited by launcher fairing sizes. For reference, the largest Atlas V fairing could contain a 20m vehicle [24].

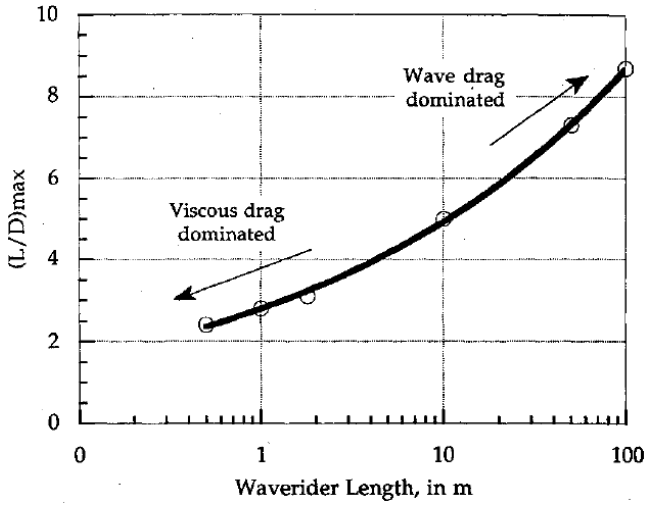

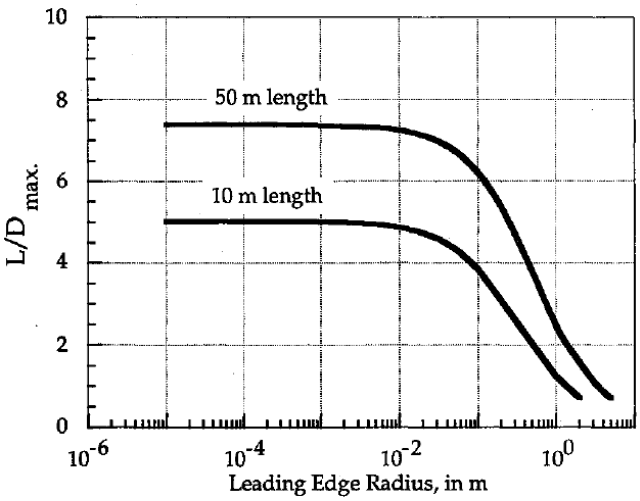

Figure 16 (Left) – Maximum L/D versus vehicle length for a typical waverider at Venus [7].
Figure 17 (Right) – Maximum L/D versus leading edge radius and vehicle length for a Venus waverider [7].

3.4 State of the Art

Two hypersonic vehicle case studies have been reported here to give a general understanding of the state-of-the-art and provide reference points for the following analyses and discussions. Focus is given to the thermal loads and thermal protection systems.

3.4.1 HTV-2

The Hypersonic Technology Vehicle-2 (HTV-2) was a 'boost-glide' test vehicle built by Lockheed Martin as part of DARPA's Falcon Project to develop Mach 20 rated vehicles. It had a planned range of 17,000 km and was tested in 2010 and 2011 [25]. Boost-glide weapons have minimal on-board propulsion capability and must be given a large initial energy by a separate vehicle, often a rocket booster. Figure 18 illustrates a typical boost-glide flight profile.

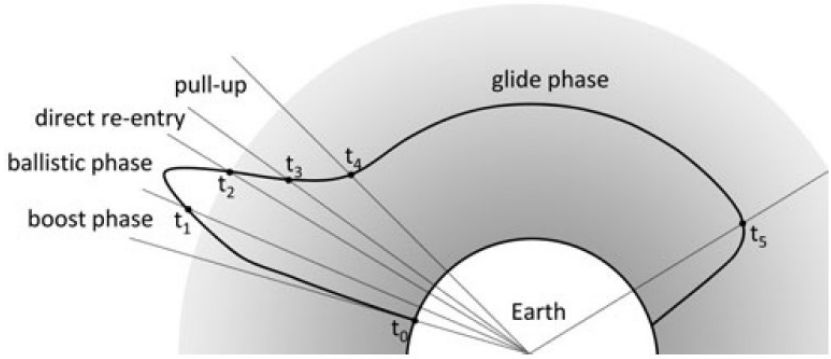

Figure 18 - Typical flight profile of a boost-glide hypersonic re-entry vehicle [25].

Figure 19 – Rendering of the HTV-2 attached to an upper stage [26].

Little information is publicly available about the vehicle. The analyses of Acton [25] and Wright [27] provide the best insight into its likely characteristics. It is thought that the vehicle was developed for an equilibrium gliding re-entry profile in order to limit the peak thermal fluxes. This is the same approach that would likely be adopted for an AGA mission. HTV-2 was designed for 3000 seconds of atmospheric gliding [28], which is considerably longer than a typical AGA atmospheric flight and suggests that its TPS was entirely passive.

Wright estimates that the vehicle likely has a width of about 2m, a length of about 5m, and a mass of about 1000 kg. Acton estimates that the L/D ratio of the vehicle is about 2.6. This is considerably lower than the maximum L/D predicted by Figure 16 for a vehicle of this length. Acton proposes that aerodynamic performance was likely sacrificed to reduce the peak thermal fluxes on the passive aeroshell. As the detailed design objectives of the vehicle are not available, it is difficult to comment further on the sacrifices and trades offs that were made. It is not clear if the HTV-2 was designed with a waverider methodology.

High temperature materials and insulation were developed and tested for the carbon-carbon aeroshell and internal TPS, including 1980°C refractory composites, high temperature multi-layer insulation, and high temperature seals [28]. The vehicle guidance and control systems were autonomous [28], something that would also be necessary for an AGA vehicle. However, HTV-2 made use of the GPS network [29], for which a substitute is not yet available at other planets.

3.4.2 X-43A

The X-43 hypersonic aircraft were developed as part of NASA's Hyper-X program. The X-43A flights were the first ever examples of a scramjet engine propelling a hypersonic vehicle in flight [30], using an airframe-integrated and hydrogen-fuelled scramjet. The test vehicles were accelerated to their operational altitude and velocity by a Pegasus launch vehicle first stage, which was in turn dropped from a B-52. An unsuccessful flight attempt occurred in 2001, followed by 2 successful flights in 2004, the second of which operated the scramjet for 10 seconds and reached about Mach 9.7 [30]. Figure 20 provides a schematic of the vehicle.

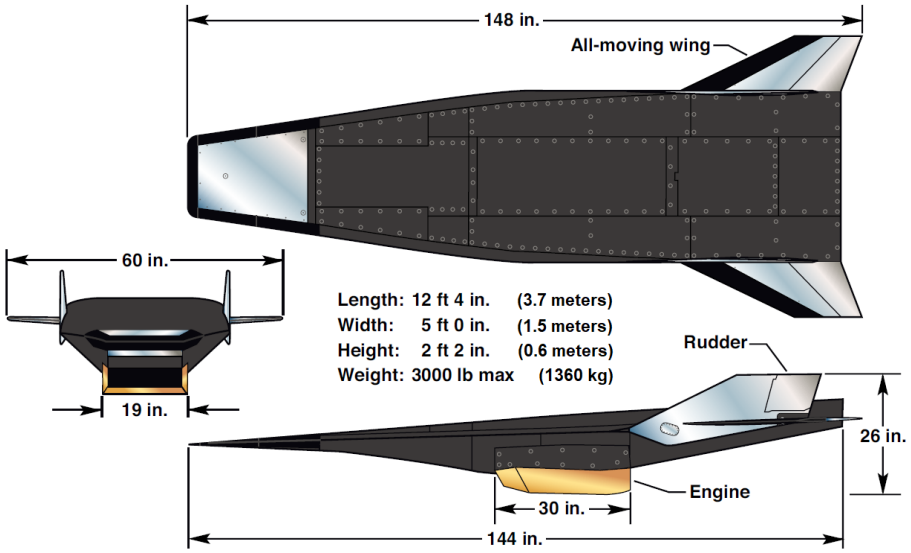

Figure 20 – Geometry and mass of the X-43A hypersonic research vehicle [31].

The thermal protection system of the X-43A was comprised of a 'patchwork' or different solutions, as is typical for sustained-flight hypersonic vehicles. Figure 21 provides an illustration of the main TPS schemes.

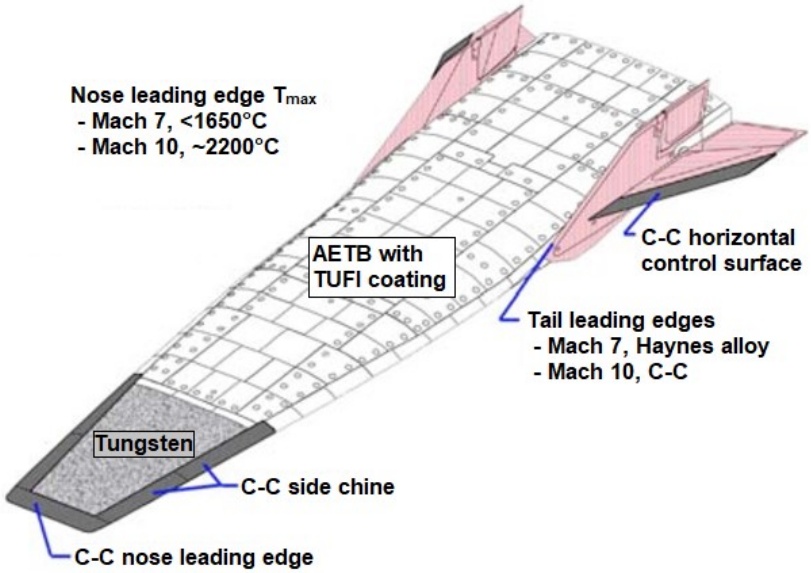

Figure 21 – X-43A thermal protection system. Adapted from [32].

The airframe structure is primarily aluminium and steel. The acreage regions are protected by alumina-enhanced-thermal-barrier (AETB) tiles coated with toughened-unipiece-fibrous-insulation (TUFI). The nose and control surfaces are made from solid tungsten and Haynes alloy respectively, with carbon-carbon leading edges on both. Gaseous nitrogen was used to pressurise the inside of the vehicle to prevent oxygen intrusion, as well as to force coolants to the scramjet engine leading edges. Pure water and a glycol-water mixture were used to cool the copper alloy engine leading edges at different stages of the flight [31].

It should be noted that the scramjet leading edges are a different component to the vehicle leading edge. Prior to reaching the scramjet engine inlet the air passes through 2 oblique shocks, as illustrated in Figure 22, causing significant compression and heating. An air-breathing scramjet would only make sense for an AGA vehicle conducting an Earth flyby. For reasons discussed in Section 6.2 Earth was not considered a suitable planet for an AGA, and so air-breathing scramjets were not considered any further in this work. Silicon-carbide and hafnium-carbide coatings were applied to the carbon-carbon pieces, and a zirconium coating applied on the external underside surfaces of the scramjet engine [33].

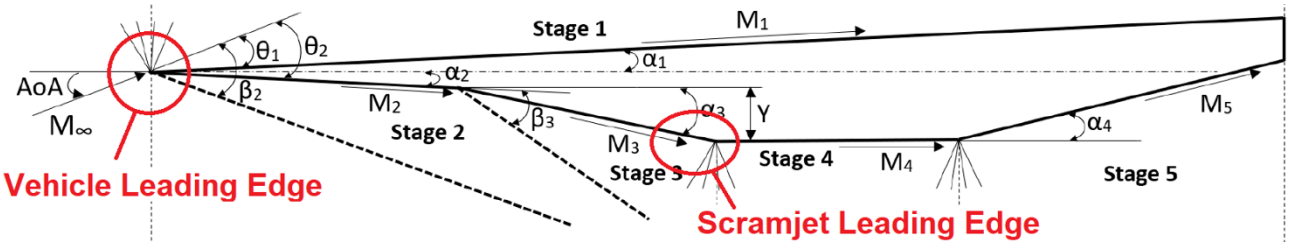

Figure 22 – Simplified X-43A geometry showing the shock and expansion regions. Adapted from [34].

Of particular interest to the present work is the passively cooled carbon-carbon leading edge employed by the X-43, shown here in Figure 23. A 3:1 biased weave of high conductivity carbon fibres, as illustrated in Figure 24, was employed to rapidly conduct heat away from the nose to lower flux regions where the heat could then be radiated away. This allowed the nose to survive a tip heat flux of approximately 15 MW/m^2 [35]. Although a more biased weave such as 4:1 or 5:1 could further improve the longitudinal conductive capabilities, the reduced strength along the spanwise direction would likely have led to failure from thermal expansion stresses [35]. Greater ablation of the C-C nose than expected was measured during testing of the original 0.76 mm radius nose, requiring an increase in the nose radius to 1.27 mm [32].

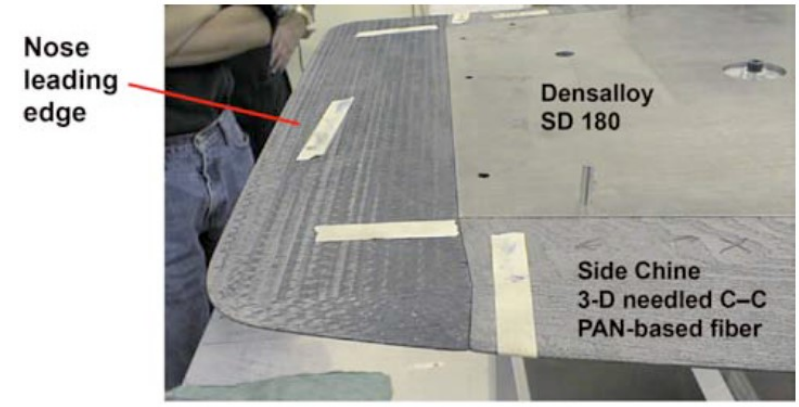

Figure 23 –X-43A leading edge prior to the Mach 7 test flight [32].

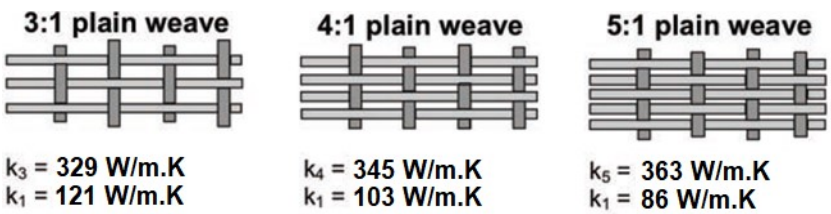

Figure 24 – Different C-C weaves considered for the X-43. Adapted from [35].

The X-43A had a lift-to-drag ration of approximately 3.5 according to the analysis of Navo and Bergada [34]. This relatively low value is not surprising given that the vehicle had a scramjet engine attached, was only 3.7m long, and was designed with a lifting body geometry rather than an optimised waverider geometry.

3.5 Unique Challenges for Hypersonic AGA Aerospacecraft

Aerospacecraft for AGA flybys will encounter problems typical of sustained-flight hypersonic vehicles. Such vehicles have small internal volumes in order to reduce drag, and compact packaging of components is necessary. High efficiency hypersonic vehicles have sharp leading edges and as a result have to deal with high heat fluxes. In order to survive these high heat fluxes over sustained-duration flights, hypersonic vehicles must also be capable of absorbing and/or rejecting large total heat loads.

Differently to Earth-bound hypersonic vehicles, increasing the speed of an AGA vehicle increases the centripetal acceleration and thus lift force which is required. As Earth-bound hypersonic vehicles increase their speed to significant fractions of orbital velocity, their lift requirement tends to 0 due to the centrifugal force cancelling out the gravitational acceleration downwards. Since an AGA vehicle is doing the opposite and trying to remain inside the atmosphere as long as possible with a super-orbital velocity, increasing the atmospheric cruise speed increases the necessary lift force. This lift force and acceleration can exceed the magnitude of launch accelerations and would likely occur along a direction orthogonal to the primary launch accelerations. Therefore, the aerospacecraft systems would need to survive strong accelerations in two directions, rather than just along the launch direction like current spacecraft.

Aerodynamic control of high L/D hypersonic vehicles at super-orbital speeds is yet to be demonstrated.

An autonomous guidance and navigation system for the atmospheric flight phase of the mission would be required. While this has been demonstrated at Earth, there are currently no GNSS systems or comparable networks at other planets where an AGA flyby would be suitable.

Finally, development of an AGA vehicle would require a new spacecraft architecture and re-thinking of the interfaces and sub-system designs that have been employed thus far on ‘traditional’ spacecraft.

4 Review of Thermal Protection Systems

Broadly speaking, a TPS prevents excess heat from entering the vehicle and compromising its structural integrity or damaging other internal systems. A TPS can serve secondary functions as well, such as carrying structural loads or harvesting thermal energy for 'productive' use. Different vehicle architectures have different atmospheric flight trajectories and thus different thermal loading profiles, as illustrated in Figure 25. Blunt re-entry vehicles typically experience large thermal fluxes but for short periods of time during their rapid deceleration in the upper atmosphere. Lifting re-entry vehicles typically experience lower thermal fluxes but larger total heat loads due to the longer duration of their re-entry. Different thermal protection schemes are required for the high flux and high total load cases, as is illustrated in Figure 26.

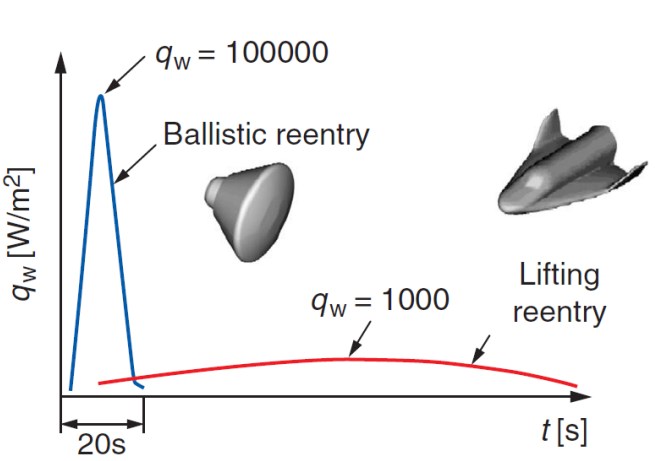

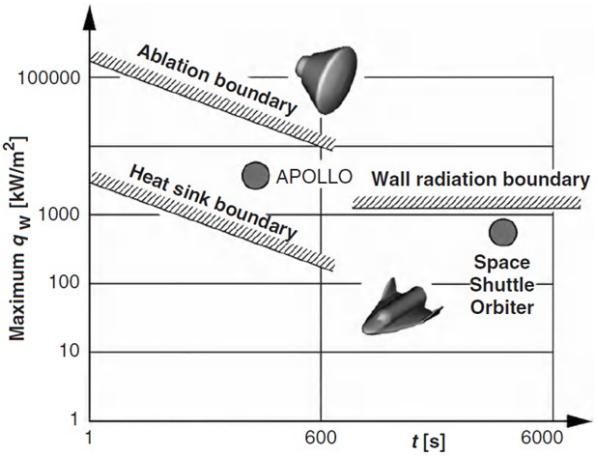

Figure 25 (Left) - Typical thermal loading profiles for Earth re-entry vehicles [36].
Figure 26 (Right) - Typical performance limits for Earth re-entry thermal protection systems [36].

A key difference between heritage re-entry vehicles and AGA vehicles is the lift-to-drag ratio. The goal of a re-entry vehicle and its TPS is to safely shed a certain quantity of kinetic energy and slow the vehicle to subsonic speeds. As a high L/D ratio is not necessary for this task, relatively blunt leading edges and rounded surfaces are typically used in the TPS to reduce convective thermal loads. The Apollo re-entry capsule had a maximum L/D ratio of approximately 0.4 [37] and the Space Shuttle Orbiter had a hypersonic L/D of approximately 1 [38], while the L/D ratios of AGA vehicles in the literature range from roughly 4 to 10. The high L/D ratios necessary for AGA imply small leading-edge radii with high heat fluxes. Additionally, sustained-flight hypersonic vehicles are more sensitive to the TPS volume, as drag is closely related to the vehicle volume and thickness-to-length ratio [35]. Thick insulative schemes such as that of the Space Shuttle Orbiter may not be suitable. Clearly AGA aerospacecraft fall into a niche most similar to sustained-flight hypersonic vehicles and missiles, therefore much inspiration will be taken from the TPS of these vehicles.

4.1 Passive Systems

Passive TPS are favoured for their relative simplicity and light weight compared to semi-active and active systems. They are typically restricted to vehicle regions with low to moderate heat fluxes.

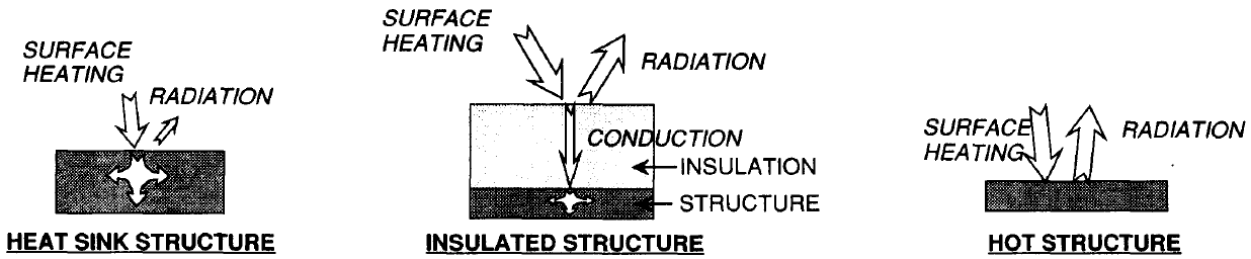

Figure 27 – Common passive TPS. Adapted from [39].

4.1.1 Heat Sinks

Heat sinks are the simplest TPS conceptually. The thermal load transferred into the vehicle is simply stored as a temperature increase in the heat sink material. The heat sink could be realised in numerous ways. In the case of the X-15, the vehicle skin was thickened to give extra thermal sink capability [40]. In the case of re-entry capsules such as the Mark 2 warhead and the Mercury capsule a dedicated heat shield was attached to the windward side of the vehicle, as illustrated in Figure 28.

Figure 28 – A Mark 2 re-entry vehicle copper heat sink on display [41].

Table 2 contains typical room temperature properties of solid materials that have been considered for use as heat sinks. The thermal properties of these materials change significantly with temperature, and so the values below should only be taken as representative.

	Density [g/cm^3]	Specific Heat [J/kg.K]	Thermal Conductivity [W/m.K]	Thermal Diffusivity [mm^2/s]	Melting Temperature [°C]	Energy Storage Potential* [MJ/kg]
Aluminium	2.60	920	230	97	660	0.55
Beryllium	1.85	1800	300	90	1290	2.09
Titanium	4.51	540	20	8	1670	0.81
Copper	8.96	380	400	117	1080	0.37
Stainless steel	7.80	500	14	4	1500	0.68
Graphite	2.25	710	133	97	3600**	2.30

Table 2 - Room temperature properties of some materials considered suitable for solid-state heat sink TPS.
**Assuming material is heated from 25°C to 90% of melting temperature. **Vaporisation temperature.*

In practice, a heat sink TPS alone is only practical for sub-orbital flights with short heat pulses of low to moderate intensity. Extended durations of heating will exceed the storage capability of the material, leading to vehicle failure. The heat storage per unit mass of a single-phase heat sink is significantly lower than what can be achieved with phase changing systems. For this reason, heat sinks were discarded and replaced with ablatives on the Mercury capsule and other programs once ablatives reached technological maturity [42].

Heat sinks can also come in liquid or gaseous form. Some sample fluid properties are given in Table 3. Water is commonly used to cool liquid rocket test engines because of its large specific heat capacity. Flight engines often pass fuel through a cooling jacket prior to combustion in order to cool the engine and nozzle. A pump or pressurising system is usually required to circulate the fluids and so these systems typically classified as ‘active’.

	Density [g/cm^3]	Specific Heat [J/kg.K]	Thermal Conductivity [W/m.K]	Thermal Diffusivity [mm^2/s]	Boiling Temperature* [°C]
Water	1.00	4200	0.6	0.14	100
Kerosene	0.79	2000	0.145	0.09	~250

Table 3 – Room temperature properties of common liquid heat sink materials.
**Boiling temperature at 1 atmosphere.*

4.1.2 Insulated Structures

An insulated structure can be used for moderate heat flux applications over limited time periods [35]. The use time is mostly limited by the residual conduction rate into the vehicle and the heat storage or dissipation capability of the vehicle. The most well-known realisation of an insulated aerospace structure is the Space Shuttle Orbiter, which was comprised of an aluminium airframe protected by insulative materials. Figure 29 provides a schematic of the Orbiter TPS and Table 4 details some properties of the primary materials.

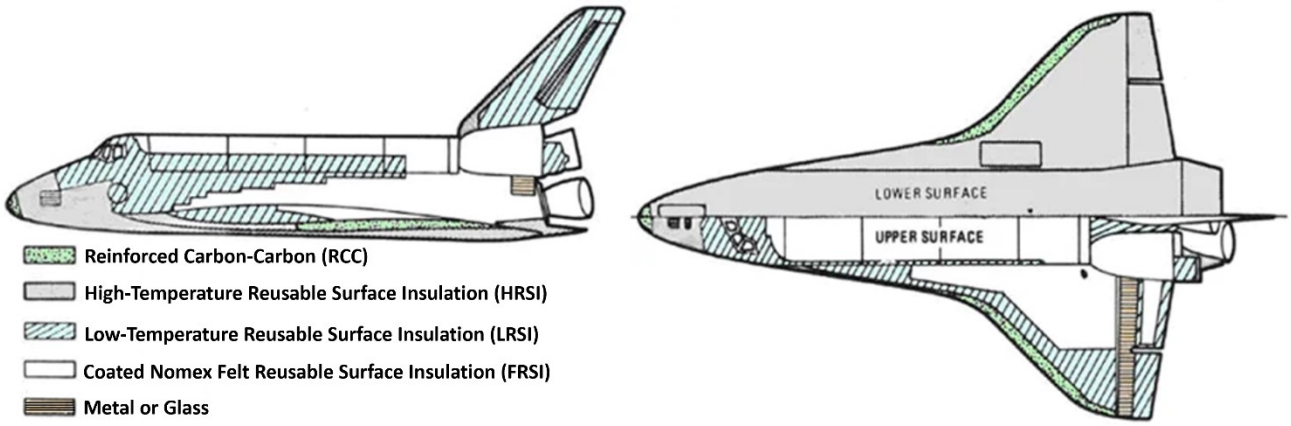

Figure 29 –Space shuttle TPS. Adapted from [43].

	Density [kg/m^3]	Areal Density [kg/m^2]	Thickness [mm]	Re-use Temp. Limit	Single use Temp. Limit	Thermal Conductivity
HRSI LI-900 Tiles	144	3.6 – 18.3	25 - 127	1260	1540	0.0485 – 0.126
AFRSI Blankets	144	1.6 – 3.4	11 - 24	370	-	-
Reinforced Carbon-Carbon	1986	12.7 - 25.4	6.4 – 12.7	1650	-	10 – 30

Table 4 – Key properties of some Space Shuttle Orbiter TPS materials [43] [17] [44].

High temperature insulating materials are typically porous ceramics. These porous ceramics generally have excellent thermal properties, but poor mechanical properties. They cannot handle structural loads or thermal-expansion loads, and therefore must be installed as separate tiles with methods of strain isolation provided between the tiles as well as between the tiles and aluminium airframe. Additionally, the tiles are fragile and easily damaged. The only load-bearing elements of the Space Shuttle Orbiter TPS were the RCC components.

As insulated structures rely on radiative cooling, high surface temperatures are required, at which high-temperature oxidation becomes a significant problem. The Orbiter tiles featured a glass coating on their external surfaces, and the RCC components required a silicon-carbide coating [44].

4.1.3 Hot Structures

Similar to the insulated TPS concept, a hot structure relies on the outer surface of the vehicle reaching high steady-state temperatures in order to reject a portion or all of the incoming thermal flux. However, with a hot structure approach the TPS is also a structural component. While an insulative TPS can be considered parasitic, a hot structure TPS serves multiple functions, making it an integral member of the vehicle. Hot structures can be lighter, more durable, and easier to maintain than an insulative TPS [45]. The most famous example of a hot structure vehicle is likely the SR-71 aeroplane, illustrated in Figure 30. The Dyna-Soar spaceplane program and the National Aero-Space Plane (NASP) program were notable for their work investigating and developing hot-structure solutions for orbital-class vehicles.

Hot structure concepts for orbital and super-orbital re-entry vehicles face a number of challenges, each of which have potential solutions at varying technology readiness levels. Large thermal gradients in all 3 axes create

complex thermal stresses and strains, as well as difficulties in joining and sealing different components of the TPS. Stability of the vehicle outer mould-line is critical for both structural and aerodynamic performance. While less fragile than insulative TPS materials, hot structure materials are typically difficult or impossible to weld and machine, presenting fabrication challenges. Although external insulation is not needed for a hot-structure concept, internal insulation will likely be required to prevent overheating of other systems. Finally, oxidation-resistant coatings are usually required given the high operating temperatures [35].

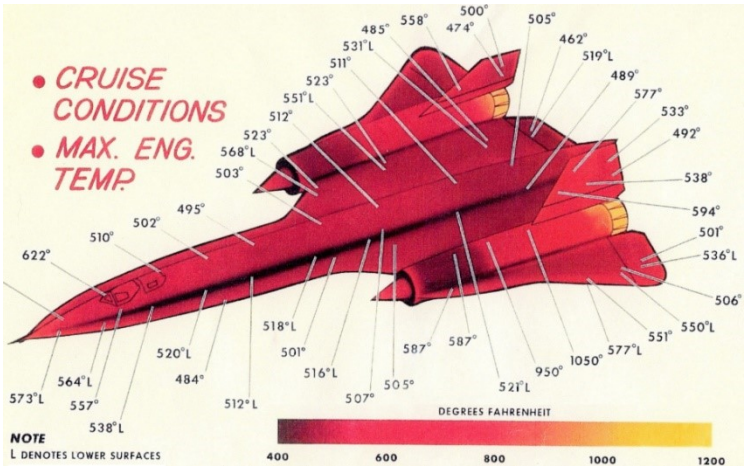

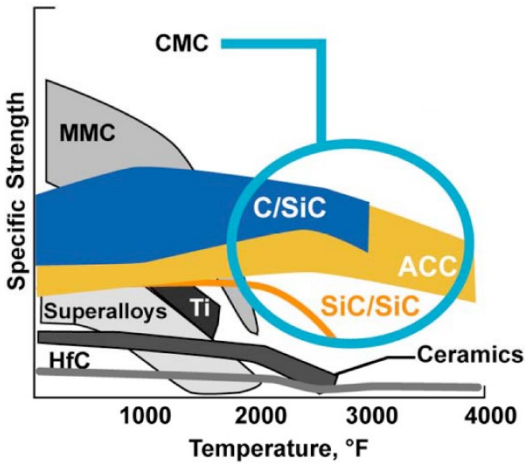

Figure 30 (Left) –Mach 3 steady-state cruise temperatures over the SR-71 airframe [46].
Figure 31 (Right) – Specific strength comparison of high temperature material families [35].

Titanium, superalloys, and metal matrix composites (MMC) are popular choices when operational temperatures are below about 1100°C. For higher temperatures, ceramic matrix composites (CMC) and refractory metals are usually selected [35]. Figure 31 illustrates the general state of the art of high temperature materials.

4.2 Semi-Passive Systems

Semi-passive TPS typically exploit a material phase change in order to reject or transport large quantities of thermal energy. Semi-passive TPS require no input or control and they can be single or multi-use.

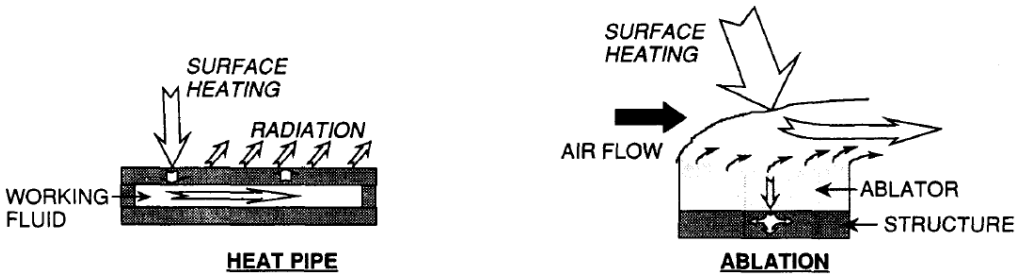

Figure 32 - Common semi-passive TPS. Adapted from [39].

4.2.1 Ablatives

Ablative materials reduce heat conduction into the vehicle by a combination of chemical and physical processes. Significant amounts of energy are absorbed by melting, vaporisation, and endothermic decomposition of the material. The gases produced during these processes enter the boundary layer and cool it down, reducing the external heat flux into the material.

Ablative materials are typically divided into 3 classes: subliming/melting, charring, and intumescent. Charring and intumescent ablators produce a carbonaceous char which both radiates heat away and carries it away as internal energy as the char particles shear off into the free stream. The general concept of a charring ablator is illustrated in Figure 33. Subliming and melting ablators absorb energy directly into solid-vapour and solid-liquid-vapour phase changes respectively and carry the heat away as liquid droplets or gaseous vapours.

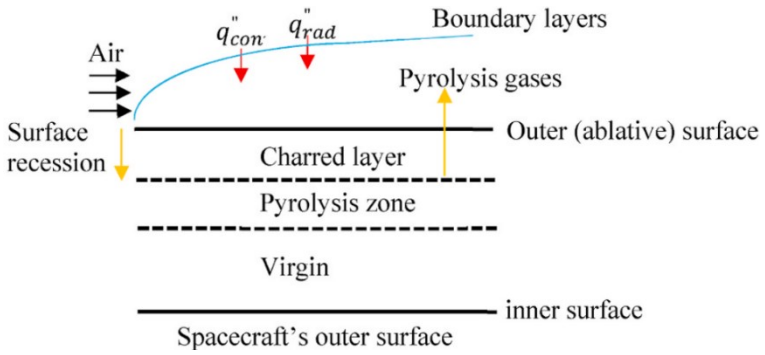

Figure 33 – Working principle of a charring ablator [47].

An ablator has two primary functions; to absorb and remove heat, and to insulate the structure. These two requirements are often competing, as high-density materials tend to have the best ablation performance and energy absorption ability but also the highest thermal conductivities, as outlined in Table 5. In most cases the ablator cannot simply be sized based on the energy to be absorbed, and a residual thickness of virgin material must be included to ensure that the vehicle structure remains well insulated [48].

	Cold wall heat of ablation[a], J/g[b]		
Material	H_s = 12,000 J/g[b] V_∞ = 4800 m/s	H_s = 24,000 J/g[b] V_∞ = 6,800 m/s	Relative thermal conductivity
carbon–carbon	32,000	39,500	high
carbon–phenolic	24,000	29,600	↕
silica–phenolic	13,000	19,000	
Teflon	6,650	10,350	low

Table 5 – Representative properties of some typical ablative materials. Adapted from [48].

Ablative materials are well suited to flight profiles with short periods of high thermal fluxes. Even with a thick layer of virgin material, sustained operation can result in excess heat conducting into the vehicle. Ablatives have typically been used on ballistic re-entry capsules where aerodynamic performance is not a primary concern, and the thermal loading time history features a sharp peak. The rough ablation surface and the variation of the aerodynamic profile as the material recesses make ablatives appear unattractive for widespread use on high L/D hypersonic vehicles. Ablatives could be considered for the high-flux stagnation regions for either partial or full duration of the flight provided that they don't trip the boundary layer into turbulence. Generally, ablative materials are not re-used and are replaced after each mission.

4.2.2 Phase Change Materials

While ablative materials undergo irreversible endothermic chemical processes, phase change materials undergo reversible physical transformations. Solid to liquid and liquid to vapour phase transitions are common choices as they can absorb large quantities of energy with minimal temperature variation. Water, paraffin waxes, salts, hydrated salts, and low-melting point metals are common choices. For reference, Table 6 compares the enthalpy storage capabilities of heating water versus its phase transitions.

Latent Heat of Fusion (Melting at 0°C)	334	kJ/kg
Liquid Heating Enthalpy Storage, 0 - 100°C	~ 400	kJ/kg.K
Latent Heat of Vaporisation (Boiling at 100°C)	2256	kJ/kg.K

Table 6 – Enthalpy storage capabilities of water at 1 atmosphere of pressure.

Phase change materials are typically used as heat sinks, in which case they are limited to transient situations, just like single-phase heat sinks and ablatives. A heat sink can be re-used repeatably if the stored heat is dissipated and the phase change is reversed between cycles.

Some interesting high-performance phase change heat sinks have been proposed over the years for hypersonic vehicles. Of particular interest for the present work is the patented idea of Hebeler [49] in which solid lithium would be stored in a metallic honeycomb structure covering the heated surface of a re-entry vehicle. The high thermal conductivity of lithium would allow it to rapidly conduct heat away from the external surface and sink it in to the vaporisation process before being vented from the vehicle. In a sense, it could be thought of as an 'internal ablative'. The honeycomb structure both contains the liquid and increases the heated surface area.

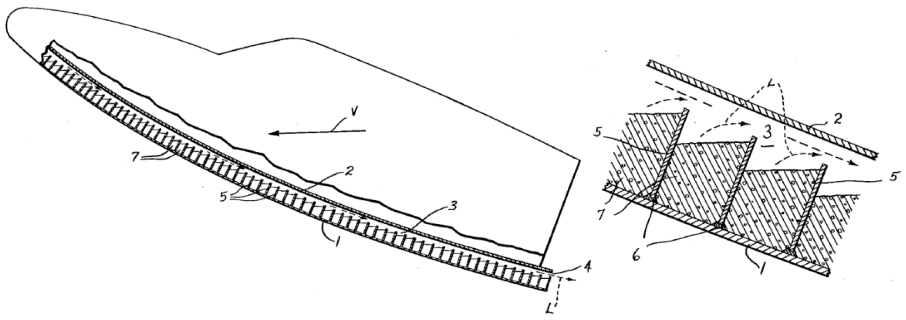

Figure 34 – Illustration of the evaporating liquid metal TPS concept of Hebeler [49].

4.2.3 Heat Pipes and Vapour Chambers

Heat pipes and vapour chambers exploit phase change materials as a method of efficiently and continuously transporting heat between different locations rather than temporarily storing it. Typically, a phase changing fluid absorbs a large, concentrated heat flux via evaporation, and then the vapour is transported via a pressure gradient to a cooler location where it can re-condense, both releasing the stored latent thermal energy to be transported away and creating a low-pressure region in the container. The fluid is then returned to the heating region by capillary driven flow through a wicking material. Figure 35 and Figure 36 illustrate the working principles of heat pipes and vapour chambers respectively. Heat pipes only transfer heat along the axis of the pipe and so they are best suited to cooling discrete heat sources, while vapour chambers can collect heat from larger areas and spread it in two dimensions [50].

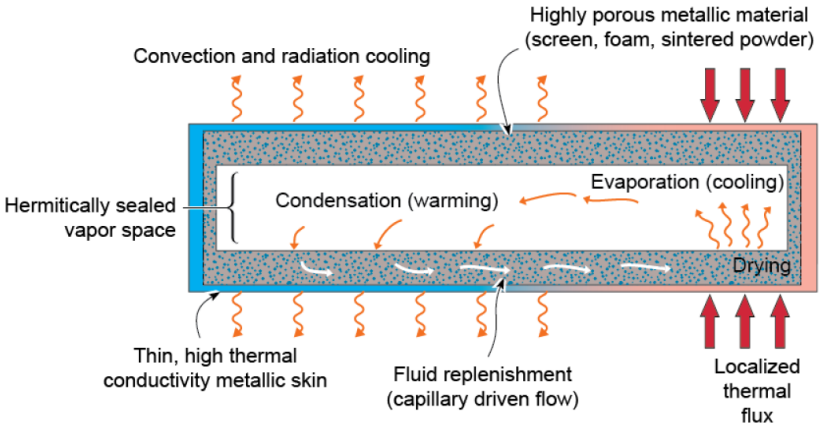

Figure 35 –Working principle of heat pipes [51].

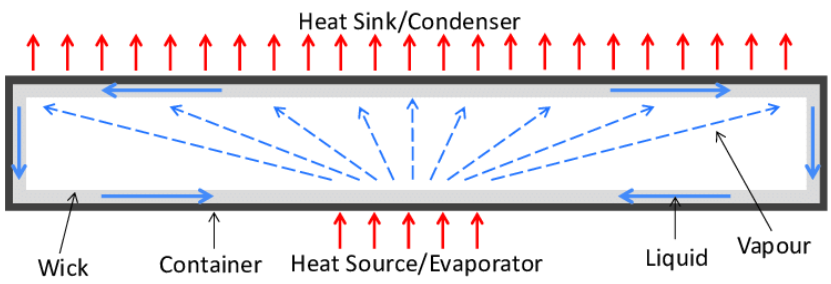

Figure 36 –Working principles of vapour chambers [52].

Vapour chambers and heat pipes can transmit large fluxes over moderate distances with only small temperature drops. They can be characterised by 'effective' thermal conductivities of up to several thousand W/m.K [52], an order of magnitude better than copper.

Heat pipes have been considered as the 'next step' in cooling solutions for hypersonic leading edges in a number of works. They can handle higher fluxes than passive radiative cooling, while also being simpler and lighter than active cooling solutions [53]. Preliminary designs have been created for vehicles such as the Space Shuttle Orbiter and the National Aerospace Plane. Figure 37 provides a representative example.

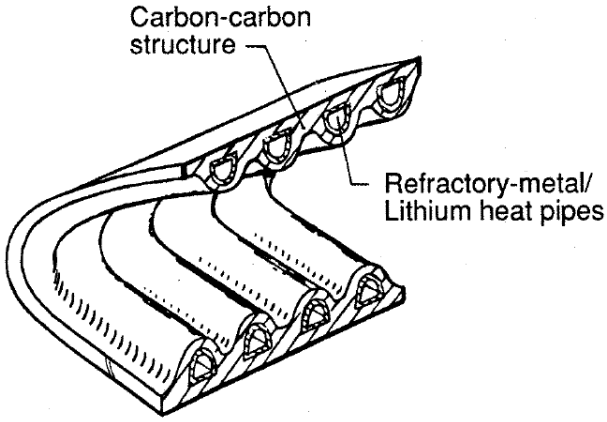

Figure 37 – High performance leading-edge heat pipe concept [54].

Of particular interest to this work are refractory metal-lithium heat pipes. Using analytical methods, Kasen [51] developed 'operational maps' for various high performance heat pipes which illustrate the various failure modes of heat pipes and when each is dominant. Figure 38 is one such operational map for a molybdenum alloy heat pipe with lithium working fluid, predicting a flux limit on the order of 10 MW/m^2. Experiments by Matthews et al on a tantalum-lithium heat pipe achieved adequate performance with heat fluxes in the range of 7.5-13 MW/m^2 [55].

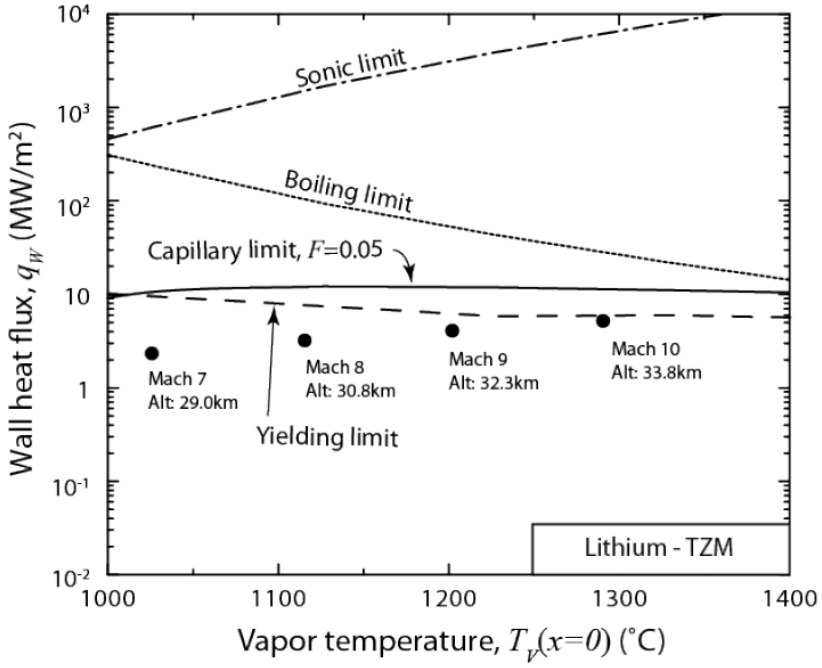

Figure 38 – Operational map for a 3mm radius leading edge lithium-TZM heat pipe [51].

An important aspect to note about heat pipes and vapour chambers is that they require a 'cool' region where they can condense and reject the absorbed heat. Typically, the cool region has a considerably larger surface area

than the heated region. In vehicles where the entire body is heated significantly, such cool regions may not be available without switching to working fluids with very high operating temperatures. This point will be discussed in detail in Chapter 8.

4.3 Active Systems

Active cooling is often needed for the highest heat flux regions in aerospace vehicles, such as in a boost-stage liquid rocket engine, where one or more of the active cooling schemes illustrated in Figure 39 are usually employed. A good example of the cooling capabilities possible with active cooling circuits comes from the Space Shuttle Main Engines, in which the heat flux transfer to the liquid hydrogen fuel at the throat was about 160 MW/m^2 [18]. Active cooling solutions are generally the most complex and heaviest. Complicated fluid passages and heavy pumping equipment are often required.

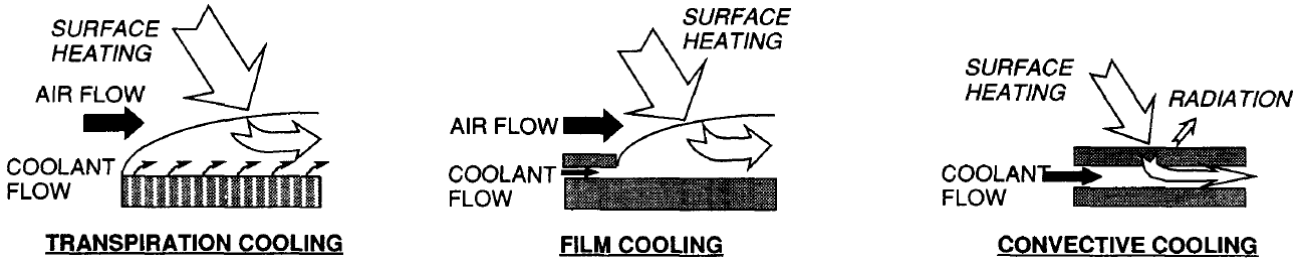

Figure 39 - Common active TPS. Adapted from [39]

4.3.1 Convective Cooling

Convective cooling solutions typically pass a cold fluid through closed channels with the channel material providing the interface between the hot and cold regions. Figure 40 illustrates come typical coolant passage configurations for liquid rocket engines. Large Reynolds numbers are generally needed to achieve high heat transfer rates, implying high fluid velocities and narrow channels. The high pressure drops associated with fast flows in small channels require high upstream pressures, and thus heavy pumping equipment and relatively thick tube walls. As an illustrative example, The Delta-IV H_2-O_2 upper stage engine has a pressure drop in its engine cooling jacket of about 17 bar with a nominal combustion chamber pressure of 44 bar [11].

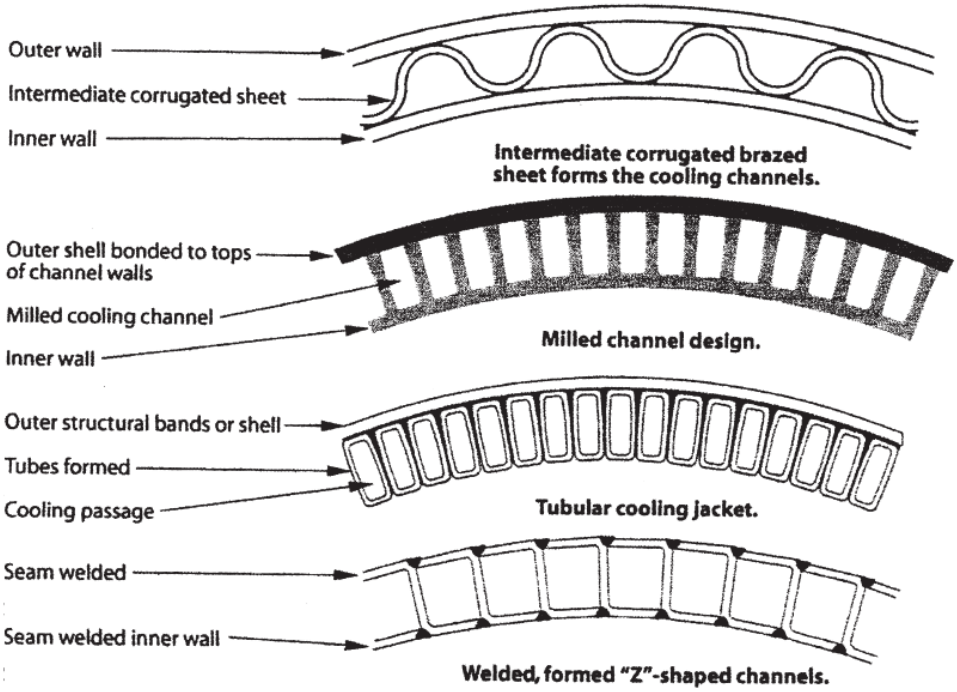

Figure 40 – Some common configurations of liquid rocket engine cooling jackets [11].

Figure 41 illustrates a typical temperature profile through a rocket engine cooling jacket. The cooling fluid bulk temperature plus the boundary layer temperature difference sets the outside temperature of the internal wall. The wall inside temperature is then the sum of the outside face temperature and the temperature difference required to conduct the thermal flux through the wall. Cold coolants and thin walls made of high conductivity materials are key to maintaining the inside face temperature low and thermal stresses within acceptable limits. The same general principles will apply in hypersonic cooling jackets.

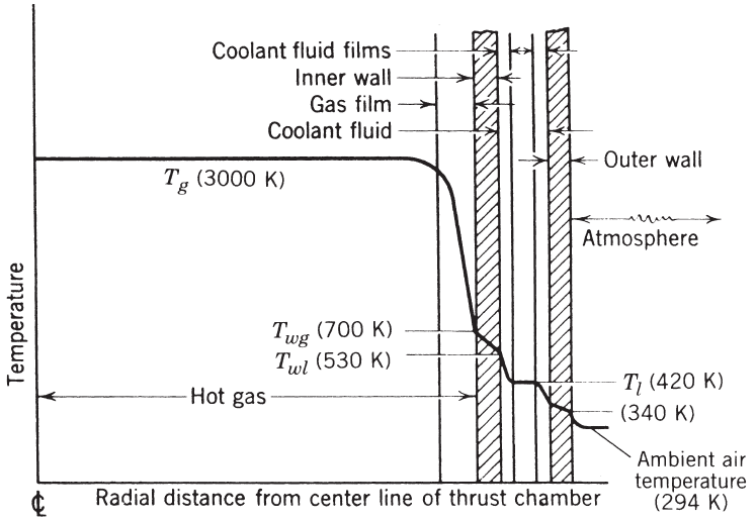

Figure 41 – Typical temperature profile through a liquid rocket engine cooling jacket [11].

In industrial applications the absorbed heat may then be rejected to the environment at a secondary heat exchanger and the fluid recycled. In aerospace applications, the coolant is typically the fuel, which is then combusted and ejected from the vehicle.

4.3.2 Film Cooling

Film cooling is a technique used at particularly high heat flux locations. A small flow of cold fluid is introduced into a hot gas stream to cool the boundary layer and reduce the heat transferred to the wall. A simple implementation with round holes in a rocket engine combustion chamber is illustrated in Figure 42. More uniform protection can be achieved by using slots to introduce the cooling fluid [11]. The slots could be radial, or tangential to the surface as illustrated in Figure 43 and Figure 44. Tangential or low-angle injections are preferable for external surfaces of flight vehicles to avoid tripping the boundary layer into turbulence [56].

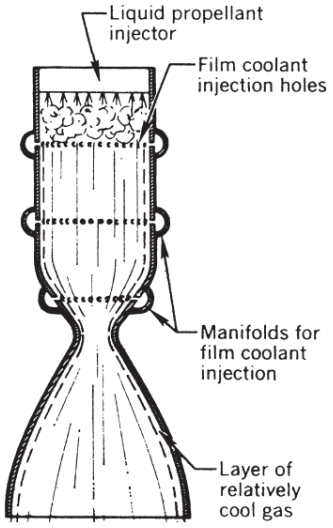

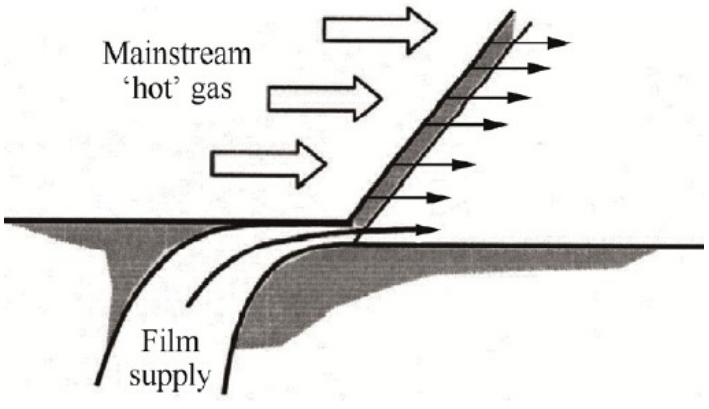

Figure 42 (Left) – A simple liquid rocket engine film cooling scheme [57].
Figure 43 (Right) – Injection of a film tangentially to the protected surface [58].

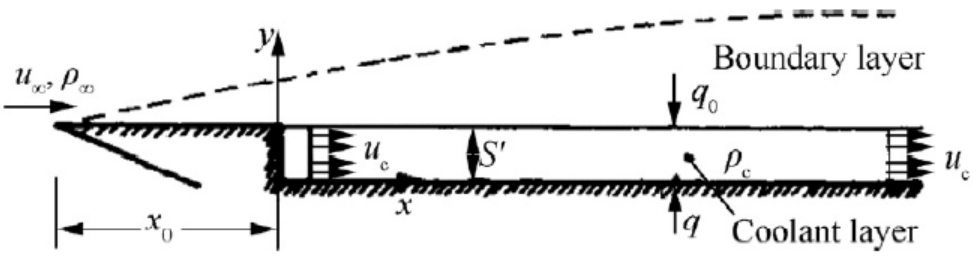

Figure 44 – Schematic of a tangential film protecting a surface [58].

Rocket engines and turbine blades have been the main applications of subsonic film cooling thus far. Supersonic and hypersonic flight are additional applications for which film cooling appears attractive. The introduction of a cooling film in supersonic and hypersonic flows can reduce wall friction as well as the wall thermal fluxes [58]. Experimental works have achieved hypersonic heat flux reductions of 40% and above [56]. Both gaseous and liquid film cooling of hypersonic leading edges are areas of ongoing research.

4.3.3 Transpiration Cooling

Similar to film cooling, transpiration cooling involves either a gaseous or liquid coolant being introduced into the hot free stream fluid. Rather than being introduced at discrete holes or slots, as is the case for film cooling, the fluid is forced through a porous structure and thus introduced in a more distributed manner. Figure 45 and Figure 46 illustrate the general concept of transpiration cooling and an applied example of a transpiration cooled hypersonic vehicle nose.

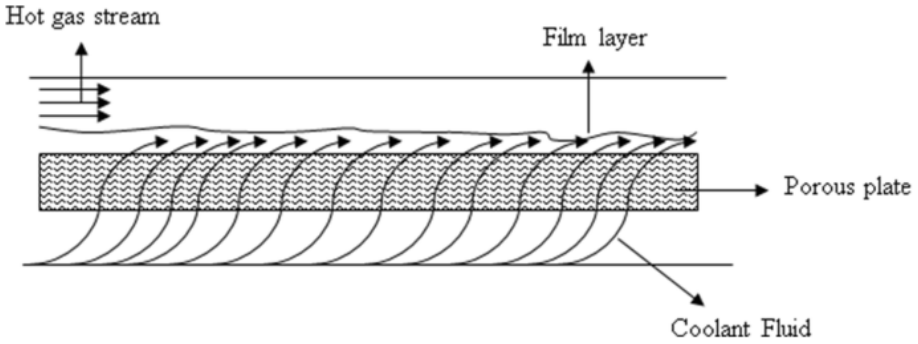

Figure 45 –Transpiration cooling working principle [59].

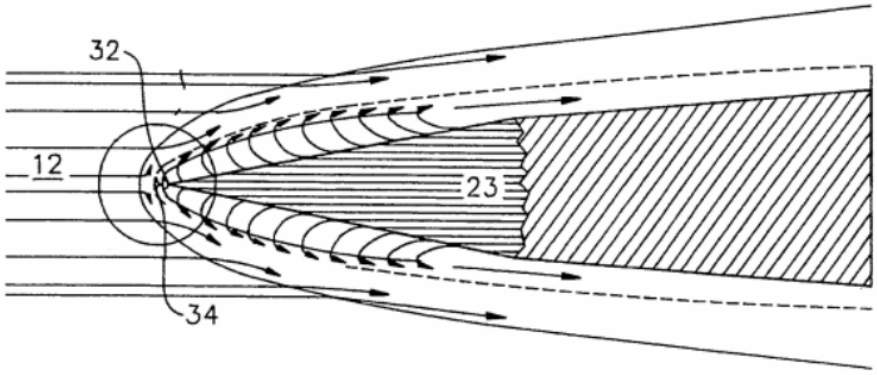

Figure 46 – Schematic of AKTiV cooling experiment on the SHEFEX II hypersonic vehicle [59].

Thermal flux reductions on the order of 50% have been achieved with Mach ~10 hypersonic test vehicles [59]. Transpiration cooling with both gaseous and liquid coolants is an area of ongoing research.

5 Analysis of Endothermic Processes for Active Cooling

5.1 Enthalpy Absorption Capability of Various Processes

Inspired by the TAGA concept, a number of different endothermic chemical and phase change processes were investigated. Emphasis was placed on identifying substances and processes which could serve a useful secondary function, such that the 'parasitic' mass component of the TPS could be minimised. The results of this search are presented in Table 7.

Cryogenic fluids were considered as they can absorb large quantities of heat as well as reduce heat exchanger wall temperatures. The Cosmic Background Explorer satellite stored liquid helium on-board for 306 days, and experienced boil off rates of between 0.26 and 0.37 percent per day [60]. Assuming these rates and if the AGA transfer time can be kept to around 100 days, the vehicle could retain approximately 75% of the coolant launch load. However, it is not clear a priori if this assumption is valid given the vastly different architectures and shapes of the vehicles.

Ablatives initially appear attractive due to their high enthalpy absorption capabilities and low required mass fractions. However, they protect structures by allowing their outer layer to degrade and ablate away over time, changing the vehicle outer mould line. Assuming an ablation rate of 0.1mm/s, the outer mould line would recess by about 3 cm over a 5-minute flight. This is not a problem for blunt re-entry capsules but would greatly change the aerodynamic characteristics of a slender waverider with an initially sharp nose. As will be seen in Section 7.3, an AGA vehicle performance is very sensitive to the nose radius and so ablatives were discarded.

The melting and vaporisation of beryllium would appear to be competitive with ablative materials. It also has the advantage of possessing a stable liquid phase. Beryllium could be stored inside the vehicle and function like an 'internal ablative', with the liquid phase ensuring good contact between the beryllium and outer surface. However, beryllium vaporisation occurs at prohibitively high temperatures, posing severe structural problems. It would only make sense if the vaporisation occurred externally, at which point the same problems of ablatives discussed above would occur.

Several liquid metals including lithium, sodium, potassium, and NaK were considered due to their high energy storage capabilities, high thermal conductivities, and low viscosities. Their high thermal properties would suggest that they could handle higher flux regions at lower flow rates than molecular fluids, reducing pressure losses and thus pumping requirements. While the vapours of these metals could be superheated and used in gas-dynamic nozzles, their high boiling points would allow little expansion before condensation occurred in the nozzle, preventing significant acceleration of the gas. Instead, sodium, lithium, and potassium have all been investigated as potential propellants for high-efficiency electric propulsion. The high enthalpy storage capabilities of lithium combined with the fact that there is ongoing research into high-I_{sp} gridded ion thrusters with lithium propellant [61] motivated the proposal of a new mission architecture based on lithium as the coolant-propellant.

The storage potential of lithium hydride is immense, as it absorbs large amounts of energy through the Li/H decomposition process, through lithium evaporation, and through heating of gaseous hydrogen. Unfortunately, it remains solid until about 960 K, posing transport and heating problems which couldn't be solved in this work.

Water electrolysis was considered, with the electrical power required assumed to be coming from a steam turbine. Investigations into electrolysis systems on the International Space Station indicated that mass flow rates of kilograms per second were not possible with a compact electrolysis system suitable for a spacecraft.

Energy Storage Process	Process Conditions	Enthalpy Mass Density [MJ/kg]	Enthalpy Volume Density [MJ/m^3]	Secondary Function
Water vaporisation and superheating	300–1800 K 5 bar	6.0	6010	Primary thermal propulsion, attitude thrusters, nose transpiration coolant, onboard power generation
Ammonia vaporisation, decomposition, and superheating	300–1800 K 5 bar	8.3	4980	Primary thermal propulsion, attitude thrusters, nose transpiration coolant, onboard power generation
Methanol vaporisation, decomposition, and superheating	300–1800 K 5 bar	11.0	8660	Primary thermal propulsion, attitude thrusters, nose transpiration coolant, onboard power generation
Liquid hydrogen vaporisation and superheating	20–1800 K 5 bar	27.7	1970	Primary thermal propulsion, attitude thrusters, transpiration coolant
Liquid methane vaporisation and superheating	110–1800 K 5 bar	12.6	5350	Primary thermal propulsion, attitude thrusters, transpiration coolant
Molten lithium vaporisation and superheating	500–1800 K 1 bar	25.7	13600	Secondary ion propulsion, re-usable heat sink
Molten sodium vaporisation and super heating	400–1800 K 1 bar	5.7	5470	Secondary ion propulsion, re-usable heat sink
Lithium hydride decomposition, lithium vaporisation, and gas mixture superheating	300–1800 K 1 bar	37.4	30670	Thermal propulsion with hydrogen
Beryllium heat sink	300–1500 K 1 bar	3.5	6390	Vehicle structure
Beryllium heating and melting	300–1800 K 1 bar	6.1	12440	Working fluid for nuclear-thermal propulsion concepts
Beryllium vaporisation [36]	300-3243 K 1 bar	~ 32		-
Carbon-phenolic ablation [47]	-	~ 30		-
Carbon-carbon ablation [47]	-	~ 40		-
Graphite ablation [36]	0-3900 K 1 bar	~ 60		-
Water electrolysis [36]	-	13.3	5630	Primary thermal or chemical propulsion, attitude thrusters, H_2 transpiration coolant

Table 7 – Thermal absorption capacity and required vehicle mass fraction of different physical and chemical processes. If no source is given, the enthalpy difference was evaluated with the NASA CEA program.

5.2 Propulsion Performance of Suitable Coolants

While the heat sink capability of the fluid is arguably of higher priority, the propulsive performance must also be carefully considered in order for the complete TPS to provide a net-benefit to the mission.

5.2.1 TAGA

The propulsion provided during the TAGA flyby will be based on standard gas-dynamic principles and use a converging-diverging nozzle. In the case of the TAGA vehicle, the energy required to vaporise and heat the propellant will come from absorbed thermal energy rather than chemical reactions or electric power.

As can be understood from Equations 10 through 12 [11] and Figure 47, the efficiency of a gas-dynamic propulsion system at a given operating temperature is strongly influenced by the molecular mass of the expelled gas, while the ratio of specific heats plays a relatively minor role. It should be noted that the molecular mass of interest is that of the gases at the nozzle throat. The original stored propellant may have reacted or decomposed via chemical or thermal means into a new mixture.

$$c = c^* C_F \tag{10}$$

$$c^* = \frac{\sqrt{\gamma R_M T}}{\gamma \sqrt{\left(\frac{2}{\gamma+1}\right)^{\frac{\gamma+1}{\gamma-1}}}} \tag{11}$$

$$C_F = \sqrt{\frac{2\gamma^2}{\gamma-1}\left(\frac{2}{\gamma+1}\right)^{\frac{\gamma+1}{\gamma-1}}\left(1-\left(\frac{P_2}{P_1}\right)^{\frac{\gamma-1}{\gamma}}\right)} + \frac{P_2 - P_3}{P_1}\frac{A_2}{A_t} \tag{12}$$

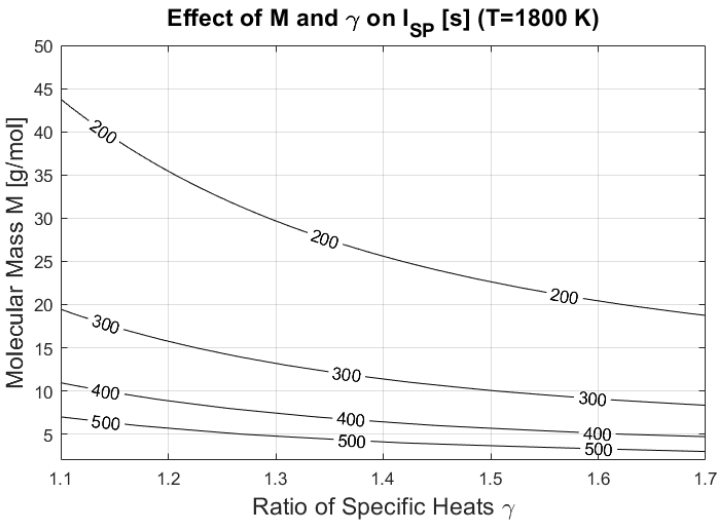

Figure 47 – Specific impulse of a perfectly expanded propulsion system with varying gas properties.

As hydrogen is the lightest element, it is a good choice if a high specific impulse is desired. This is illustrated clearly in Figure 48. As can be seen from Table 7, hydrogen can absorb large amounts of energy per unit mass. However, it is cryogenic and requires storage at around 20 K. Additionally, it has a very low density and would require a relatively large storage volume, as can also be seen from Table 7.

Methane is the next most attractive propellant from an energy sink perspective. However, it is also cryogenic and would likely lose a significant fraction of its mass on any interplanetary transits, eliminating any gains over room-temperature storable liquids. Figure 49 shows that methane's propulsion efficiency is relatively modest. While it contains a significant molar content of hydrogen, methane does not readily decompose under the considered conditions and the hydrogen remains attached to a relatively heavy carbon atom.

Ammonia's specific energy storage is very similar to methane once boil-off is factored in. Ammonia also has the advantage of being storable at room temperature, albeit at a pressure of around 10 bar. This storage pressure could be higher than that required for other fluids, increasing the mass of the tankage and piping. Of particular interest is the thermal decomposition of ammonia at high temperatures. This allows it to soak up a considerable amount of energy while also lowering the average molecular mass of the gas mixture as it decomposes into N_2 and H_2. Figure 50 shows the improved propulsion performance of ammonia.

Water is an attractive option due to its high density, inert nature, and ease of storage. From Table 7 and Figure 51, it can be seen that water is a moderate performer in both energy storage and propulsion efficiency.

Methanol is an interesting fluid which combines the advantages of water and ammonia. It is storable at room-temperature without pressurisation, and it endothermically decomposes into a gas mixture with a mole fraction

of almost 60% H_2. It has the highest enthalpy absorption per unit mass of any of the propellants discussed so far, and a propulsion efficiency slightly below that of ammonia. It has previously been considered as a multi-function propellant-coolant before for these reasons [62]. One of the decomposition products is atomic carbon, which raises concerns about coking of small flow passages.

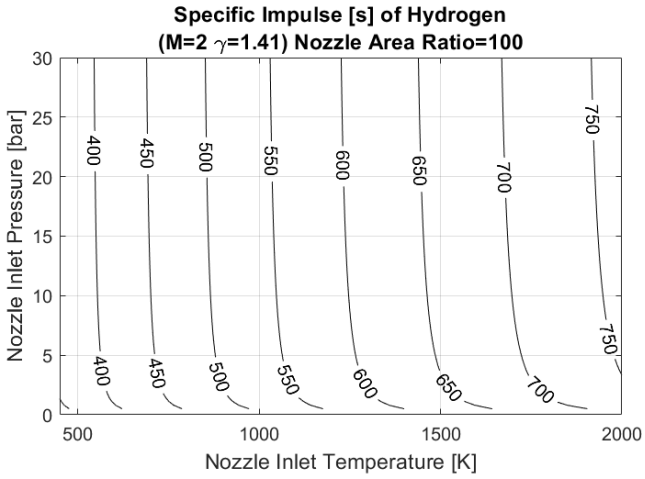

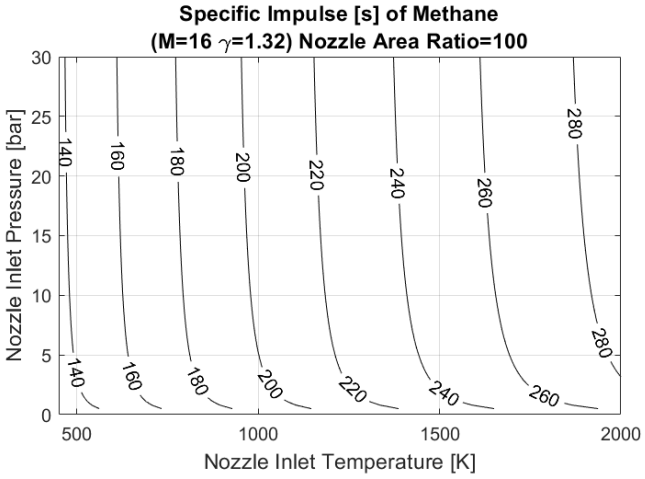

Figure 48 (Left) – I_{sp} vs temperature and pressure for hydrogen.
Figure 49 (Right) - I_{sp} vs temperature and pressure for methane.

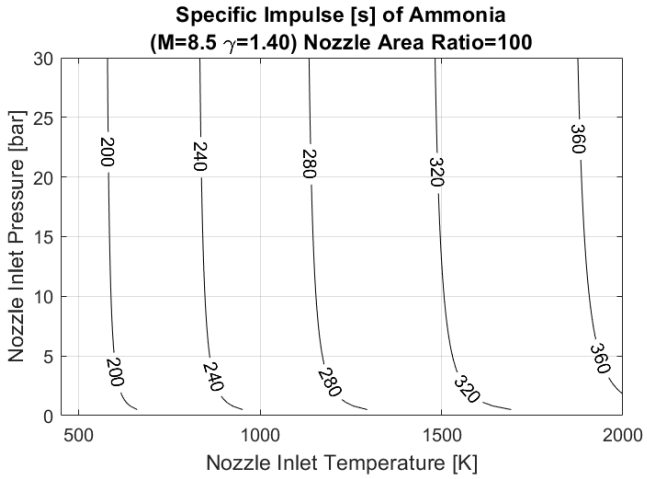

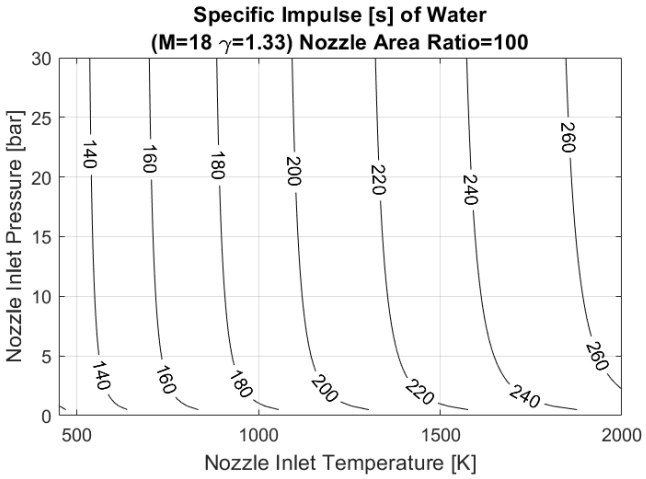

Figure 50 (Left) - I_{sp} vs temperature and pressure for decomposed ammonia.
Figure 51 (Right) - I_{sp} vs temperature and pressure for water.

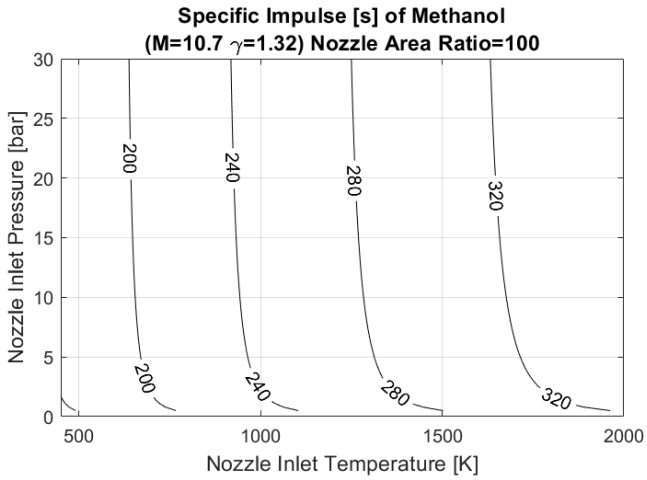

Figure 52 - I_{sp} vs temperature and pressure for decomposed methanol.

Liquid hydrogen, water, and ammonia were selected for further analysis.

5.2.2 AGA-EP

The high thermal storage capabilities of lithium as well as ongoing research into its use a propellant for gridded ion-thrusters motivated the development of a mission architecture based around these strengths. The proposed mission is hereon referred to as the AGA-EP mission. In contrast to a TAGA mission, propulsive thrusting would occur for extended periods in deep space in order to compensate for drag losses during the AGA flyby.

Thrusting with a given magnitude force during the atmospheric phase of a TAGA flight would be more energy efficient than in deep space due to gains from the Oberth effect. However, the I_{sp} of electric propulsion can be an order of magnitude higher than for gas-dynamic propulsion, meaning that a much smaller propellant load is needed even once the orbital energy inefficiencies of low-thrust trajectories are considered.

Only brief consideration was given to electric propulsion propellants other than lithium. Some electrothermal options were considered but judged to be outside the scope of this work. Hybrid systems with a closed-loop lithium cycle and a heat-exchanger to vaporise a molecular propellant for in-atmosphere thrusting were briefly considered and discarded. Ammonia and water electrothermal systems are worth briefly mentioning since the propellants were leading contenders for the TAGA mission. Ammonia has often been studied as a propellant for electrothermal systems such as resistojets and arcjets [63]. Water has also seen a recent surge in popularity as an inert, non-toxic propellant for electrothermal propulsion systems [64]. For both fluids, residual propellant from a TAGA flyby could be used for moderate-efficiency trajectory correction manoeuvres or attitude control.

The aim of this analysis was to highlight the two ‘extreme’ design cases of TAGA and AGA-EP missions and not get caught up on hybrid missions with multiple propulsion systems. Only TAGA and AGA-EP were considered in the remainder of this work.

6 Interplanetary Mission Analysis

A reference mission was identified which is logically coherent with an aerogravity assist spacecraft and is valid from an energy perspective. Given the large uncertainties in many of the mission variables, no detailed optimisation has been conducted.

6.1 Target Planet

One of the main advantages of an aerogravity mission within the Solar system is that it can remove the need for a Jupiter flyby, relaxing launch window constraints. All previous missions to the outer planets have been assisted by a flyby at Jupiter, and so an outer planet mission was selected in an attempt to demonstrate the possible benefits of AGA. Given the likely complexity and mass penalty of an AGA vehicle TPS, a mission was selected which makes the most use of the TPS. Secondary uses of the TPS could come from aerocapture and orbit circularisation or an AGA flyby of a moon to capture the vehicle into the target planetary system. Uranus and Neptune were considered as target planets as they have not yet been visited by an orbiter, and both are compatible with aerocapture. Uranus was selected as it has the lower heliocentric orbit of the two planets, allowing a less demanding AGA and thus lower loads on the TPS.

6.2 AGA Planet

Earth, Venus, and Mars are all atmospheric planets suitable for an AGA flyby. Earth and Venus are attractive from an aerodynamic perspective as their thick atmospheres allow flight at high Reynolds numbers and L/D ratios above 10 in some instances [8]. Given that the vehicle will likely have a nuclear power source, an Earth AGA is not a desirable choice in case a vehicle failure should occur during the atmospheric flyby. Additionally, the greater masses of Earth and Venus relative to Mars means that for a given heliocentric flyby velocity the atmospheric flight speed at periapsis is also correspondingly greater, as illustrated in Figure 53. This increased periapsis velocity increases the required centripetal acceleration to maintain a constant altitude during the flyby, as illustrated in Figure 54, thus increasing the structural loading on the vehicle. Any centripetal acceleration reduction from the larger radius of Venus is outweighed by the periapsis velocity increase. The higher periapsis speed also greatly increases the thermal loading, which scales with exponents of 3 and above. Clearly a flyby at Venus will place higher peak structural and thermal demands on the vehicle.

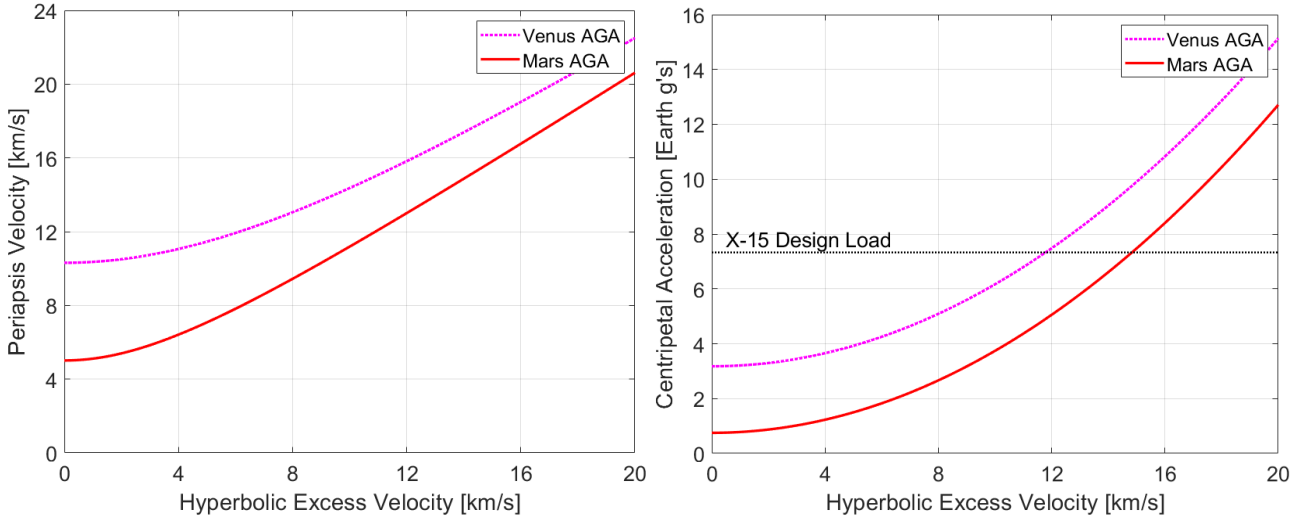

Figure 53 (Left) – Periapsis velocity vs hyperbolic escape velocity at Mars and Venus.
Figure 54 (Right) – Centripetal acceleration required for constant altitude flight at Mars and Venus.

A potential saving grace for Venus and Earth is that their increased mass causes a greater gravitational deflection component, thus requiring a smaller atmospheric deflection angle for a given total flyby deflection. The atmospheric flight time will be shorter, and the total heat load may be reduced with respect to a Mars flyby. As

this work is exploring the limits of TPS technologies, Mars was selected for the flyby in order to reduce the peak loads on the TPS. Mars has the lowest gravitational parameter and thus lowest ratio of periapsis velocity to hyperbolic excess velocity of the planets considered. Further work could explore the comparative benefits of Venus and Mars AGA's.

In summary, the heliocentric flyby velocity is a critical parameter for the mission design which should be maximised, while the atmospheric flight velocity is a critical parameter for the TPS which should be minimised if low peak thermal and structural loads are a priority.

6.3 Vehicle Aerodynamic Properties

Both a propulsive flyby for the TAGA mission and non-propulsive flyby for the AGA-EP mission were explored. Both vehicle concepts utilise an active cooling system, but with different coolants and different propulsion strategies. The same vehicle geometry is assumed for both cases, with a 'natural' L/D of 5. A L/D ratio of 5 appears to be a reasonable first estimate for a vehicle of about 10m length from consideration of Figure 16 and Figure 17.

In the TAGA flyby, propulsion is provided during the atmospheric flight via gas-dynamic acceleration and ejection of the vapourised coolant. In the AGA-EP case the lower effective L/D and greater energy loss during the atmospheric flight is accepted, and a high efficiency electric propulsion system used in deep-space in order to recover the orbital energy deficit with respect to the TAGA case. The TAGA thrust-to-drag ratio was taken as 0.3, raising the 'effective' L/D to 7.1. Previous work by Murakami used a value of 0.4 for a water based TAGA vehicle [1].

6.4 Preliminary Mission Design

A study of similar proposed missions was conducted to help select reasonable targets for the present analysis and to allow basic comparisons of AGA and traditional missions. Table 8 details the relevant high-level aspects of the proposed MUSE, OCEANUS, and QUEST missions to Uranus. It is important to note that all 3 of the considered missions either require a Jupiter gravity assist or an extended period of high-power Solar Electric Propulsion (SEP). The alignment of Jupiter and Uranus restricts the launch windows to every 12-13 years. It was not stated in the OCEANUS document what power level was required for the SEP system, just that it would only be operated within 1.5 AU of the Sun, suggesting a power of at least several kilowatts.

	MUSE [65]	OCEANUS [66]	QUEST	
Proposal Origin	Alpbach Summer School 2012, 2013 JPL PSSS	2017 JPL Planetary Science Summer School	2018 JPL Planetary Science Summer School	
Time of Flight to Uranus	14 - 18	11	13	years
Earth-Uranus Trajectory	1 x Earth GA, 1 x Mars GA, 1 x Jupiter GA, 2 x DSM (Δv=1.5 km/s)	1 x Earth GA, 2 x Venus GA, 7 years of multi-kW SEP, Uranus capture burn	1 x Jupiter GA, DSM (Δv=0.65 km/s), Uranus capture burn (Δv=0.95 km/s)	
Launch Vehicle	Ariane 5 or Atlas V 511	Atlas V 511	Atlas V 511	
Launch C_3	10 - 15	~20	29	km^2/s^2
Dry Mass	2073	1533	1210	kg
Launch Mass	4240	3939	~3000[i]	kg
Power	ASRG*, 320W at EOL	eMMRTG**, 290 W at EOL	eMMRTG**, 220 W at EOL	

Table 8 – Summary of previous proposed missions to Uranus.
**Advanced Stirling Radioisotope Generator. **Enhanced Multi-Mission Radioisotope Thermoelectric Generator.*

A comparable mission profile was sought for an AGA spacecraft using the Tisserand plane. This method assumes that all the planets have circular, coplanar orbits. As can be seen from Table 9, these assumptions are accurate enough for a preliminary analysis. Another limitation of the Tisserand plane is that it does not consider

phasing of the planets in their respective orbits. Also shown in Table 9 are the 2-planet synodic periods for Earth-Mars and Mars-Uranus, and they do not share a neat integer multiple. The 3-planet syzygy only approximately repeats every 9 years, thus non-ideal transfers will be needed on one or both legs of the journey to Uranus. To compensate for off-nominal conditions, a nominal AGA at Mars and Mars-Uranus transfer was assumed and the vehicle mass reduced to allow variation in the Earth departure C_3.

	Earth	Mars	Uranus
Eccentricity	0.017	0.094	0.046
Inclination [°]	0.0	1.9	0.8
Orbital Period [years]	1.0	1.8	83.8
Synodic Period [years]		2.25	1.84

Table 9 – Relevant orbital parameters of planets under consideration

The main drivers during the mission selection were time of flight to Uranus, Mars flyby velocity, Earth departure velocity, and Uranus encounter velocity. An acceptable time-of-flight range of 10-12 years was selected to be competitive with the missions proposed in Table 8. Much shorter flight times are possible with AGA, but these require higher Mars encounter velocities and increased thermal loading. Additionally, the Mars encounter velocity is the primary driver of the Earth departure velocity unless a Venus or Earth GA is exploited before the AGA flyby . A lower Mars encounter velocity allows a lower Earth departure C_3 and thus a more massive vehicle. Given the exploratory nature of this study, large mass margins and reduced thermal loads are desirable, and so a relatively low Mars encounter velocity was selected.

For both TAGA and AGA-EP an RTG system similar to that of the Voyager spacecraft was assumed, providing both electrical and thermal power [67]. While a lithium-fuelled EP system that could achieve an I_{sp} as high as 50 000s is under development [61], I_{sp} and thrust-to-power values of a heritage EP thruster were assumed. [68]. Table 10, Table 11, Figure 55, and Figure 56 summarise the key parameters of both missions.

	TAGA	AGA-EP	
Spacecraft Launch Mass [kg]	2500		kg
Flyby Thrust-to-Drag Ratio	0.3	-	
Effective L/D	7.1	5	
Propulsion Specific Impulse	300	3000	s
Electric Power Available	500		W
Thermal Power Available	7600		W
EP Thrust	-	20	mN

Table 10 –TAGA and AGA-EP vehicle aerodynamic and propulsion parameters .

	TAGA	AGA-EP	
Earth Departure Velocity	6.0		km/s
Earth Departure C_3	36.0		km^2/s^2
Atmospheric Turn Angle	68		°
Mars Flyby Initial v_∞	10.9		km/s
Mars Flyby Final v_∞	9.1	8.6	km/s
Mars Flyby Initial v_p	12.0		km/s
Mars Flyby Final v_p	10.4	9.7	km/s
Atmospheric Cruise Time	361	373	s
Pre-Flyby Heliocentric v	25.9		km/s
Post-Flyby Heliocentric v	33.0	32.4	km/s
Magnitude of Δv vector	13.1	12.3	km/s
Pre-Flyby Heliocentric Energy	-246.8		MJ/kg
Post-Flyby Heliocentric Energy	-36.6	-57.6	MJ/kg
Uranus Arrival v_∞	5.5	5.2	km/s

Table 11 – Comparison of TAGA and AGA performance parameters.

A key point to note is the heliocentric speed increase of 6-7 km/s and total heliocentric delta-V of 12-13 km/s. The magnitude of the delta-V vector is greater than the speed change as it also considers the ~90° rotation of the spacecraft's heliocentric orbit. When leaving Mars, the spacecraft is now close to its heliocentric periapsis. For both missions, the flyby delta-V is greater than any that has ever been provided by a deep-space propulsion system [61]. The heliocentric speed change is also comparable to those that have been achieved via gravity assists at the outer planets. Voyager 2 gained about 10 km/s at Jupiter and 5 km/s at Saturn [69].

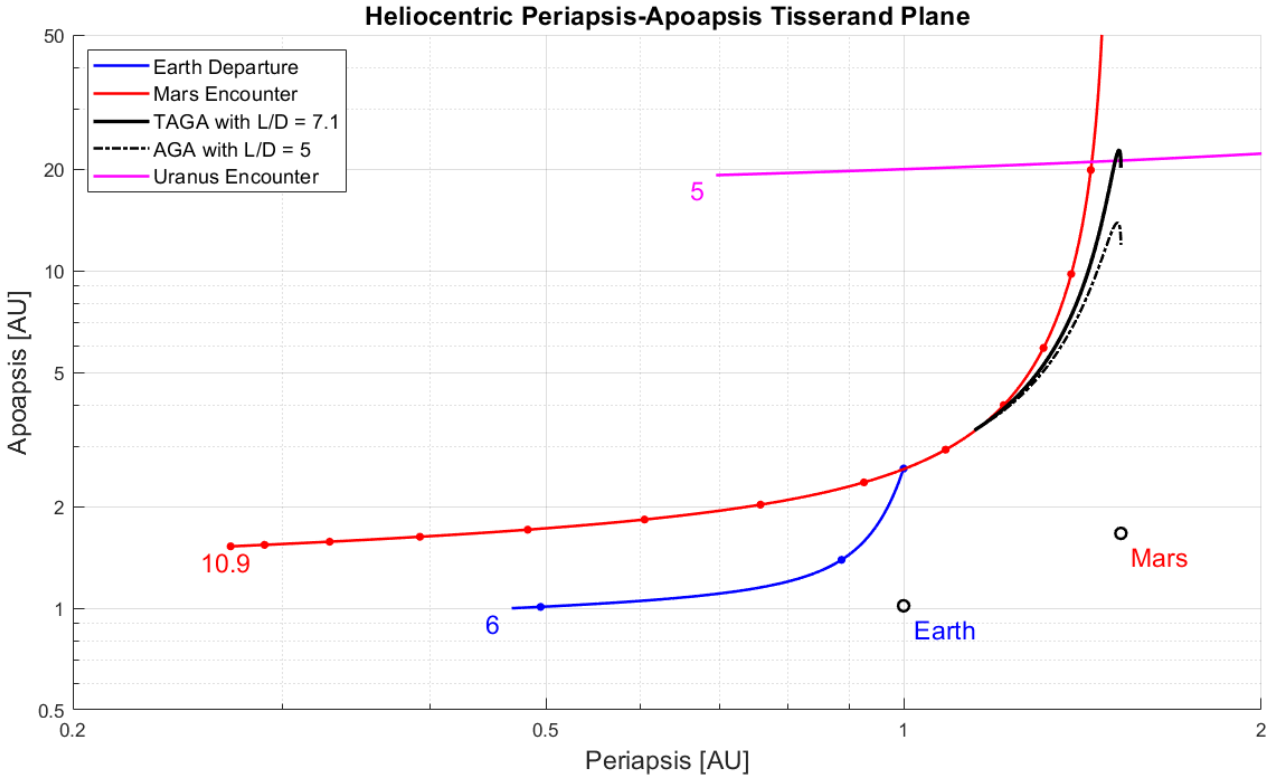

Figure 55 - Apoapsis Tisserand plane showing TAGA and AGA-EP flyby performance curves.

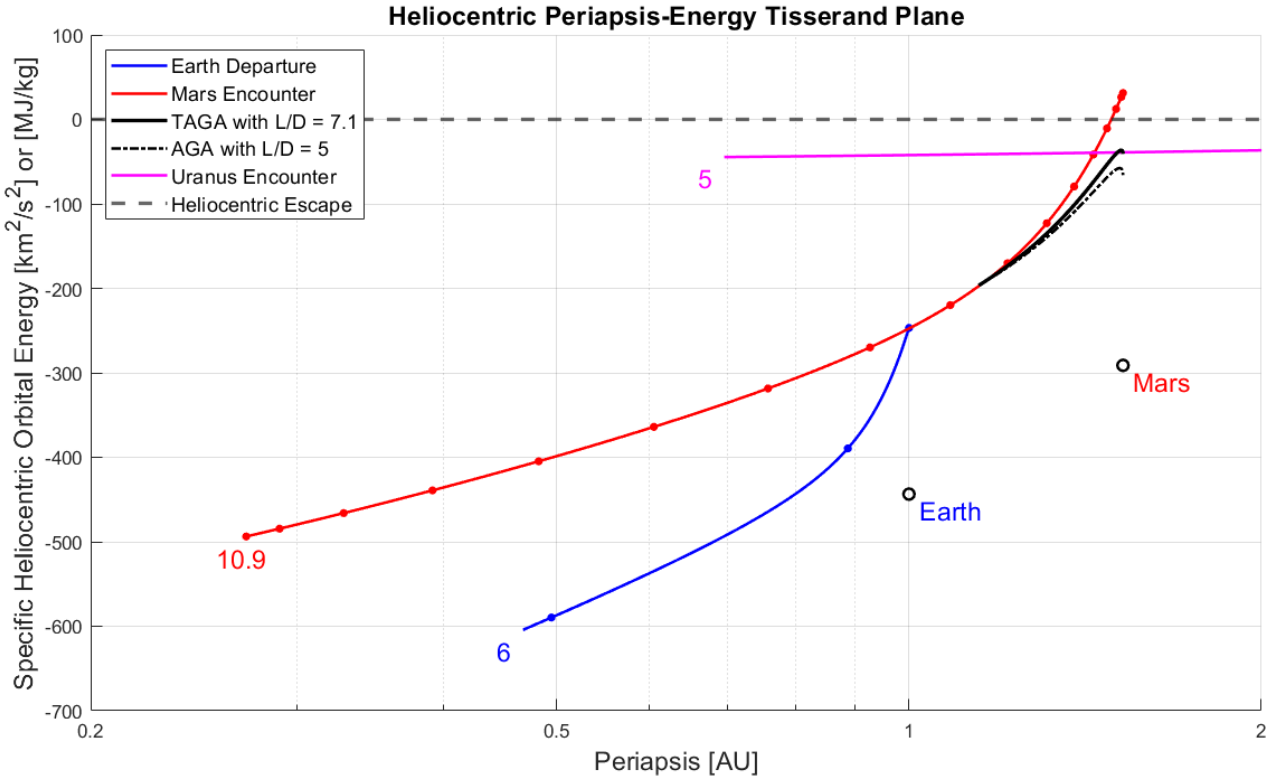

Figure 56 – Orbital energy Tisserand plane showing TAGA and AGA-EP flyby performance curves.

The Earth departure C_3 value was rounded to 40 km^2/s^2 to give some margin for off-nominal planetary alignments. The Atlas V 511 was selected to provide a direct comparison with the reference missions. As can be seen from Figure 57, it can provide C_3 of 40 km^2/s^2 to a payload of approximately 2500 kg.

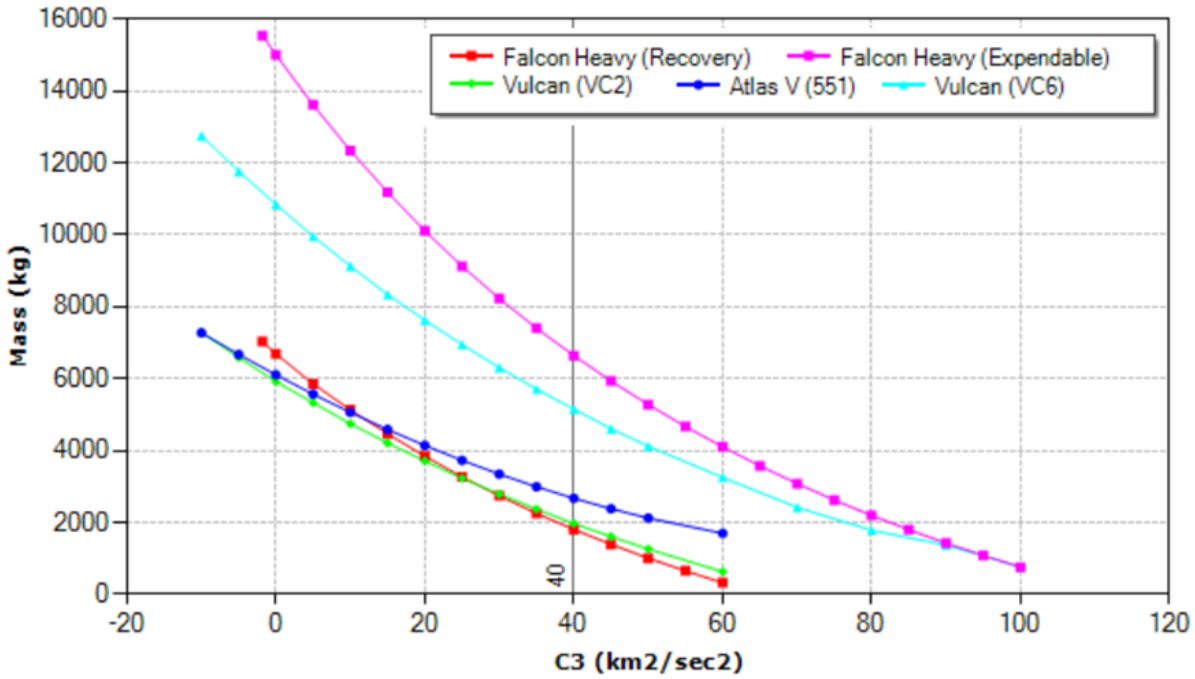

Figure 57 – C_3 performance curves of selected U.S. launch vehicles [70].

From a first glance at Table 10 and Table 8 it would appear that the AGA mission is at a serious disadvantage as its launch mass is about 40% lower than that of the other proposed missions. However, it should be noted that the propellant load is between 50% and 60% of the launch mass for the proposals in Table 8. Preliminary analyses suggest that the AGA vehicle coolant/propellant load could be as low as 10-20%. This would enable delivery of up to 2250 kg of dry mass to Uranus orbit. Additionally, the need for a Jupiter gravity assist is eliminated, giving the AGA mission a launch window every 2-3 years instead of every 12-13.

Given the vastly different vehicle architectures, the most meaningful mass comparison will be the scientific payload mass delivered to Uranus orbit. A detailed estimate of the payload mass is outside the scope of this work. Instead, the dry mass delivered to Uranus orbit minus the TPS mass will be estimated and compared.

Analysis of Uranus aerocapture is also outside the scope of this work. A periapsis delta-V of about 1.5 km/s is required to be captured from a hyperbolic trajectory of 5.5 km/s excess velocity. Given the high periapsis velocity of about 22 km/s, the AGA vehicle would enter the Uranus upper atmosphere at a large angle of attack in order to minimise the free-stream density required. The high intensity portion of this manoeuvre would likely last 20-30 seconds, in which some coolant may be cycled, or degradation of the TPS accepted. Repeated atmospheric passes could be made with the AGA vehicle to lower and circularise the orbit more than is possible with the other proposals.

6.5 Preliminary Heat Load and Propellant Analysis

To guide the selection of TPS schemes to be analysed further, the total heat load over a typical non-propulsive AGA was estimated using the results from Table 11. Only a small portion of the kinetic energy lost during the atmospheric flight will actually be transferred into the vehicle as heat. Analyses of the X-20 Dyna-Soar spaceplane estimated that 2-5% of the energy loss would be absorbed into the vehicle as heat [71]. A similar range of energy transfer percentages has also been observed in liquid rocket engine combustion chamber cooling jackets [11]. For this initial analysis, a 5% conversion ratio was assumed.

Flyby Specific Kinetic Energy Loss	25.4	MJ/kg
Kinetic-Thermal Conversion Ratio	0.05	
Flyby Specific Thermal Energy Absorption	1.27	MJ/kg
Vehicle Mass	2500	kg
Total Thermal Energy Absorption	3175	MJ

Table 12 – Preliminary estimation of total thermal load during the AGA flyby.

From comparing the values in Table 12 with those in Table 2 it is clear that only beryllium and graphite are worth considering as solid-state heat sinks, but even these high-performance options would require an excessive vehicle mass fraction. Clearly a heat sink as the primary element of the TPS is not feasible. However, a vehicle structure comprised of beryllium, titanium, or aluminium alloys may be capable of absorbing a non-negligible portion of the total heat load. While the strength of the materials will reduce as the structure temperature increases over the flight, the aerodynamic and thermal loads will also decrease as the vehicle loses speed and its equilibrium cruise altitude increases.

It is mathematically possible to radiate away this level of heat if the entire vehicle surface is kept at something like 2200 K. However, this would likely require a heavy network of heat distribution devices.

By combining the estimated specific energy absorption with Table 7, the vehicle mass fraction required for each of the feasible endothermic processes can be estimated, and these are reported in Table 13. Also reported are the storage volume requirements. As the vehicle volume can't be normalised without knowledge of the geometry, only the absolute volume requirement is reported here.

Energy Storage Process	Enthalpy Mass Density [MJ/kg]	Stored Density [kg/m^3]	Enthalpy Volume Density [MJ/m^3]	Vehicle Mass Fraction	Required Storage Volume [m^3]
Water vaporisation and superheating	6.0	1000	6010	0.210	0.53
Ammonia vaporisation, decomposition, and superheating	8.3	600	4980	0.137	0.64
Methanol vaporisation, decomposition, and superheating	11.0	790	8660	0.115	0.37
Liquid hydrogen vaporisation and superheating	27.7	71	1970	0.047	1.61
Molten lithium vaporisation and superheating	25.7	530	13600	0.050	0.23
Beryllium heat sink	3.5	1850	6390	0.368	0.50

Table 13 – Preliminary estimation of the vehicle mass fraction and total volume required for each heat sink material.

6.5.1 TAGA Propellant Requirements

The selection of the thrust level for a TAGA flyby is a trade-off between post-flyby heliocentric orbital energy and propellant load. As the vehicle mass is fixed in this study, any increase in propellant load implies a reduction in payload mass. As can be seen in Figure 58, increasing the vehicle lift-to-drag ratio increases the post-flyby heliocentric orbital energy monotonically. The gradient of improvement is much greater at lower L/D ratios and approaches 0 as the L/D ratio goes to infinity. When propulsion is added, huge increases can occur in the effective L/D, as illustrated in Figure 59. As the thrust-to-drag ratio is increased the effective drag tends to 0, causing the effective L/D to tend to infinity. In the case of a T/D equal to 1, the vehicle would not slow down during its flyby. These L/D and T/D curve separately are not enough to properly understand the trade-space, and a coupled analysis is needed. Figure 60 maps the flyby performance of various L/D and T/D combinations for the present mission.

By considering vertical lines of constant natural L/D it is clear that the gradient of improvement is much larger for vehicles with a lower natural L/D. At high L/D values there is less energy to be gained by adding thrust. However, the thrust required to realise performance improvements will be low, as a higher L/D implies a lower drag force. For low L/D vehicles there are huge potential gains, but the relatively high drag force implies a large propulsive force and therefore propellant load.

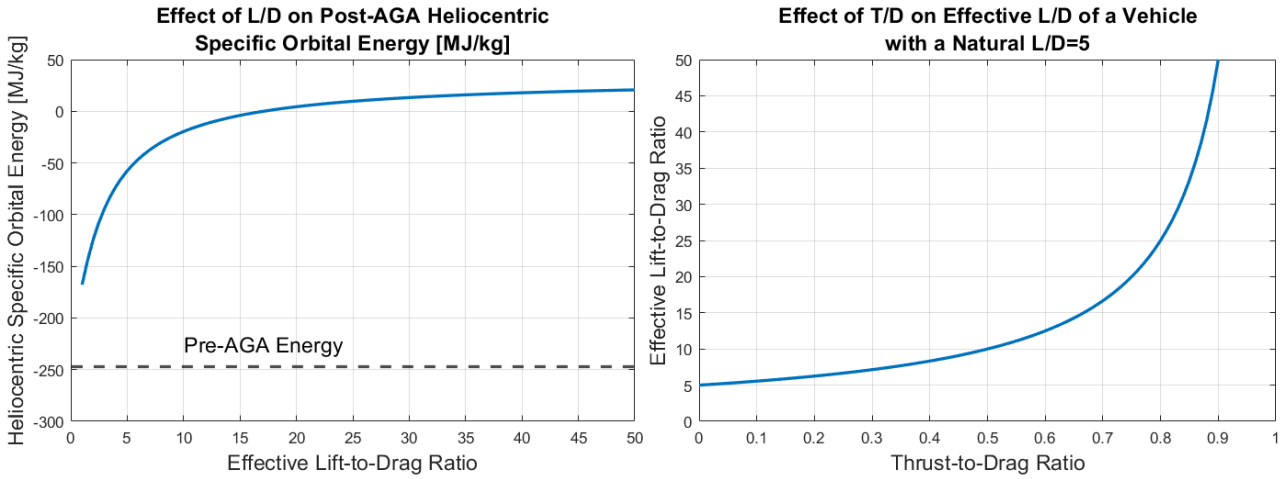

Figure 58 (Left) –Post-TAGA heliocentric energy vs effective L/D.
Figure 59 (Right) – Effective L/D vs T/D for a vehicle with a natural L/D of 5.

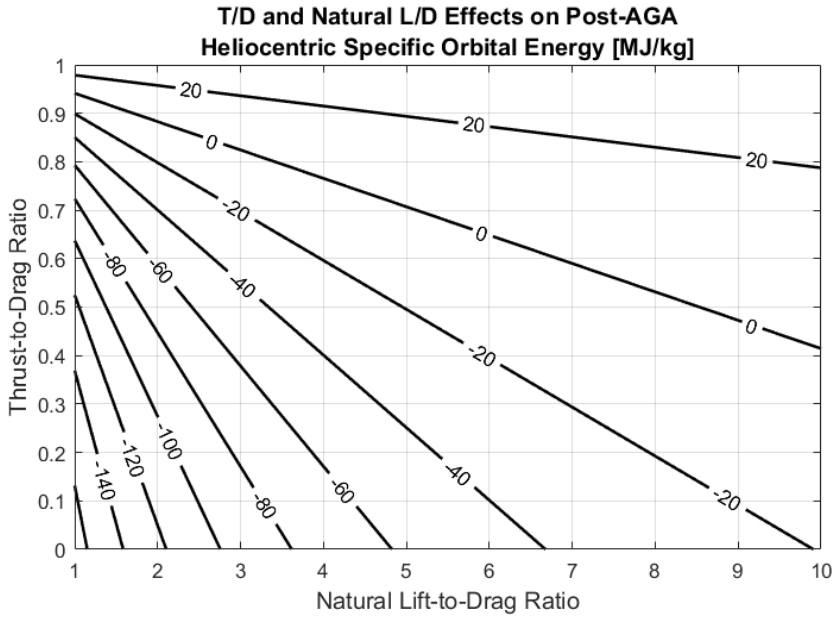

Figure 60 – Coupled effect of natural L/D and T/D on post-flyby heliocentric energy for the current mission.

The implications of L/D and T/D on the propellant load of a generic vehicle can be understood by rearranging Equation 13 and dividing both sides by the vehicle mass. Equation 14 now contains a non-dimensional 'mass-fraction rate', which describes instantaneously the mass fraction of the vehicle that should be ejected with the assumed I_{sp} to generate the longitudinal acceleration a.

$$I_{sp} = \frac{T}{\dot{m}\, g_0} \tag{13}$$

$$a = I_{sp}\, g_0 \frac{\dot{m}}{m} \tag{14}$$

The vehicle's velocity history throughout the flyby by can be calculated from Equations 3 and 4, and then differentiated to find the acceleration history. Multiplying the vehicle non-propulsive acceleration profile by the desired T/D ratio will provide the propulsive acceleration history for Equation 14. The non-dimensional propellant mass fraction can then be plotted against L/D and T/D, as has been done in Figure 61.

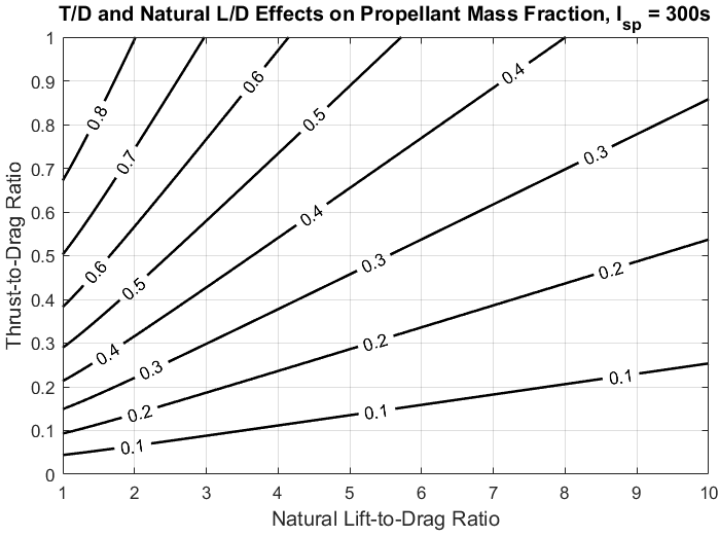

Figure 61 – Coupled effect of natural L/D and T/D on the propellant mass fraction for the current mission.

As expected, only small propellant mass fractions are required to provide a moderate T/D ratio to high L/D vehicles, while huge propellant mass fractions are required to provide the same T/D ratio to low L/D vehicles. Figure 60 and Figure 61 should be considered together when selecting a target L/D and T/D for a TAGA vehicle. No optimisation scheme was applied in this present work but would be useful for further work.

It is worth commenting now that lower L/D vehicles tend to have larger wedge angles and thus higher lift coefficients. This enables cruising at higher altitudes with reduced nose and leading-edge thermal fluxes but increased oblique shock temperatures and acreage thermal fluxes. High L/D vehicles with reduced lift coefficients require flight at lower altitudes where the nose and leading-edge fluxes become very large. Of course, high L/D vehicles also have the option of flying at higher angles of attack with a L/D lower than their maximum value, which could be useful for initial stages of the flight to reduce peak thermal fluxes.

For the present analysis of a waverider with an L/D of 5, a T/D of 0.3 was selected, requiring a propellant mass fraction of about 0.2. The final value will depend on the I_{sp} of the propulsion system. The propulsion and thermal demands on the propellant must be balanced in order to provide an efficient overall package. If the coolant mass flow rate for thermal protection exceeds the mass flow rate required for propulsion or vice versa, the temperature of the expelled fluid will be lower than ideal and thus the I_{sp} of will also be lower. Figure 62, Figure 63, and Figure 64 give the velocity, acceleration, and propellant depletion time histories.

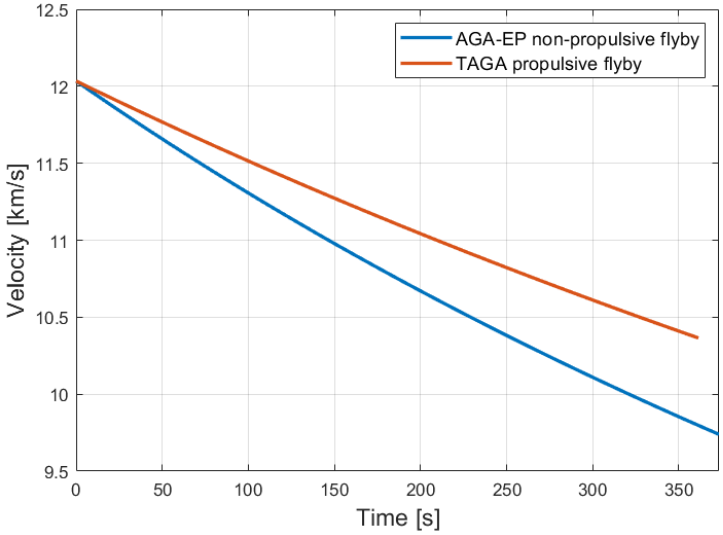

Figure 62 – Velocity time histories of AGA-EP and TAGA flybys.

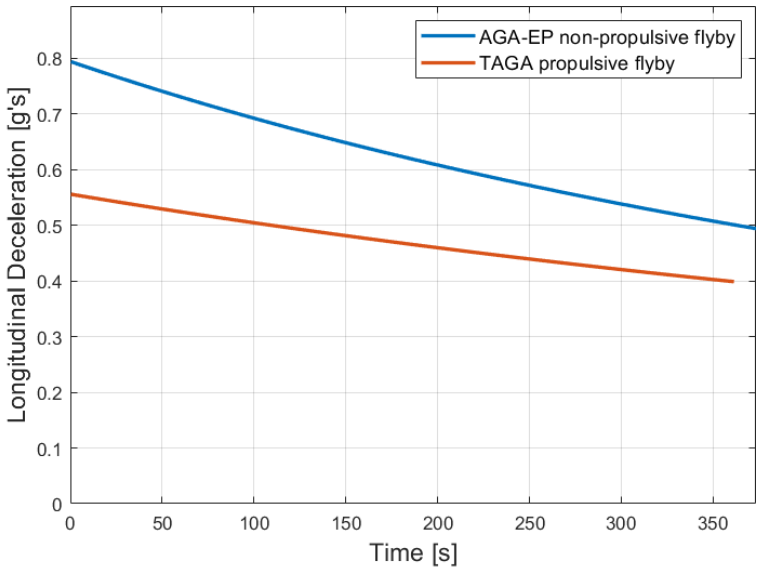

Figure 63 – Deceleration time histories of AGA-EP and TAGA flybys

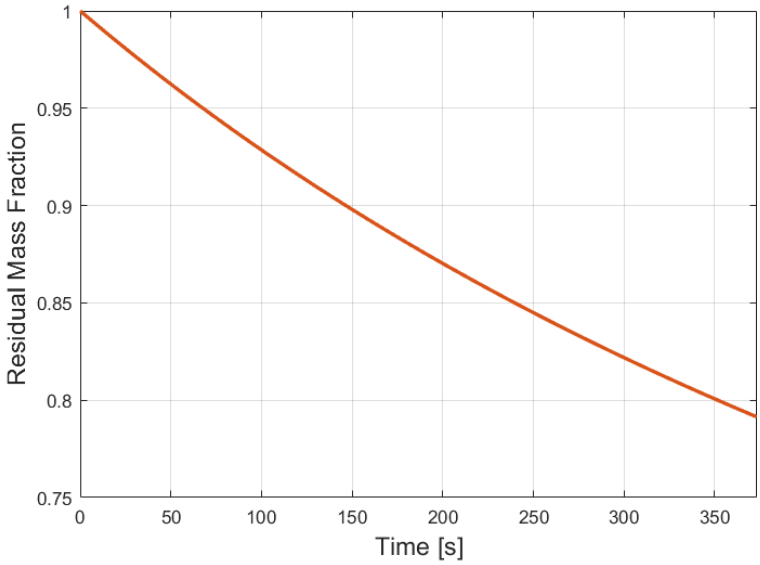

Figure 64 – Vehicle residual mass fraction history for the TAGA flyby.

6.5.2 AGA-EP Propellant Requirements

The orbital energy deficit of the AGA-EP flyby with respect to the TAGA flyby is compensated by a period of operation of the low-thrust EP system. As can be seen from Table 11, the deficit could be compensated by an impulsive delta-V of approximately 0.6 km/s. With an EP system, such a manoeuvre will take on the order of years to complete and the assumption of an impulsive manoeuvre is not valid. As the spacecraft travels higher in its orbit its velocity will decrease, and thus the energy efficiency of thrusting maneuverers decreases. This phenomenon is known as the Oberth effect, and it is illustrated for the current situation in Figure 65.

To efficiently increase orbital energy the thrust vector should be aligned with the tangential component of the velocity vector, and the change in tangential velocity used to calculate the thrusting delta-V required. For eccentric orbits such as the Mars-Uranus transfer orbit, away from the periapsis the velocity vector is dominated by the radial component. Therefore, the tangential velocity component will be a small component of the total velocity vector and a greater spacecraft-frame delta-V will be required than for a given orbital energy increase.

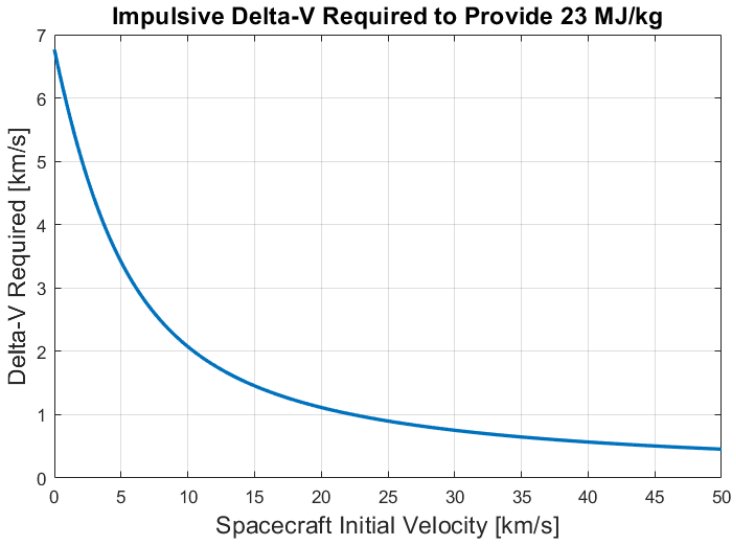

Figure 65 – Impulsive ΔV required to compensate for the AGA-EP energy loss at varying speeds.

A simplified low-thrust analysis was conducted to estimate the spacecraft-frame delta-V and propellant requirements for this manoeuvre. The EP system performance parameters used were those from Table 10, and the thrust was assumed to be always applied tangentially. The Gauss planetary equations method was used, in which a set of 6 differential equations are integrated, with each equation representing the change in one of the Keplerian elements due to orbital perturbations [72]. All orbits were considered to be co-planar, and the only applied orbital perturbation was the EP thrust. The varying heliocentric orbit was propagated until two conditions were met; the transfer orbit apoapsis had to exceed the orbital radius of Uranus, and the specific orbital energy of the AGA mission post-flyby orbit had to match that of the TAGA post-flyby orbit.

Using the EP thrust level, thrusting time, and Equation 15, the propellant mass fraction and the spacecraft-frame delta-V requirements were calculated. The key parameters of the EP manoeuvre are detailed in Table 14. This EP propellant mass must be provided by residual propellant/coolant from the AGA flyby if the TPS is closed cycle or treated as an additional propellant requirement if the TPS is open cycle.

$$\Delta v = I_{sp} * g_0 * \ln\left(\frac{M_0}{M_f}\right) \qquad 15$$

Thrusting time	3.75	years
Spacecraft-frame delta-V	1.34	km/s
Propellant mass-fraction for manoeuvre	0.045	

Table 14 – Key performance parameters of the low-thrust EP manoeuvre.

6.6 Mission Summary

Figure 66 and Figure 67 illustrate the final mission trajectories and Table 15 summarises the flight times.

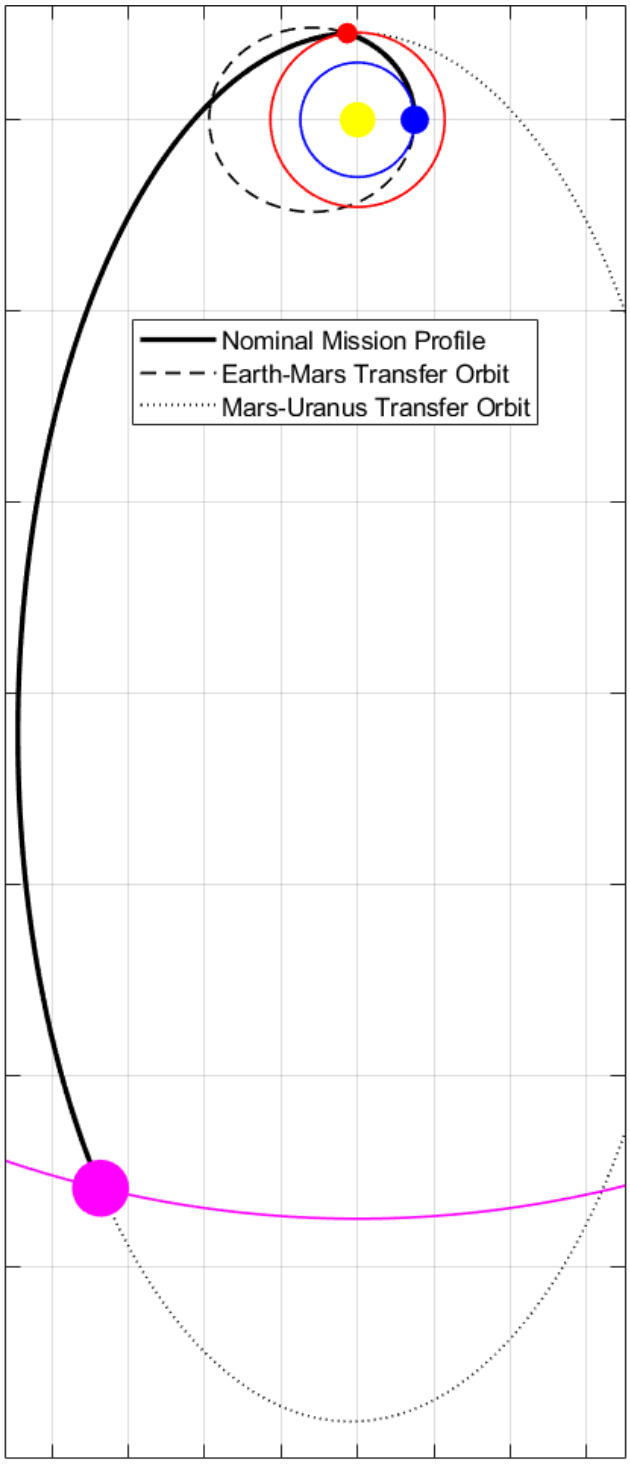

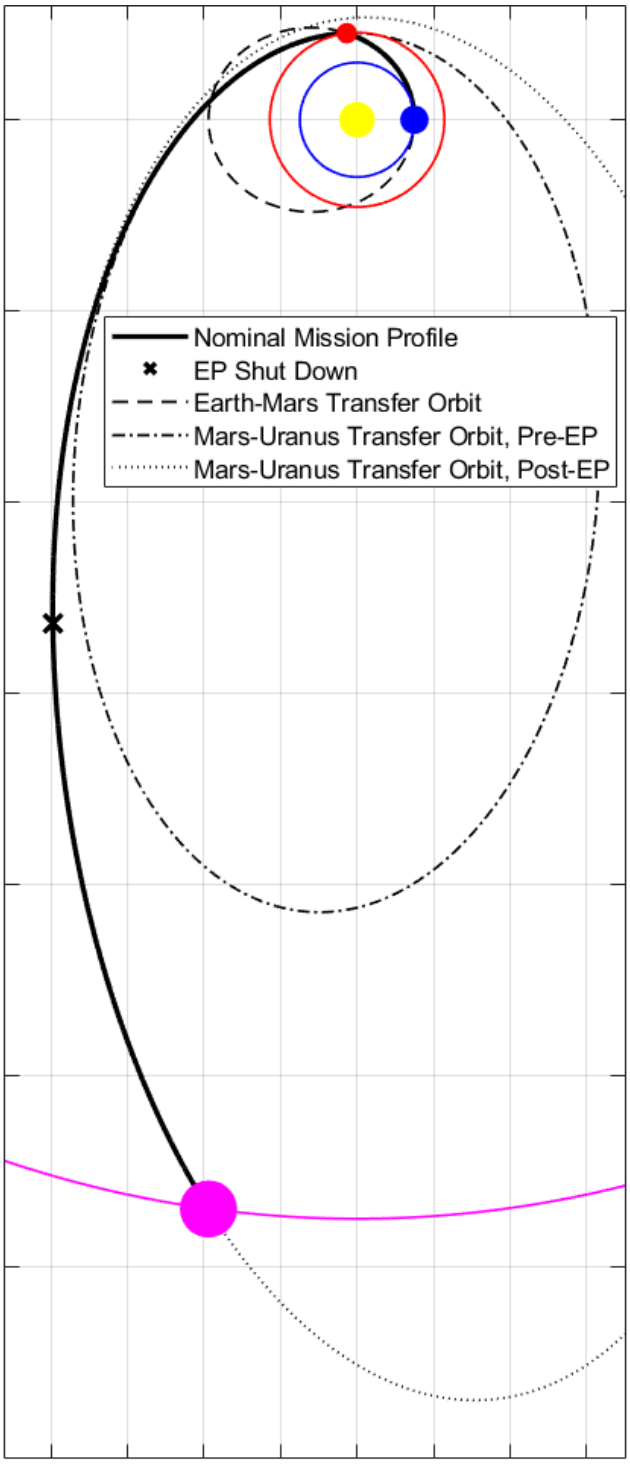

Figure 66 (Left) – TAGA patched conics trajectory, assuming no perturbations.
Figure 67 (Right) –AGA-EP patched conics trajectory, with low-thrust 'perturbation'.

	TAGA	AGA-EP	
Earth-Mars Transfer Time	0.31		years
Mars-Uranus Transfer Time	11.06	11.48	years
Earth-Uranus Total Time of Flight	11.37	11.79	years

Table 15 – Interplanetary transfer times.

7 Atmospheric Flight Analysis

A preliminary analysis of the atmospheric flight phase was conducted to select appropriate vehicle dimensions. The aim of this analysis was to understand the general trends that occur as the geometry is varied. As in the previous analyses, many simplifying assumptions were made, and these will be explained in the following sections. Representative values for the vehicle length, width, wedge angle, nose radius, and leading-edge radius were selected to allow a more detailed consideration of the TPS.

7.1 Atmospheric Flight Model

7.1.1 Overview

Figure 68 describes the logic of the atmsopheric flight model. The model provides a steady state solution which can be evaluated at differenent velocity values over the flight profile to estimate the instantaneous flight characteristics such as altitude, lift, drag, and thermal fluxes.

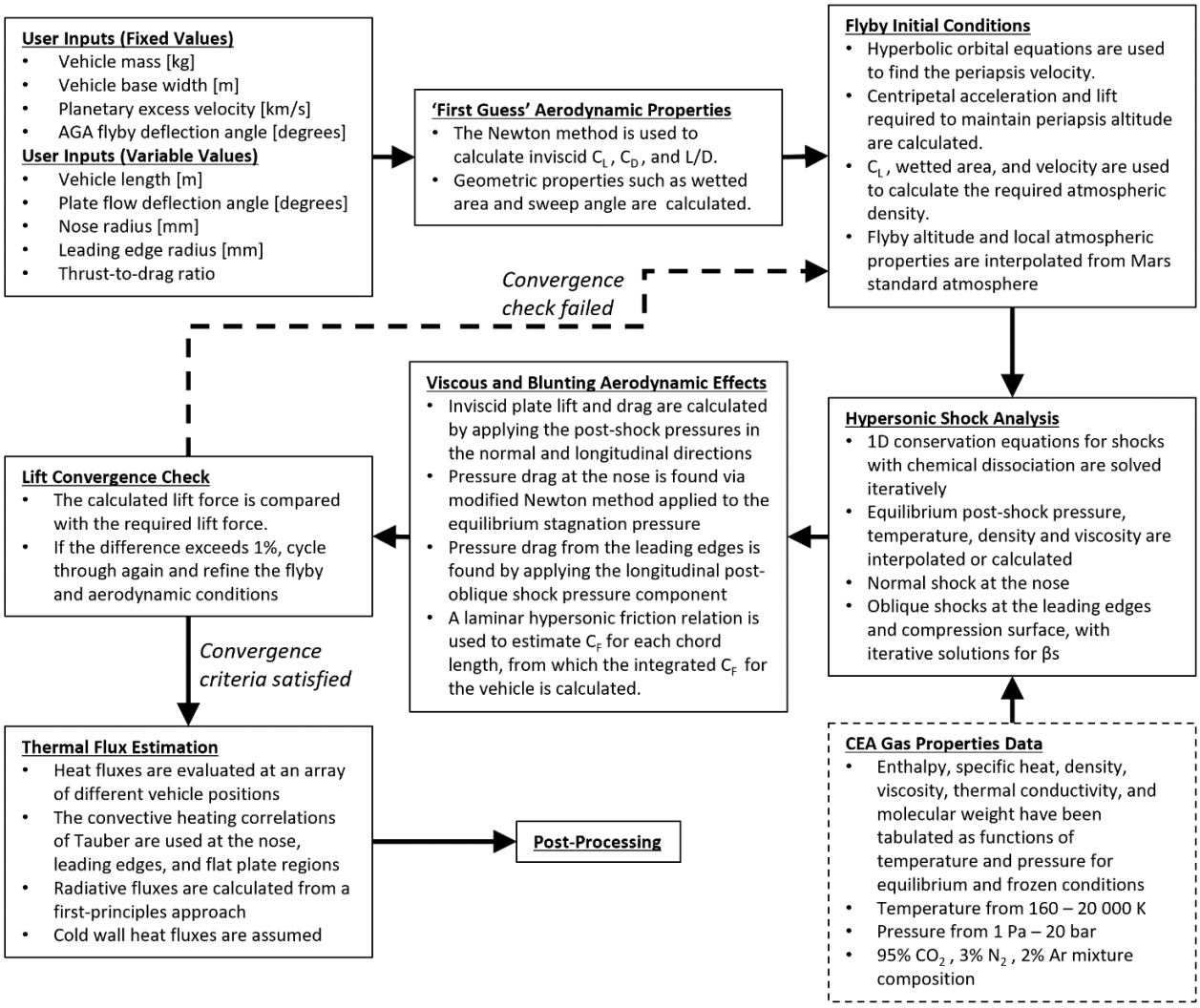

Figure 68 – Flowchart of the MATLAB atmospheric flight model.

7.1.2 Atmosphere Model

Atmospheric temperature, pressure, and density data were populated using the Mars Climate Database tool [73]. The profiles were generated up to an altitude of 250km for a typical summer afternoon at the equator. Figure 69 and Figure 70 illustrate these properties over the altitude range of interest for an AGA flight.

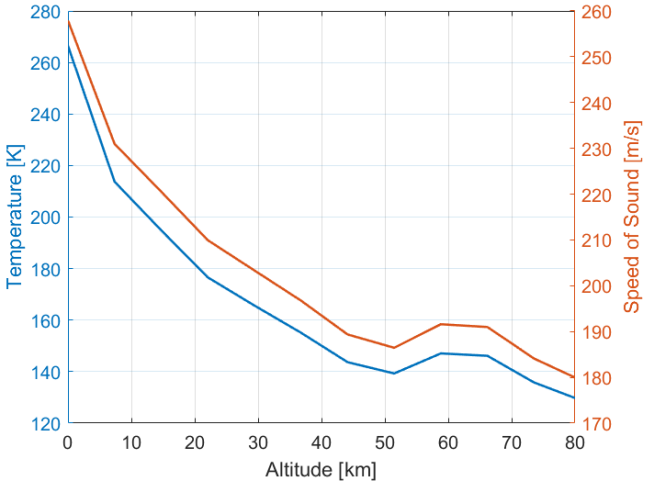

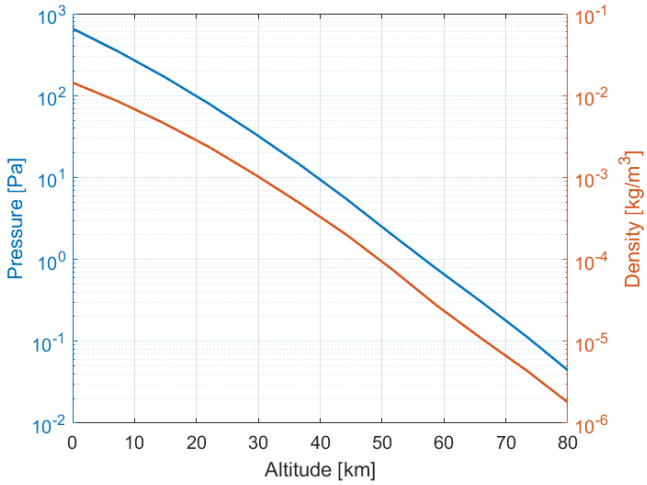

Figure 69 (Left) – Mars atmosphere temperature and speed of sound profiles.
Figure 70 (Right) – Mars atmosphere pressure and density profiles.

7.1.3 Aerodynamics with the Newton Method

The Newton method of estimating hypersonic aerodynamic coefficients is used to provide first guess values for an iterative scheme later. The Newton method considers only inviscid effects but is relatively accurate for simple geometries at high Mach numbers and low angles of attack. Conveniently, no information about the free-stream gas properties is required, and so a priori knowledge of the flight altitude is not necessary. Equations 16, 17, and 18 detail the calculation of the lift and drag coefficients, plus the lift-to-drag ratio [74].

$$C_L = 2 * sin^2(\alpha) * \cos(\alpha) \quad (16)$$

$$C_D = 2 * sin^3(\alpha) \quad (17)$$

$$\frac{L}{D} = cot(\alpha) \quad (18)$$

7.1.4 Equilibrium Flight Conditions

The flight altitude is needed in order to refine the aerodynamic coefficients. As the variation of flight altitude is negligible with respect to the planet's radius, the flight velocity and planet's surface radius can be inserted into Equation 19 to solve for the required aerodynamic centripetal acceleration. This acceleration, as well as the vehicle mass, lifting surface area, and most recent lift coefficient estimate can be inserted into Equation 20 to find the free-stream density required to generate the necessary lift. The atmospheric density profile is then interpolated to find the equilibrium flight altitude.

$$a_{lift} = \frac{V^2}{R_{Mars}} - \frac{\mu_{Mars}}{R_{Mars}^2} \quad (19)$$

$$\rho = \frac{2\, a_{lift}\, m}{S C_L V^2} \quad (20)$$

There are a couple of points worth noting about Equation 20. Firstly, for a given vehicle and velocity, the lift coefficient is the primary determinant of flight altitude. Vehicles with larger wedge angles and/or higher angles of attack will cruise at higher altitudes. Secondly, for a given lift coefficient and velocity, vehicles with a lower mass-to-lifting area ratio, aka wing loading, will cruise at higher altitudes. Higher altitudes are thermally desirable for their lower gas densities and thus reduced fluxes, while lower altitudes are aerodynamically

desirable due to the increased Reynolds numbers and thus reduced viscous drag that can be achieved in higher density flows.

7.1.5 Hypersonic Shocks and Gas Properties

At hypersonic flight conditions with Mach numbers greater than about 5, the analytical expressions for pressure, density and temperature ratios across a shock can be simplified to those shown below [10].

$$\frac{p_2}{p_1} = \frac{2\gamma}{\gamma+1} M_1^2 \sin^2 \beta \qquad \frac{\rho_2}{\rho_1} = \frac{\gamma+1}{\gamma-1} \qquad \frac{T_2}{T_1} = \frac{2\gamma(\gamma-1)}{(\gamma+1)^2} M_1^2 \sin^2 \beta$$

For the present AGA mission, the vehicle will be travelling at Mach numbers upwards of 50. Chemical dissociation will occur at the nose and possibly in the oblique shock regions, at which point the ratio of specific heats γ can't be assumed constant. In order to avoid detailed thermochemical modelling, gas properties over a range of temperatures and pressures were populated using the NASA CEA code. A Mars representative gas mixture of 95% CO_2, 3% N_2, and 2% Ar was analysed at pressures from 1 Pa to 50 bar and temperatures from 160 K to 20 000 K. Properties for both equilibrium and frozen conditions were extracted. Figure 71 illustrates the variation of key properties under equilibrium conditions.

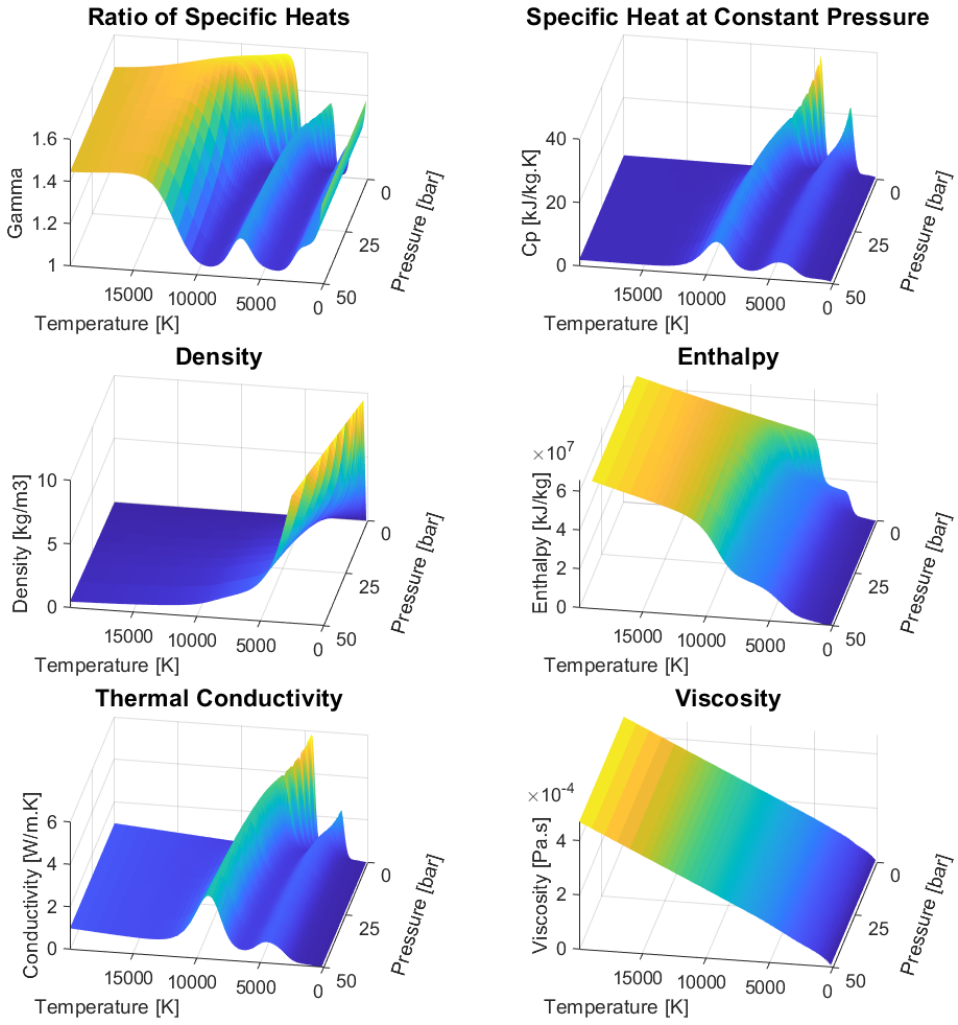

Figure 71 – CEA prediction of equilibrium gas properties of a Mars representative gas mixture.

This data set was sufficient for the oblique shock regions where the normal component of the oblique shocks remained below about Mach 10, and relatively little dissociation or ionisation occurred. At the nose region

where the flow was completely stagnated from 9-12 km/s, the enthalpy capabilities of this data set was exceeded. As explained by Capitelli et al. [75], the work of Gordon and McBride on which the CEA code is based relies on the Gurvich tables for high temperature properties above 6000 K. The Gurvich tables use a reduced form of the electronic partition function, leading to large underestimations of the specific heat capacities of ionised atoms and molecules at high temperatures [75]. In turn this leads to a large overprediction of the equilibrium stagnation temperature for a given enthalpy level. As the desired use of the nose stagnation temperature was simply to allow an 'order-of-magnitude' estimate of the radiative flux, a simple work-around was used. The velocity vs. stagnation temperature data calculated by Page and Woodward [76] for a Venus entry was used and interpolated as required. This assumption was deemed acceptable for this work as both the Martian and Venusian atmospheres are greater than 90% CO_2, and the atmospheric flight speeds considered in both studies are between 9 and 12 km/s.

To determine whether the frozen or equilibrium data set should be used at a given location, the local Knudsen and Damköhler numbers were evaluated at the nose and various positions along the leading edge and compression side surface. The Knudsen number, evaluated via Equation 21, is a ratio of the atomic/molecular free path length between collisions to a relevant length scale. The value relates to the number of particle collisions in a given length scale and indicates if the gas should be treated as a continuum, rarefied, or somewhere in between [77]. The Damköhler number, evaluated via Equation 22, gives a ratio of the time scale associated with convection of a fluid to the time scale associated with a given physical or chemical process occurring in the fluid [77]. The mean free path λ and average particle speed $\bar{c}$ were evaluated using the methods detailed in Anderson [10].

$$Kn_{loc} = \frac{\lambda_{loc}}{L} \tag{21}$$

$$Da_{loc} = \frac{1}{Kn_{loc}} \frac{\bar{c}_{loc}}{V_{loc}} \tag{22}$$

A small Knudsen number on the order of 0.001 or less, and/or a large Damköhler on the order of thousands or more indicate that the flow is likely in equilibrium. Knudsen and Damköhler numbers satisfying the equilibrium flow criteria were consistently observed at all locations over the vehicle in the following analysis, and so equilibrium flow was assumed everywhere. This assumption would appear to agree with analysis found in the literature. The vehicles considered in the present work were found to typically fly at speeds of 9-12 km/s and at altitudes of 25-30 km. If the equilibrium flow regime illustrated in Figure 72 can be extrapolated, then equilibrium flow could be expected for such vehicles.

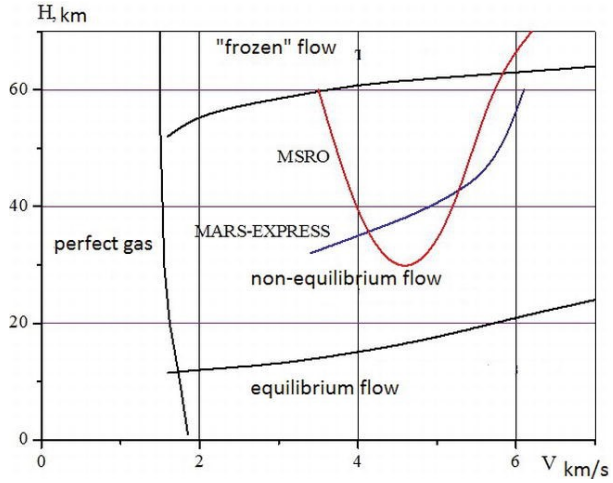

Figure 72 – Flow regimes predicted for selected spacecraft entering Mars' atmosphere [78].

To find the post-shock properties with chemical effects, the iterative method detailed in Chapter 16 of Anderson [74] was used. An adapted version for this project is briefly summarised below.

1. Assume an initial guess for ρ_1/ρ_2. Here this value is taken as $(\gamma-1)/(\gamma+1)$ where γ is the non-reacting ratio of specific heats of the gas.
2. Calculate P_2 and h_2 from Equations 23 and 24 respectively.
3. Interpolate the pressure-temperature-enthalpy matrix to determine T_2.
4. Interpolate the pressure-temperature-density matrix to determine ρ_2.
5. Repeat steps 1-4 until convergence of the properties occurs.
6. Interpolate the other pressure-temperature-variable matrices to determine all the gas properties.

$$P_2 = P_1 + \rho_1 u_1^2 \left(1 - \left(\frac{\rho_1}{\rho_2}\right)^2\right) \quad 23$$

$$h_2 = h_1 + \frac{u_1^2}{2}\left(1 - \left(\frac{\rho_1}{\rho_2}\right)^2\right) \quad 24$$

In the case of normal shocks, the above procedure can be directly applied. For an oblique shock, the above procedure becomes a sub-routine which is applied to the normal component of the shock. The iterative scheme for calculating the oblique shock angle β and post-shock properties is briefly summarised below.

1. Assume an initial guess for β. Here this value is taken as $\theta(\gamma+1)/2$ where θ is the flow deflection angle and γ is the non-reacting ratio of specific heats of the gas.
2. Calculate the normal shock component using Equation 25, and with knowledge of the local speed of sound the normal flow velocity can be found.
3. Run the above normal shock routine with the free-stream properties and the normal velocity.
4. Calculate a new β value using the post-shock normal velocity and Equation 26.
5. Repeat steps 1-4 until β converges.

$$M_{n1} = M_1 \sin(\beta) \quad 25$$

$$\beta_{new} = \operatorname{atan}\left(\frac{u_2}{w_1}\right) + \theta \quad 26$$

7.1.6 Refined Aerodynamics

The vehicle is treated as a thin triangular plate with blunted leading edges. Figure 73 provides a schematic of how the compression and expansion region pressures are evaluated.

The compression side pressure is evaluated using the oblique shock iterative algorithm. The pressure in the expansion region behind a flat plate would normally be evaluated using the Prandtl-Meyer expansion fan approach. However, as the AGA vehicle will actually be wedge shaped and fly at low angles of attack, the cold-side flow should experience little deflection. The pressure in the expansion region is just taken as the free-stream pressure, underestimating the pressure differential by a small amount. The inviscid lift and drag forces are calculated by multiplying the compression-expansion pressure differential by the wetted area and then applying the appropriate trigonometric relations to extract the longitudinal and vertical components.

The finite thickness of the nose and leading edges introduce additional pressure drag components. The axial components of the pressure in these regions directly acts to slow the vehicle, as illustrated in Figure 74.

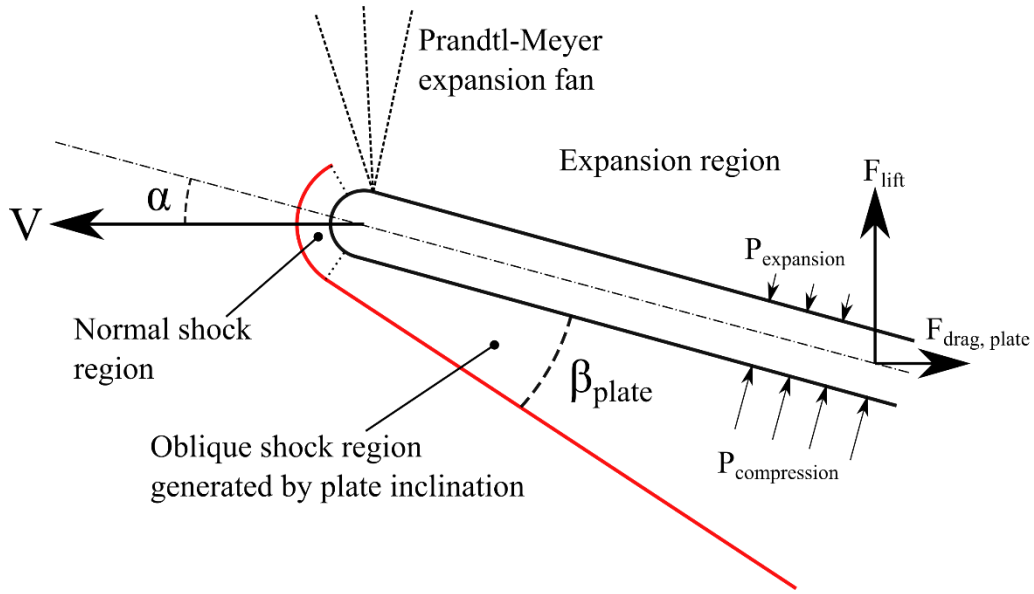

Figure 73 - Chord section showing the normal and oblique shock regions, and inviscid aerodynamic forces.

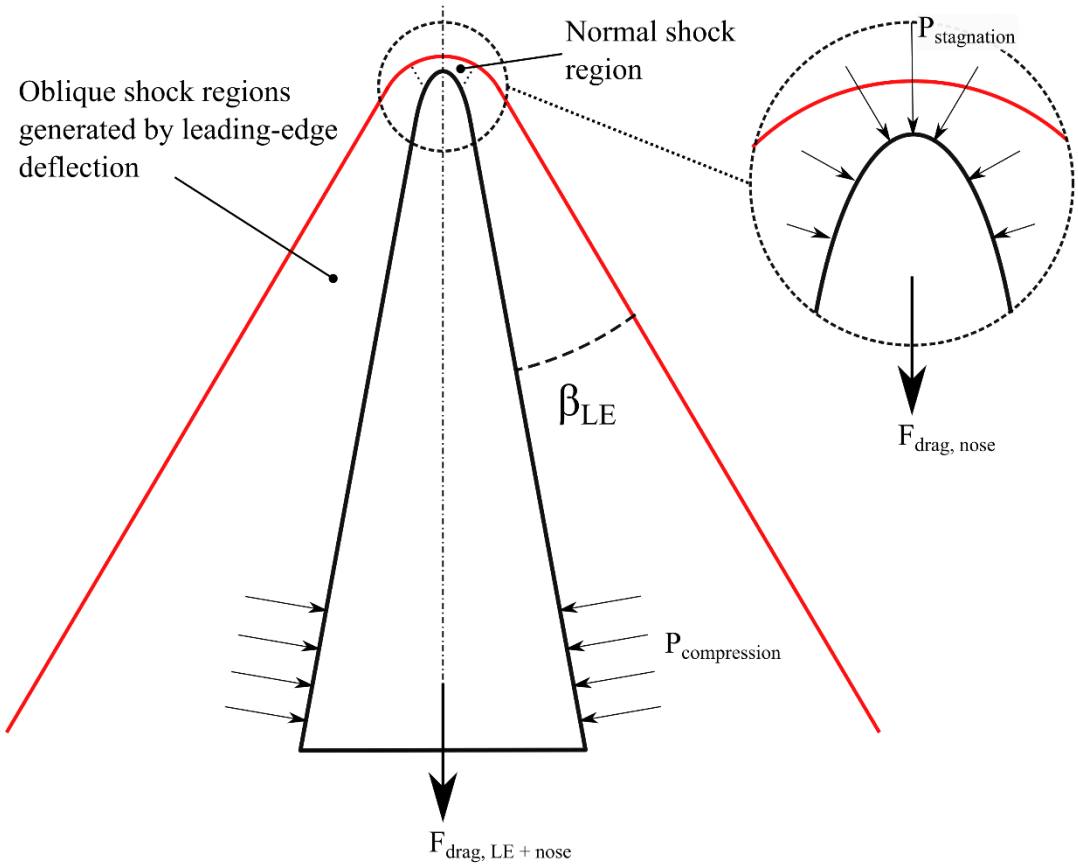

Figure 74 – Planform view showing the pressure drag on the nose and leading-edges.

The modified Newton method is used to calculate the pressure distribution over the nose, as described in Equation 27. The stagnation pressure used to calculate the maximum reference C_P is the post-normal shock pressure calculated by the normal shock iterative scheme.

The longitudinal components of the calculated spherical and cylindrical pressure distributions are extracted and then integrated over the nose and leading-edge areas respectively, giving their longitudinal drag contributions.

$$C_P = C_{P(max)} sin^2\theta \quad (27)$$

$$C_{P(\max)} = \frac{P_{stag} - P_\infty}{\frac{1}{2}\rho_\infty v_\infty^2} \quad (28)$$

When evaluating the viscous drag component, completely laminar flow was assumed. This approach was taken from Murakami [1], in turn based on the work of Tauber [16]. Figure 75 and Figure 76, originally presented by Tauber, compare Mach number and the laminar-turbulent transition Reynolds number for sharp cones in supersonic and hypersonic flows. At hypersonic Mach numbers, there is a general trend of increasing turbulent transition Reynolds numbers as the Mach number increases.

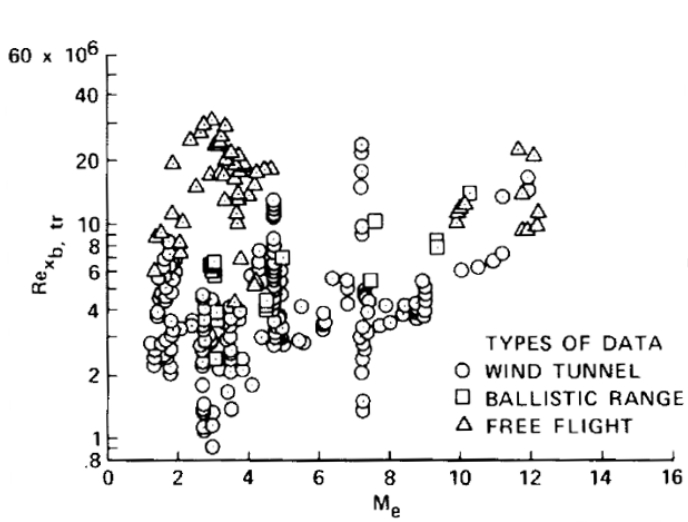

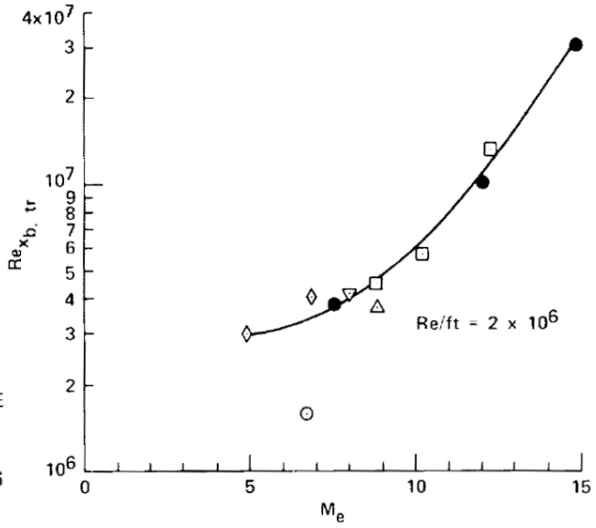

Figure 75 (Left) –Hypersonic laminar-turbulent transition Reynolds number at various Mach numbers [16].
Figure 76 (Right) – Curve fitting of the hypersonic laminar-turbulent transition Reynolds number [16].

While AGA vehicles fly at very high speeds, the low free-stream density of their typical cruising altitudes results in relatively low Reynolds numbers. Typical values seen in this studied were in the range of 10-50 million at Mach 50-60. If the trends presented in the above figures can be extended, it is likely that laminar flow would exist over the whole body, assuming there are no surface or flow irregularities that could trip the boundary layer. Further work is needed to validate these assumptions.

The local viscous friction coefficient is calculated using the laminar flow relation provided in [15], repeated here as equation 29. C_w is the Chapman-Rubesin parameter which can be treated as $(T_w/T_e)^{r-1}$ with r assumed to be 0.75 [15].

$$C_f = \frac{0.664\sqrt{C_w \frac{P_e}{P_\infty}}}{\sqrt{Re_{x,\infty}}} \quad (29)$$

In order to evaluate the effective friction coefficient for the whole vehicle, the vehicle geometry was discretised spanwise into different chord sections, as illustrated in Figure 77. The full-length flat plate Reynolds number is evaluated for each chord length and inserted into Equation 30, the global form of Equation 29. These chord properties are then integrated over the vehicle span to determine the effective friction coefficient.

$$C_F = \frac{1.328\sqrt{C_w \frac{P_e}{P_\infty}}}{\sqrt{Re_{L,\infty}}} \quad (30)$$

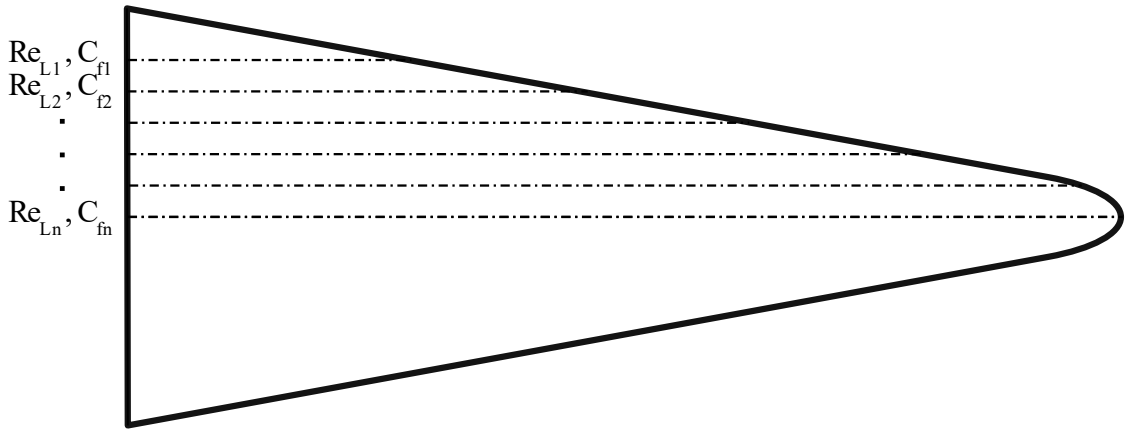

Figure 77 – Schematic of the friction coefficient evaluation first along longitudinal strips, followed by spanwise integration.

The dimensional lift and drag values are calculated for the complete geometry using the flight conditions and the coefficients introduce above, and the L/D ratio is calculated directly from these forces.

7.1.7 Convergence

The aerodynamic performance depends on the free-stream properties. However, the aerodynamic performance is needed in order to calculate the flight altitude and the free-stream properties. An iterative approach was adopted to solve this problem, as was illustrated in Figure 68.

The equilibrium flight conditions, hypersonic gas properties, and vehicle aerodynamic properties sub-routines are cycled until convergence occurs. Convergence is determined by the difference in the estimated lift force between iterations. Note this is not the required lift force to maintain a constant altitude, but the 'actual' lift force provided by the vehicle, as estimated from the hypersonic aerodynamic analysis. With the selected tolerance of 1%, convergence is typically achieved within 3 iterations.

7.1.8 Convective Thermal Flux Estimation

To estimate the convective fluxes, the correlations developed by Tauber [79] for bodies entering the Martian atmosphere are used. A fully catalytic wall is assumed, likely giving conservative estimates [71]. Equation 31 estimates the nose peak flux and shows the dependencies on velocity, nose radius, and atmospheric density. For the initial flight analysis, the ratio h_w/h_{aw} was neglected in the following equations for simplicity as the wall enthalpy was found to typically be only a few percent of the flow enthalpy. Thus, the cold-wall heat fluxes were estimated.

$$q_{nose} = 1.35 * 10^{-8} * \sqrt{\frac{\rho_\infty}{r_{nose}}} * V^{3.04} * (1 - \frac{h_w}{h_{tot}}) \quad 31$$

The heating along the leading edge is a combination of swept cylinder flow deflection effects and flat plate heating as the deflected gas flows downstream along the surface of the leading edge. Equations 32 through 34 estimate the leading-edge peak flux distribution. Equation 34 is also used directly to estimate the fluxes on the compression side of the vehicle, with the leading-edge sweep angle replaced by the flow deflection angle of the compression surface. It is important to note that Equation 34 is applicable to laminar flow situations. Further work is needed to evaluate the validity of the laminar flow assumption, as turbulent flows can greatly increase the convective heat transfer.

$$q_{LE} \approx \sqrt{q_{cyl}^2 + q_{FP}^2 \sin^2 \Lambda_e} \quad 32$$

$$q_{cyl} = 0.955 * 10^{-8} \sqrt{\frac{\rho_\infty}{r_{LE}}} * V^{3.04} * (1 - 0.2 \sin^2 \Lambda_e)(\cos \Lambda_e)(1 - \frac{h_w}{h_{aw}}) \quad 33$$

$$q_{FP} = 1.87 * 10^{-9} \sqrt{\frac{\rho_\infty \cos \theta_{FP}}{x}} * V^{3.24} * \sin \theta_{FP} * \left(1 - \frac{h_w}{h_{aw}}\right) \quad 34$$

To estimate the heat fluxes on the expansion side, Reynold's analogy has been used with the local C_f value evaluated via Equation 29. Equation 35 is used to calculate the local Stanton number C_H. With the assumption of the cold-wall relation for hypersonic laminar flow detailed in Equation 36, Equation 37 can then rearranged to provide the local heat flux q_w. This approach and Equations 35 through 37 were taken from Anderson [10].

$$\frac{C_H}{C_f} = \frac{1}{2} Pr^{-2/3} \quad 35$$

$$h_{aw} \approx \sqrt{Pr} * \frac{u^2}{2} \quad 36$$

$$C_H \approx \frac{q_w}{\rho u h_{aw}} \quad 37$$

7.1.9 Radiative Thermal Flux Estimation

Unfortunately, there are no suitable engineering correlations for estimating radiative thermal fluxes. Correlations have been developed in the literature for radiative heating during Mars atmospheric entries [57], but these are restricted to bodies with a nose radius greater than 1 m and travelling at speeds below 9 km/s. The method detailed in Chapter 18 of Anderson [10], from which the following equations are sourced, and a crude estimation of the gas radiative properties were used to get an order-of-magnitude estimate of the stagnation point radiative flux.

The radiative flux transferred to an infinite flat body by a corresponding infinite slice of a transparent gas can be calculated with Equation 38. For a body with a finite radius, illustrated in Figure 78, the shock stand-off distance can be estimated via Equation 39.

$$q = \frac{E\delta}{2} \quad 38$$

$$\frac{\delta}{r} = \frac{\rho_\infty / \rho_s}{1 + \sqrt{2(\rho_\infty / \rho_s)}} \quad 39$$

Equations 38 and 39 can be combined to give Equation 40, which shows that the stagnation point radiative flux increases directly with an increasing nose radius. This trend is opposite that of stagnation point convective fluxes, which decrease with an increasing radius. There will clearly be a trade-off required to select an appropriate nose radius, with aerodynamic performance and radiative heating favouring small radii, and convective heating favouring large radii.

$$q_{stag} = \frac{E}{2} r \left(\frac{\rho_\infty}{\rho_s}\right) \quad 40$$

The total power emitted per unit volume, E, is evaluated by integrating the radiative intensity, J, over the unit sphere, giving Equation 41. In turn, J can be calculated by evaluating Equation 42.

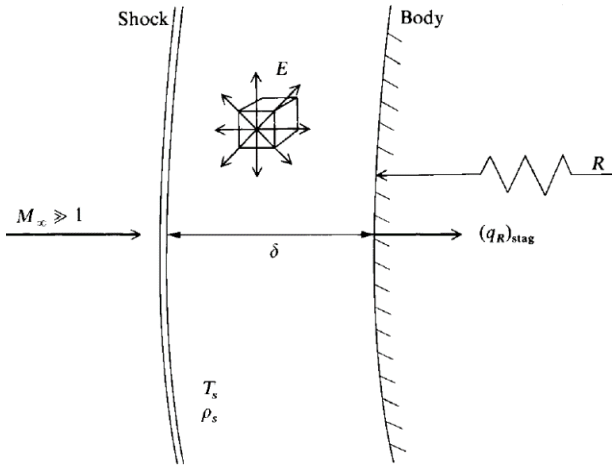

Figure 78 – Illustration of nose radius, shock stand-off distance, and radiating gas [10].

$$E = 4 * \pi * J \tag{41}$$

$$J = \int_0^\infty \kappa_\upsilon B_\upsilon d\upsilon \tag{42}$$

The direct evaluation of the absorption coefficient for a gas mixture at a given set of conditions entails a complex series of computations. To simplify this procedure, the temperature-intensity data generated in [80] and illustrated in Figure 79 was used. This data gives the radiation intensity components of a Mars representative 97% CO_2 , 3% N_2 gas mixture at 1 bar across a temperature range of 2000 – 15000 K.

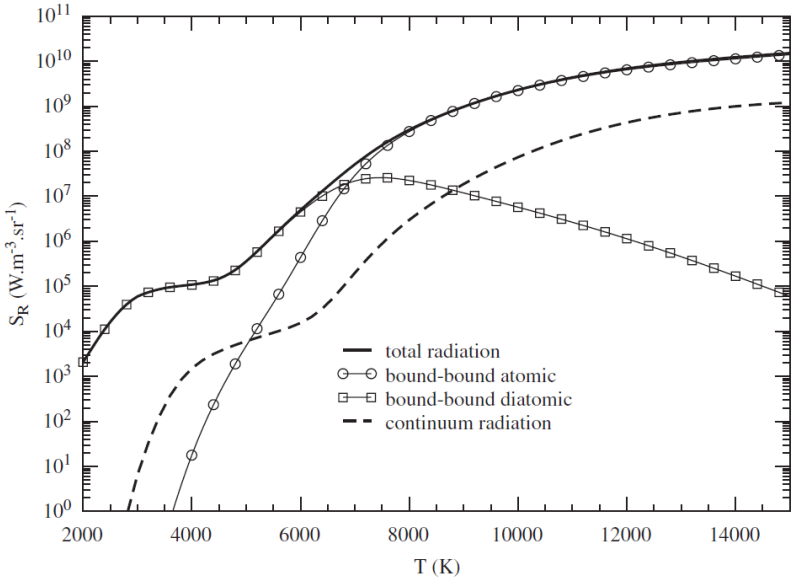

Figure 79 – Integrated spectral radiation intensities of a CO_2 dominant gas mixture [80].

Typical nose stagnation temperatures observed in this present work ranged between 8000 and 14000 K. As the absorption coefficient is directly related to the number of particles per unit volume [81], the absorption coefficient was scaled linearly with the stagnation pressure.

The continuum properties and equations 38 through 42 were used to calculate the initial radiative flux, with the assumption of an adiabatic and transparent layer of radiating gas which is un-coupled with the stagnation point boundary layer. These assumptions lead to a large overprediction of the radiative flux to the body, as can be seen from Figure 80, in which the method detailed above was used to create the line labelled ‘Equation 5’.

In reality, the gas is not adiabatic as it is constantly radiating heat away and reducing in temperature as it approaches the stagnation surface, lowering the radiative flux experienced by the vehicle. Again in Figure 80, this difference is particularly noticeable as the stagnation point radius and thus shock stand-off distance increases. Figure 81 provides a practical illustration of the possible radiative flux reductions, showing the stagnation point radiative and convective flux histories of the Galileo probe during its Jupiter entry with and without coupling effects [82]. It should be noted that in this case, virtually all the heat transferred to the surface was via radiation as the TPS ablation effectively eliminated convective heat transfer [10].

To calculate the coupled radiative flux, the radiation loss parameter Γ is calculated from Equation 43 [83], and then inserted into Equation 44 [84] with an atmospheric constant κ equal to ~3 for Mars.

$$\Gamma = \frac{E\delta}{\frac{1}{2}\rho_\infty V_\infty^2} \tag{43}$$

$$q_{cpl} = \frac{q_{unc}}{1 + \kappa\Gamma^{0.7}} \tag{44}$$

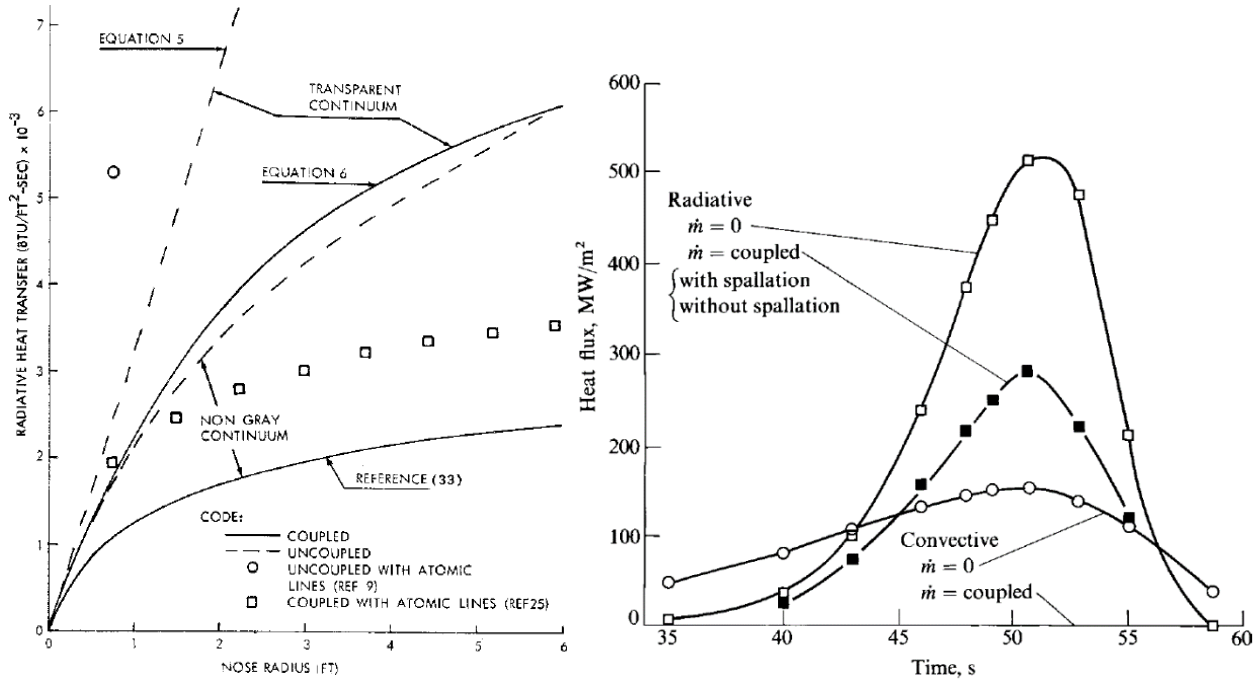

Figure 80 (Left) – Illustration of the large variation in radiative flux with different estimation methods [83].
Figure 81 (Right) –Heat flux predictions with and without coupling for the Galileo Jupiter probe [82].

As can be seen from Figure 80, further reductions in the evaluated radiative flux are possible if the gas is treated as non-grey. However, this requires more detailed specular information of the absorption coefficient. Given the general nature of this analysis and the desire for simplicity and conservatism, the gas was treated as coupled and transparent.

The detailed analysis of Venus-entry radiative fluxes by Page and Woodward [76] was used to fine-tune the absorption coefficient data curve provided in Figure 79. Page and Woodward considered the atomic and ion continuums as well as atomic lines and vacuum UV contributions for a 90% CO_2 – 10% N_2 atmosphere representative of Venus.

7.1.10 Model Validation

In order to verify the model aerodynamic and thermal predictions, several cases were taken from the literature for comparison. Table 16 compares the aerodynamic coefficients predicted by the current flat-plate model and

those predicted in [8] for a hypersonic Mars encounter with an optimised waverider. The velocities of this reference MAGA encounter are much lower than the present mission MAGA-Uranus mission, but this was the best comparison that could be found. In any case, both situations are well within the high-hypersonic regime, and it is hoped that hypersonic similarity will allow acceptable application of the model to Mach 50+.

Mach	V [km/s]	Θ [deg]	Altitude [km]		Re	C_L	C_D**	C_f	L/D
19	-	7.5*	20	Anderson et al. [8]	1.03e7	0.0342	0.00515	0.0013	6.63
19.0	4.0	6.0	20.5	*Present work*	1.20e7	0.0331	0.057	0.0017	5.78
19	-	7.5*	30	Anderson et al. [8]	2.51e6	0.0334	0.00629	0.00266	5.38
19.1	3.9	6.0	29.2	*Present work*	5.04e6	0.0336	0.0067	0.0027	4.99

Table 16 – Comparison of aerodynamic coefficients generated by the present model and a previous study analysing Mars AGAs.
**Θ is the waverider generation cone angle in [8], and the flat-plate flow deflection angle in the present study. A lower flow deflection angle was used for the flat plate to compensate for the 3-D relieving effect experienced by cones in supersonic flows [10].*
*** The C_D value includes the viscous and inviscid components, thus L/D = C_L / C_D.*

As expected, the L/D ratios predicted by the present flat plate model are lower than those of an optimised geometry. For the purposes of this current study, it is satisfactory that the L/D values are quantitatively similar. Accuracy of the lift coefficient is more important as C_L has a direct effect on the required free stream density via Equation 20, which in turn has a direct effect on the flight altitude and thermal fluxes. Good agreement is seen between the lift coefficients. The differences in Reynolds number could be due to differing atmospheric models. It was not clear which atmospheric model was used in [8].

To evaluate the convective heat flux predictions, the variables of the case study propsed by Murakami [1] and summarised in Table 17 were used and the results compared. Figure 82 and Figure 83 were taken from Murakami and show the heat flux distribution along the vehicle centreline and a chordline respectively. Figure 84 was output from the present flat-plate model.

Flight Speed	11.6	km/s
Flight Altitude	29.4	km
Vehicle length	9	m
Vehicle width	4.5	m
Wedge Angle	8.5	degrees
Nose and leading-edge radii	43	mm

Table 17 – Summary of the design case used by Murakami [1].

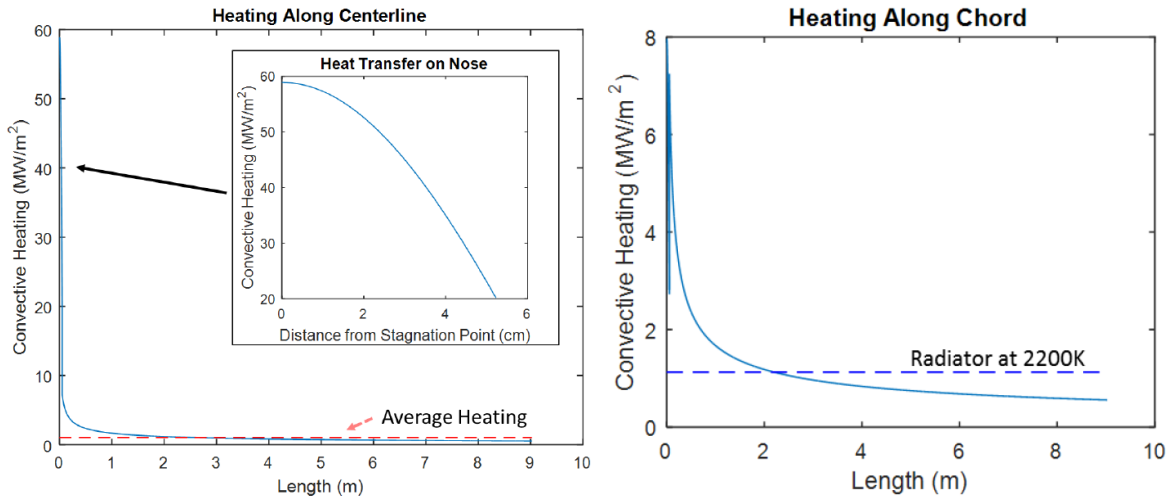

Figure 82 (Left) – Predicted centreline convective heating of TAGA vehicle by Murakami [1].
Figure 83 (Right) – Predicted chord line convective heating of TAGA vehicle by Murakami [1].

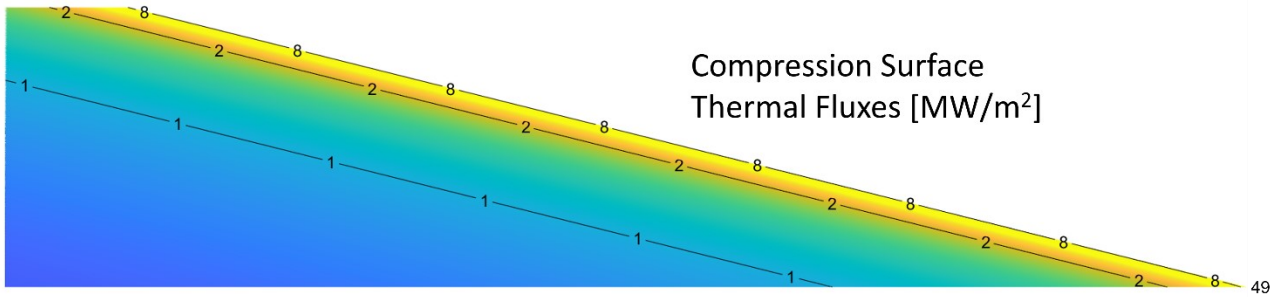

Figure 84 - Compression-side thermal flux map predicted by the present atmospheric flight model for Murakami's case.

Good agreement is seen over the entire vehicle body. This was to be expected as Murakami's analysis used largely the same heat transfer correlations and relationships.

The nose radiative flux predictions were compared to those of Page and Woodward [76] and the absorption coefficient introduced in Figure 79 was adjusted to tune the results. As the results of Page and Woodward were generated at discrete stagnation pressures of 1 and 10 bar, the flux-to-stagnation pressure ratio was used here to scale to intermediate values. The radiated flux from a shock layer is directly dependent on its density and thus pressure. The target value for the model-tuning was thus the flux-to-pressure ratio. Table 18 summarises the results of the model after tuning.

	Planet	Nose Radius [mm]	Velocity [km/s]	Mach	Stagnation Pressure [bar]	Stagnation Temperature [K]	Radiative Flux [MW/m^2]	Flux: Pressure Ratio
Page & Woodward [76]	Venus	220	9	-	10	~8 500	17.1	1.71
Present Work	Mars	220	9	43.8	1.28	7950	24.7	1.92
Page & Woodward [76]	Venus	220	12	-	10	~13 800	171	17.1
Present Work	Mars	220	12	57.8	2.50	13 500	46.7	18.7

Table 18 –Radiative thermal flux predictions of present model and reference work.

7.2 Analysis Inputs and Limits

The spacecraft initial mass, initial atmospheric velocity, and bend angle were 2500 kg, 12.0 km/s, and 68° respectively. To maximise lifting area and vehicle internal volume, a 4.5 m vehicle base width was selected, which is the largest value compatible with the internal diameter of the Atlas V 5-m fairings, as illustrated in Figure 85. Likewise, the maximum AGA vehicle length to be analysed was taken as 16 m.

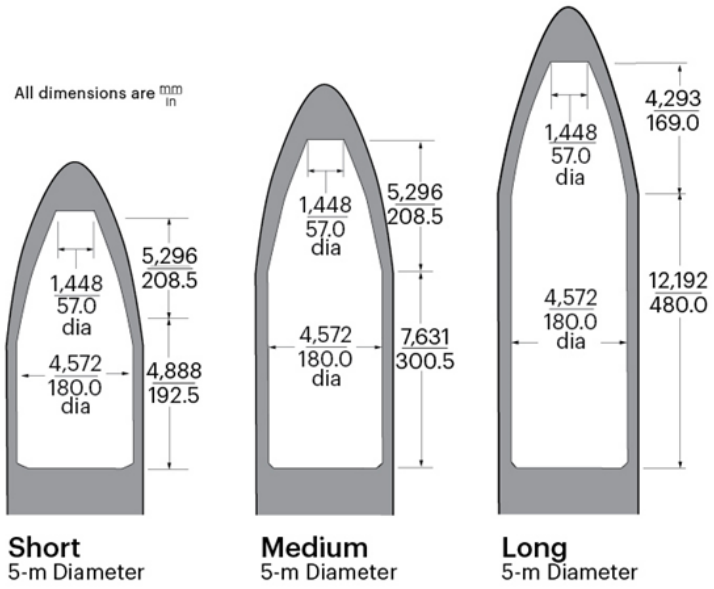

Figure 85 – Atlas V launcher 5-m fairings [24].

Given the high aerodynamic performance characteristics of the vehicle, a fairing-less launch configuration could be considered, allowing an increase in the aerospacecraft launch mass. Figure 86 and Figure 87 illustrate such launch configurations for the Dyna-Soar spaceplane. The practicalities of such an implementation are not clear, and serious analysis would be required to demonstrate if the concept is practical.

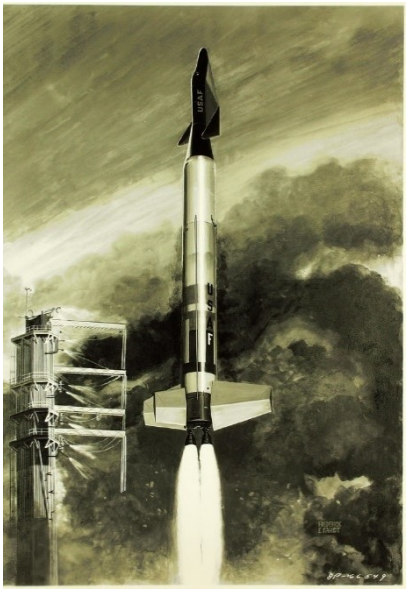

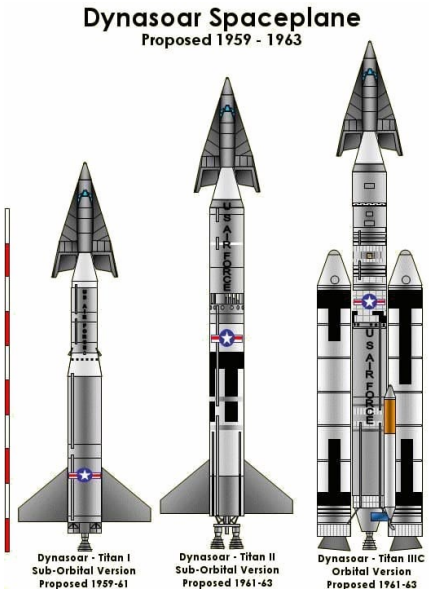

Figure 86 (Left) – Artist's impression of a Dyna-Soar spaceplane launch [85].
Figure 87 –Various Dyna-Soar launch configurations [86].

No hard-coded limits were applied to any of the performance criteria; however, some key variables were expected to stay within reasonable limits in order for the vehicle to be considered feasible.

- It was expected that the flat plate L/D should be at least 4, in order to give an optimised waverider geometry a good chance of achieving a natural L/D of 5.
- It was expected that the peak thermal fluxes should remain below approximately 150 MW/m^2. The heat transfer rate at the throat of the Space Shuttle Main Engines was about 160 MW/m^2, which is representative of the current state of the art for high-flux aerospace technology.
- It was expected that the nose stagnation pressure should remain below approximately 5 bar, in order to allow the possibility of film or transpiration cooling without needing high delivery pressures.

7.3 Sensitivity Analysis Results

Figure 89 through Figure 98 in the following pages detail the variation of key performance parameters as the nose radius, leading edge radius, vehicle length, and plate deflection angle are varied. It is important to note that the AGA performance parameters are highly coupled, and not always in immediately obvious ways. The following comments address some interesting relationships.

- The plate deflection angle has a strong effect on the cruising altitude. A greater flow deflection angle creates a greater lift coefficient, which in turn means that a lower density free stream is required.
    - When considering the plate deflection angle, it is important to consider that the wedge angle of an actual vehicle must be less than or equal to the flow deflection angle to avoid generating an upper surface shock as well. Previous AGA studies have typically proposed vehicles with generating angles of approximately 6 to 9 degrees.

- Higher altitude flights and their lower free stream densities lead to lower Reynolds numbers. Thus, lower altitude flights are better for achieving a high L/D as the higher gas densities can generate higher Reynolds numbers and thus lower skin friction coefficients.
- The L/D curves of the coupled analysis do not directly correlate with fixed-flow L/D curves such as Figure 88. In the present model, the aerodynamic performance and free stream properties are coupled.

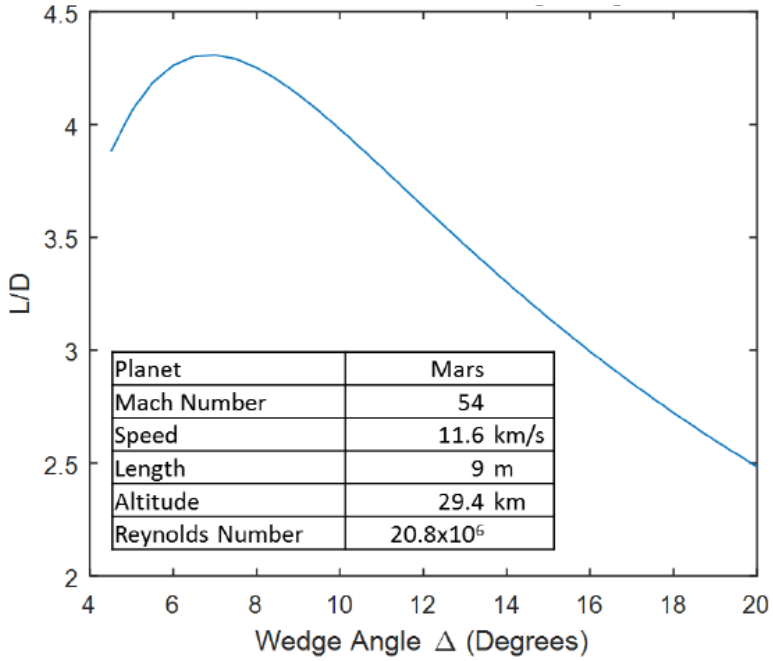

Figure 88 – Typical L/D curve for a hypersonic vehicle operating in a fixed flow [1].

- Low altitude flights generate high stagnation pressures, which can create large pressure drag components and ruin the aerodynamic performance if the nose and leading-edge radii are thus surface areas are too large.
- Aerodynamic performance is much more dependent on the nose radius than the leading-edge radius. Total stagnation occurs at the nose, while the large sweep angles of the studied vehicles greatly reduce the flow velocity component normal to the leading-edge surface.
- Large nose radii strongly decrease the convective flux and strongly increase the radiative flux. When combined, there is a weak trend favouring smaller radii for reduced thermal loading at the initial flight velocity. It should be noted that as the vehicle slows, radiative heating will drop off much quicker than convective heating. To make a fully informed decision an integrated heat load and average heat flux over the full mission profile is required, as well as consideration of the aerodynamic effects.
- The leading-edge flux is primarily determined by the flight altitude. This is logical as the radius and velocity are fixed, leaving free-stream density as the only floating variable in Equation 31.
- The average heat flux on the body is strongly correlated with the wing loading. For a given vehicle mass, smaller vehicles will have a smaller lifting area and thus require higher wing loads and lower flight altitudes. Their vehicle average flux is biased higher as they lack the large trailing-end region of the longer vehicles, which feature high Reynolds number flows and correspondingly lower thermal fluxes.
- Lower altitude flights have higher nose and leading-edge peak thermal fluxes but lower total heat loads, and the reverse is true for high altitude flights.

- A balance of high aerodynamic performance and moderate thermal fluxes can be achieved by long vehicles with correspondingly low wing-loadings. The TPS mass implications of these larger vehicles needs further study.

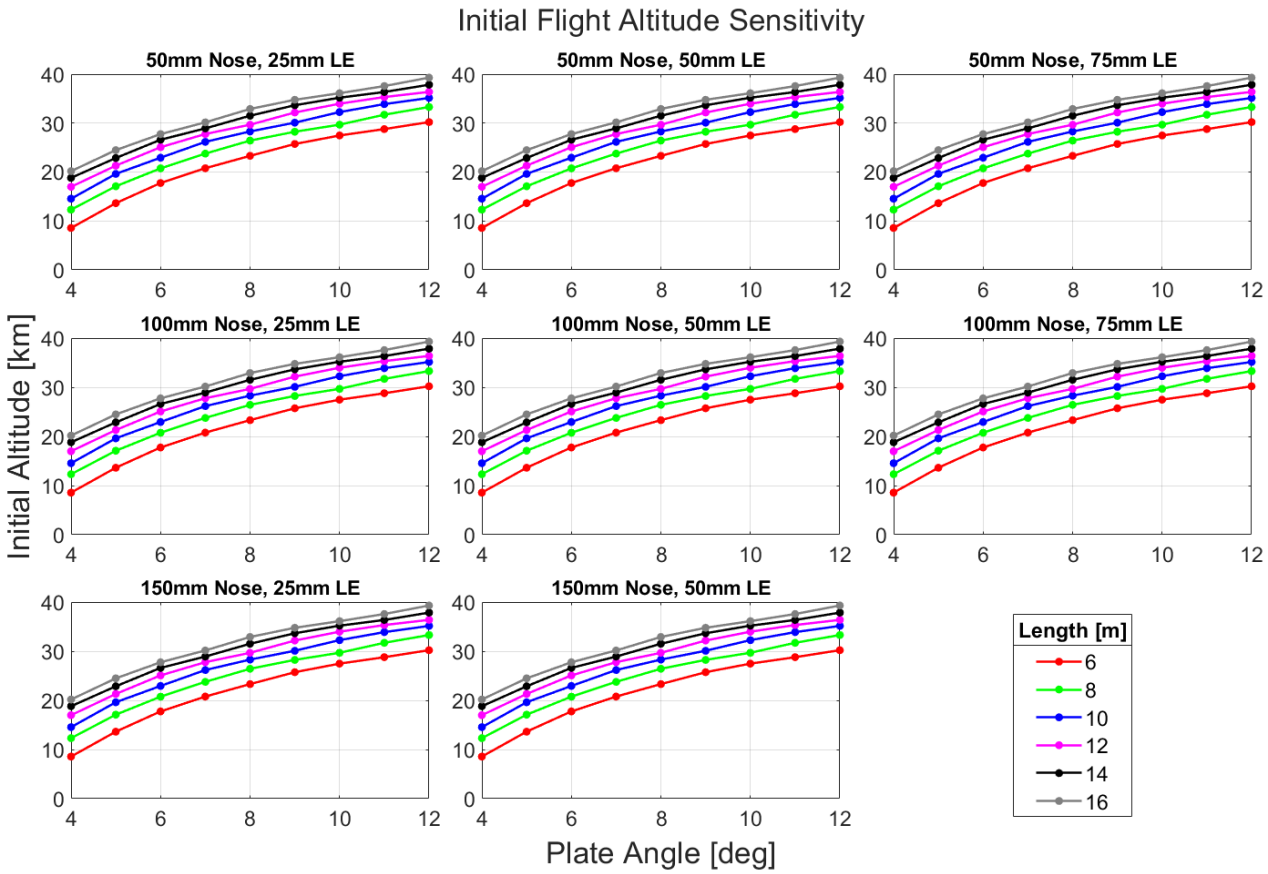

Figure 89 - Initial flight altitude vs vehicle length, angle of attack, leading-edge radius, and nose radius.

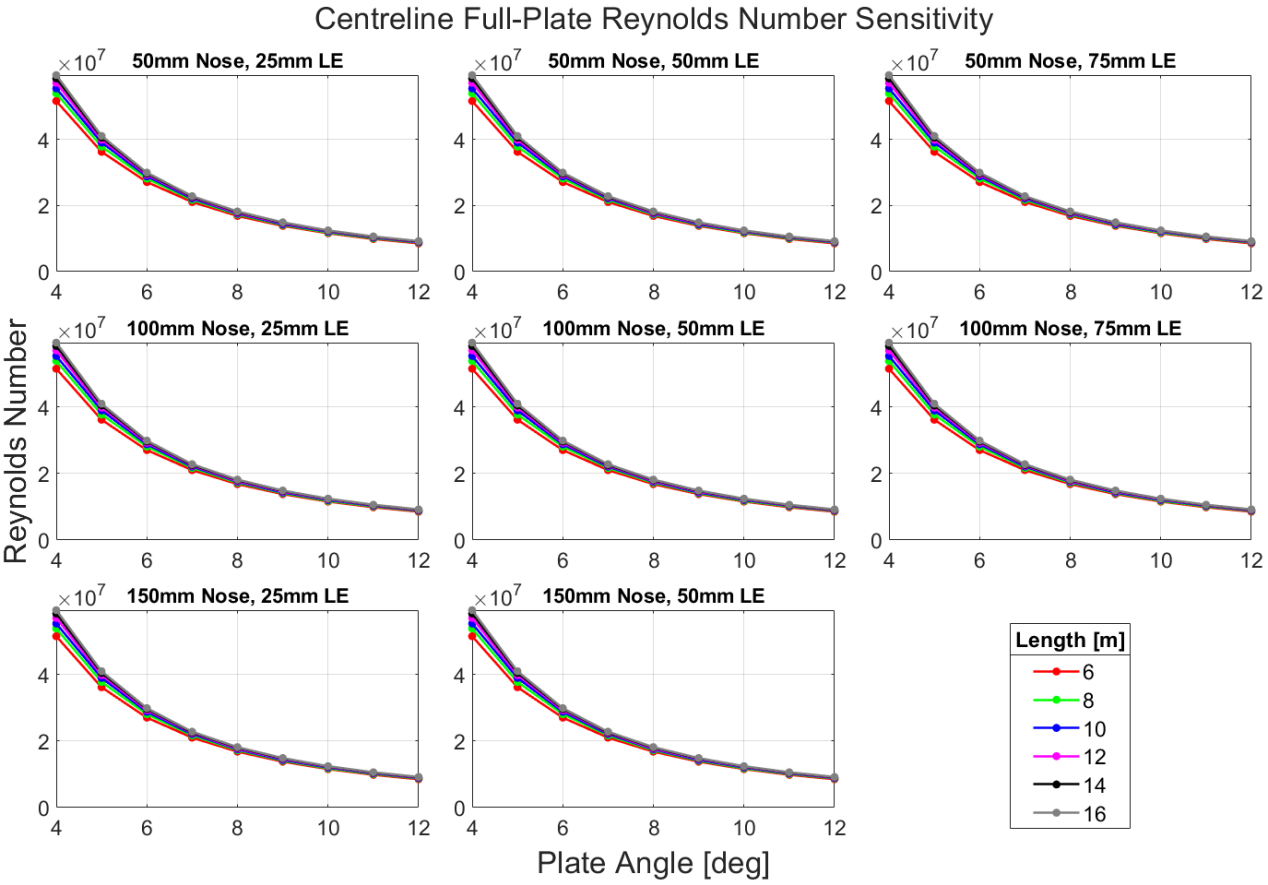

Figure 90 - Initial centreline Reynolds number vs vehicle length, angle of attack, leading-edge radius, and nose radius.

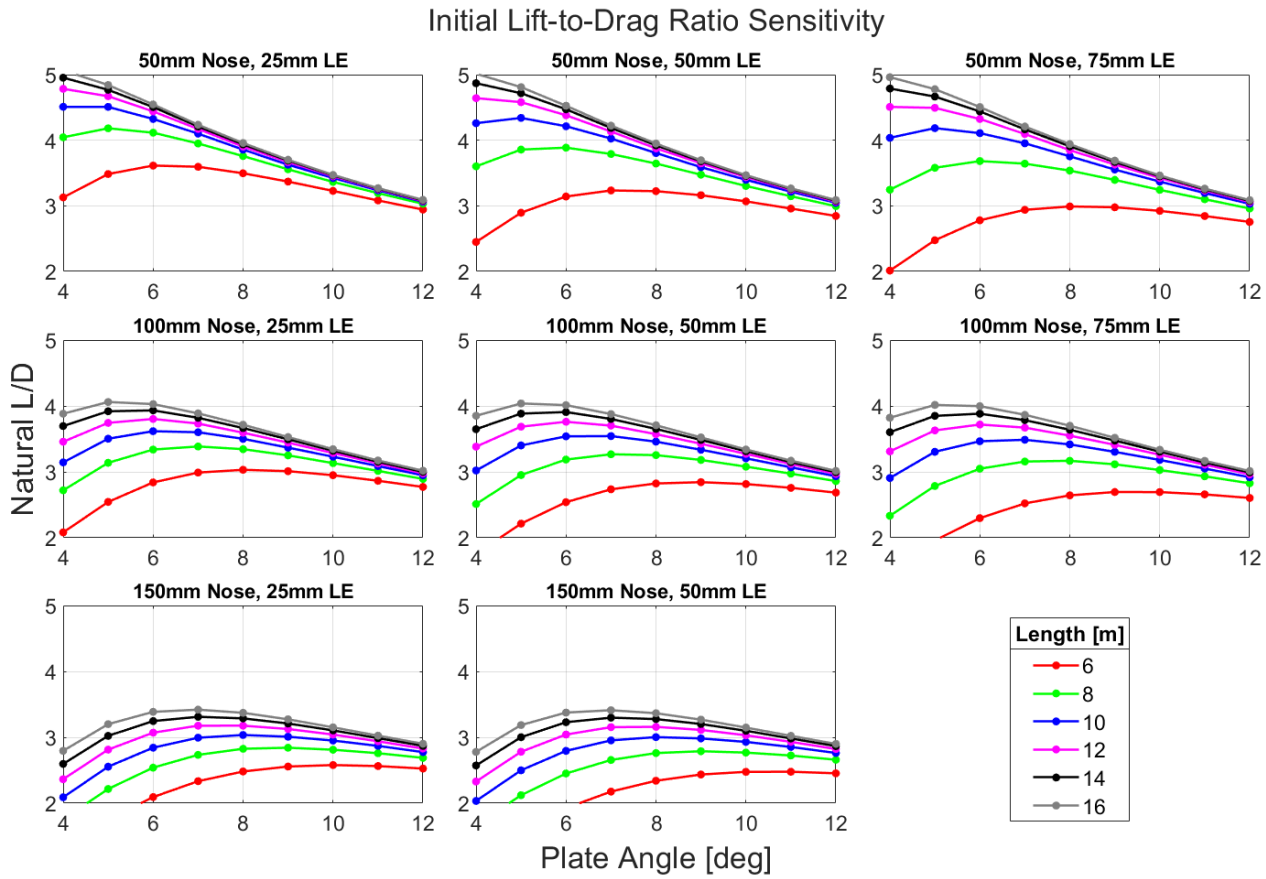

Figure 91 - Initial lift-to-drag ratio vs vehicle length, angle of attack, leading-edge radius, and nose radius.

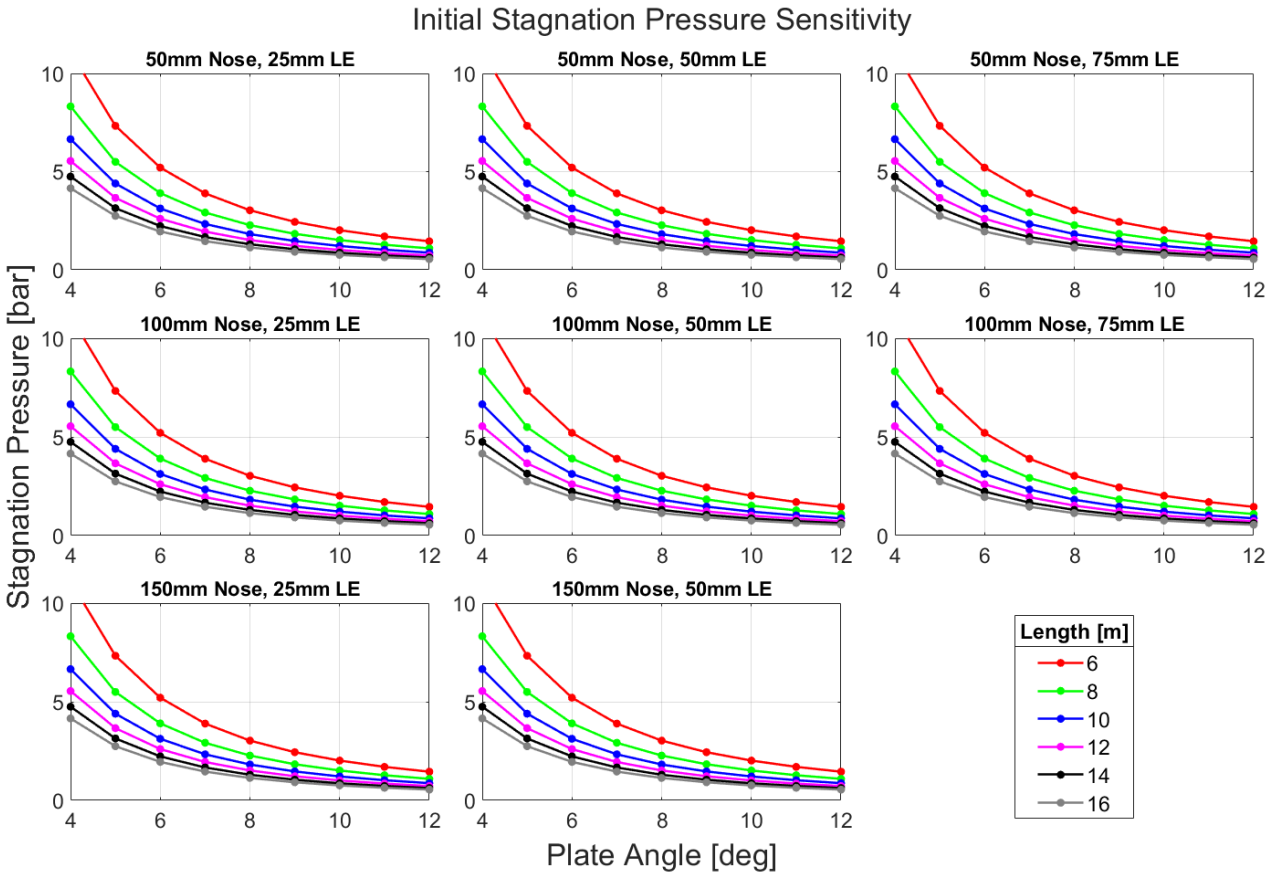

Figure 92 - Initial nose stagnation pressure vs vehicle length, angle of attack, leading-edge radius, and nose radius.

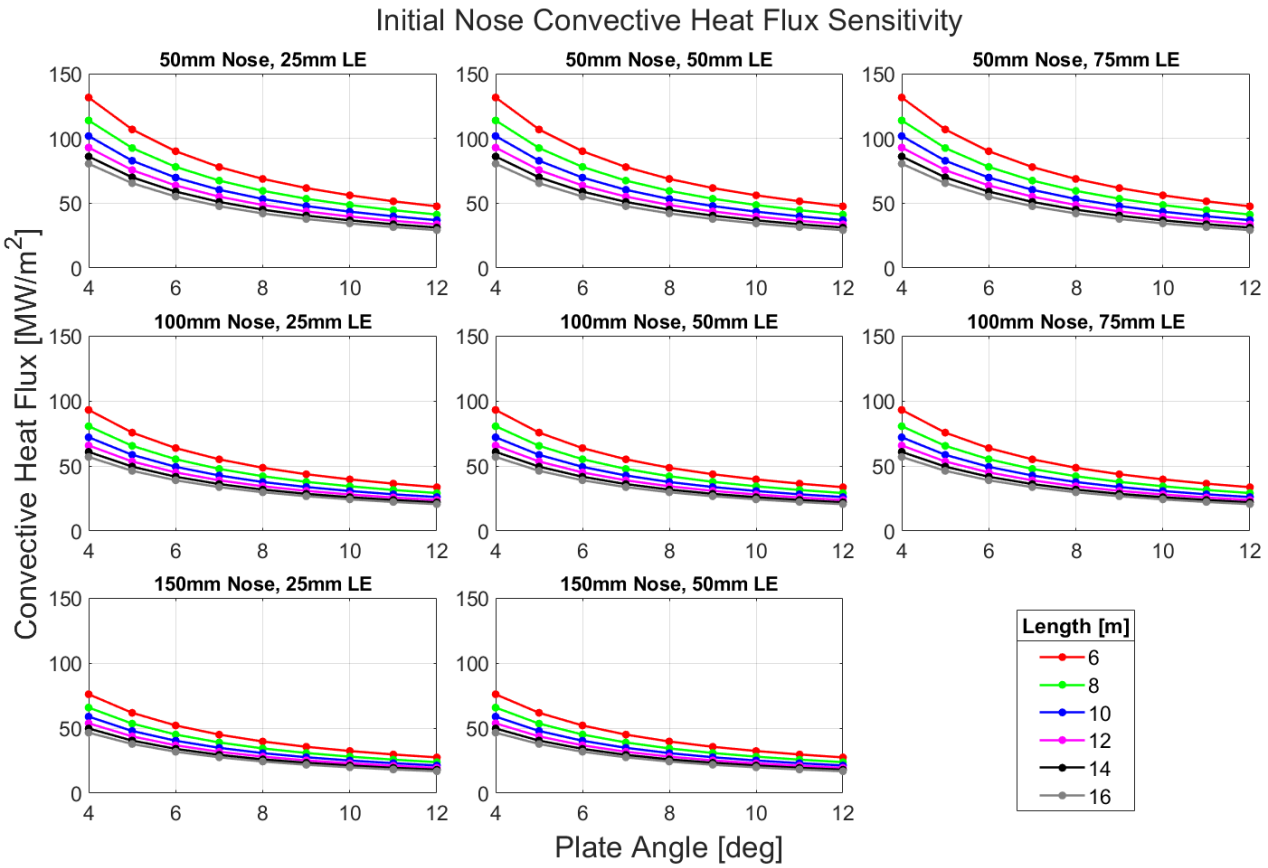

Figure 93 - Initial nose convective flux vs vehicle length, angle of attack, leading-edge radius, and nose radius.

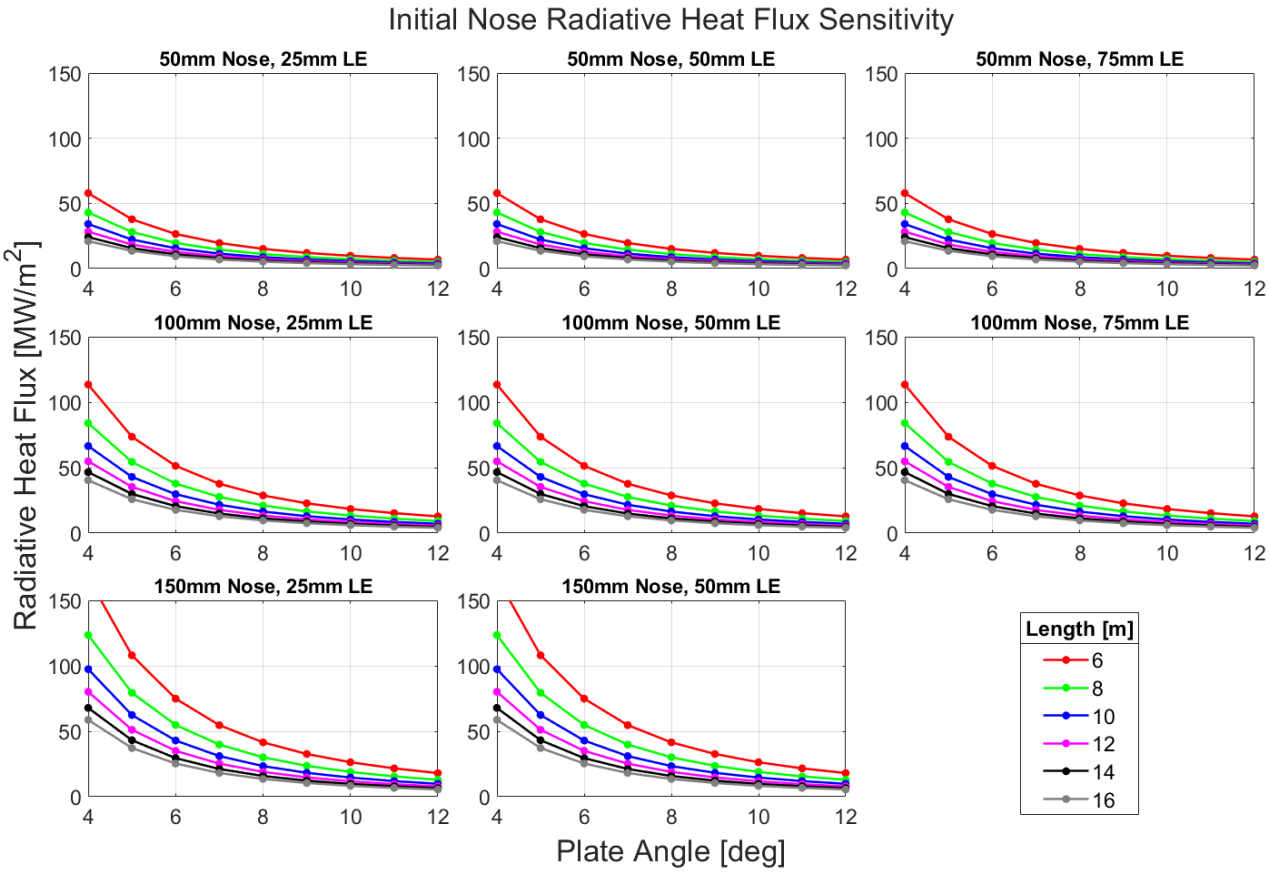

Figure 94 - Initial nose radiatve flux vs vehicle length, angle of attack, leading-edge radius, and nose radius.

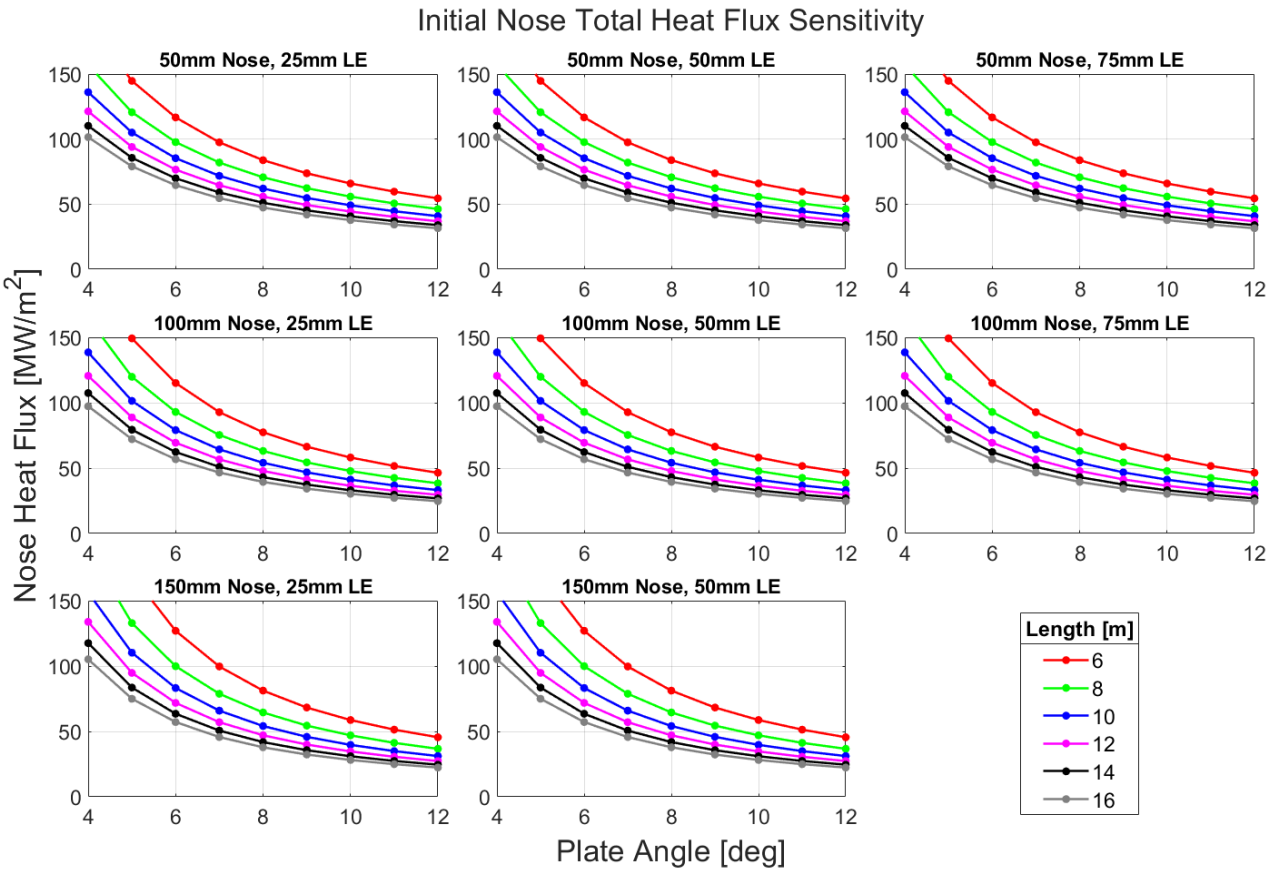

Figure 95 - Initial nose combined heat flux vs vehicle length, angle of attack, leading-edge radius, and nose radius.

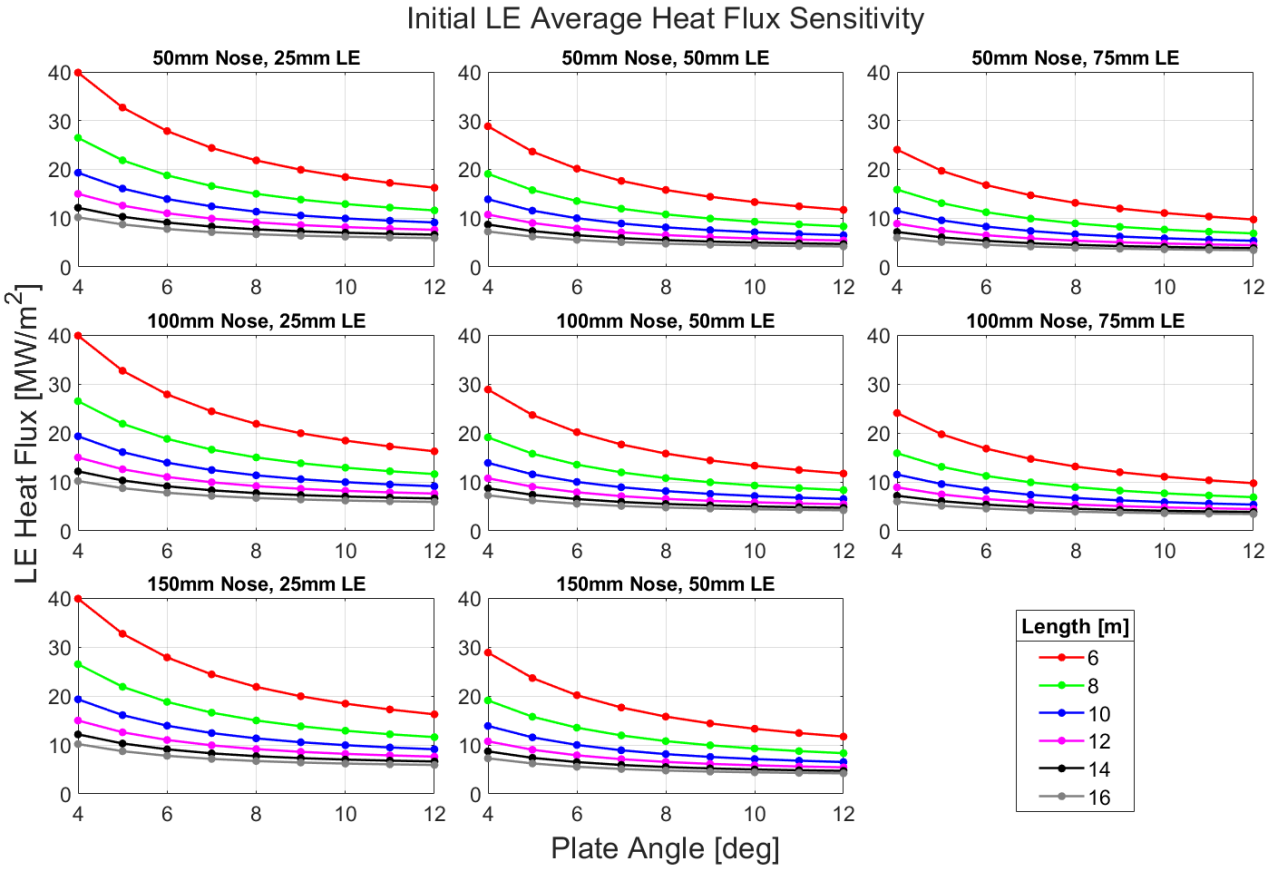

Figure 96 - Initial leading-edge average heat flux vs vehicle length, angle of attack, and leading-edge and nose radii.

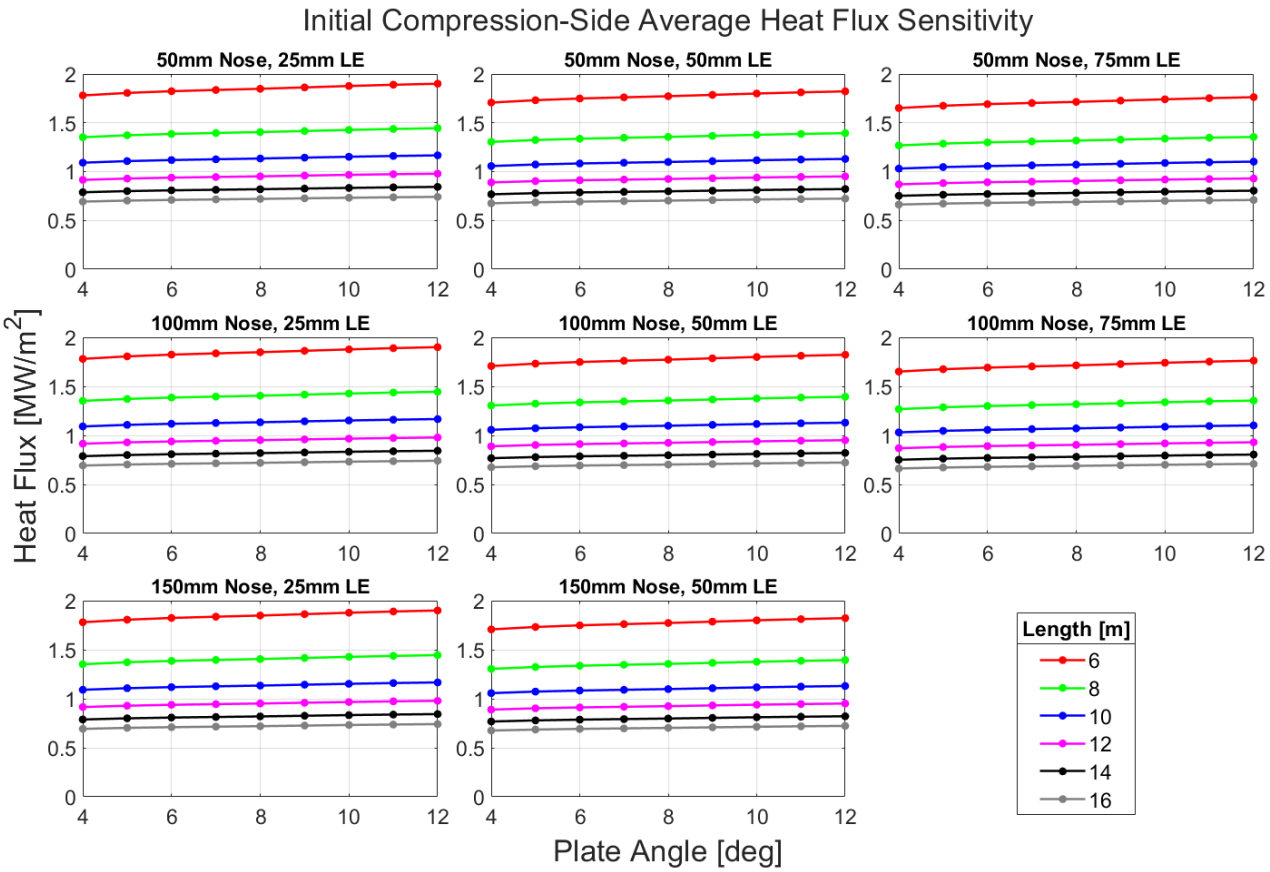

Figure 97 - Initial compression-side average heat flux vs vehicle length, angle of attack, leading-edge radius, and nose radius.

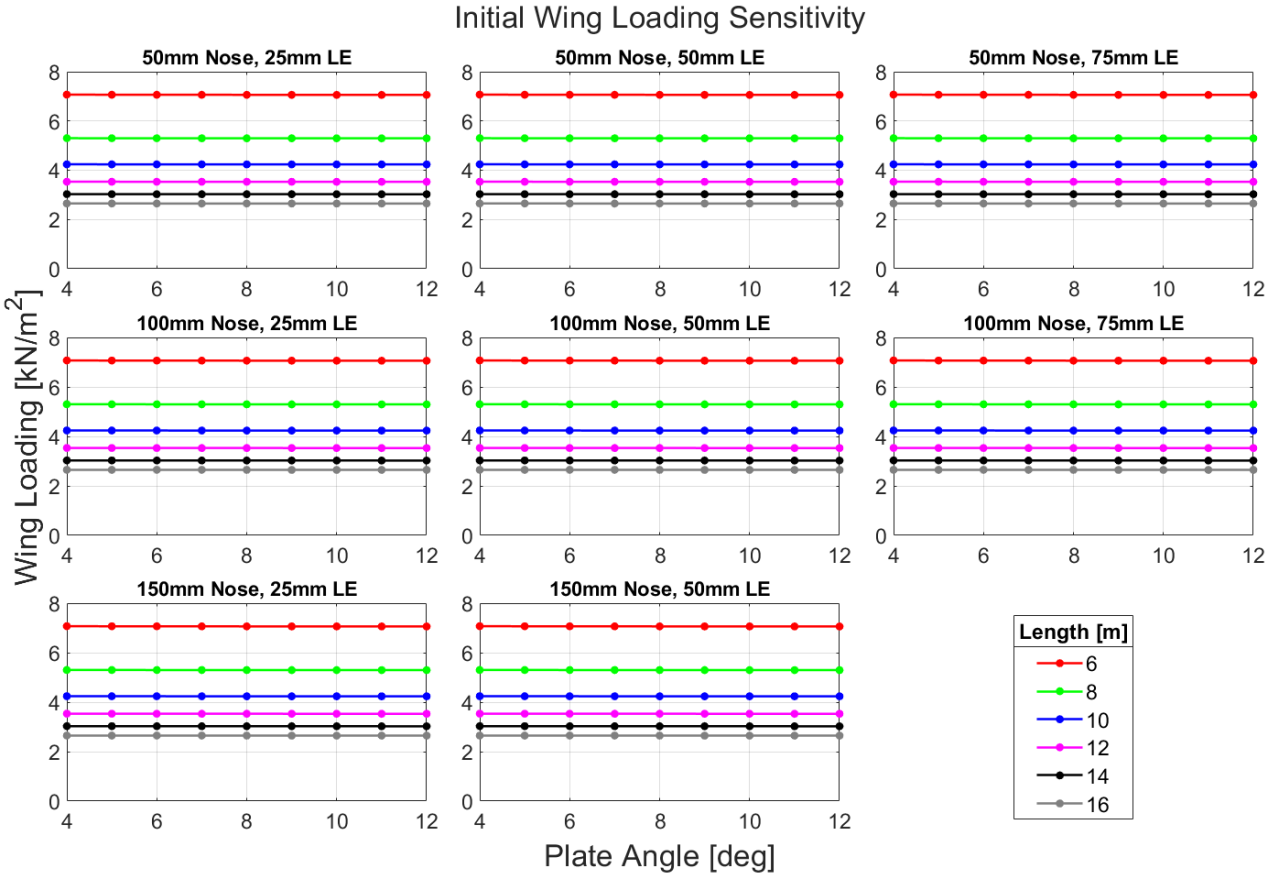

Figure 98 – Initial wing loading vs vehicle length, angle of attack, leading-edge radius, and nose radius.

7.4 Vehicle Geometry Selection

Based on the previous figures and discussion, a vehicle with the parameters detailed in Table 19 was selected. Due to the uncertainties in many of the variables and the need for more detailed information on the TPS, no optimisation was attempted. Instead, the particular case was manually selected by attempting to balance the peak thermal fluxes, aerodynamic performance, and vehicle size. For reference, the end-of-flight vehicle parameters for a vehicle with a T/D ratio of 0 and a mass loss of 10% have also been provided.

	Initial Value	Final Value	
Length	10		m
Wedge Angle	7		degrees
Nose Radius	50		mm
Leading Edge Radius	50		mm
Mass	2500	2250	kg
Flight Velocity	12.0	9.7	km/s
Flight Altitude	26.2	28.1	km
Mach Number	57.8	47.2	
Flat Plate L/D	4.0	4.0	
Drag Magnitude	23.7	12.6	kN
Nose Peak Cold-Wall Thermal Flux*	72	29.5	MW/m^2
Leading-Edge Average Cold-Wall Thermal Flux*	8.9	4.2	MW/m^2

Table 19 – Summary of vehicle geometry and initial and final conditions.

Figure 99 and Figure 100 illustrate the initial cold-wall heat flux distribution over the compression and expansion sides of the vehicle. It is clear that the highest heating rates are confined to the nose and leading-edge regions, while the majority of the vehicle surface experiences a comparatively low heat flux.

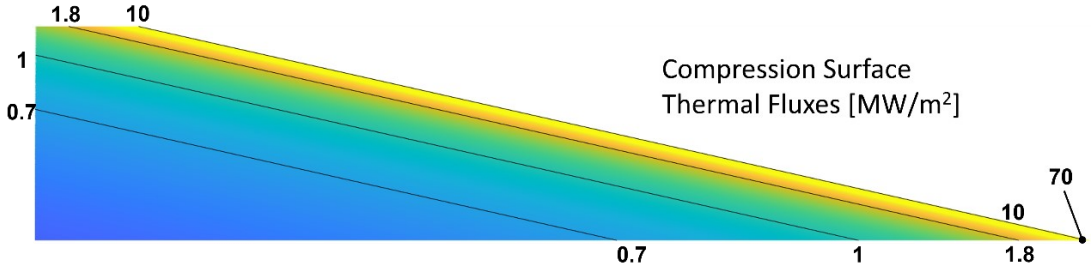

Figure 99 – Initial thermal flux map over the compression surface. Symmetric about vehicle centreline.

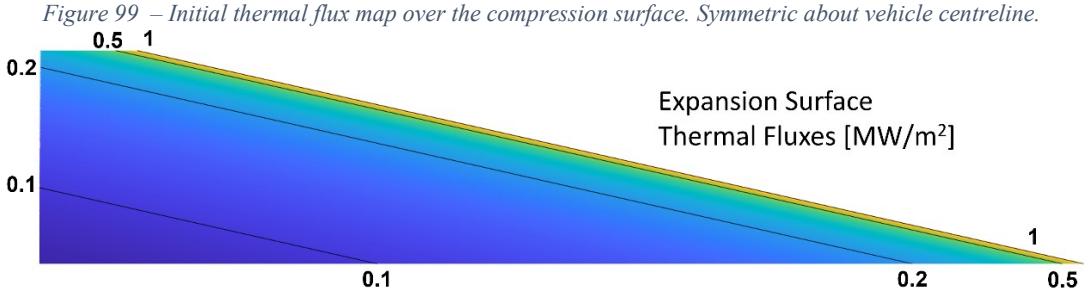

Figure 100 – Initial thermal flux map over the expansion surface. Symmetric about vehicle centreline.

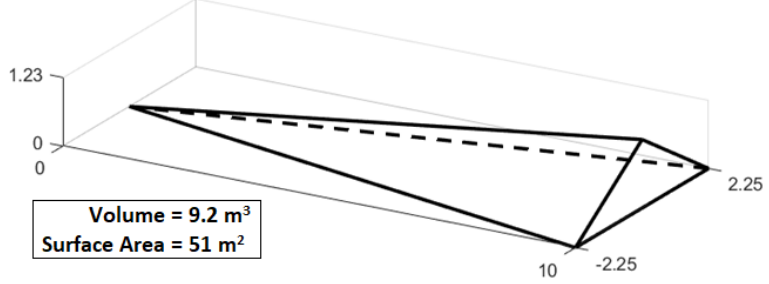

Figure 101 – Wireframe model of a simplified vehicle geometry based on the flat plate dimensions and flight angle.

To estimate the total heat load to be absorbed by the vehicle, the local cold-wall fluxes were integrated over the vehicle to provide a total vehicle heating rate. The temporally varying heating rate was in turn integrated over the atmospheric flight to provide the total heat load. During these integrations the assumed radiative heat rejection capability of the TPS was varied in order to understand the significance of radiative cooling. Regions of the vehicle that were above the specified heat flux limit were assumed to have active cooling and negligible wall radiation. The results of this analysis are illustrated in Figure 102. The 2 – 5% energy absorption range predicted for the Dyna-Soar vehicle [71] is labelled for reference.

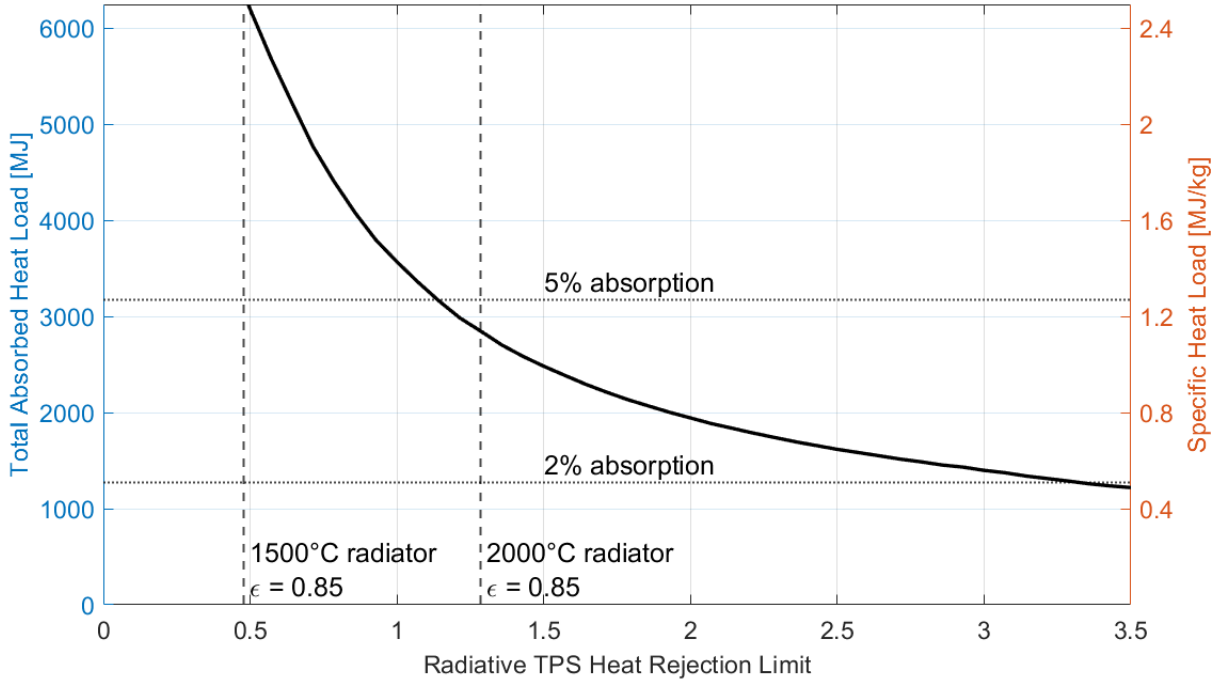

Figure 102 – Radiative heat rejection limit versus total and specific absorbed heat loads for the non-propulsive AGA flight.

It is immediately clear that the total heat load is dominated by the component from the low flux acreage regions. As the TPS heat rejection capability increases, the total heat load asymptotes to a relatively small value which comes from the nose and leading edges. While these regions experience very high fluxes, their small surface area constrains the area-integrated heating rate to a relatively small value. Clearly, a TPS which can reject low and moderate heat fluxes is critical for reducing the total absorbed energy, which in turn reduces the TPS mass.

High wall temperatures are required to generate the radiative fluxes needed for significant heat rejection. A hot-structure vehicle featuring materials with high temperature strength and high emissivity is an attractive option. If a high temperature aeroshell constructed of carbon-carbon ceramics can be constructed, it would appear the heat absorption fraction can be reduced well below the 5% value assumed earlier.

The analysis presented in Figure 102 has some important limitations which should be noted. It effectively assumes a constant temperature and emissivity over the entire vehicle outer surface. It is not clear a priori if the passive and actively cooled regions will have the same outer surface temperatures or similar emissivity values. It is also not clear what temperatures can safely be assumed, which creates a large uncertainty in the heat soak requirement of the coolant. Additionally, the perfect insulation of the vehicle internals from the low-flux regions of the aeroshell is assumed. In reality, some fraction of the rejected heat will leak in through the insulation materials, increasing the total heat load. It should also be recalled that laminar flow has been assumed over the entire vehicle. As the total heat load will be dominated by the acreage regions, which are the regions where turbulent flow is most likely to occur, more detailed analysis of the likelihood of turbulent flow occurring is needed in further work.

It is clear that the TPS will likely be discretised into passive and active regions. A passive TP scheme featuring low density, high temperature, high emissivity materials should be investigated for the acreage regions. An active TP scheme with an emphasis on high flux capability should be investigated for the nose and leading-edge regions.

7.5 Atmospheric Dissociation and TPS Oxidation

High temperature materials considered for hypersonic applications often become susceptible to rapid oxidation at elevated temperatures. Oxidation is of particular concern at Earth, where oxygen constitutes about 20% of the atmosphere. At Mars, the atmospheric O_2 concentration is only 0.13% [87]. This is an important point, as the development of oxidation-resistant coatings have proved difficult in the past and often limits the operation temperature. The Space Shuttle RCC components required a multi-step impregnation and coating procedure using silicon-carbide and tetraethyl orthosilicate [44] to prevent thermal-expansion cracking. If oxidation protection is not required, the TPS materials can likely be operated at higher temperatures.

Even if there is a low oxygen content in the atmosphere, high post-shock temperatures can lead to the generation of oxygen via the dissociation of other molecules. CO_2, which comprises about 95% of Mars' atmosphere, is one such molecule. To understand the severity of this problem, the equilibrium shock temperature was probed at key locations across the selected AGA vehicle geometry at its initial atmospheric entry velocity. Table 20 reports these values.

Nose Stagnation Point	13 300	K
Leading Edge Tip	2400	K
Oblique Shock Region	1450	K

Table 20 – Estimated gas temperatures at key locations of the vehicle outer surface.

The oblique has a calculated β angle of 8° at Mach 57, which corresponds to a normal shock of only Mach 7.8. As can be seen from Figure 103, this temperature is insufficient to induce any meaningful dissociation. The higher temperature at the leading-edge region is enough to induce partial dissociation, resulting in a gas mixture of approximately 5% O_2. Oxidation protection will likely be required along the leading edges and will certainly be required at the nose as total CO_2 dissociation into CO and O will occur there.

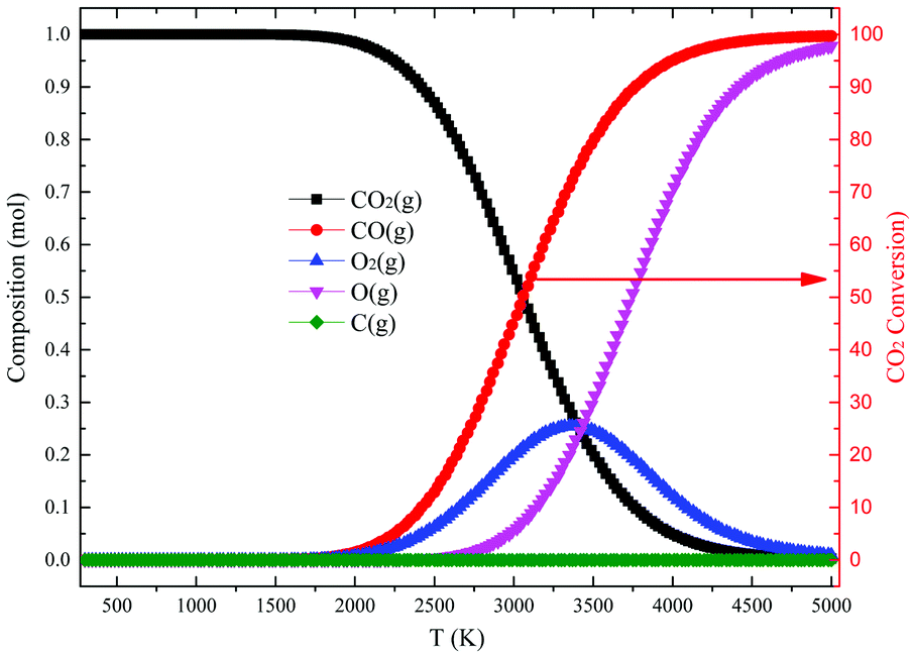

Figure 103 – Temperature-dissociation curve for CO_2 at 1 bar pressure [88].

8 Thermal Protection System Analysis and Sizing

8.1 Requirements

A TPS mass target of 1000 kg was selected so that 1500 kg of dry mass would be available for the core spacecraft equipment, which is competitive with the reference missions.

An insulated volume sufficient to house the spacecraft scientific payload and supporting systems is also required. The mass and dimensions of the New Horizons Spacecraft [89] were used to estimate a reasonable 'spacecraft density' value of approximately 300 kg/m^3. Thus 5 m^3 of insulated volume is required.

The thermal flux requirements of each TPS section were iteratively developed and are introduced later.

8.2 TPS Architecture

A hot structure carbon-carbon aeroshell was selected to form the basis of the TPS for mass reduction and TPS material volume minimisation. Figure 104 and Figure 105 show details of a hot structure carbon-carbon aeroshell employed on the HTV-2 which could withstand temperatures of nearly 2000°C [90].The vehicle was about 5m long and weighed approximately 1000 kg [27].

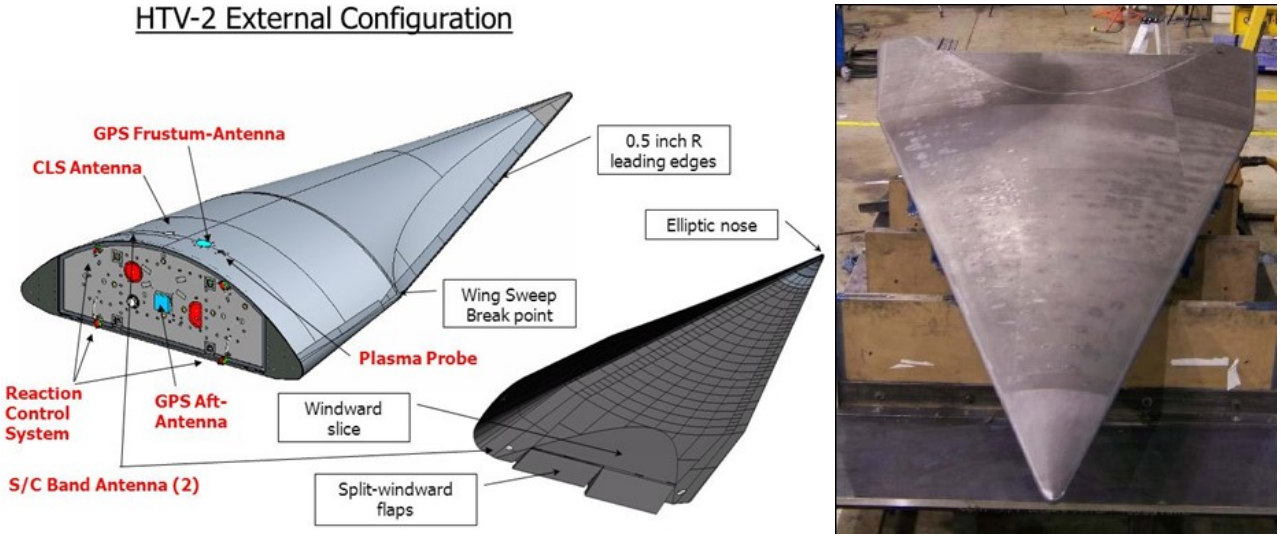

Figure 104 (Left) – Basic external configuration of DARPA's HTV-2 [26].
Figure 105 (Right) – Compression side of HTV-2's carbon-carbon aeroshell [26].

The TPS of the AGA vehicle has three distinct approaches across the vehicle, as illustrated in Figure 106. The highest flux regions near the nose and leading edges will be actively cooled by a pressure-fed fluid system.

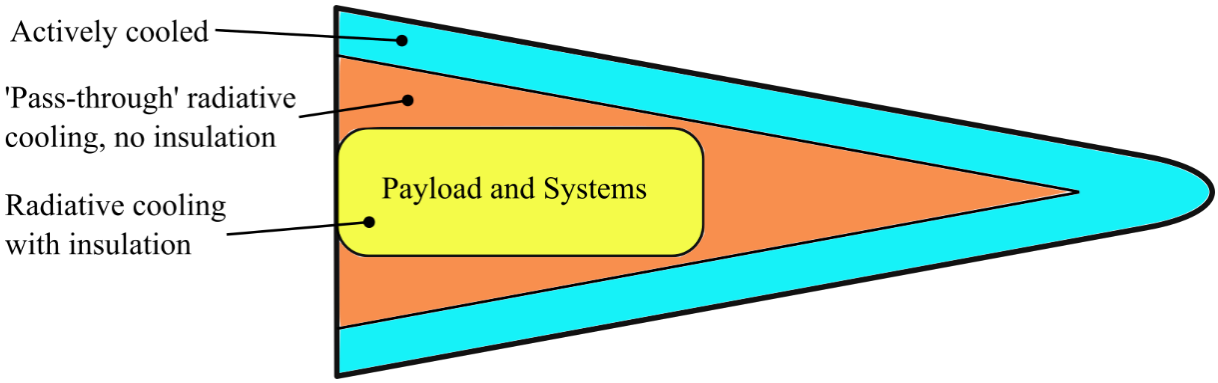

Figure 106 – Planform schematic of the selected protection schemes for the AGA waverider aeroshell.

Figure 107 and Figure 108 illustrate the general architectures of the TAGA and AGA-EP vehicle active cooling systems respectively. Pressurisation of the TAGA vehicle coolant tank could be done autogenously or with a separate gas. Pressurisation of the AGA-EP tank would require a separate gas or other mechanism.

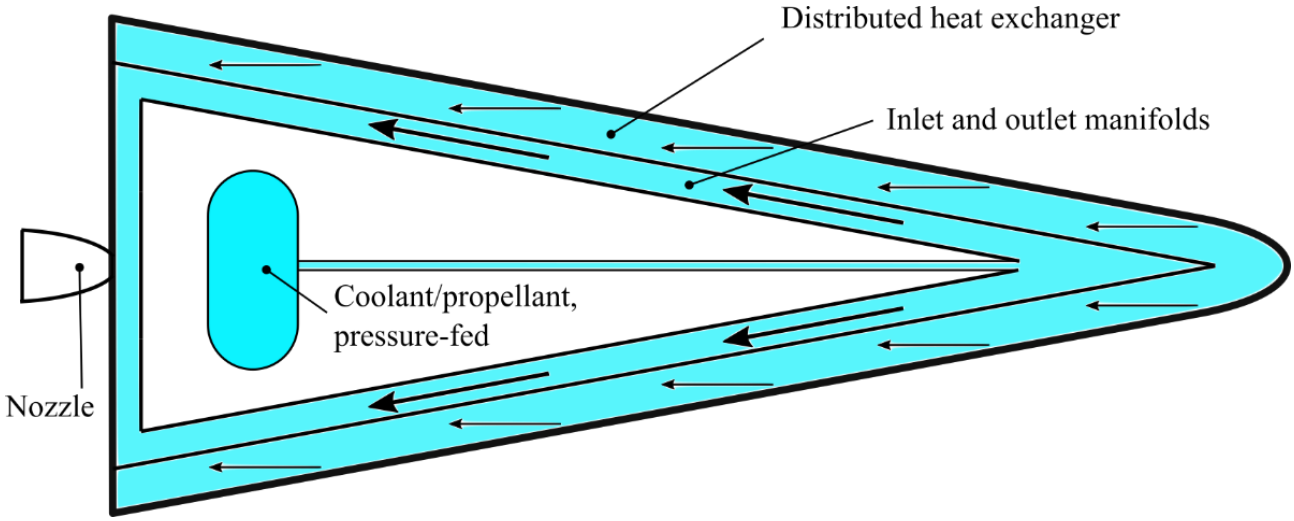

Figure 107 – Schematic of the TAGA active cooling and propulsion concept.

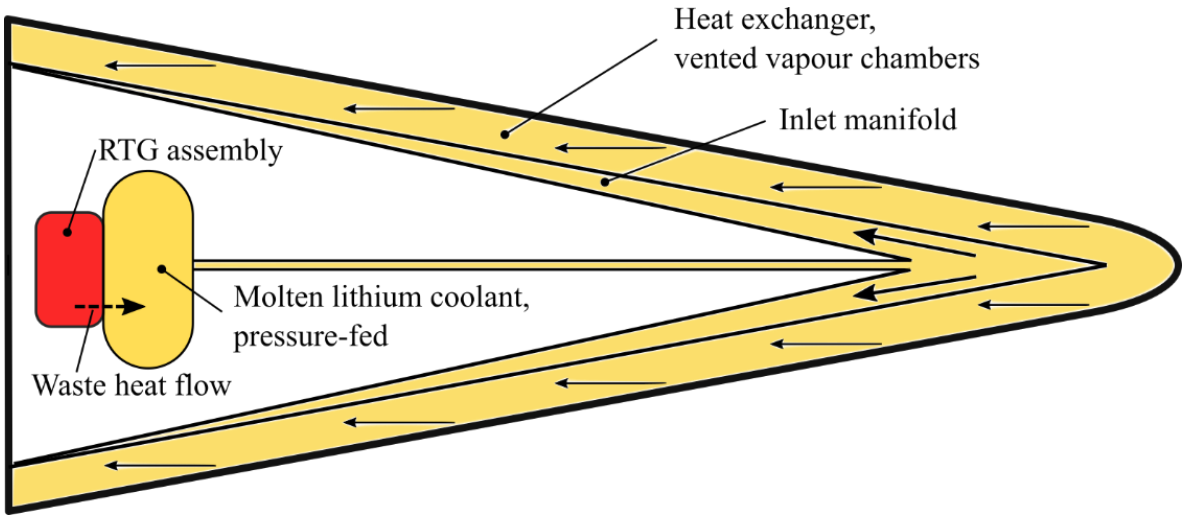

Figure 108 – Schematic of the AGA-EP active cooling concept.

In the moderate flux regions of the vehicle active cooling is no longer required, and a 'pass-through' passive scheme was selected. A large portion of the incoming flux would be rejected directly by external radiation from the compression-side of the aeroshell. The remaining portion would be transferred via radiation to the cooler suction side of the aeroshell for re-radiation into deep space. This allows both sides of the compression-side aeroshell material to be utilised for radiative cooling. Figure 109 illustrates the concept. Regions of the vehicle utilising this scheme would need to be reasonably hollow and any structural members would need to either be protected by reflective coatings or constructed of high-temperature materials. Figure 111 highlights a wing region of the Dyna-Soar spaceplane for which such a scheme could be well-suited.

Finally, the lowest-flux regions would have internal insulation to prevent excessive heat from transferring into other systems, as illustrated in Figure 110. Sub-frames and mounting panels would likely be constructed from materials with a high heat sink capability in order to provide a further transient thermal barrier between the aeroshell and instruments.

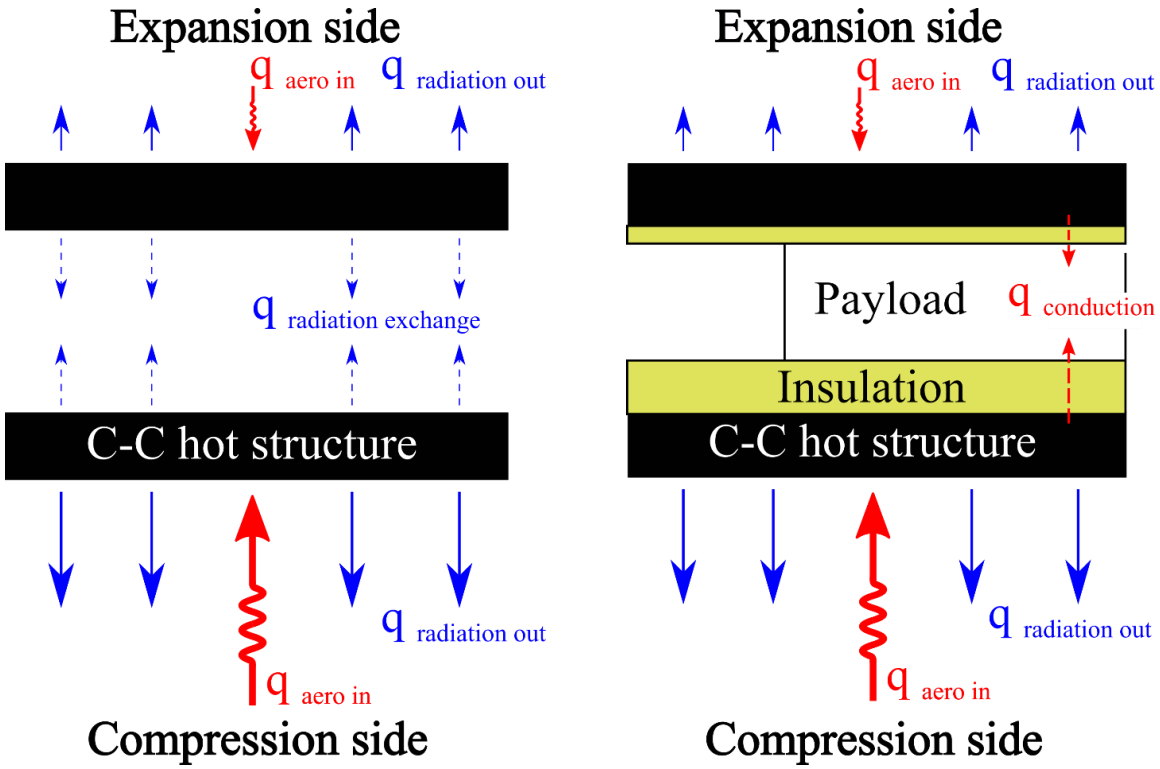

Figure 109 (Left) – 'Pass-through' passive TPS concept for moderate flux regions.
Figure 110 (Right) – Insulated passive TPS concept for the payload bay.

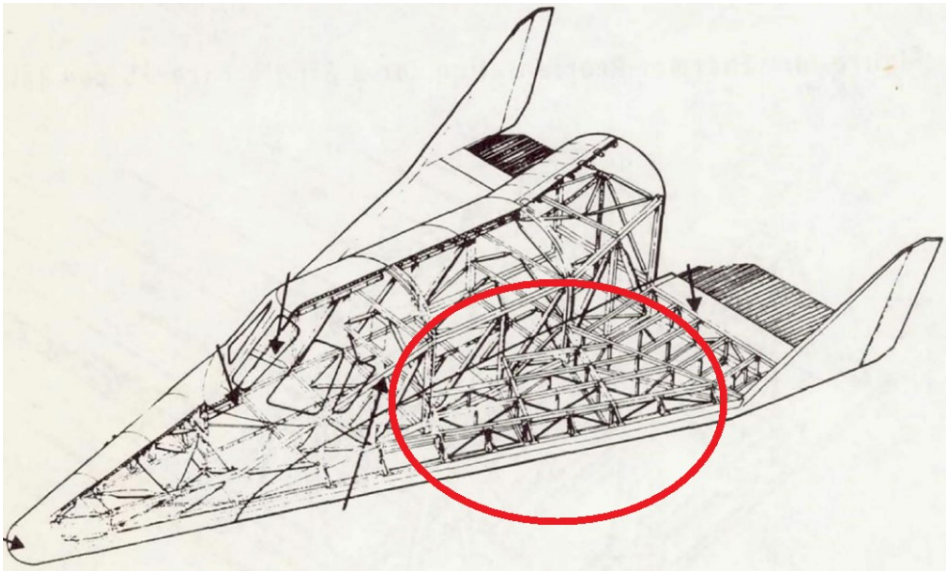

Figure 111 – Structure of the Dyna-Soar spaceplane, with a region suitable for pass-through cooling circled. Adapted from [71].

8.3 Aeroshell Initial Sizing

As a hot structure aeroshell will serve structural and thermal functions, both load cases must be considered when sizing the system. The key variable of interest for this early-stage analysis is the thickness of the carbon-carbon laminate as it drives the mass of the passively cooled regions. A detailed structural analysis is outside the scope of this work. Instead, some case studies were examined, and a rudimentary analysis conducted to try and ensure a reasonable thickness was selected.

The reinforced carbon-carbon components used on the space shuttle varied in thickness between about 6.35 mm and 12.8 mm [91]. RCC was used in areas where the strength of the HRSI tiles was insufficient, such as leading

edges and fuel tank attachment points. Both of these applications featured relatively complex geometry and/or concentrated loads. As the carbon-carbon panels on an AGA vehicle will have only gentle curves and distributed loads rather than point loads, it is hoped that the thickness can be reduced considerably compared to the Space Shuttle. The material properties of carbon-carbon have also increased over time.

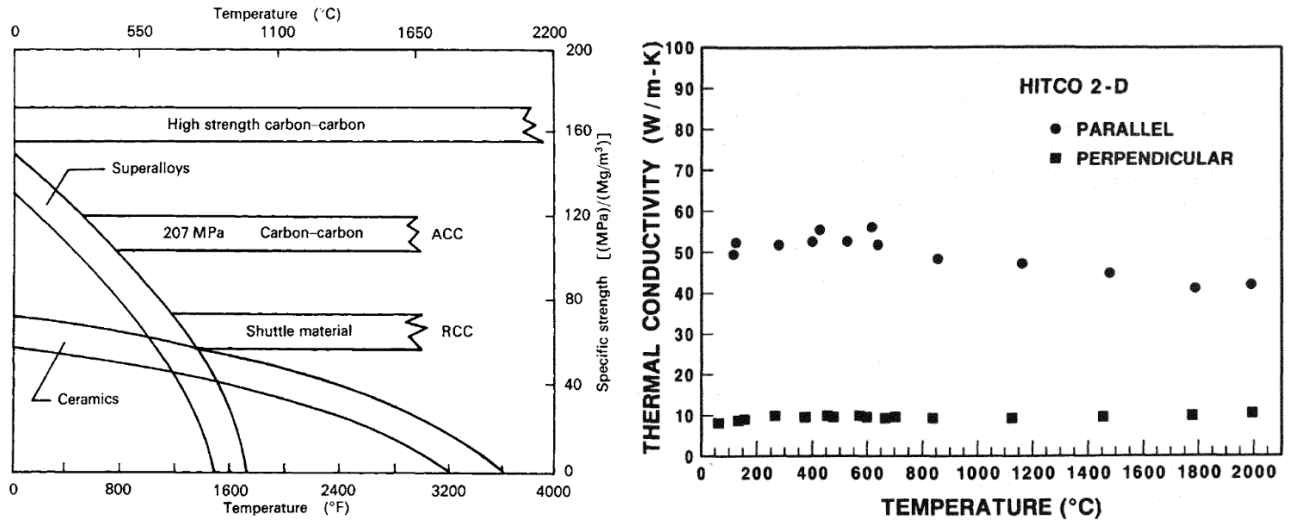

Figure 112 (Left) – Specific strength variation with temperature of common high-temperature materials [92].
Figure 113 (Right) – Typical in-plane and out-of-plane thermal conductivities of a 2-D woven C-C laminate [93].

		Temperature		K
		300	2478	
Density		1.45		g/cm^3
Specific Heat		1.298	2.260	kJ/(kg.K)
Thermal Conductivity	- In-plane - Out-of-plane	31.3 13.8		W/(m.K)
Ultimate Tensile Strength	- In-plane - Out-of-plane	93 5	110 9	MPa
Compressive Strength	- In-plane - Out-of-plane	93 44	93 62	MPa
Thermal Expansion	- In-plane - Out-of-plane	0.9 2.5	3.1 5.0	m/m/K

Table 21 – Typical room temperature and elevated temperature properties of a 2-D woven C-C laminate [94].

A preliminary investigation into a similar AGA waverider mission to the outer planets suggested a carbon-carbon aeroshell with a thickness of approximately 3mm [95]. This value was also assumed for the present work, and a basic static bending analysis conducted with steady-state conditions to give an initial indication of feasibility. Dynamic loads, acoustic loads, and stiffness requirements will likely be the dominant factors in a real design. In this present analysis, a large safety factor on static loads was considered satisfactory.

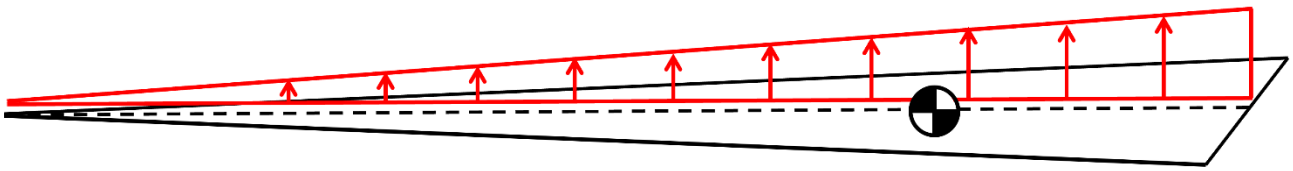

Figure 114 – Free body diagram showing the compression-side distributed pressure load.

A simple script was written to the evaluate the bending moment resulting from the pressure loads illustrated in Figure 114, as well as the cross-section properties of the geometry from Figure 101. Figure 115 through Figure *118* present the results of the bending analysis evaluated along the centreline of the vehicle. The high peaks observed in Figure 117 and Figure *118* are an artifact due to the small second moment of area at the nose. In

reality, the nose region would be considerably reinforced, and these peak stresses would not be realised. Additionally, collapsing the vehicle to a point mass increases the peak bending moment. If the vehicle mass could be distributed to exactly match the aerodynamic pressure distribution, there would be no longitudinal bending stress at all. Reality will lie somewhere between these two extremes.

A safety factor ranging from about 4-10 on the static bending stress is maintained everywhere, suggesting this thickness is acceptable for now. Compressive stress and buckling of the suction side surface would appear to be key areas of investigation for further work. Out-of-plane loading is also an important load case given the much-reduced properties of carbon-carbon in shear. This was not analysed here as it was assumed that the vehicle would have an internal structure to handle the shear loads, much like a sandwich panel.

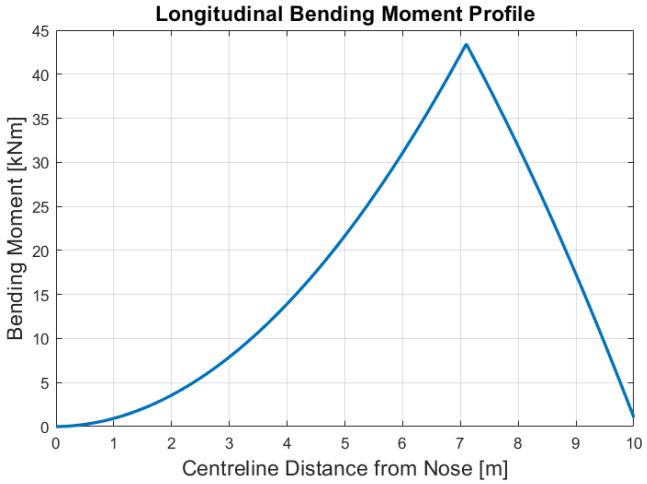

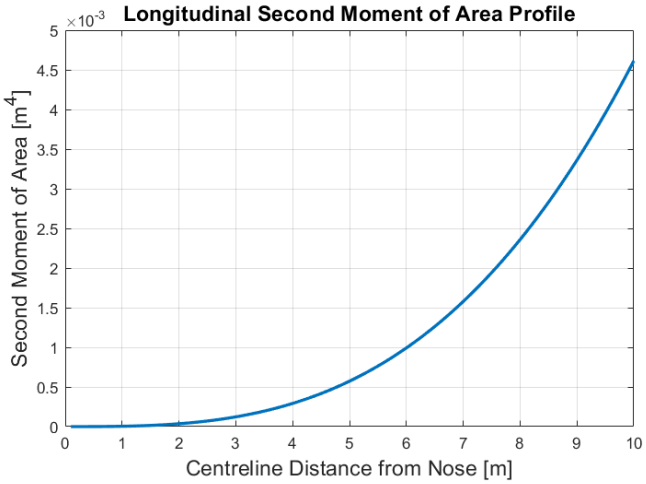

Figure 115 (Left) – Bending moment due to the pressure loads on the simplified geometry.
Figure 116 (Right) – Longitudinal profile of the second moment of area about the bending axis.

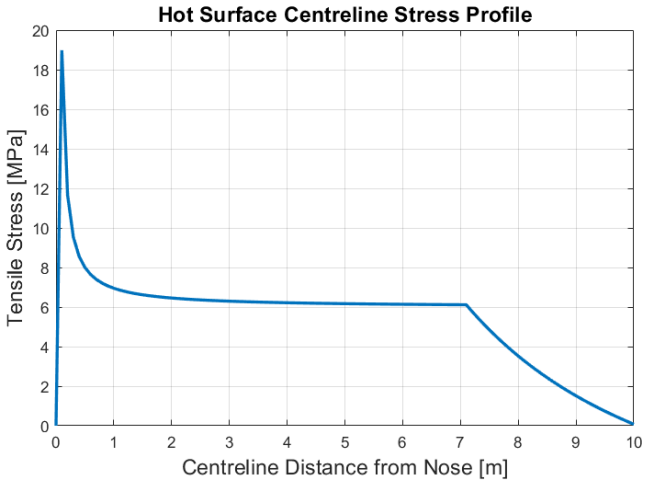

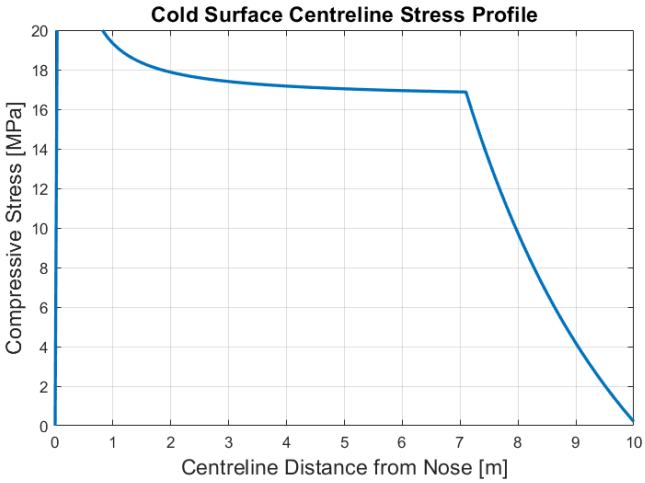

Figure 117 (Left) – Bending stress profile along the expansion-side surface.
Figure 118 (Right) – Bending stress profile along the compression-side surface.

8.4 1D Thermal Analysis

A steady state 1D analysis was written to estimate the flux capabilities of each protection scheme. The script is iterative in nature as it uses temperature dependent material properties. It considers heat transfer between parallel slabs of unit area. 2D in-plane effects such as longitudinal or lateral conduction across the vehicle skin are not considered. The general nature of the algorithm is detailed below.

1. User specifies # of layers, layer material, layer thickness, number of nodes in each layer, the thermal interfaces (conduction/convection/radiation) between the layers, and an initial guess for the outer wall temperature on the compression side of the vehicle.
2. Outer wall enthalpy is calculated at the guessed temperature, and the reduced 'hot wall' flux is calculated using Equation 45.
3. The radiatively rejected flux is calculated at the compression side outer surface, with the residual flux being conducted into the structure.
4. The residual flux is propagated through the layers of the TPS, and the temperature profile calculated. Equation 46 is used for conduction, Equation 47 for radiative transfer between parallel walls, and Equation 48 for convection. Temperature dependent materials properties are interpolated from material data sheets.
5. If the simulation is considering the 'pass-through' scheme, the temperature of the final node is checked to ensure that it is high enough to reject both the heat flux transferred through the vehicle and the incoming convective flux on the expansion side surface.
6. The effective thermal resistance of each layer is calculated using equation 49 for conduction, 50 for radiative transfer between parallel walls, and 51 for convection.
7. At the end of each iteration, the thermal resistance of immediate radiative rejection is compared to the thermal resistance of the pathway into the vehicle. If the thermal fluxes in each path are not in balance with the thermal resistances, the outer wall temperature is modified, and steps 2-6 repeated.

$$q_{hot\ wall} = q_{cold\ wall}\left(1 - \frac{h_{wall}}{h_{tot}}\right) \tag{45}$$

$$q_{cond} = -k\frac{T_1 - T_2}{x_1 - x_2} \tag{46}$$

$$q_{rad} = -\frac{\sigma(T_1^4 - T_2^4)}{\frac{1}{\varepsilon_1} + \frac{1}{\varepsilon_2} - 1} \tag{47}$$

$$q_{conv} = -h(T_1 - T_2) \tag{48}$$

$$R_{cond} = \frac{\Delta T}{q} = \frac{L}{k} \tag{49}$$

$$R_{rad} = \frac{1}{\varepsilon_{avg}\,\sigma\,(T_1^2 + T_2^2)(T_1 + T_2)} \tag{50}$$

$$R_{cond} = \frac{1}{h} \tag{51}$$

The script was primarily used for analysis of the insulative and pass-through TPS schemes. The lower wall temperatures and simpler geometry of the active cooling system allowed a simpler analytical approach.

8.5 TPS Sizing

8.5.1 Passive TPS

The primary TPS component for the passively cooled regions of the vehicle is the 3mm carbon-carbon aeroshell. As the passively cooled TPS is the lightest of the methods considered, there is a strong motivation to use it on as large an area of the vehicle as possible. This implies operating the radiating material at the highest temperature possible. A temperature limit of 2300 K was assumed for the carbon-carbon material based on the information of Table 21 and [90]. This temperature would pose a severe oxidation challenge in an oxygen-rich environment,

but as discussed in Section 7.5, a negligible quantity of oxygen is expected in the oblique shock region and expansion regions. In any case, a silicon-carbide coating of the carbon-carbon was assumed to increase the emissivity to about 0.85 [96]. Oxidation reduction is an added benefit. Potential cracking of the coating would hopefully not be a serious concern due to the low level of oxygen present.

The thermal properties for the following sections were also taken from Table 21. In plane thermal conduction from hotter regions to colder regions was not considered in theses 1D analyses for simplicity. This effect could slightly increase the peak flux capability of each passive TPS strategy.

8.5.1.1 Low Flux Regions

The insulated hot structure TPS was found to be capable of handling a cold wall flux of approximately 1.4 MW/m^2 with a maximum aeroshell temperature of 2300 K. The actual flux into the structure reduces to about 1.3 MW/m^2 once the wall enthalpy is included. This is largely independent of the insulation material, depending mainly on the carbon-carbon radiative properties and temperature limit. The insulation properties primarily determine the quantity of insulation required and the flux that leaks into the vehicle core. Generally, more than 99% of the incoming flux is rejected via radiation at the outer surface on the compression side of the vehicle. The additional mass and complication of the insulation material provides a strong motivation to only use this scheme where it is strictly necessary and limit the insulation thickness as much as possible.

A brief investigation was conducted into the payload bay sizing in order to understand better the insulated area requirements and the fluxes that the insulated region would be subjected to, rather than the peak fluxes possible. Ideally, the spacecraft core should be as dense and compact as possible to minimise the area of insulation required. Figure 119 shows a possible payload volume configuration which meets the 5m^3 requirement and maintains a constant initial chord length, and thus peak thermal flux in the payload region. For simplicity, centre of mass and centre of pressure requirements have not been considered.

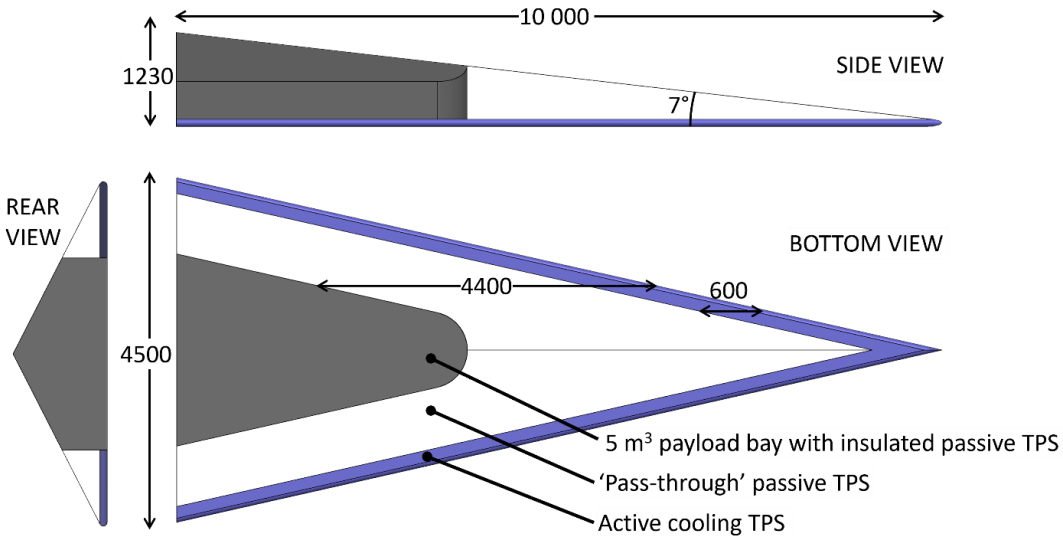

Figure 119 – Dimensioned schematic of TPS regions and payload bay.

At a 4400 mm chord length, the cold wall thermal flux at the beginning of the flight is approximately 0.7 MW/m^2. This was used as the design flux and a multi-layer insulation scheme was sized so that the final radiative flux into the payload bay would be approximately 1300 W/m^2, equivalent to that of solar radiation at Earth orbit. The material properties of Denka Alcen NBK80A [97], an alumina based insulating blanket, were used for the MLI. The material data sheet is provided in Appendix A. Reflective coatings on each side of the blankets with an emissivity of 0.1 were assumed. The same scheme was used on the expansion side, but with 2 layers rather than 3 due to the reduced flux of about 0.2 MW/m^2. Figure 120 illustrates the temperature profile through the C-C wall and insulation layers as well as the fluxes in and out of the system.

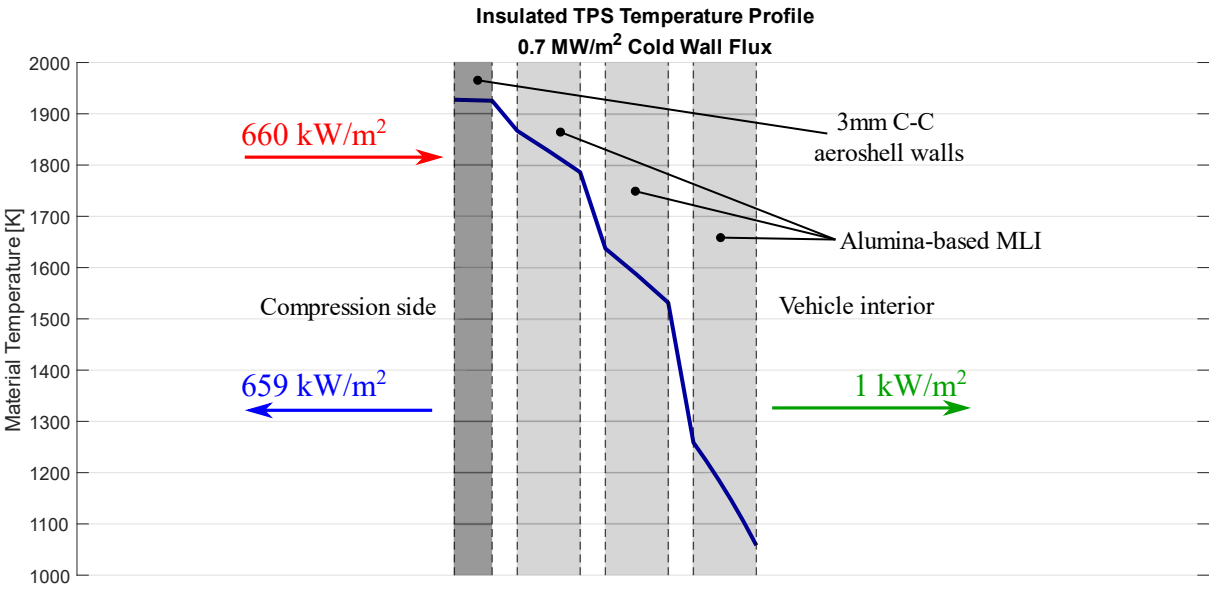

Figure 120 – Temperature profile through the compression side hot-structure and insulation.

8.5.1.2 Moderate Flux Regions

The 'pass-through' hot structure system was found to be capable of handling a cold wall flux of approximately 1.80 MW/m^2 with a maximum operating temperature of 2300 K. Once the wall enthalpy was included, the flux into the structure on the compression surface is reduced to about 1.71 MW/m^2. Of this, approximately 1.35 MW/m^2 is rejected via radiation on the compression side of the vehicle, with the remaining 0.36 MW/m^2 conducted and radiated to the suction side of the vehicle, where it is finally radiated away to deep space. This scheme would be confined to regions of the vehicle which are not geometrically favourable for storage of payload or vehicle systems. Figure 121 illustrates the incoming and outgoing fluxes at both the compression side and expansion side surfaces as well as the temperature profile across the vehicle thickness. An internal vacuum is assumed.

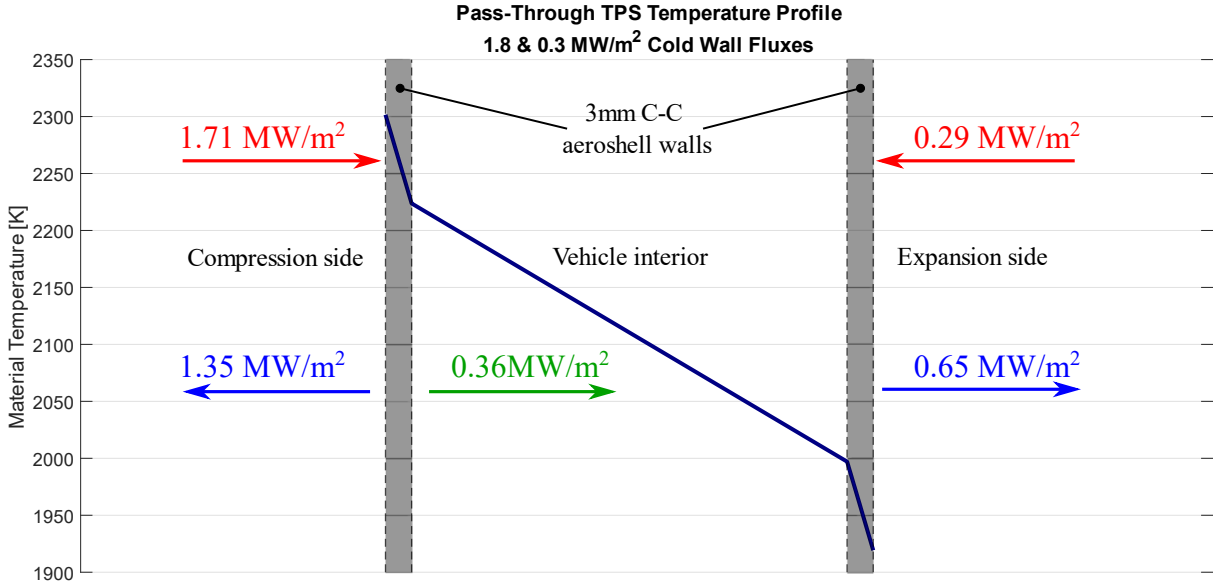

Figure 121 - Temperature profile through hollow vehicle section with pass-through TPS.

While a detailed consideration of the vehicle internal structure is outside the scope of this work, it is assumed that a scheme similar to that illustrated in Figure 122 would be used to connect the lower and upper skins of the

aeroshell in the hollow regions. The rotating truss concept allows for relative thermal expansion of the skins and other connected components without excessive thermal stresses.

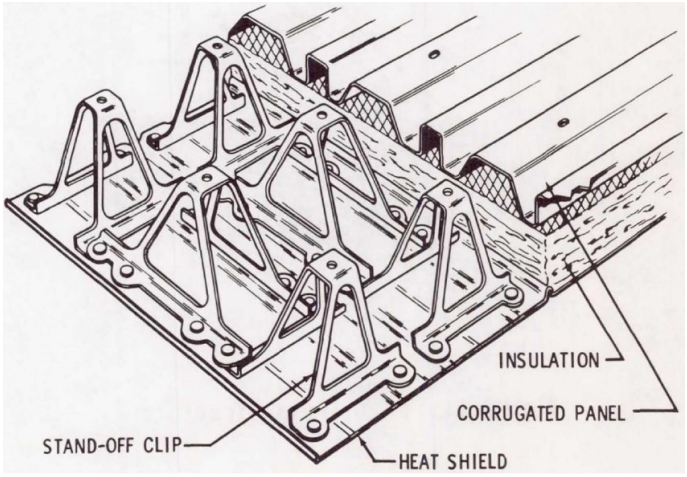

Figure 122 –Thermal-expansion isolation scheme proposed for the Dyna-Soar spaceplane [71].

8.5.2 Semi-Passive TPS

8.5.2.1 Phase Change Heat Sink

A semi-active TPS system such as that discussed in 4.2.2 could be considered as an alternative to the two passive methods introduced above. The heat rejection capabilities of the insulated scheme are reduced as half of the C-C surface can't be used for heat transfer. The 'pass-through' scheme has a higher flux limit as it exploits the internal surface of the C-C shell for radiative heat transfer. However, it requires a relatively hollow vehicle section. A semi-passive system could still make use of the C-C internal surface while requiring only a small volume relative to the entire cross section.

As discussed in [49] and illustrated previously in Figure 34, a molybdenum honeycomb structure storing a small quantity of solid lithium in each cell could be used as a semi-passive system. Initial searching [98] [99] suggests that the pool-boiling capability of such a system could be on the order of MW/m^2, depending on the fluid layer thickness. The semi-passive flux capability could exceed the back-side heat transfer rate of the 'pass-through' system while being more compact than the insulated scheme.

There would likely be a mass penalty compared to the pass-through system, as a fluid and additional materials are required. The added complexity of a venting pathway for the lithium vapour would tend to favour the selection of an insulated scheme unless there was a strong motivation for high flux capability in a tightly packed region of the vehicle.

8.5.2.2 Heat Pipes

Refractory metal/lithium heat pipes that would be capable of functioning over significant portions of the leading-edge regions of the vehicle have been analysed [51] and tested [55]. As can be seen from Figure 123, very high heat fluxes can be removed with suitably thin wicking structures. Thin wicking structures and the correspondingly thin fluid layers allow heat to be conducted rapidly to the liquid-vapour interface for evaporation without the need for boiling. Bubble formation at the hot surface and in the wick interfere with the thermal flow path, reducing maximum thermal flux capability [51].

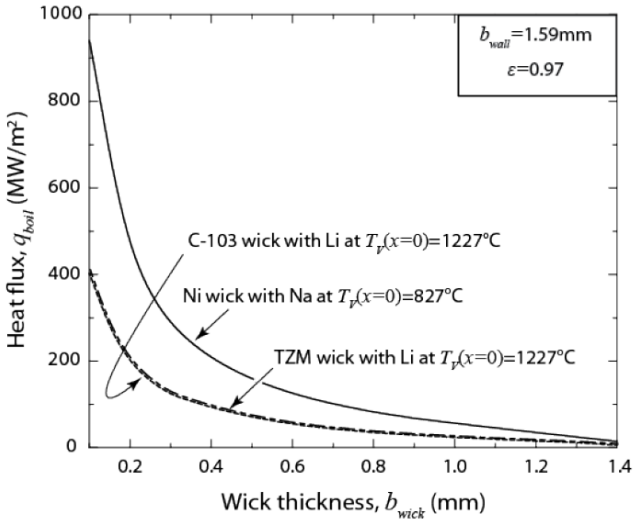

Figure 123 – Theoretical heat pipe flux boiling flux limits for a 3mm radius hypersonic leading edge heat pipe [51].

Heat pipes and vapour chambers work on the principle of absorbing heat in one location and releasing it in another, and herein lies the problem for the present work: it is not possible to reject the heat even if it can be absorbed. The vast majority of the AGA vehicle is passively cooled via radiation, rejecting fluxes in the range of 0.1–1.7 MW/m^2 by operating at temperatures of between about 1200 – 2500 K. A heat pipe cooled via radiation can only reject heat at the operating temperature of the fluid. Even if the 1 atmosphere pressure boiling point of lithium (~1600 K) is assumed, a radiative rejection flux of only about 0.3 MW/m^2 is possible. From Figure 100, it is clear that only at a small area on the trailing edge of the expansion surface would the heat pipe rejection flux overpower the incoming convective flux. Higher operating temperature heat pipes, such as a silver-charged pipe, could be investigated. Such a device was not considered in this work as it still did not appear feasible after a cursory analysis.

This logic can also be extended to an X-43 style passively cooled leading edge. While the tip may be capable of conducting away ~15 MW/m^2 on a Mach 10 vehicle, at Mach 60 the entire vehicle surface is heated to such an extent that sufficient temperature gradients to conduct this heat away don't exist and, like in the heat-pipe case, there is insufficient area available to radiate the conducted heat away.

8.5.3 Active TPS

8.5.3.1 Coolant/Propellant Loads

The total heat load that is required to be absorbed by the coolant can now be estimated by interrogating Figure 102 with the calculated heat flux rejection capabilities of the radiatively cooled TPS. The pass-through carbon-carbon structure operating at 2300 K can reject approximately 1.9 MW/m^2, leaving a residual specific heat load of approximately 0.81 MJ/kg. This is equivalent to about 2030 MJ, or 3.2% of the total mechanical energy loss. The advantage of maximising the operating temperature of radiative hot structures is clear. Table 22 provides the updated estimates of the propellant loads and storage volumes required for cooling purposes.

Coolant/Propellant	Enthalpy Mass Density [MJ/kg]	Vehicle Mass Fraction	Required Mass [kg]	Stored Density [kg/m^3]	Enthalpy Volume Density [MJ/m^3]	Vehicle Volume Fraction	Required Volume [m^3]
Water	6.0	0.135	337	1000	6010	0.037	0.34
Ammonia	8.3	0.098	244	600	4980	0.044	0.41
Liquid hydrogen	27.7	0.029	73	71	1970	0.112	1.03
Lithium	25.7	0.032	79	530	13600	0.016	0.15

Table 22 – Updated estimation of the fluid requirements for cooling purposes.

When the fluid requirements for cooling purposes presented in Table 22 are compared with the fluid requirements for the TAGA flyby propulsion in Table 23, a problem emerges.

Coolant/Propellant	I_{SP}* [s]	T/D	Vehicle Mass Fraction	Required Mass [kg]
Water	250	0.3	0.245	613
Ammonia	330	0.3	0.191	478
Liquid hydrogen	700	0.3	0.095	238

Table 23- Estimate of the fluid requirements for propulsion purposes.

**I_{SP} calculated at 5 bar and 1800 K with a nozzle area ratio of 100.*

For the given combination of mission, vehicle geometry, and passive TPS capability, the absorbed thermal energy is much lower than the thermal energy required to heat and vaporise a sufficient quantity of fluid for the selected thrust-drag ratio. There is an energy imbalance in the coolant/propellant mass fractions.

An obvious solution is to increase the actively cooled area of the vehicle, thus increasing the total absorbed heat load. However, the relatively high areal mass of active cooling panels would likely lead to an excessive TPS mass. A more drastic solution would be to revise the vehicle geometry to have a higher natural L/D. An increased L/D would reduce the drag load and thus thrust required, while also forcing the vehicle to fly at lower altitudes where nose and leading-edge heating would be increased. The gap between thermal and propulsion energy demands on the fluid could be closed or possibly closed in this way.

Alternatively, a lower T/D could just be accepted, and the initial flyby velocity increased to compensate for the additional losses. This would increase the heat fluxes and total heat load while reducing the propulsion requirements, again closing the energy gap. However, it would also decrease the launch mass of the vehicle due to the increased C_3 required.

A more practical solution is to simply increase the mass flow rate of the coolant and accept the resulting lower propellant temperature and I_{sp}. This reduced I_{sp} in turn increases the propellant needed and care needs to be taken that the propellant load doesn't spiral out of control. This solution would be best suited to liquid hydrogen as its light molecular mass allows it to still achieve relatively high I_{sp} values at moderate temperatures. However, even if state-of-the art insulation is assumed, the boil-off corrected vehicle volume fraction for liquid hydrogen storage would approach 0.5. This would leave insufficient volume for the payload with the current vehicle geometry as well as prevent the use of pass-through cooling. A hydrogen based TAGA vehicle may be practical with a larger aeroshell vehicle with a correspondingly larger internal cavity and reduced wing loading.

A similar mass-flow increase approach could be attempted with water or ammonia. However, a large fraction of their enthalpy absorption capability is wrapped up in phase changes and dissociation. Any enthalpy decrease would act mostly on the gas heating stage, significantly dropping the final gas temperature and ruining propulsion performance. One solution to compensate for this enthalpy drop is by chemically reacting the fluid in a bi-propellant propulsion system. Such a system could be implemented for an ammonia based TAGA vehicle with hydrogen peroxide as the oxidiser. With a 0.5:0.5 fuel-to-oxidiser mass ratio of superheated ammonia and catalytically decomposed peroxide this system could achieve a vacuum I_{sp} of about 340s, requiring a total propellant mass fraction of about 0.2. Even with this complex solution the coolant-propellant requirements for a TAGA mission are almost triple that of the AGA-EP mission, as can be seen from Table 24.

Mission	Coolant/Propellant	Coolant Mass Fraction	Propellant Mass Fraction	Total Mass Fraction	Required Mass [kg]
TAGA	Ammonia	-	0.098	0.2	500
	Hydrogen Peroxide	-	0.102		
AGA-EP	Lithium	0.032	0.045	0.077	175

Table 24 – Summary of fluid loads for each mission concept

Remember that these propellant loads produce equivalent heliocentric energy changes. Both missions also now require an 'augmented' propulsion system that is more complex than a simple outlet pipe and nozzle. For the purposes of this work the TAGA concept won't be analysed any further. This is not to say that it is not a viable solution for an AGA mission, just that it does not initially appear to be a viable solution for this present mission with its particular variables and constraints.

It is worth recalling that while the 50,000s I_{SP} lithium-fuelled gridded ion thruster introduced earlier does not currently exist, the AGA-EP mission design was conducted with an I_{SP} value of 3000s produced by a heritage xenon-fuelled thruster. A near-future implementation of the AGA-EP mission could simply use lithium as a light-weight thermal protection solution, and a separate fuel for the electric propulsion. Realisation of lithium's high theoretical I_{sp} would greatly reduce the propellant mass fraction reported in Table 24, providing a strong motivation for relying on lithium for both cooling and propulsion.

8.5.3.2 Coolant Distribution Strategy

The design case for the actively cooled TPS will be the fluxes and area-integrated heating rate at the beginning of the atmospheric cruise as this is the most demanding instantaneous load. The area of the vehicle to be actively cooled is relatively large for the small mass flow rate of coolant, introducing some peculiarities in the proposed solution. The flow rate per unit area value in the last row of Table 25 can be visualised as the speed at which a $1m^2$ column of coolant would need to fall in order to distribute the coolant at the required rate. It can also be visualised as the channel depth required to generate a flow velocity of 1m/s parallel to the plate surface.

Heating Rate	11.0	MW
Enthalpy Mass Density	25.7	MJ/kg
Liquid Density	514	kg/m^3
Mass Flow Rate	0.428	kg/s
Total Leading-Edge Length	20.5	m
Mass Flow per Unit Length	0.018	kg/(s.m)
Cooled Surface Area	3.0	m^2
Mass Flow per Unit Area	0.143	$kg/(m^2.s)$
Flow Rate Normal to Unit Area	0.18	mm/s

Table 25 – Breakdown of the coolant mass flow rate requirement.

High flow velocities on the order of metres per second are needed to generate the large Reynolds numbers and heat transfer coefficients required to cool the leading-edge fluxes. Clearly, very small cooling channels would be required for a single pass cooling jacket. As can be seen from the Darcy-Weisbach equation, repeated here as Equation 52, high flow velocities in small single-pass channels imply high pressure losses from friction.

$$\Delta P = C_f \frac{\rho}{2} \frac{v^2}{D} L \qquad 52$$

A workaround to this would be to lump the flow into n channels per metre span, with each lumped channel making n passes across the plate. While the wetted area and thus frictional losses would be reduced, a large number of direction changes would be required, introducing additional pressure losses. It is not clear a priori which solution would present the lowest pressure losses.

High pressure losses can be overcome with correspondingly high initial pressures, but this would increase the mass of the pressurising system. There is also a strong thermodynamic motivation for operating at lower pressures; the boiling point of lithium is considerably reduced at low pressures, allowing a lower operating temperature and thus wall temperature of the structural material. While the total enthalpy absorbed by the coolant will be reduced at lower operating temperatures, this loss is not significant as about 70-80% of lithium's storage capability comes from the vaporisation process. As can be seen in Figure 124, lithium's heat of vaporisation increases at lower pressures, largely compensating for the reduced temperature change.

To minimise the system operating pressure a jet impingement strategy was selected rather than a cooling jacket style solution.

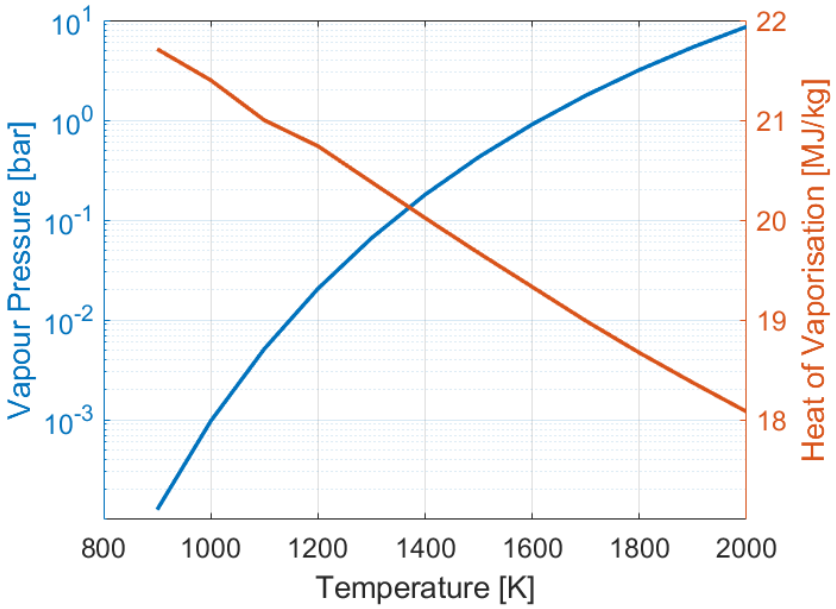

Figure 124 - Vapour pressure and heat of vaporisation of lithium vs temperature. Data from [100].

8.5.3.3 Jet Impingement Cooling

Jet impingement is a cooling technique in which a fluid is accelerated and impacted upon a target surface. Figure 125 illustrates some typical configurations. Very thin boundary layers on the order of microns can be achieved near the stagnation region, enabling heat transfer coefficients on the order of 100's of kW/m^2K and the removal of heat fluxes of several 100's of MW/m^2 [1]. Most relevantly for the present work, a thin layer of fluid can be delivered efficiently to large target surfaces by combining many jets into arrays and/or manifolds.

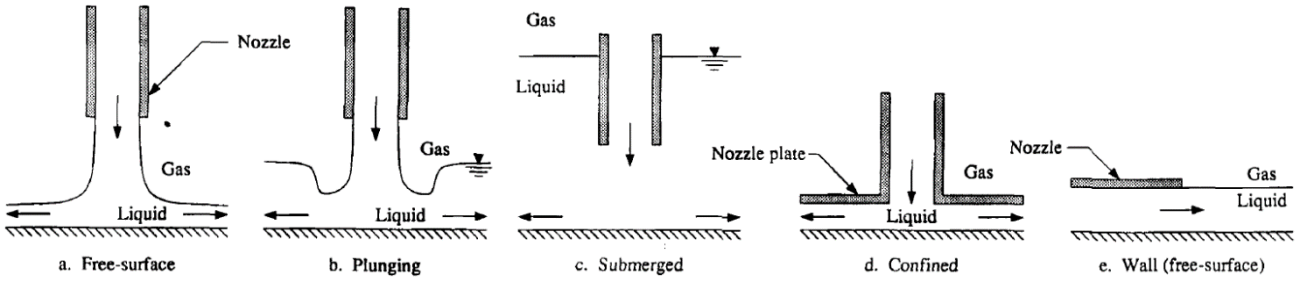

Figure 125 – Different impinging jet configurations. Adapted from [101].

Jet impingement cooling is complex to analyse. The flow and heat transfer properties vary spatially around the jet impingement zones. The impingement region can be delineated into stagnation, acceleration, and parallel-flow regions, as illustrated in Figure 126. Also shown are the general variation of static pressure and flow velocity around the impingement zone. It is important to note that the local boiling temperature will vary with the local pressure throughout the jet impingement zone. The heat transfer benefits of an impinging jet are largely concentrated in the stagnation and acceleration zones, decaying to the typical transfer properties of external flat-plate flows in the parallel-flow region [101]. The flows from closely space jets can interact with each other and form fountain regions, as illustrated in Figure 130, further complicating the analysis.

The majority of jet impingement research thus far has been conducted with water and other molecular coolants. Such fluids often require fluid velocities on the order of 10's to 100's of metres per second in order to remove the high heat fluxes mentioned previously [102]. Recent work by Silverman et al. [102] has investigated the use

of liquid metals for jet impingement cooling. Compared to molecular fluids, liquid metals typically have much higher thermal conductivities and lower viscosities, resulting in more efficient heat transfer and lower jet speeds. A lower jet speed in turn implies a lower upstream system pressure, and thus lower system mass.

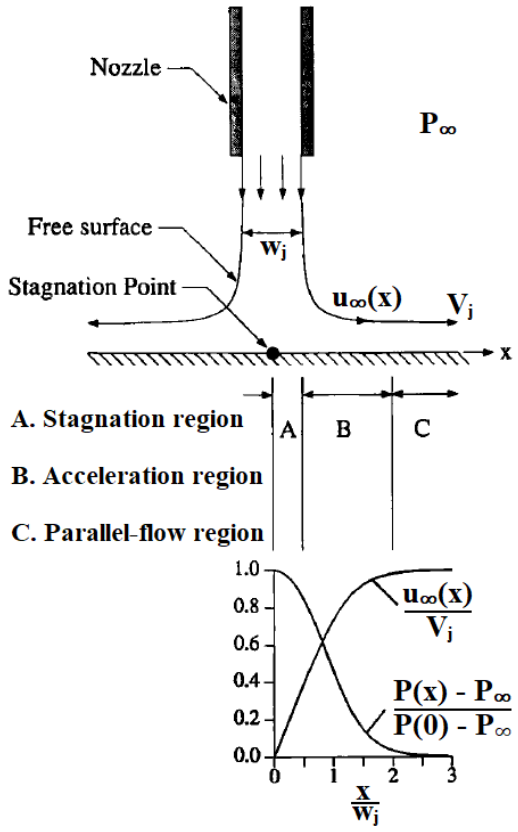

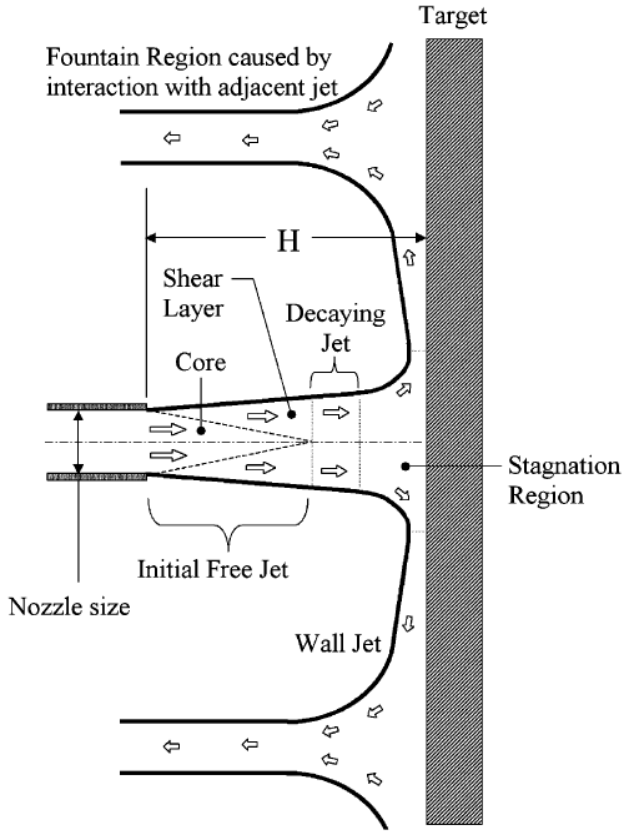

Figure 126 (Left) –Typical flow regions and pressure-velocity variations near an impingement jet. Adapted from [101].
Figure 127 (Right) – Additional reference regions in the jet flow, and interaction fountains. Adapted from [103]

As the experiments of Silverman et al are the most similar to the AGA vehicle requirements, their analysis methods will be used here. It should be noted that the purpose of the present work is not to conduct a detailed analysis and design on a jet-impingement system. The remainder of this work will investigate the high-level feasibility of such a system and leave a more thorough analysis to later work.

Equations 53 through 55 detail the key parameters outlined in [102] for analytical estimation of the heat transfer properties of single-phase jet impingement cooling with a liquid metal. Table 26 details a sample calculation of the heat transfer coefficient by Silverman et al. It is important to note that Equation 55 predicts the heat transfer coefficient at the stagnation point of the jet.

$$Re = \frac{\rho V_0 d}{\mu} \tag{53}$$

$$Nu = \sqrt{\frac{2}{\pi}}\, Re^{1/2}\, Pr^{1/2} \sqrt{\frac{d}{H}} \tag{54}$$

$$h = \sqrt{\frac{2}{\pi}}\, k \sqrt{\frac{V_0}{H\kappa}} \tag{55}$$

Figure 128 illustrates typical variations of the Nusselt number, and thus heat transfer coefficient, for varying jet H/D ratios. Large H/D jets are fully penetrated by the shear layer and thus turbulent, as is the case in Figure

127, resulting in a high heat transfer peak in the stagnation zone. Low H/D jets are typically laminar in the stagnation region, and it is thought that the secondary heat transfer peak is associated with the transition from laminar to turbulent flow [104].

Liquid Metal	77% Gallium, 23% Indium	
Melting Temperature	15.7	°C
Boiling Temperature	2000	°C
Viscosity	1.69×10^{-3}	kg/m.s
Prandtl Number	0.02	
Thermal Conductivity	41.8	W/m.K
Thermal Diffusivity	1.32×10^{-5}	m^2/s
Nozzle Diameter	5	mm
Nozzle-Target Distance	4	mm
Flow Velocity	3.25	m/s
Calculated Heat Transfer Coefficient	261	$kW/m^2.K$

Table 26 – Sample heat transfer coefficient calculation from Silverman et al. [102].

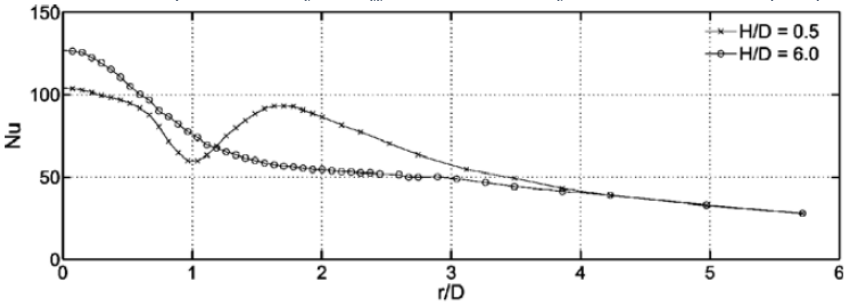

Figure 128 – Radial variation of Nusselt number with varying height: diameter ratios for a Re=30 000 water jet [104].

8.5.3.4 Leading Edge and Nose Cooling

Figure 129 illustrates the proposed solution for active cooling of the leading edge and nose with molten lithium. It can be thought of as an 'evacuated vapour chamber'. The 'cool' side of the leading edge is too hot and too small to condense the vapour and radiatively reject the absorbed latent heat, as would occur in a true vapour chamber. Instead, the vapourised coolant is simply vented, and fresh propellant supplied via an array of jets on a manifold. The system would be pressure fed for simplicity, with the lithium kept molten via waste heat from an RTG power source.

Something like 20 chambers of 500mm length could be used on each leading edge. Compressible graphite spacers could be installed between the chambers in order to relieve thermal expansion strains, as suggested in [1]. It is not clear if venting the lithium vapour along the upper surface of the vehicle is acceptable. Lithium condensation on the surface, erosion from condensed lithium in the free stream, chemical reactions between lithium and oxygen and/or nitrogen, as well as tripping the boundary layer into turbulence are potential problems which would require further evaluation. It may be more beneficial to vent onto the compression side where the compressed gas temperature is above the boiling point of lithium, and the lithium film could reduce downstream heat fluxes and skin friction. If this direct venting proves unacceptable, the individual chamber vents could be collected into an exhaust manifold which then vents out the rear of the vehicle.

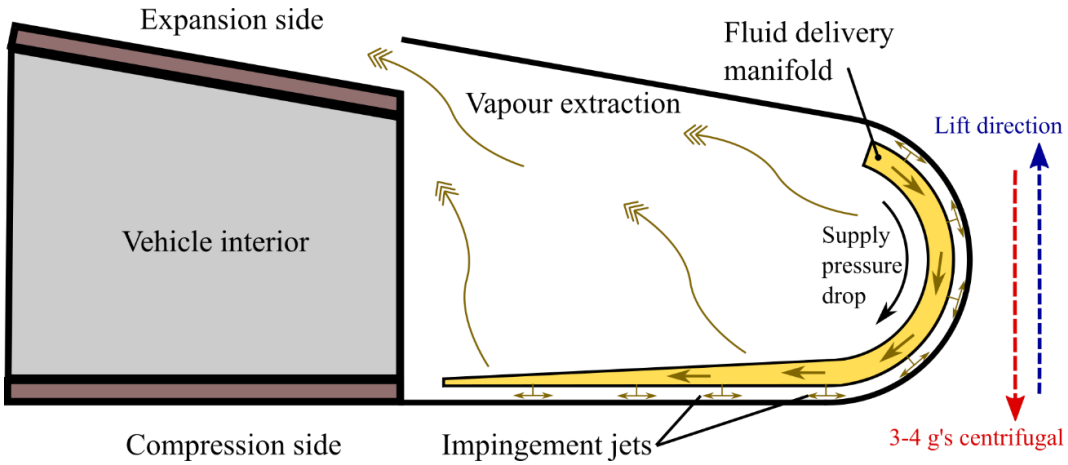

Figure 129 – Cross section schematic of the nose and leading-edge evaporator concept.

It is thought that such a system would be relatively tolerant of small impact damage from micrometeoroids. Figure 130 shows the envisioned operation of the leading-edge chamber after a micrometeoroid impact. Unlike cooling jacket solutions, the outer surface of the chamber does not contain any cooling passages, which are susceptible to blockages upon impacts and deformation. The internal manifold passageways cover a relatively small fraction of the cross-sectional area, providing only a small target, as illustrated in Figure 131.

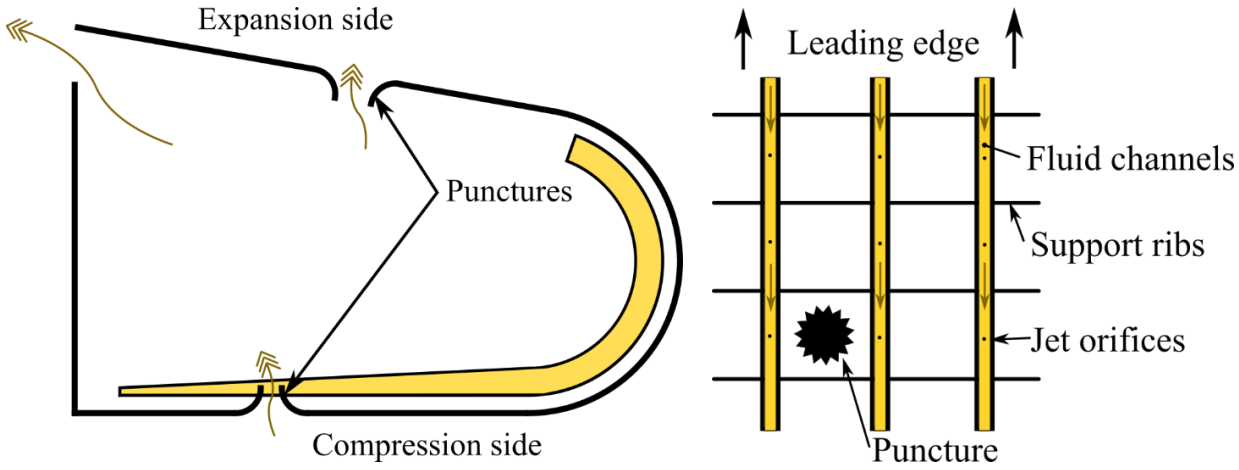

Figure 130 (Left) – Cross section schematic of possible gas and vapour flow when punctures are present.
Figure 131 (Right) – Top view of manifold showing the relatively low probability of an impact damaging fluid lines.

Any high temperature gases leaking into the chamber will be cooled by the lithium vapours inside before being exhausted together. There would likely be exothermic reactions between the lithium vapours and oxygen and/or nitrogen present in the atmospheric gases and the severity of such reactions would require careful consideration.

The molybdenum alloy TZM was selected for the chamber walls. TZM contains 0.5% titanium, 0.08% zirconium, and 0.02% carbon, with the balance being molybdenum. Molybdenum is a refractory metal often used in high temperature applications. In particular, it is compatible with lithium and has been employed in lithium heat pipes previously [53]. As can be seen from Figure 132 and Figure 133, TZM has much greater high temperature strength properties than pure molybdenum whilst still retaining good thermal conductivity. Molybdenum rapidly oxidises at temperatures above about 800°C. As some oxygen content is expected at the nose and leading edges, an oxidisation resistant coating is needed. Vapour-deposited molybdenum disilicide coatings with small additions of iron or chromium have been successfully tested for several days at 1450°C [105]. A chromium-nickel-chromium coating has been successfully tested for short durations of about 30 minutes at 1480°C [106]. Detailed consideration of coatings is outside the scope of this work, but it should be noted that on an AGA trajectory the peak heating scenario will occur for a few minutes at most.

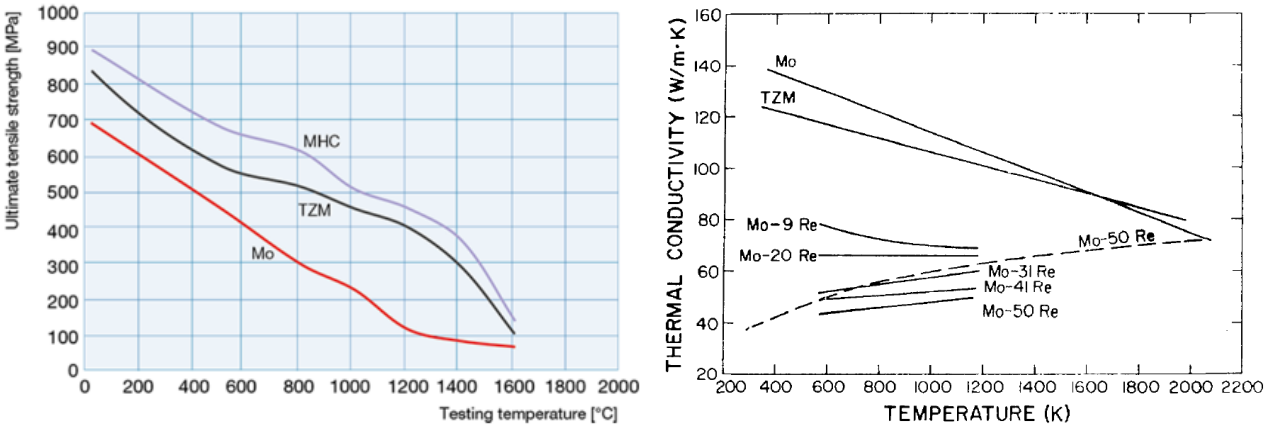

Figure 132 (Left) – Ultimate strength vs temperature for pure molybdenum, TZM, and molybdenum-hafnium-carbide [107].
Figure 133 (Right) – Thermal conductivity vs temperature for various molybdenum alloys [108].

The cold-wall thermal flux profiles of the nose and leading edge were evaluated according to the scheme illustrated in Figure 134. The results of these evaluations are shown in Figure 135 and Figure 136. It should be noted that the profiles are taken along the vehicle's longitudinal axis while the axis of the leading-edge radius is swept-back. This longitudinal section then produces an elliptical section which continues several nominal leading-edge radii down the length of the profile. Both the leading edge and nose profiles have the same flux profiles away from the initial radius, with the nose featuring a much larger peak flux than the leading edges. For simplicity, the average flux across each region was evaluated and only these cases were designed for.

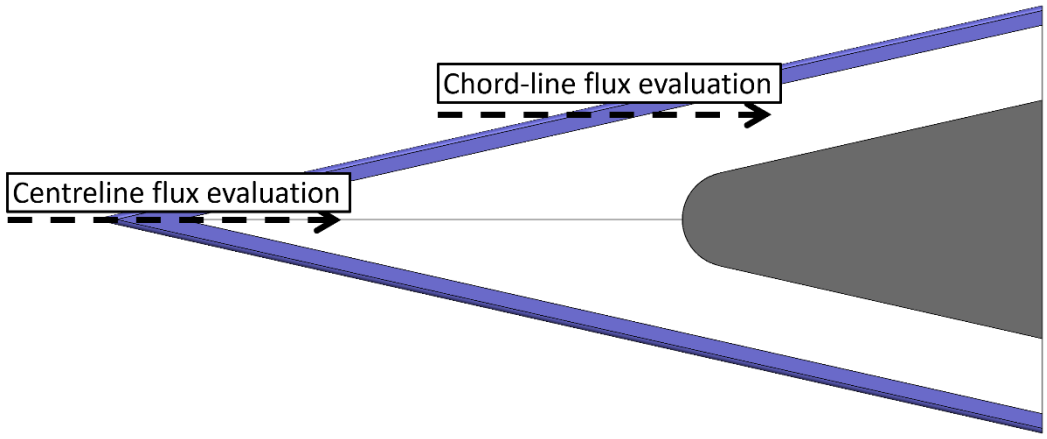

Figure 134 – Schematic of leading edge and nose flux profile evaluations.

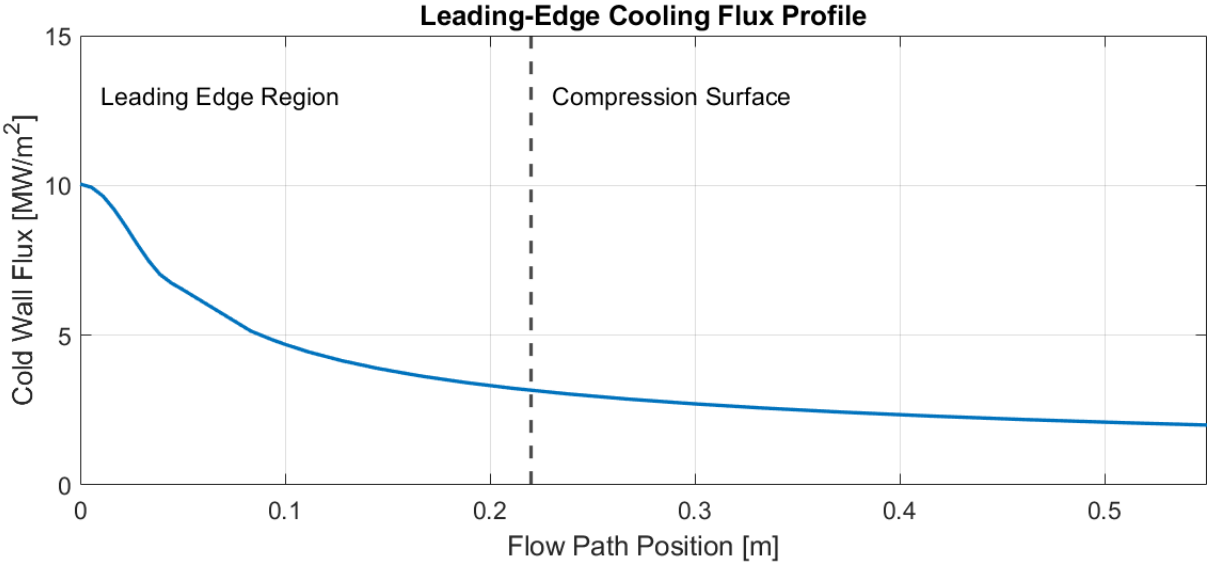

Figure 135 – Cold-wall thermal flux profile along an average chord section.

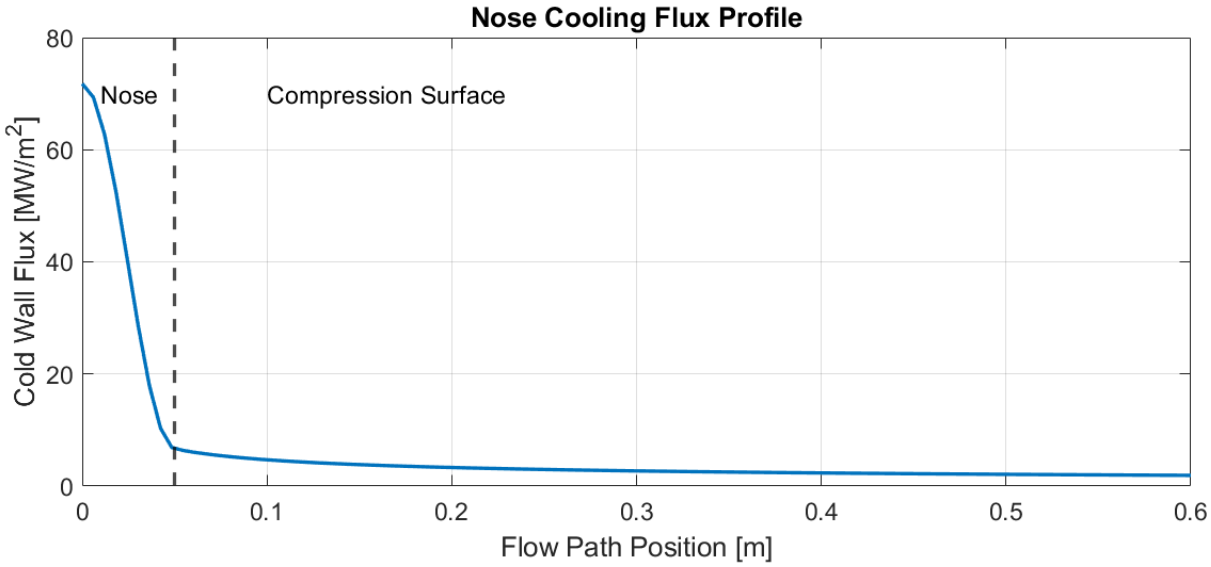

Figure 136 – Cold-wall thermal flux profile along the vehicle centrline.

A chamber static pressure target of similar magnitude to the leading-edge static pressure was selected in order to reduce any potential gas exchange at a puncture. The pressure differential across a puncture on the expansion side would cause a lithium vapour stream to flow outwards from the chamber. A pressure differential across a puncture near the nose stagnation point or leading edges tips would cause an in-flow of gas from the external environment. Table 27 details the calculated pressure levels at key locations on the vehicle, as well as the chamber target operational pressure and temperature.

Nose Stagnation Pressure	233	kPa
Leading Edge Pressure	12.8	
Compression Surface Pressure	4.3	
Expansion Surface Pressure	0.5	
Chamber Static Pressure Target	10	
Lithium Boiling Temperature at Chamber Pressure	1330	K
	1057	°C

Table 27 – Static pressure at key points of the vehicle at the beginning of the atmospheric cruise.

Compatibility between the mass flow rate requirement and the target chamber static pressure can be enforced by consideration of the exit area. Excluding super-sonic cases, the lowest static pressure for a given mass flow rate at a given total pressure occurs when the flow is sonic. If it is assumed that the chamber static pressure target is measured at the chamber exit, and that the flow is sonic at the exit, the required total pressure can be calculated by rearranging Equation 56 [74].

$$\frac{P^*}{P_0} = \left(\frac{2}{\gamma+1}\right)^{\frac{\gamma}{\gamma-1}} \tag{56}$$

Taking 1.45 as the ratio of specific heats for lithium vapour at 1320 K, the required total pressure is approximately 0.19 bar, or 19 kPa. Now Equation 57 [11] can be employed to calculate the required chamber exit area. As the combined vent will run the entire length of the leading edge, a unit span and the mass flow rate per unit length of the leading edge from Table 25 will be used to evaluate the required vent height.

$$\dot{m} = \frac{A_t v}{a} = A_t \frac{P_0\,\gamma\sqrt{\left(\frac{2}{\gamma+1}\right)^{\frac{\gamma+1}{\gamma-1}}}}{\sqrt{\gamma R_M T_0}} \tag{57}$$

The resulting vent height comes out at about 18 mm. The vent height can be varied by changing the operating temperature and pressure of the chamber. Assuming negligible superheating of the vapour, the operating pressure and temperature are linked through the vapour pressure curve of lithium shown previously.

The final step of the pressure analysis is to determine the jet velocities and system pressure, ensuring that they are compatible with each other as well as the chamber operating pressure. This analysis is coupled with the heat transfer coefficient estimation.

The different regions called out in Figure 135 and Figure 136 were integrated to provide average flux design cases. Average areal mass flow rates for each region could then be calculated from these average fluxes and the updated enthalpy capacity of the lithium coolant. The values are provided at the top of Table 29.

Selection of the orifice sizing, orifice spacing, and jet velocity is then a matter of balancing the competing mass flow and heat transfer requirements. As can be seen from Equation 55, high jet velocities produce higher heat transfer coefficients at the impingement point. However, high jet velocities also imply a high mass flow rate per orifice, and thus a sparse distribution of jets when the areal mass flow rate is small.

An orifice size at the smaller end of typical liquid rocket engine injector diameters [11] was selected in order to keep the spacing between orifices small, with the goal of preventing dry-out. Jet velocities as low as possible were selected to further reduce the orifice spacing. As can be seen from the results in Table 29, the orifice spacing-to-diameter ratio is still quite large. Further work would be needed to decide if this is acceptable. An immediate solution to reduce the orifice spacing would be to increase the coolant load and thus allowable mass flow rates. The large orifice spacing does however suggest that Equation 55 for non-interacting jets is valid. The orifice: stand-off distance ratio was kept within a range of 2-8, as this often provides optimal performance [103].

The fresh fluid exiting the jet is significantly sub-cooled with respect to the boiling point. It would likely enter at a temperature slightly above the melting point of lithium, which is about 450 K. A value of 500 K was assumed in the analysis. Boiling of the fluid will not occur for some small distance from the stagnation point. For illustrative purposes, ‘boiling transition radii’ were calculated by finding the area around the stagnation point required to heat the given mass flow rate from 500 to 1330 K with a constant wall flux.

A crude estimate of the heat transfer coefficient in the parallel flow region was calculated using the Nusselt number correlation for low Prandtl number fluids flowing over a flat plate, repeated here as Equation 58 [109]. Equation 58 is intended for use with single-phase laminar flows, but previous works [110] have argued that laminar flow correlations should hold for turbulent flow in liquid metals due to their low Prandtl numbers. In any case, the increase in the heat transfer coefficient when phase change effects are included would likely outweigh any laminar-turbulence differences. The local length was calculated as the radial distance from the stagnation point. For simplicity, the Reynolds number was calculated with the nominal nozzle exit velocity. In reality there will be a favourable pressure gradient in the chamber acting to accelerate the fluid film along the wall and viscous effects at the wall acting to slow it.

$$Nu_x = \frac{h_x x}{k} = 0.565\ (Re_x Pr)^{\frac{1}{2}} \qquad 58$$

Huge increases in the heat transfer rate can occur during boiling as the mechanism of heat transport changes. Figure 137 is a typical Nukiyama curve for pool-boiling of water which illustrates the order of magnitude heat flux increases that are possible.

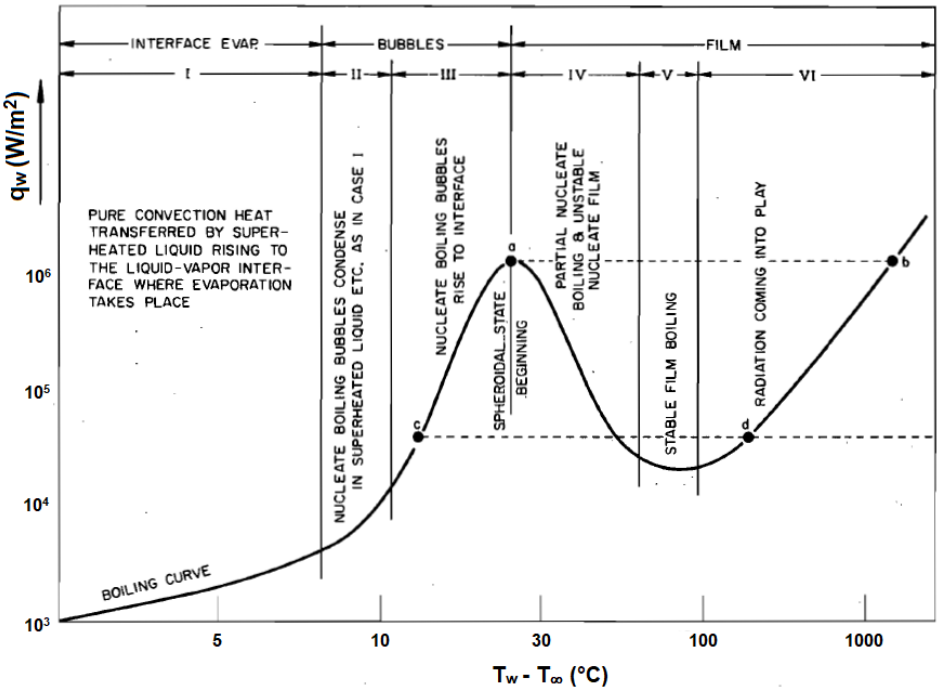

Figure 137 – Nukiyama curve for pool boiling of water at 1 bar. Adapted from [111]

The difference in properties between molecular fluids like water and liquid metals results in quite different boiling behaviour, with liquid metals typically requiring much greater superheats for bubble formation to occur. Table 28 presents the key properties of water, sodium, and lithium.

	Water	Sodium	Lithium	
Molecular Mass	18	23	6.9	g/mol
Boiling Point	373	1151	1615	K
Specific Vapour Volume	1.67	3.78	18.3	m^3/kg
Liquid Density	958	743	401	kg/m^3
Latent Heat of Vaporisation	2256	3742	19330	J/kg
Thermal Conductivity	0.68	52.1	68.5	W/m.K
Surface Tension	0.063	0.112	0.238	N/m
Normalised Superheat for Bubble Formation	1	8	21	

Table 28 – Boiling point properties of selected fluids at 1 bar pressure [111] [112] [100].

Also presented in the final row is a calculation of the wall superheat required for equilibrium bubble formation, relative to the superheat required by water. This was calculated via Equation 59 [111] for an arbitrary bubble radius, as only the ratios between fluids were of interest here.

$$T_v - T_{sat} = \frac{2\,R_M\,T_{sat}^2\,\sigma}{h_{vap}\,r\,P} \qquad 59$$

Clearly lithium would require a superheat in the order of 100's of K to initiate stage III nucleate boiling, illustrated in Figure 137, increasing the chamber wall operating temperature significantly. This suggests that highest flux areas of the chamber should supplied with an excess of sub-cooled, non-boiling fluid. The evaporation and/or boiling could happen downstream at lower flux regions where the wall temperature gradient is reduced and there is more margin for wall superheat.

Given the much greater thermal conductivities of liquid metals, the difference between the convective and boiling heat transfer rates is not as great as it is for low conductivity fluids such as water [111]. Figure 138 provides an illustration of the difference in the boiling: convective heat transfer ratio of water and potassium.

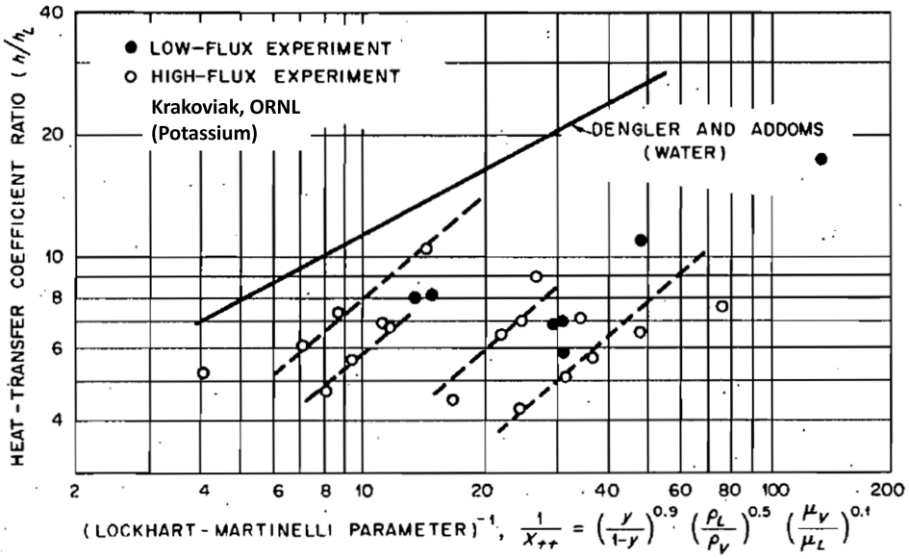

Figure 138 – Boiling: convective heat transfer ratio of water and potassium at various liquid/vapour fractions [111].

All this has been to say that the heat transfer rate predicted by Equation 58 is likely low by a factor of something like 5 if vaporisation is occurring. However, relatively large wall superheats will still be required if the high heat fluxes of stage III nucleate boiling are required. Given the high single-phase heat transfer coefficients of liquid metals and the thin fluid layers in this application it is conceivable that the parallel flow regions of the chamber may operate nominally under stage I or II boiling conditions. It is worth recalling Figure 123 which shows the increasing heat transfer performance of lithium undergoing stage I boiling as the wicking layer thickness is reduced.

Given the lack of external flow boiling correlations for liquid metals, no further attempt has been made to estimate the boiling heat transfer coefficient. More detailed modelling and/or experiments would be needed to develop this idea further. Table 29 presents the results from the discussed calculations thus far.

	Acreage Panels	Leading Edge	Nose	
Design Thermal Flux (Region Averages)	2.4	5.0	39	MW/m^2
Updated Lithium Enthalpy Storage	24.3			MJ/kg
Required Areal Mass Flow Rate	99	208	1610	$g/(m^2.s)$
Orifice Diameter	0.5	0.5	0.5	mm
Orifice Discharge Coefficient	0.6	0.6	0.6	
Jet Velocity	0.3	0.7	5.0	m/s
Jet Dynamic Pressure	0.05	0.25	13	kPa
Mass Flow Rate Per Orifice	0.019	0.045	0.32	g/s
Orifices Per Square Metre	5110	4600	4990	
Orifice Spacing (Pitch)	14	15	14	mm
Boiling Transition Radius	3	3.2	3	mm
Orifice-Target Stand-Off Distance	2	2	1	mm
Single-Phase Heat Transfer Coefficient, Stagnation Point	99	151	570	kW/m^2K
Single-Phase Heat Transfer Coefficient, Boiling Transition Radius	60	89	243	kW/m^2K
Single-Phase Heat Transfer Coefficient, ½ Orifice Pitch	39	58	159	kW/m^2K
Assumed Fluid Supply Temperature	500			K
Stagnation Point Wall Superheat (T_w - T_∞)	24	33	68	K

Table 29 – Summary of orifice sizing and heat transfer rate calculations.

The final step is to consider the temperature profile within the chamber wall. A given heat flux in a material with a given thermal conductivity implies a certain temperature drop per unit length, as detailed earlier in Equation 53. To reduce the temperature differential and thus maximum temperature in the material, the small wall thicknesses should be selected. Reducing the wall thickness also reduces the thermal stress experienced due to differential thermal expansion. The throat of the Space Shuttle Main Engine, which transferred a heat flux of 160 MW/m^2, had a wall thickness of approximately 0.7 mm [18]. This value was selected for the leading-edge chamber analysis. A representative high-temperature thermal conductivity value of 90 W/mK was chosen for TZM based on Figure 133. At 1700 K TZM still has an ultimate tensile strength of about 300 MPa. The temperature drop in the wall can be combined with the wall superheat and a maximum allowable fluid bulk temperature can be calculated for each region. The single-phase stagnation point wall superheat has been taken as representative of each region. The results of this analysis are presented in Table 30.

	Acreage Panels	Leading Edge	Nose	
Peak Thermal Flux (Reference Only)	4	14	70	MW/m^2
Design Thermal Flux (Region Averages)	2.4	5.0	39	MW/m^2
Thermal conductivity	90			W/m.K
Wall Thickness	0.7			mm
Wall Temperature Differential	19	39	303	K
Stagnation Point Wall Superheat (T_w - T_∞)	24	33	68	K
Maximum Fluid Temperature	1657	1628	1329	K

Table 30 – Wall temperature and maximum fluid temperature calculations.

For the acreage and leading-edge regions, the maximum allowable fluid temperature at the average flux is considerably above the 1330 K boiling temperature of lithium at 0.1 bar, meaning that boiling can safely be allowed to occur. At the nose the average flux causes the maximum allowable fluid temperature to drop below the boiling point, meaning that boiling shouldn't be allowed to occur. The same calculation with the nose peak flux of 70 MW/m^2 produces a maximum fluid temperature of 1030, well below the boiling point. This suggests that the sparsely distributed jet strategy should be reconsidered at the nose. Instead, a large concentration of high-velocity jets should be located at the tip to ensure a large mass flow of sub-cooled fluid in order to prevent the boiling temperature being reached. The residual inertia of the fluid could be used to distribute it to downstream lower flux regions where boiling can then safely occur.

A crude analysis of the thermal stresses was conducted using Equation Figure 49 [51] and high temperature material properties. The results of these calculations are presented in Table 31

$$\sigma_{th} = \frac{E\alpha}{1-v}\Delta T \qquad 60$$

	Acreage Panels	Leading Edge	Nose	
Average Wall Temperature Differential	19	39	303	K
Elastic Modulus at Elevated Temperature [113]	200 - 160			GPa
Coefficient of Thermal Expansion	6			(μm/m)/K
Poisson's Ratio	0.38			
Yield Strength at Elevated Temperature	100 - 400			MPa
Calculated Thermal Stress	~30	~60	~470	MPa

Table 31 – Basic calculation of representative thermal stresses in chamber walls.

It would appear the average thermal stresses in the acreage and leading-edge regions are manageable. Since the TPS will only be cycled two times at most, some yielding may be acceptable. The thermal stress at the nose appears to be unacceptably high, even with just the average flux. As can be seen from Equation 60, the options

available are to choose materials with lower stiffness, lower thermal expansion, or reduce the temperature differential by using thinner walls and more conductive materials. As TZM is already one of the most competitive options, it could be better instead to reduce the thermal flux via film or transpiration cooling, possibly with lithium liquid or vapour. A final option would be to instead use a much lower operating temperature fluid at the nose, such as liquid hydrogen, in order to bring the material temperature low enough to take advantage of TZM's high strength at low-to-moderate temperatures.

Figure 139 provides a low fidelity conceptual illustration of the discussed leading edge concept.

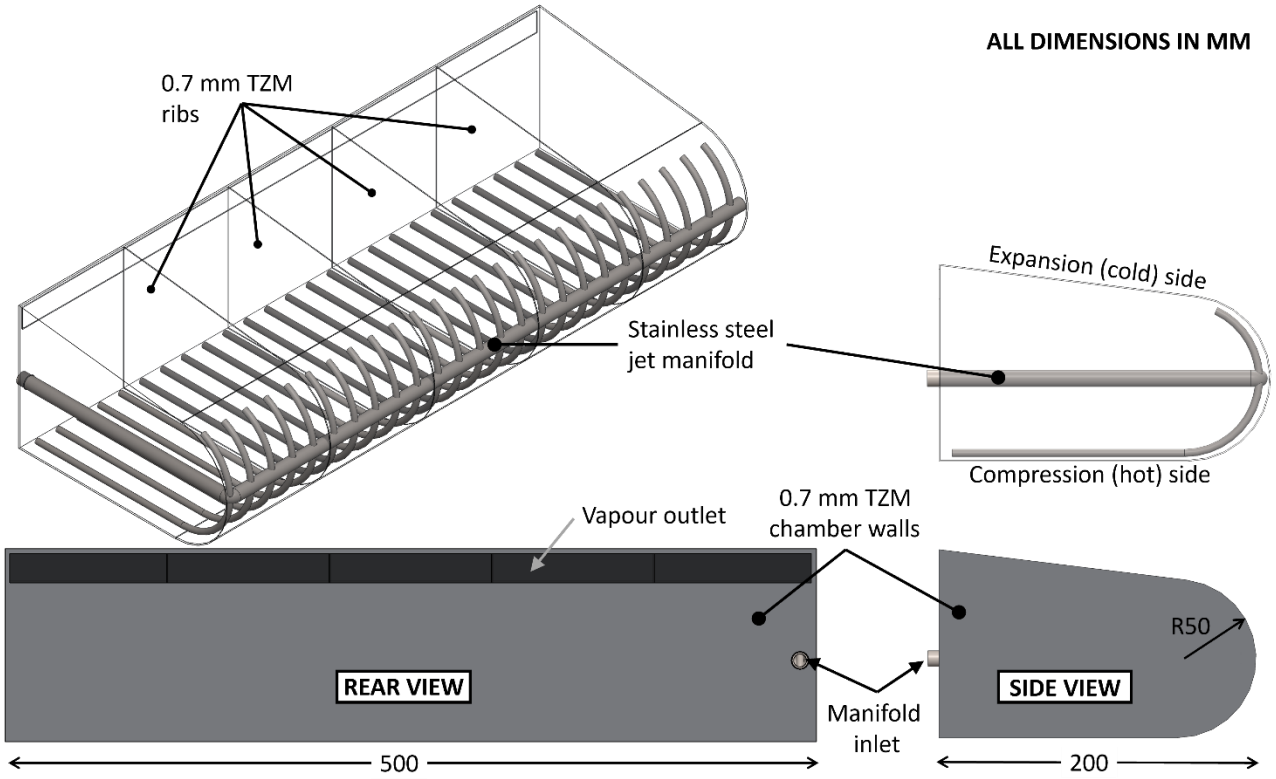

Figure 139 – Low fidelity CAD model of the leading-edge chamber concept for coarse mass estimation.

A key advantage of this lithium leading-edge cooling concept is the low operating pressure. It is estimated that only 1-2 bar of tank pressure would be sufficient to drive the system

8.6 TPS Summary and Discussion

Table 32 summarises the estimated mass and volume of each of the TPS components. The system mass, volume, and power demands are discussed individually in the following sub-sections. It is believed that relatively conservative estimates have been made in most areas, leaving room for mass reductions. It is also important to note the key components which have not been considered:

- Hardware for mounting and connecting TPS components internally.
- Hardware for connecting the TPS to the vehicle structure.
- The vehicle internal structure connecting the upper and lower skins of the aeroshell to each other and to the payload bay.
- Aerodynamic control surfaces.

All of the spacecraft core systems such as attitude control, communications, power etc. are accounted for in the 'payload'. In this way, the payload mass of the AGA vehicle can be directly compared with the dry masses of the reference vehicles from Table 8.

	Area	Areal Density	Length	Linear Density	Thickness	Mass	Volume
	[m^2]	[kg/m^2]	[m]	[kg/m]	[mm]	[kg]	[m^3]
TPS SURFACE COMPONENTS							
Insulative, compression side	6.2	7.1	-	-	24	53.3	0.15
Insulative, expansion side	7	6.6	-	-	18	60.2	0.13
Pass-through skin, compression side	12.4	5.6	-	-	3	69.4	0.04
Pass-through skin, suction side	17.8	5.6	-	-	3	99.7	0.05
Pass-through, hollow region	-	-	-	-	-	-	3.03
Actively cooled leading edges	4.1	-	20.5	8	100	164.0	0.41
Vehicle base	3.3	3.8	-	-	3	12.5	0.01
TOTAL						**459.1**	**3.82**
TPS FLUIDS AND TANKGAGE							
Lithium	-	-	-	-	-	196.0	-
Lithium tank (2 bar, molybdenum)	-	-	-	-	-	10.0	0.40
Lithium delivery manifold (molybdenum)	-	-	-	-	-	20.0	-
Helium	-	-	-	-	-	0.2	-
Helium tank (20 bar, composite)	-	-	-	-	-	5.0	0.04
TOTAL						**231.2**	**0.44**
OTHER VEHICLE SYSTEMS							
Gridded ion thruster assembly	-	-	-	-	-	70.0	-
Vehicle Core Systems and Payload	-	-	-	-	-	1500.0	5.00
TOTAL						**1570.0**	**5.00**
TPS TOTALS						**690.3**	**4.26**
VEHICLE TOTALS						**2260.3**	**9.26**

Table 32 –Estimated mass and volume properties of the TPS and AGA-EP vehicle.

8.6.1 Mass

It appears that the core system mass delivered to Uranus could be competitive with that of the reference studies. More work is needed, particularly on the vehicle structure and aerodynamic effects on the structure, to give a definitive answer. The preliminary analysis of an interplanetary AGA waverider by Randolph et al [95] estimated that the TPS and vehicle structure together would comprise about 50% of the vehicle total mass. The results of the present TPS analysis would appear consistent with these values , as a TPS mass fraction of about 28% has been predicted without consideration of the internal structure and mounting hardware. The mass breakdown from Randolph et al is provided in Appendix B.

8.6.2 Volume

The volume physically occupied by TPS components is small, about 1.2 m^3 or 13% of the vehicle volume. However, the pass-through cooled sections are required to be relatively hollow, effectively preventing another 33% of the vehicle from being used for other systems. It appears that sufficient volume still remains for a scientific payload.

In contrast to historic hypersonic vehicles, a lithium cooled AGA vehicle needs only about 5% of the vehicle volume for coolant/propellant storage. Former lifting body re-entry vehicles, such as the X-33, experienced significant development problems as odd-shaped structural tanks were required to fit the relatively large

propellant load in the tightly packed vehicle [114]. Only a small spherical tank is needed to meet the lithium storage requirements.

The compact payload bay and its unique shape will no doubt create packaging problems for other vehicle systems. Solar panels are conveniently not very useful for a deep space mission, and so deployable panels can be avoided. Some form of deployable antenna will almost certainly be required if meaningful quantities of data are to be returned to Earth over the long interplanetary distances considered here. Randolph et al proposed using a deployable optical telescope for both scientific and communication purposes. The concept is illustrated in Figure 140.

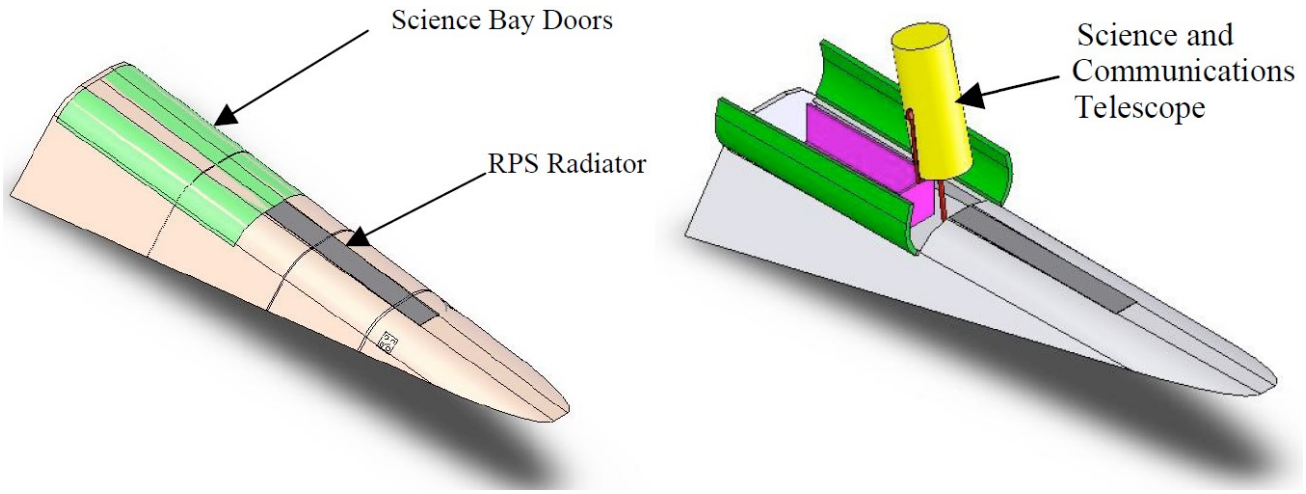

Figure 140 – Deployable optical telescope for scientific observations and long-distance communication with Earth [95].

Multi-function systems like this and the TPS proposed here will likely be typical of AGA waverider vehicles in order to comply with the strict volume requirements.

8.6.3 Power

As the actively cooled portion of the TPS is a pressure-fed blow down system the only power required is that needed for sensors, actuators, and the control system, perhaps on the order of 10's of Watts.

It is hoped that by the time an AGA vehicle could be developed, more efficient thermoelectric conversion technologies such as the Stirling radioisotope generator would have reached maturity. The mass of the nuclear power supply could then be reduced or alternatively, more powerful electric propulsion and communication technologies could be implemented for the same mass power supply.

In any case, it is envisioned that the waste heat from the nuclear power supply would be carried via heat pipes to the base of the vehicle for radiative rejection into deep space. A secondary heat pipe could be routed to an insulated lithium tank in order to keep the lithium molten. Once the lithium tank is depleted this second heat pipe would cease to function and the entire heat load would be rejected via the primary heat pipes.

9 Conclusion

In this work the Thermal Aerogravity Assist (TAGA) concept developed previously in the literature was introduced. Taking inspiration from this concept, additional endothermic processes on which multi-function thermal protection systems could be based were explored. As a result of this analysis, the AGA-EP concept was proposed, in which the lithium coolant would be used for electric propulsion (EP) in deep space after the AGA flyby rather than during the atmospheric flight as is the case for a TAGA.

An interplanetary mission featuring a Mars AGA similar to the original TAGA paper was developed. Two versions of the trajectory were created, one for the TAGA mission with a higher efficiency flyby due to its in-flight propulsion, and one for the AGA-EP mission with a lower efficiency flyby but higher efficiency propulsion in deep space.

A detailed sensitivity analysis of the atmospheric flight phase of an AGA mission was conducted in order to select a suitable baseline vehicle geometry. The coupled nature of the sensitivity analysis provided new insights into the trade-offs involved when designing an AGA mission. A vehicle geometry was selected which balanced aerodynamic performance, thermal fluxes, total heat load, and vehicle mass. An energy imbalance was found in the TAGA mission between the propulsion and thermal requirements for the coolant. Solutions to this problem were explored but were judged to be unsuitable for the present mission, and so the TAGA concept was disregarded for this mission.

Engineering correlations, 1D thermal analyses, and case studies were used to size a thermal protection system (TPS) for the AGA-EP vehicle. The TPS uses a mixture of passive and active cooling strategies. A carbon-carbon aeroshell provides the external structure and passive thermal protection for the majority of the vehicle, while an active cooling system based on jet-impingement and vaporisation of lithium is used at the leading edges and nose. The performance of this system appears satisfactory at everywhere except the nose-tip.

A first-pass estimate of the TPS mass and volume was completed, with the results appearing positive enough to justify further investigation. The payload mass that could be delivered to Uranus appears to be competitive with comparable case studies of missions to Uranus with ‘traditional’ non-atmospheric spacecraft. A strong advantage of the AGA-EP concept over the traditional missions is that a gravity-assist at Jupiter is not required, increasing the launch window frequency from about once every 12-13 years to once every 2-3 years.

The envisioned next step in exploring the feasibility of an AGA mission would be a multi-disciplinary analysis by a small team spanning all the key subsystems. Of particular interest would be:

- A more accurate analysis of the vehicle structure, with a focus on transient aerodynamics, aeroacoustics, and combined thermal and structural loads, and with the goal of providing a more accurate structural mass estimate.
- More accurate aerothermal analyses of the aeroshell, with a focus on validating or invalidating the assumptions made here regarding operating temperature, oxidation, emissivity etc.
- A solution for the nose mechanical/thermal problems found in the present work.
- Application of optimisation methods to the mission design and sensitivity analyses introduced in this work, with the goal of minimising the aerodynamic and thermal loads.
- Detailed consideration of AGA waverider mass and volume constraints on the communication system and scientific payload.

Additional steps which would be required to advance the AGA-EP concept in particular are:

- Prototyping and testing of a lithium jet-impingement cooling system.
- Continued development of a lithium-fuelled gridded ion thruster.

References

[1] D. Murakami, “Combined Thermal Protection and Thermal Propulsion for Aerogravity Assist Missions,” Stanford University, 2016.

[2] A. McRonald and J. Randolph, “Hypersonic Maneuvering to Proivde Planetary Gravity Assist,” AIAA Paper 90-0539, 1990.

[3] A. McRonald and J. Randolph, “Hypersonic Maneuvering for Augmenting Planetary Gravity Assist,” *Journal of Spacecraft and Rockets,* vol. 29, no. 2, pp. 216-222, 1992.

[4] A. Bowers, D. Banks, Randolph and J, “Hypersonic Interplanetary Flight: Aero Gravity Assist,” NASA Jet Propulsion Laboratory, 2006.

[5] F. Lohar, A. Misra and D. Mateescu, “Optimal Aero-Gravity Assist with Heliocentric Plane Change,” *Acta Astronautica,* vol. 4, no. 8, pp. 445-456, 2996.

[6] J. Sims, J. Longuski and M. Patel, “Aerogravity-Assist Trajectories to the Outer Planets and the Effect of Drag,” *Journal of Spacecraft and Rockets,* vol. 31, no. 1, pp. 49-55, 2000.

[7] M. Lewis and A. McRonald, “Design of Hypersonic Waveriders for Aeroassisted Interplanetary Trajectories,” *Journal of Spacecraft and Rockets,* vol. 29, no. 5, pp. 653-660, 1992.

[8] J. Anderson, M. Lewis and A. Kothari, “Hypersonic Waveriders for Planetary Atmospheres,” *Journal of Spacecraft,* vol. 28, no. 4, pp. 401 - 410, 1991.

[9] K. Bowcutt, J. Anderson and D. Capriotti, “Viscous Optimized Waveriders,” in *AIAA 25th Aerospace Sciences Meeting*, 1987.

[10] J. Anderson, Hypersonic and High Temperature Gas Dynamics, American Institute of Aeronautics and Astronautics, 2006.

[11] G. Sutton and O. Biblarz, Rocket Propusion Elements, 9th Ed., John Wiley & Sons, 2017.

[12] The Planetary Society, “What is Solar Sailing?,” 2021. [Online]. Available: https://www.planetary.org/articles/what-is-solar-sailing. [Accessed 08 12 2021].

[13] J. Prussing and B. Conway, Orbital Mechanics, Oxford University Press, 1993.

[14] H. Curtis, Orbital Mechanics for Engineering Students, Elsevier Ltd., 2014.

[15] R. Armellin, M. Lavagna, R. Starkey and M. Lewis, “Aero-Gravity Assist Maneuvers: Coupled Trajectory and Vehicle Shape Optimisation,” in *AIAA/AAS Astrodynamics Specialist Conference and Exhibit*, Keystone, USA, 2006.

[16] M. Tauber, “A Review of High-Speed Convective, Heat Transfer Computation Methods,” NASA, 1989.

[17] S. Whitmore, “MAE 5420 Course Notes, Appendix to Section 3,” 2021. [Online]. Available: http://mae-nas.eng.usu.edu/MAE_5420_Web/MAE_5420_2020.html. [Accessed 28 10 2021].

[18] R. Cook and G. Coffey, “Space Shuttle Orbiter Engine Main Combustion Chamber Cooling and Life,” in *AIAA/SAE 9th Propulsion Conference*, Las Vegas, 1973.

[19] N. Strange and J. Longuski, “Graphical Method for Gravity-Assist Trajectory Design,” *Journal of Spacecraft and Rockets,* vol. 39, no. 1, pp. 9-16, 2002.

[20] D. Sangra, E. Fantion, R. Flores, O. Lozano and C. Estelrich, “An Automatic Tree Search Algorithm for the Tisserand Graph,” *Alexadria Engineering Journal,* 2020.

[21] D. Williams, “Planetary Fact Sheet - Metric,” NASA Goddard Space Flight Centre, 09 10 2019. [Online]. Available: https://nssdc.gsfc.nasa.gov/planetary/factsheet/. [Accessed 07 12 2021].

[22] Kuchemann, The Aerodynamic Design of Aircraft, Oxford: Pergamon, 1978.

[23] K. G. Bowcutt, J. Anderson and D. Capriotti, “Numerical Optimization of Conical Flow Waveriders Including Detailed Viscous Effects,” in *Advisory Group for Aerospace Research and Development Conference*, 1987.

[24] United Launch Alliance, “Atlas V Launch Services User's Guide,” 2010.

[25] J. Acton, “Hypersonic Boost-Glide Weapons,” *Science & Global Security,* vol. 23, no. 3, pp. 191-219, 2015.

[26] Defence Advanced Research Projects Agency (DARPA), “Falcon HTV-2,” [Online]. Available: https://www.darpa.mil/about-us/timeline/falcon-htv-2. [Accessed 13 11 2021].

[27] D. Wright, “Research Note to Hypersonic Boost-Glide Weaspons by James M. Acton: Analysis of the Boost Phase of the HTV-2 Hypersonic Glider Tests,” *Science & Global Security,* vol. 23, pp. 220-229, 2015.

[28] S. Walker and J. Sherk, “The DARPA/AF Falcon Program: The Hypersonic Technology Vehicle #2 (HTV-2) Flight Demonstration Phase,” in *15th AIAA International Space Planes and Hypersonic Systems and Technologies Conference*, Dayton, Ohio, 2008.

[29] P. Erbland, “Falcon HTV-2 (Archived),” DARPA, [Online]. Available: https://www.darpa.mil/program/falcon-htv-2. [Accessed 14 11 2021].

[30] R. Voland, L. Huebner and C. McClinton, “X-43A Hypersonic Vehicle Technology Development,” *Acta Astronautica,* vol. 59, pp. 181-191, 2006.

[31] L. Marshall and G. Corpening, “A Chief Engineer's View of the NASA X-43A Scramjet Flight Test,” in *AIAA/CIRA 13th International Space Planes and Hypersonics Systems and Technologies*, 2005.

[32] C. Ohlhorst, D. Glass, W. Bruce, M. Lindell, W. Vaughn and R. Smith, “Development of X-43A Mach 10 Leading Edges,” NASA Langley Research Centre, 2005.

[33] L. Marshall, C. Bahm, G. Corpening and R. Sherril, “Overview with Results and Lessons Learned of the X-43A Mach 10 Flight,” NASA, 2005.

[34] A. Navo and J. Bergada, “Aerodynamic Study of the NASA X-43A Hypersonic Aircraft,” *Applied Sciences,* vol. 10, no. 8211, 2020.

[35] D. Glass, “Ceramic Matrix Composite Thermal Protection Systems and Hot Structures for Hypersonic Vehicles,” in *15th AIAA Space Planes and Hypersonic Systems and Technologies Conference*, 2008.

[36] W. Ley, K. Wittmann and W. Hallmann, Handbook of Space Technology, John Wiley & Sons, 2009.

[37] E. Hillje, “Entry Aerodynamics at Lunar Return Conditions Obtained from the Flight of Apollo 4,” NASA, Houston, Texas, 1969.

[38] N. Hall, “Space Shuttle as a Glider,” NASA, 13 05 2021. [Online]. Available: https://www.grc.nasa.gov/www/k-12/airplane/glidshuttle.html. [Accessed 29 08 2021].

[39] H. Kelly and M. Blosser, “Active Cooling From the Sixties to NASP,” NASA Langley Research Centre, 1994.

[40] J. Becker, *The X-15 Program in Retrospect.*

[41] “Heatsink Nose,” Air Force Space & Missile Museum, 2021. [Online]. Available: https://afspacemuseum.org/artifacts/heatsink-nose-cone/. [Accessed 01 10 2021].

[42] L. J. Swenson, J. Grimwood and C. Alexander, *This New Ocean: A History of Project Mercury,* 1989.

[43] A. Pirolini, “Materials Used in Space Shuttle Thermal Protection Systems,” AZO Materials, 10 10 2014. [Online]. Available: https://www.azom.com/article.aspx?ArticleID=11443. [Accessed 28 10 2021].

[44] R. Oakes, “Space Shuttle Ceramic Tiles,” University of Washington, [Online]. Available: https://depts.washington.edu/matseed/mse_resources/Webpage/Space%20Shuttle%20Tiles/Space%20Shuttle%20Tiles.htm. [Accessed 28 10 2021].

[45] K. Rivers and D. Glass, “Advances in Hot Structure Development,” NASA Langley Research Centre.

[46] B. Carpenter, “Kelly's Greatest Challenge - The Blackbirds,” 04 2017. [Online]. Available: https://ieeexplore.ieee.org/stamp/stamp.jsp?arnumber=8012052. [Accessed 27 10 2021].

[47] O. Uyanna and H. Najafi, “Thermal protection systems for space vehicles: A review on technology development, current challenges, and future prospects,” *Acta Astronautica,* vol. 176, pp. 341-356, 2020.

[48] M. Favaloro, “Ablative Materials,” in *Kirk-Othmer Encyclopedia of Chemical Technology*, John Wiley & Sons Inc., 2004, pp. 1-8.

[49] H. Hebeler, “Hypersonic Cooling System”. United States Patent 3089318, 14 05 1963.

[50] Advanced Cooling Technologies, “Vapor Chambers Explained,” 2021. [Online]. Available: https://www.1-act.com/resources/heat-pipe-fundamentals/different-types-of-heat-pipes/vapor-chambers/. [Accessed 17 11 2021].

[51] S. Kasen, “Thermal Management at Hypersonic Leading Edges, PhD Thesis,” University of Virginia, 2013.

[52] J. Velardo, R. Singh, A. Date and A. Date, “An Investigation into the Effective Thermal Conductivity of Vapour Chamber Heat Spreaders,” *Energy Procedia,* vol. 110, pp. 256-261, 2017.

[53] D. Paul, C. Clay, B. Harber and H. Croop, “Extreme Environment Structures,” in *Structures Technology for Future Aerospace Systems*, American Institute of Aeronautics and Astronautics, 2000, pp. 145-200.

[54] D. Tenney, W. Lisagor and S. Dixon, “Materials and Structures for Hypersonic Vehicles,” *Journal of Aircraft,* vol. 26, no. 11, pp. 398-415, 1989.

[55] G. Matthews, R. Nygren, T. Morgan, S. Silburn, P. Cooper, R. Otin and A. Tallarigo, “Testing of High Temperature Radiatively Cooled Li/Ta Heat Pipe in Magnum-PSI,” *Fusion Engineering and Design,* vol. 146, 2019.

[56] K. Heufer and H. Olivier, “Film Cooling for Hypersonic Flow Conditions,” in *Thermal Protection Systems and Hot Structures, Proceedings of the 5th European Workshop*, Noordwijk, 2006.

[57] M. Tauber and K. Sutton, “Stagnation-Point Radiative Heating Relations for Earth and Mars Entries,” *Journal of Spacecraft,* vol. 28, no. 1, pp. 40-42, 1990.

[58] Y. Zhu, W. Peng, R. Xu and P. Jiang, “Review on Active Thermal Protection and its Heat Transfer for Airbreathing Hypersonic Vehicles,” *Chinese Journal of Aeronautics,* vol. 31, no. 10, pp. 1929-1953, 2017.

[59] H. Bohrk, “Transpiration-Cooling with Poroous Ceramic Composites in Hypersonic Flow,” NATO - OTAN.

[60] D. Chato and M. Doherty, “NASA Perspectives on Cryo H2 Storage,” NASA Glenn Research Centre, 2011.

[61] J. Brophy, J. Polk and D. Goebel, “Development of a 50,000s Lithium-fueled Gridded Ion Thruster,” in *35th International Electric Propulsion Conference*, Atlanta, USA, 2017.

[62] Pioneer Astronautics, “NASA 1998 SBIR Phase I - Mars In-Situ Based Rocket Propulsion Using Methanol,” Pioneer Astronautics, 1998. [Online]. Available: https://sbir.gsfc.nasa.gov/SBIR/abstracts/98/sbir/phase1/SBIR-98-1-04.03-0890B.html. [Accessed 29 10 2021].

[63] S. Oleson and J. Sankovic, “Benefits of Low-Power Electrothermal Propulsion,” in *1996 Propulsion and Joint Subcommittee Meetings*, 1996.

[64] D. Werner, “Water Propulsion Technologies Picking Up Steam,” SpaceNews, 27 08 2019. [Online]. Available: https://spacenews.com/water-propulsion-technologies-picking-up-steam/. [Accessed 29 10 2021].

[65] T. Bocanegra-Bahamón, C. Bracken, M. Sitjà, Dirkx, G. I. K. Konstantinidis, C. Labrianidis, M. Laneuville, A. Luntzer, J. MacArthur, A. Maier, A. Morschhauser, T. Nordheim, R. Sallantin and R. Tlustos, “MUSE - Mission to the Uranian System: Unveiling the evolution and formation of ice giants,” *Advances in Space Research,* 2015.

[66] C. Elder, A. Bramson, L. Blum, H. Chilton, A. Chopra, C. Chu, A. Das, A. Davis, A. Delgado, J. Fulton, L. Jozwiak, A. Khayat, M. Landis, J. Molaro, M. Slipski, S. Valencia, J. Watkins, C. Young, C. Budney and K. Mitchell, “OCEANUS: A high science return Uranus orbiter with a low-cost instrument suite,” *Acta Astronautica,* 2018.

[67] NASA Goddard Space Flight Centre, “Voyager 2,” 29 09 2021. [Online]. Available: https://nssdc.gsfc.nasa.gov/nmc/spacecraft/display.action?id=1977-076A. [Accessed 07 10 2021].

[68] J. Brophy, “The Dawn Ion Propulsion System,” in *The Dawn Mission to Minor Planets 4 Vesta and 1 Ceres*, Springer, 2011, pp. 251-261.

[69] NASA Science, “Basics of Space Flight - Section 1: Environment, Chapter 4: Trajectories,” [Online]. Available: https://solarsystem.nasa.gov/basics/chapter4-1/. [Accessed 23 11 2021].

[70] “NASA Launch Services Program Launch Vehicle Performance Website,” NASA, [Online]. Available: https://elvperf.ksc.nasa.gov/Pages/Query.aspx. [Accessed 17 3 2021].

[71] C. J. Hargis, “The X-20 (Dyna-Soar) Progress Report,” U.S. Air Force, 1964.

[72] C. Colombo, “Orbital Mechanicals Lecture Notes, Section 6: Orbit Pertubations,” Politecnico di Milano, Milano, 2019.

[73] Millour, F. F. E, A. Spiga, M. Vals, V. Zakharov, L. Montabone, F. Lefevre, F. Montmessin, J. Chaufray, M. Lopez-Valverde, F. Gonzalez-Galindo, S. Lewis, P. Read, M. Desjean and F. Cipriani, “The Mars Climate Database (Version 5.3),” in *Scientific Workship: "From Mars Express to ExoMars"*, Madrid, 2018.

[74] J. Anderson, Modern Compressible Flow, McGraw-Hill Education, 2002.

[75] M. Capitelli, G. Colonna, D. Giordano, L. Marraffa, A. Cassavola, P. Minelli, D. Pagano, L. Pietanza and F. Taccogna, “High-Temperature Thermodynamic Properties of Mars-Atmosphere Components,” *Journal of Spacecraft and Rockets,* vol. 42, no. 6, pp. 980-989, 2005.

[76] W. Page and H. Woodward, “Radiative and Convective Heating During Venus Entry,” *American Institution of Aeronautics and Astronautics Journal,* vol. 10, no. 10, pp. 1379-1381, 1972.

[77] A. Verhoff, “Numerical Simulation of Transitional, Hypersonic Flows Using a Hybrid Particle-Continuum Method, PhD Dissertation,” The University of Michigan, 2015.

[78] Y. Shevelev, “Numerical Modeling of Hypersonic Aerodynamics and Heat Transfer Problems of the Martian Descent Modules,” in *Advances in Some Hypersonic Vehicle Technologies*, IntechOpen, 2017.

[79] M. Tauber and J. Bowles, “Use of Atmospheric Braking During Mars Mission,” *Journal of Spacecraft,* vol. 27, no. 5, pp. 514-521, 1989.

[80] Y. Babou, R. P, M. Perrin and A. Soufiani, “Spectroscopic Data for the Prediction of Radiative Transfer in CO2-N2 Plasmas,” *Journal of Quantitative Spectroscopy & Radiative Transfer,* vol. 110, pp. 89-108, 2008.

[81] C. Ho, N. Golshan and A. Kiore, “Chapter 4 - Mars Atmospheric Gaseous Attenuation,” in *Radio Wave Propagation Handbook for Communication on and Around Mars*, NASA JPL, 2002, p. 45.

[82] J. Moss and A. Simmonds, “Galileo Probe Forebody Flowfield Predictions During Jupiter Entry,” in *AIAA/ASME 3rd Joint Thermophysics, Fluids, Plasma and Heat Transfer Conference*, St. Louis, 1982.

[83] J. Anderson, “An Engineering Survey of Radiating Shock Layers,” *Journal of Spacecraft and Rockets,* vol. 7, no. 9, pp. 1665-1675, 2003.

[84] NASA, “Lecture #1: Stagnation Point Heating,” in *NASA Thermal & Fluids Analysis Workshop*, 2012.

[85] San Diego Air and Space Museum Archive, “SDASM Archives - Space Shuttle Program,” 04 05 2012. [Online]. Available: https://www.flickr.com/photos/sdasmarchives/7142851749/in/photostream/. [Accessed 27 10 2021].

[86] R. Barton, “Dyna Soar Launchers,” 16 07 2005. [Online]. Available: https://commons.wikimedia.org/wiki/File:Dyna_Soar_launchers.png. [Accessed 27 10 2021].

[87] Amos and Jonathan, “NASA's Rover Makes Breathable Oxygen on Mars,” BBC, 22 04 2021. [Online]. Available: https://www.bbc.com/news/science-environment-56844601. [Accessed 2 11 2021].

[88] Y. Yin, T. Yang, Z. Li, E. Devid, D. Auerbach and A. Kelyn, “CO2 Conversion by Plasma: How to Get Efficient CO2 Conversion and High Energy Efficiency,” *Physical Chemistry Chemical Physics,* vol. 23, pp. 7974-7987, 2021.

[89] G. Rogers, S. Flanigan and D. Stanbridge, “Effects of Radiosotope Thermoelectric Generator on Dynamics of the New Horizons Spacecraft,” *Advances in the Astronautical Sciences,* vol. 151, 2014.

[90] Space.com, “US Military Video Shows Hypersonic Aircraft Test Flight,” 25 08 2011. [Online]. Available: https://www.space.com/12739-video-hypersonic-military-aircraft-flight-darpa-htv2.html. [Accessed 31 10 2021].

[91] NASA, “Reinforced Carbon-Carbon (RCC) Panels,” [Online]. Available: https://www.nasa.gov/centers/kennedy/pdf/167435main_RCCpanels-06.pdf. [Accessed 31 10 2021].

[92] F. Matthews and R. Rawlings, “Ceramic Matrix Composites,” in *Composite Materials: Engineering and Science*, Woodhead Publishing, 1999, pp. 118-167.

[93] E. Roth, R. Watson, M. Moss and W. Drotning, “Thermophysical Properties of Advanced Carbon Materials for Tokamak Limiters,” Sandia National Laboratories, 1989.

[94] NASA, “SP-8115 Solid Rocket Motor Nozzles,” NASA, 1975.

[95] J. Randolph, M. Davis, T. Leavens and R. Miyake, “A Waverider Application of an Advanced Nuclear Power Source,” NASA JPL, Pasadena, California, USA, 2005.

[96] M. Postlethwait, K. Sikka, M. Modest and J. Hellmann, “High Temperature, Normal Spectral Emittance of Silicon Carbide Based Materials,” *Journal of Thermophysics and Heat Transfer,* vol. 8, no. 3, pp. 412-418, 1994.

[97] Morgan Thermal Ceramics, “Denka Alcen Blankets,” 02 2016. [Online]. Available: https://www.morganthermalceramics.com/media/2075/denkar_alcenr_blankets.pdf. [Accessed 19 11 2021].

[98] S. Bankoff and H. Pauske, “Improved Prediction of Critical Heat Flux in Liquid Metal Pool Boiling,” in *5th International Heat Transfer Conference*, Tokyo, 1974.

[99] L. Yong-Bum, H. Hahn, W. Chang and Y. Kwon, “US Department of Energy Office of Scientific and Technical Information,” 09 1999. [Online]. Available: https://www.osti.gov/etdeweb/servlets/purl/20101192. [Accessed 15 11 2021].

[100] Thermal-FluidsPedia, “Thermophysical Properties: Lithium,” Thermal-Fluids Central, [Online]. Available: https://thermalfluidscentral.org/encyclopedia/index.php/Thermophysical_Properties:_Lithium. [Accessed 5 11 2021].

[101] D. Wolf, F. Incropera and R. Viskanta, “Jet Impingement Boiling,” in *Advances in Heat Transfer Volume 23*, Academic Press, 1993.

[102] I. Silverman, A. Yarin, S. Reznik, A. Areshtam, D. Kijet and A. Nagler, “High Heat-Flux Accelerator Targets: Cooling with Liquid Metal Jet Impingement,” *International Journal of Heat and Mass Transfer,* Vols. 2782-2792, p. 49, 2006.

[103] N. Zuckerman and N. Lior, “Jet Impingement Heat Transfer: Physics, Correlations, and Numerical Modeling,” *Advances in Heat Transfer,* vol. 39, pp. 565-631, 2006.

[104] T. O'Donovan and D. Murray, “Jet Impingement Heat Transfer - Part I: Mean and Root-Mean-Square Heat Transfer and Velocity Distributions,” *International Journal of Heat and Mass Transfer,* vol. 50, pp. 3291-3301, 2007.

[105] A. Cox and R. Brown, “Protection of Molybdenum from Oxidation by Molybdenum Disilicide Based Coatings,” *Journal of the Less-Common Metals,* vol. 6, pp. 51-69, 1963.

[106] M. Levy, “A Protective Coating System for a TZM Alloy Re-Entry Vehicle,” US Army Materials Research Agency, 1965.

[107] Plansee, “Molybdenum,” [Online]. Available: https://www.plansee.com/en/materials/molybdenum.html. [Accessed 09 11 2021].

[108] L. Lundberg, “A Critical Evaluation of Molybdenum and Its Alloys for Use in Space Reactor Core Heat Pipes,” Los Alamos Scientific Laboratory, Los Alamos, New Mexico, 2918.

[109] ANSYS Inc., “Forced Convection Over a Flat Plate,” 2020.

[110] J. Lienhard, “Liquid Jet Impingement,” in *Annual Review of Heat Transfer*, Begell House, 1995, p. Chapter 6.

[111] A. Krakoviak, “Notes on the Liquid-Metal Boiling Phenomenon,” Oak Ridge National Laboratory, 1963.

[112] “Thermophysical Properties: Sodium,” Thermal-Fluids Central, [Online]. Available: https://www.thermalfluidscentral.org/encyclopedia/index.php/Thermophysical_Properties:_Sodium. [Accessed 17 11 2021].

[113] “Molybdenum - Mechanical Properties and Material Application,” AZO Materials, 20 12 2012. [Online]. Available: https://www.azom.com/article.aspx?ArticleID=7637. [Accessed 25 11 2021].

[114] C. Bergin, “X-33 VentureStar, What really happened,” NASA Spaceflight.com, 04 01 2006. [Online]. Available: https://www.nasaspaceflight.com/2006/01/x-33venturestar-what-really-happened/. [Accessed 24 11 2021].

Appendix A

The material data sheet for the Denka Alcen NBK80 is provided below. Several layers of such an insulation blanket were used in the analysis of the insulated regions of the vehicle. The full document can be found at Reference [97].

Denka® Alcen® Blankets

Blanket Product Name	Denka Alcen NBK80	Denka Alcen NBK95
Fiber Class	PCW	PCW
Physical Properties		
Color	white	white
Classification Temperature, °F	2912	2912
Classification Temperature, °C	1600	1600
Melting Temperature, °F	3632	3632
Melting Temperature, °C	2000	2000
Density, pcf	6, 8	6
Denisty, kg/m^3	96, 128	96
Fiber diameter, µm	3-5	3-5
Linear shrinkage, %		
After 24 hrs, isothermal heating @ 2500°F (1371°C)	<1	-
After 24 hrs, isothermal heating @ 2912°F (1600°C)	1.5	-
Chemical Analysis, % weight basis after firing		
Alumina, Al_2O_3	80	95
Silica, SiO_2	20	5
Other	trace	trace
Thermal Conductivity, BTU•in/hr•ft^2, per ASTM C201		
Density, pcf	6	6
500°F	0.38	-
1000°F	0.74	-
1500°F	1.3	-
2000°F	2.07	-
2500°F	3.04	-
Thermal Conductivity, W/m•K, per ASTM C201		
Density, kg/m^3	96	96
260°C	0.05	-
538°C	0.11	-
816°C	0.19	-
1093°C	0.3	-
1371°C	0.44	-

Appendix B

Reproduced below are selected tables and images from Randolph et al [95] detailing the vehicle requirements for their study and the resulting power and mass breakdowns, as well as an illustration of the vehicle architecture.

TABLE 1. Waverider Vehicle Design Requirements.

TOPIC	REQUIREMENT
Aerodynamic Performance	High L/D Ratio (> 8) at M > 30
Aerodynamic Stability	CG forward of CP lg/lp = 1.2 lg = distance from the aft bulkhead to the CG lp = distance from the aft bulkhead to the CP
Thermal Protection	Stagnation temperature ≥ 5000K Leading edge materials and boundary layer design, T ≥ 5000K
Thermal Control of Avionics	250K ≤ T ≤ 300K
Avionics Packaging	Volume ≤ $2m^3$
Instrument Accommodation	Volume ≤ $6m^3$

TABLE 2. Wavrider Power Requirements and Modes.

Power Modes:									
A	Cruise without tracking data								
B	Cruise with data return								
C	Propulsive maneuvers								
D	AGA Atmospheric pass								
E	Science data acquisition								
F	Science data playback								
Power Loads:	CBE	Contingency	Design reqr.	Power Modes					
	(W)	%/100	(W)	**A**	**B**	**C**	**D**	**E**	**F**
CDH									
CPU	8	0.3	10	8	8	7	8	8	8
Camera & Memory boards	5	0.3	6.5	-	6.5	-	-	6.5	6.5
Aero Actuator Control board	5	0.3	6.5	-	-	-	6.5	-	-
Gimbal Control board	5	0.3	6.5	-	-	-	-	-	-
FPGA	5	0.3	6.5	6.5	6.5	6.5	6.5	6.5	6.5
Backplane	2	0.3	2.5		2.5	2.5	2.5	2.5	2.5
Power Distr. & Control	1.2	0.3	1.5	1.5	1.5	1.5	1.5	1.5	1.5
Battery Control	3	0.3	4	4	4	4	4	4	4
Shunt Radiator Control	0.08	0.3	1	1	1	1	1	1	1
ACS									
Inertial Reference Unit	20	0.3	2.5	-	-	2.5	2.5	2.5	-
Actuators	50	0.3	65	-	-	-	65	-	-
Star Trackers	5	0.3	6.5	6.5	6.5	6.5	-	6.5	6.5
Thermal Control	10	0.3	13	13	13	13	-	13	13
Science									
Camera	2	0.3	2.5	-	-	-	-	2.5	-
Spectrometer	10	0.3	13					13	
Telecom									
Receiver	5	0.3	6.5	-	6.5	-	-	-	6.5
Transmitter	100	0.3	130	-	130	-	-	-	130
Propulsion	10	0.3	13			13			
TOTALS				40.5	186	58	98	68	186

TABLE 4. Waverider Mass Estimates.

ITEM	CBE* Mass (kg)	Heritage
Structure		
Fuselage and Bulkheads	300	New
Thermal Protection	300	New
Power System		
RPS	159	Wylie
Battery	7	New
Control	4	New
Radiator	23	New
Avionics	21	Fox
Actuators & Electronics	27	Fox
Attitude/Propulsion	45	New
Science Telescope & Instruments	60	New
Telecommunications	30	New
Subtotal	976	
Reserves (30%)	293	New
TOTAL	1268	
ATLAS 521 Performance @ C_3 = 50 km^2/sec^2	1590	
Launch Margin	322	20%

* CBE = Current Best Estimate

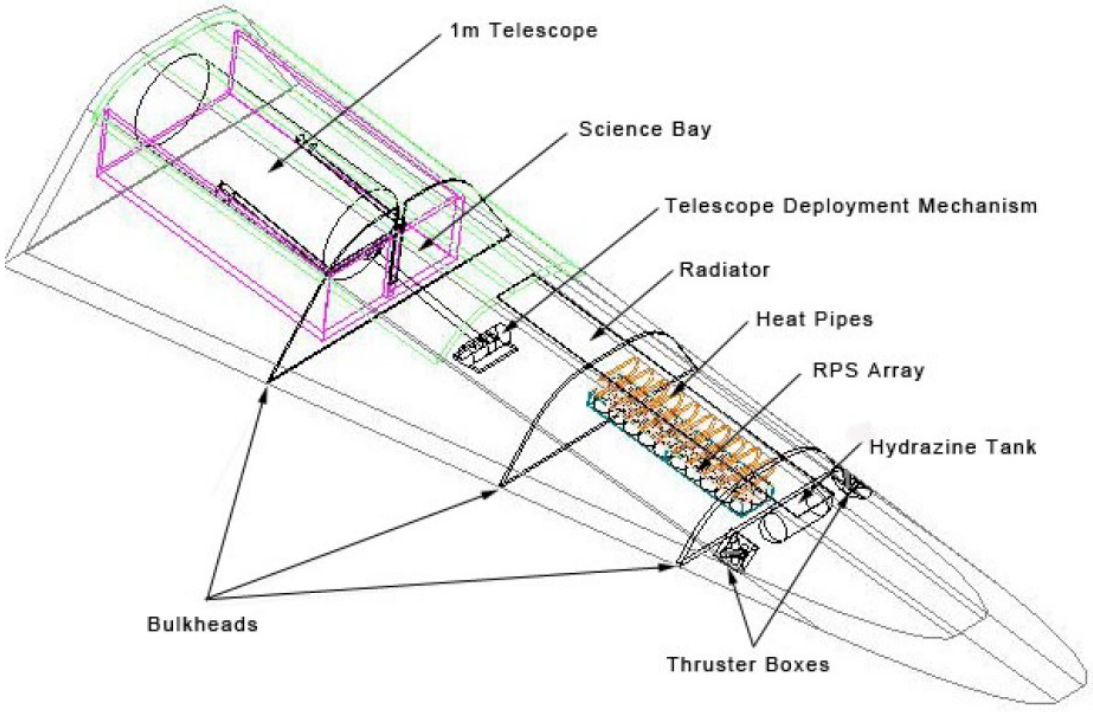

FIGURE 10. Waverider View Showing the Accommodation of the RPS and Other Key Elements.